Multiscale modelling of the action of low salinity



Zachary Wilmott

St Anne's College

University of Oxford

A thesis submitted for the degree of

Doctor of Philosophy

Trinity 2018

Acknowledgements

I would like to thank my supervisors Chris Breward and Jon Chapman for their insight and guidance throughout my studies. Their endless enthusiasm has made this an enjoyable experience, and their attention to detail and continuous encouragement has ensured that I perform to the best of my mathematical ability.

I would like to thank my industrial sponsors BP for sharing their knowledge and welcoming me into their research group. In particular, I would like to thank Bilal Rashid, John Couves, Tim Totton, and Pete Salino for their support throughout this project.

I would also like to thank my good friends and colleagues Andrew Krause and Michael Gomez for providing an invaluable source of knowledge and advice, and for allowing me to distract them when they had much more important things to be doing.

Finally, I would like to thank my family for their support and understanding, especially my partner Rebecca for her encouragement and patience throughout my PhD studies.

Abstract

Experimental evidence shows that injecting low salinity water into an oil reservoir can lead to an increase in the amount of oil recovered. However, due to the complexity of the chemical interactions involved in this process, there has been much debate over the dominant mechanism causing this effect. Numerous mechanisms have been proposed, and, in recent years, one which has gained notable support is the multicomponent ionic exchange (MIE) mechanism.

The aim of this thesis is to understand how the microscale reactions described by the MIE mechanism affect the oil recovery on the macroscopic scale. We first consider a simple two-dimensional model for the motion of an oil slug through a clay pore throat in order to determine the effect of the ion-exchange reactions on the fluid dynamics at the pore scale. We further this investigation by studying two-phase flow through a three-dimensional channel with varying elliptic cross section in the limit in which the water phase is restricted to a thin film between the oil and the surface of the throat. We then investigate the effect of salinity on the permeability of a periodic porous structure for the case in which the water phase is confined to a thin film coating the solid surface, and derive a method for estimating the permeability using a network model. We develop this approach further by presenting a network model for two-phase flow through a porous structure. Finally, we use a discrete form of the method of multiple scales to homogenise our network model and derive a set of continuum equations for the saturation and ion concentrations which are applicable on the macroscopic scale.

Contents

1 Introduction **1**

1.1 Background 1

1.2 Composition of brine, clay, and oil 2

1.2.1 Brine 2

1.2.2 Clay 3

1.2.3 Oil 4

1.3 Low salinity mechanisms 5

1.3.1 Multicomponent Ionic Exchange (MIE) 5

1.3.2 Fines Migration 5

1.3.3 Local pH increase 6

1.3.4 Salting-in 7

1.4 Literature review 8

1.5 Thesis outline 10

1.6 Statement of originality 11

2 The effect of ions on the motion of an oil slug through a capillary **12**

2.1 Introduction 12

2.1.1 Previous work 13

2.2 Model Formulation 15

2.2.1 Governing Equations 17

2.2.2 Boundary Conditions 18

2.2.3 Modelling surface reactions 19

2.2.4 Capturing salinity variations 22

2.2.5 Dimensionless system of equations 24

2.2.6 Dimensionless parameters 26

2.2.7 Typical non-dimensional parameter sizes 28

2.2.8 Dimensionless system, neglecting small terms 28

2.3 Solution to the electrical probem 31

2.3.1 In the oil phase . . . 31
2.3.2 In the clay phase . . . 31
2.3.3 In the water phase . . . 31
2.3.4 In the water phase: Regions I and III . . . 32
2.3.5 In the water phase: Region II . . . 34
2.3.6 In the water phase: Regions IV and V . . . 35
2.3.7 Expressions for the surface charge densities . . . 36
2.3.8 Electric potential near the capillary wall . . . 39
2.3.9 Modelling the pH increase mechanism . . . 39
2.4 Solution to the fluid dynamics problem . . . 42
2.4.1 Shape of the oil-water interface at the front end of the oil slug 42
2.4.2 Travelling wave solution . . . 45
2.4.3 Correction to the radius of curvature . . . 46
2.4.4 Shape of the oil-water interface in the transition region . . . 47
2.4.5 Correction to the radius of curvature . . . 48
2.4.6 Macroscopic capillary problem . . . 48
2.4.7 Macroscopic capillary problem: Regions I and III . . . 50
2.4.8 Macroscopic capillary problem: Region II . . . 51
2.4.9 Effective slip . . . 51
2.4.10 Macroscopic flux . . . 52
2.4.11 Solution when $P^* \gg \epsilon_2$ . . . 54
2.4.12 Solution when $P^* \ll \epsilon_2^{3/2}$ . . . 54
2.4.13 Shape of the oil-water interface for large $\epsilon_2^{-3/2} P^*$ . . . 58
2.4.14 Velocity of the oil slug for large $\epsilon_2^{-3/2} P^*$ . . . 59
2.5 Conclusions . . . 59

3 Slip flow through a channel with varying elliptical cross section 62
3.1 Introduction . . . 62
3.1.1 Previous work . . . 64
3.2 Model formulation . . . 65
3.2.1 Governing equations . . . 65
3.2.2 Nondimensionalisation . . . 67
3.2.3 Elliptic coordinates . . . 68
3.3 Solution . . . 69
3.3.1 Flux through the channel . . . 69
3.3.2 Solution for small eccentricity . . . 73

3.3.3 Comparison between flux estimation methods 74
3.4 Flow through irregularly-shaped channels 78
3.4.1 Aissen approximation 79
3.4.2 Hydraulic radius approximation 80
3.4.3 Comparing methods 80
3.5 Conclusions 83

4 Slip flow through a periodic porous structure 85
4.1 Introduction 85
4.1.1 Previous work 87
4.2 Darcy flow with slip boundary condition 88
4.2.1 Governing Equations 89
4.2.2 Non-dimensionalisation 89
4.2.3 Multiple-scales solution 90
4.2.4 Example: Unit cell with simple circular inclusion 94
4.3 Simply-connected periodic domains 97
4.3.1 Simple permeability estimates 97
4.3.2 Slip flow through an irregular channel 100
4.3.3 Estimating the permeability using the flux 103
4.3.4 Comparison between the different geometries 104
4.4 Multiply-connected periodic domains 105
4.4.1 Determining the neighbouring inclusions from an image 107
4.4.2 Extracting the channel network from an image 108
4.4.3 Flux through a network of channels 111
4.4.4 Comparison between the network model and the finite element solution 113
4.5 Conclusions 116

5 Network models of two-phase flow 119
5.1 Introduction 119
5.1.1 Quasi-static network models 120
5.1.2 Semi-dynamic network models 122
5.1.3 Dynamic network models 123
5.1.4 Washburn equation 123
5.1.5 Annular flow 125
5.2 Model formulation 127
5.2.1 Throat saturation 127

5.2.2 Phase-weighted pressure . . . 129
5.2.3 Governing equations . . . 130
5.2.4 Boundary conditions . . . 131
5.3 Model solution . . . 132
5.3.1 Non-dimensionalisation . . . 133
5.3.2 Vector formulation . . . 134
5.4 Waterflood simulation . . . 137
5.4.1 Drainage stage . . . 137
5.4.2 Waterflood stage . . . 139
5.5 Conclusions . . . 143

6 Network homogenisation **146**
6.1 Introduction . . . 146
6.1.1 Previous work . . . 148
6.2 Single-phase, one-dimensional flow . . . 149
6.2.1 Multiple scales . . . 150
6.2.2 Asymptotic solution . . . 151
6.2.3 Flux . . . 152
6.3 Homogenisation of a two-dimensional network, neglecting the effects of entry pressure . . . 153
6.3.1 Multiple scales . . . 156
6.3.2 Pressure . . . 159
6.3.3 Saturation . . . 162
6.3.4 Ion concentrations . . . 166
6.3.5 Results for a one-dimensional network . . . 169
6.4 Homogenisation of a one-dimensional network, including the effects of entry pressure . . . 174
6.4.1 Model formulation . . . 174
6.4.2 Homogenisation . . . 177
6.4.3 Results . . . 182
6.4.4 Comparison with Buckley-Leverett theory . . . 186
6.5 Conclusions . . . 187

7 Conclusions **191**
7.1 Summary of results . . . 191
7.2 Future work . . . 195
7.3 Closing remarks . . . 197

A Transition region boundary conditions **198**

B Capillary-pressure-saturation relationship **201**

C Matrix properties **207**

Bibliography **209**

Chapter 1

Introduction

1.1 Background

The process of recovering oil from a reservoir traditionally comprises three stages. When first drilling into a reservoir, the high pressure in the rock forces out hydrocarbons in the form of gases and oils; this process is referred to as primary oil recovery. Eventually, the naturally high pressure in the reservoir drops, and water needs to be injected to maintain the rate at which the oil is retrieved. Typically, seawater is used for this secondary waterflood. However, a high percentage of the oil remains undisturbed, and a tertiary waterflood is often performed to remove some of the oil that can't be recovered using seawater alone. Numerous technologies have been developed for this tertiary recovery stage, such as alkaline flooding, polymer flooding, and gas injection. One technology which is particularly appealing due to its ease of implementation is the use of low salinity water as either a secondary or tertiary process.

Research into the effects of brine composition on a reservoir waterflood began during the late 1980s and early 1990s with the work of Buckley *et al.* [19] and Jadhunandan [43] in an effort to understand which factors increase water wettability. They observe that a change in the injected brine composition could lead to significant changes in the recovery rate, and that this is dependent on both the composition of the connate brine (the brine present in the reservoir before any waterflooding has taken place) and the types of oil present. Further experimental research was undertaken during the 1990s [44, 45, 124, 125] to confirm these results and determine the conditions necessary for an increase in oil recovery. A good summary of these requirements is given by Austad *et al.* [7]. However, the key requirements for achieving an increase are:

- Clay minerals must be present in the porous medium, since no effect is observed in pure carbonates.
- Polar compounds must be present in the oil, since no effect is observed for refined oils, such as mineral oil, which are free from polar components.
- Connate water must be present in the reservoir, and it must contain divalent ions (Ca^{2+}, Mg^{2+}).

Despite the fact that the conditions required for a low salinity waterflood to be effective are relatively well understood, there is little consensus on the dominant causal mechanism underlying the process. A number of possible mechanisms have been proposed over the last couple of decades, but there is little theoretical understanding of how to quantitatively relate the various microscale low salinity mechanisms to the macroscopic oil recovery process. Without a framework to connect the microscale to the macroscale, it is difficult to accurately determine the dominant process. Our aim is to model mathematically one proposed mechanism, multicomponent ionic exchange, at the microscale and, using a number of upscaling methods, to determine the effect of this mechanism on the macroscopic scale.

In order to better understand the various low salinity mechanisms which have been proposed, we first review the composition of brine, clay, and oil, and provide some background information about how they interact in an oil reservoir.

1.2 Composition of brine, clay, and oil

1.2.1 Brine

Brine used in low salinity waterflooding is an aqueous solution of both monovalent and divalent ions, such as Na^+, Cl^-, Ca^{2+}, and Mg^{2+}. Various experiments have been conducted to determine the dependence of the amount of oil recovered during a waterflood on the composition of both the connate brine and the injection brine [44, 45]. In order to observe an increase the amount oil recovered, divalent ions must be present in the connate brine, and a reduction in the concentration of the divalent ions in the injection brine is necessary. Typical concentrations are between 1000-2000 ppm for Na^+ and Cl^- in low salinity water, and above 10,000 ppm in high salinity water. Concentrations of Mg^{2+} and Ca^{2+} range from approximately 20 ppm in low salinity water up to 500 ppm in high salinity water.

1.2.2 Clay

Clays within an oil reservoir usually have an overall surface charge, which can be split into two categories; permanent and pH dependent [30, 73]. The permanent charge is primarily due to ion substitution at the surface, but may also be the result of imperfections in the clay structure. Ion substitution occurs when a positively-charged cation in the clay structure is replaced by a cation with a lower valency, resulting in a negatively charged site on the clay surface. This is typically due to either Si^{4+} ions being replaced by Al^{3+} ions, or Al^{3+} ions being replaced by Mg^{2+} or Fe^{2+} ions.

There may also be a pH-driven surface charge due to hydroxyl groups on the surface undergoing the following dissociation reactions,

$$\text{Clay-OH} + H^+ \rightleftharpoons \text{Clay-OH}_2^+, \tag{1.1}$$

$$\text{Clay-OH} + OH^- \rightleftharpoons \text{Clay-O}^- + H_2O. \tag{1.2}$$

Depending on the pH of the surrounding fluid, either one of the mechanisms described in (1.1) or (1.2) may occur, resulting in either a positively or negatively charged site on the surface of the clay. However, for most clays, the effect of this pH-driven charge is negligible in comparison with the permanent charge induced by ion exchange. Hence, throughout this thesis we will assume that the sites on the clay surface are negatively charged.

Solvated cations in the surrounding fluid are attracted to the negatively charged sites on the clay surface. Due to the different ion sizes and charges, some ions bond to the sites more readily than others. The preferential order of bonding is [7]

$$Li^+ < Na^+ < K^+ < Mg^{2+} < Ca^{2+} < H^+. \tag{1.3}$$

As the concentration of the different ion species varies in the bulk of the fluid, ions may adsorb or desorb from the negatively charged sites in order to balance the diffusion within the fluid with the attraction to the surface. Hence, we refer to these sites as 'exchange sites' due to the exchange which may occur between the different ion species.

The positively-charged cations which bond to the negatively-charged exchange sites act to partially neutralise the surface charge of the clay. The remaining charge attracts counterions to the surface, and a diffuse layer of ions is formed. This shields the remaining surface charge from the bulk of the fluid [1, 5, 92]. This diffuse layer,

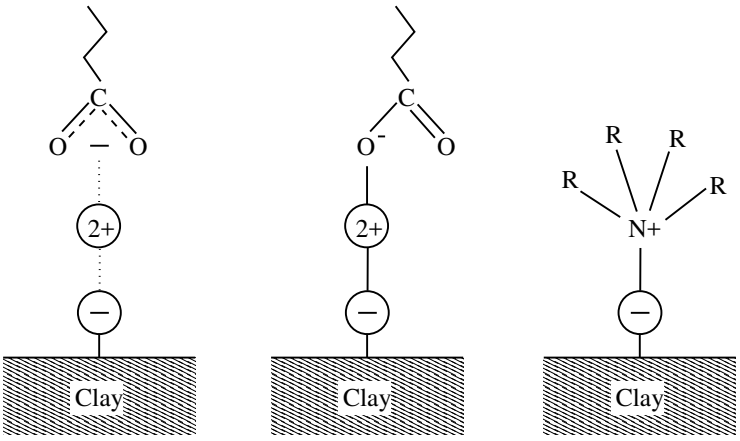


Figure 1.1: Schematic diagram of the bonding mechanisms between oil and clay. From left to right: Cation bridging, ligand exchange, cation exchange.

known as the 'electric double layer', typically has a thickness determined by the Debye length, λ_D, which is given by

$$\lambda_D = \left(\frac{\epsilon k_B T}{\sum_i c_i z_i^2 q^2} \right)^{1/2}, \tag{1.4}$$

where ϵ is the permittivity of the surrounding fluid, k_B is Boltzmann's constant, T is the temperature, c_i is the bulk concentration of ion i, z_i is the valence of ion i, and q is the charge of an electron.

1.2.3 Oil

Crude oils found in petroleum reservoirs are a mixture of many compounds, and the composition may vary greatly between different regions. However, crude oils will often contain polar compounds, which results in the presence of a number of charged sites along the oil-water interfaces within a reservoir. Ions in the salt solution may interact and bond with these charged sites, which enables the oil to bond to the clay molecules present within a reservoir by cation bridging and ligand exchange across the thin water layer which separates the oil from the clay surface. Cation bridging occurs when a divalent ion weakly bonds to both a negative site on the clay surface and a negatively charged polar functional group on the oil surface, and ligand exchange occurs when a carboxylate group on the oil surface bonds to a multivalent ion adsorbed on the clay surface. Cation exchange, in which a quaternized nitrogen group or heterocyclic ring in the oil replaces a cation on the clay surface, also occurs but to a lesser extent. A schematic diagram of these bonding mechanisms is shown in Figure 1.1.

Experimental evidence suggests that polar compounds must be present in the oil in order for a low salinity injection to be effective [7]. Since the presence of polar compounds affects the bond between the oil and the clay, a number of authors believe that the dominant mechanism causing the low salinity effect occurs along the oil-clay interface [7, 12, 60, 62, 98].

1.3 Low salinity mechanisms

A number of mechanisms have been proposed to explain the low salinity effect. In this section, we briefly review some of these proposals and discuss some of the evidence which supports or opposes them.

1.3.1 Multicomponent Ionic Exchange (MIE)

Lager *et al.* [60] propose the multicomponent ionic exchange (MIE) mechanism to explain the low salinity effect. They suggest that the increased recovery observed during a low-salinity injection is the result of two processes. First, the electric double layer expands in the low salinity regime, which causes the thin wetting layer between the oil and the clay to expand. This weakens the bonds between the oil and the clay formed by cation bridging and ligand exchange. Second, reducing the concentration of divalent ions in the bulk encourages the desorption of these ions at the surface. This allows monovalent ions to adsorb at the exchange sites, which reduces the overall attraction of the oil to the clay surface.

To test their mechanism proposal experimentally, Lager *et al.* [60] flush a core sample repeatedly with brine containing only NaCl until all of the multivalent cations present on the mineral surface have been replaced by Na^+. They then perform a high salinity waterflood followed by a low salinity waterflood on the sample, and compare the results with a waterflood performed on a conventional sample (i.e. a sample with divalent cations present on the mineral surface). They observe that the removal of divalent cations prior to waterflooding leads to a higher recovery, irrespective of the salinity of the injection water. This suggests that the low salinity effect occurs due to the exchange of divalent cations on the mineral surface, which supports the MIE mechanism.

1.3.2 Fines Migration

During the injection process, fines (small particles of clay) attached to the pore walls within a reservoir may become detached and move with the fluid. The tendency of

fines to be stripped from a pore wall depends on the strength of the colloidal forces between the fine particles and the wall. When the salinity in the surrounding fluid is reduced, the electrical double layer in the aqueous phase between the fines and the wall expands. This reduces the strength of the colloidal forces and increases the tendency for the fines to become detached from the pore wall. Tang and Morrow [101] suggest that this leads to an increase in the oil recovered due to a combination of the following effects:

- *Surface oil removal.* Oil attached to the surface of the pore is removed with the fine, resulting in greater oil recovery.

- *Surfactant.* If the fine is oil wet when attached to the pore wall, once it is displaced the previously unwetted part of the fine will become water wet which enables it to act as a surfactant at the oil-water interface. A reduction in the oil-water surface tension leads to greater mixing of the oil-in-water emulsion, and therefore to an increase in the amount of oil recovered.

- *Permeability alteration.* The fines removed will be transported with the fluid, potentially blocking up pores with a high flow through them that have already been flushed of oil. This leads to a pressure increase, as well as forcing the water to find new paths through the pores. Hence, oil that had previously been missed can be recovered.

However, in tests performed by Lager *et al.* [60], there were many cases in which an increase in the amount of oil recovered was observed, but no fines migration or significant permeability reduction occurred. This suggests that, although fines migration may contribute to the low salinity effect, it isn't the dominant causal mechanism.

1.3.3 Local pH increase

During a low salinity injection, some studies have observed an increase in the pH of the brine [7, 60]. This is due to two mechanisms:

- *Cation exchange.* As low salinity water is injected, there is a net desorption of cations such as Ca^{2+} and Mg^{2+} at the clay surface due to the lower concentration of ions in the bulk of the fluid. The now vacant exchange sites at the clay surface attract H^+ present in the water, leading to a local pH increase close to the clay surface. The reaction is of the form

$$\text{Clay-M}^{n+} + \text{H}_2\text{O} \rightarrow \text{Clay-H}^+ + \text{M}^{n+} + \text{OH}^-, \tag{1.5}$$

where M is the ion type and n is the valence.

- *Carbonate dissolution.* Dissolution of calcium carbonate leads to a global pH increase through the following reactions;

$$\mathrm{CaCO_3} \rightleftharpoons \mathrm{Ca^{2+}} + \mathrm{CO_3^{2-}}, \tag{1.6}$$

$$\mathrm{CO_3^{2-}} + \mathrm{H_2O} \rightleftharpoons \mathrm{HCO_3^-} + \mathrm{OH^-}. \tag{1.7}$$

  This is a much slower process than the cation exchange mechanism and depends on the amount of carbonate present, so it is generally assumed that cation exchange is the primary cause of pH increase.

Austad *et al.* [7] suggest that the local pH increase encourages the following reactions which result in oil detaching from the clay surfaces,

$$\text{Clay-NHR}_3^+ + \mathrm{OH^-} \rightleftharpoons \text{Clay} + \mathrm{NR_3} + \mathrm{H_2O}, \tag{1.8}$$

$$\text{Clay-RCOOH} + \mathrm{OH^-} \rightleftharpoons \text{Clay} + \mathrm{RCOO^-} + \mathrm{H_2O}, \tag{1.9}$$

where R is a non-polar hydrocarbon chain. However, Lager *et al.* [60] argue that due to (i) proton buffering, in which $\mathrm{H^+}$ is desorbed from oxides and organic matter, and (ii) the presence of $\mathrm{CO_2}$, which acts a pH buffer, the pH increase during a low salinity injection is not significant enough to have an effect on the amount of oil being released.

1.3.4 Salting-in

Salt ions in the water surrounding an oil droplet may bond to carboxylic groups in the oil by the following dissociation reaction,

$$\mathrm{RCOONa} \rightleftharpoons \mathrm{RCOO^-} + \mathrm{Na^+}. \tag{1.10}$$

In low-salinity water, due to the global shift in the concentration of cations in the brine, salt ions desorb from the carboxylic groups in the oil. Since the non-polar hydrophobic hydrocarbon chain, R, is soluble in the oil, and the hydrophilic polar end, $\mathrm{COO^-}$, is soluble in water by ion-dipole interactions, this decreases the interfacial tension which enables the formation of an oil-in-water emulsion. An increase in the amount of oil recovered is caused by the increased solubility of the oil [72, 85].

1.4 Literature review

Our investigation into the effect of salinity on the oil recovery process spans multiple lengthscales. We will provide a comprehensive review of the relevant literature to the problem we are considering at the start of each chapter. However, in this section, we give an overview of the existing literature which relates to the various models we will study throughout this thesis.

The majority of experimental studies which investigate the effect of salinity on the oil recovery process utilise core-scale experiments, in which a sample of reservoir rock, a cylindrical 'core', approximately 10 cm $\times$ 4 cm^2, is waterflooded with brine [43, 44, 45, 60, 67, 84, 124, 125]. By studying the amount of oil produced during coreflood experiments, and the composition of the brine produced at the outlet for different oil, rock, and inlet brine compositions, these experiments provide a basis for the understanding of the requirements for effective low salinity oil recovery which we outlined in §1.1 – §1.3.4. As an alternative to a coreflood experiment, Berg *et al.* [12] pass water over oil on a clay surface and demonstrate the weakening of the adhesion forces between the oil and clay in the low salinity regime. They observe that the oil droplets lift from the clay surface as the salinity of the surrounding fluid reduces. These results support the surface reaction-based mechanisms such as pH increase and MIE.

A key component in the surface-based mechanisms, such as MIE, is the expansion of the thin water film between the oil and clay. Lee *et al.* [62] use Small Angle Neutron Scattering to measure the thickness of the film, h^*, for various salinities, and find that h^* increases from 0.9 nm in the high salinity regime to 1.3 nm in the low salinity regime. Theoretical predictions for the thickness of the thin layer of water between the clay and the oil are derived using the Derjaguin-Landau-Verwey-Overbeek (DLVO) theory of colloidal stability [26, 108]. For example, Hirasaki [39] presents a method for determining the film thickness by balancing van der Waals, electrostatic, and structural forces within the water layer for a two-dimensional interface. Wong *et al.* [119] extends this work to three-dimensional capillaries for a general disjoining pressure. For a moving fluid, additional contributions to the film thickness come from the viscous effects of the fluid motion. These effects were first studied in the context of the motion of a gas bubble through a capillary tube by Bretherton [15], and this work was later developed by Tanner [102] to describe the spreading of oil on a horizontal surface.

The salinity-dependent thickness of the aqueous layer between the oil and the clay within a reservoir affects the motion of the oil through the pore spaces. The motion of a fluid through a prewetted capillary in the presence of a disjoining pressure has been previously studied by Egorov *et al.* [28] and Starov *et al.* [99]. However, electrostatic effects are neglected in these models. On the other hand, Kuchin *et al.* [59] study the profile of a static capillary meniscus with the inclusion of electrostatic effects. Hodges and Jensen [40] study the viscous spreading of a biological cell, combining the effects of adhesion and viscous fluid motion in their model. However, the attractive force between the cell and the surface in their model is of a different form from the electrostatic ion-exchange reactions we are concerned with.

There are a number of approaches for upscaling the dynamics within a single pore to the scale of a porous structure. Whitaker [113, 114] uses a volume-averaging method to homogenise single-phase and two-phase flow in porous media. For the single-phase case they recover the Darcy model, and determine a closure problem for the permeability of the structure. In the two-phase case, they derive a set of momentum equations which govern the macroscale flow, and define a closure problem for the coefficients in the equation. However, the solution to this closure problem is restricted to the steady flow case since the position of the fluid-fluid interface is unknown when the flow is unsteady. For this reason, the majority of homogenisation approaches are restricted to the single flow case. However, further progress can be made for the case in which the water phase is limited to a thin film along the solid surface, which results in an effective slip boundary condition for the oil phase. For example, Valdes-Parada *et al.* [105] use volume averaging to homogenise slip-flow through a porous structure, and derive a Darcy-Brinkman type equation [16] on the macroscopic scale. Skjetne & Auriault [97] use the method of multiple scales to homogenise wall-slip gas flow through a porous structure, and derive a Darcy-Klinkenberg equation for the macroscopic flow [51].

As an alternative to homogenisation, a number of authors study the interaction of multiple flow paths in porous medium using network models of two-phase flow [24, 46, 53, 93]. In this approach, the motion of each phase occurs discretely according to a microscale model for the flow. Dahle & Celia [24] and Koplik & Lasseter [53] model the two-phase flow of oil and water by tracking the motion of each phase. They define a set of displacement rules to determine when each phase enters or leaves a pore. In contrast, Joekar-Niasar *et al.* [46] and Sheng & Thomson [93] study an annular flow model in which each phase is present throughout the network, and they track the saturation. While the use of network models enables the study of multiphase

flow through a porous structure, they can be extremely computationally expensive to run. However, there exist techniques for deriving continuum equations from network models using a discrete form of the method of multiple scales [14, 21, 49, 56]. This method is typically used to homogenise network models of particle motion on a lattice in order to determine the effective macroscale diffusivity. However, Kropat & Meyer-Nieberg [57] successfully use this approach to homogenise a network model in which the microscale is governed by a system of singularly perturbed diffusion-advection-reaction equations.

1.5 Thesis outline

In this thesis, we will derive a number of mathematical models spanning multiple length scales to describe the effect of salinity on the oil recovery process. In Chapter 2, we will present a model for the motion of an oil slug through a brine-filled clay pore throat. We will model the multicomponent ionic exchange mechanism using an ion dissociation model in order to derive expressions for the surface charges of the oil and clay surfaces as functions of the salinity. We will show that the thin water layer separating the oil from the clay supplies an effective slip boundary condition to the pore-scale motion of the oil slug, and that the slip length depends on the salinity of the brine. We will determine the velocity of the oil slug through the throat as a function of the salinity. In Chapter 3, we will study slip flow through a channel with varying elliptic cross section in order to understand the effect of the throat geometry on the motion of oil through a pore throat in the presence of a thin water layer. We will present two new methods for using our analytical solution for the flux through a channel with varying elliptical cross section to estimate the flux through a throat with arbitrary shape. We will compare our methods with existing flux-estimation methods for both elliptical pore throats and an arbitrarily-shaped pore throat. In Chapter 4, we will study slip flow through periodic porous structures. We will present a method for estimating the permeability of a periodic structure for the case in which the repeated cell contains a single inclusion. We will extend this result to porous structures constructed from unit cells containing multiple inclusions by modelling the cell as a network of pores and throats. In Chapter 5, we will develop a network model for the two-phase flow of oil and water through a porous medium, in which we include the effect of salinity by imposing a slip boundary condition on the oil phase. We will derive a simple expression for the local capillary-pressure-saturation curve within a square pore. We will include the effects of entry pressure in our model by

imposing that oil can only enter a downstream throat if the capillary pressure within the upstream pore exceeds the entry pressure of the throat. We will numerically simulate a waterflood process, separating the process into a drainage stage (in which oil invades a water-filled network by the action of capillary forces) and a waterflood stage (in which water is injected into an oil-filled network). In Chapter 6, we will use the method of multiple scales to homogenise the network model we develop in Chapter 5. We will first demonstrate how to apply this method to a two-dimensional network by neglecting the effects of entry pressure from our model, before homogenising a one-dimensional version of our full network model, including the effects of entry pressure. We will compare our homogenised model with our full network model by numerically simulating high-salinity and low-salinity waterfloods. We will derive an expression for the residual oil saturation as a function of the salinity, from which we will compute the total oil recovered. Finally, in Chapter 7, we will summarise the results from the previous chapters and discuss future extensions to our work.

1.6 Statement of originality

The research described in this thesis was performed in the Mathematical Institute at the University of Oxford between July 2014 and September 2018, and was supervised by Professor Chris Breward and Professor Jon Chapman.

At the time of submission, some of the work in this thesis has been published. A paper based on the oil slug model presented in Chapter 2 has been published in the *Journal of Fluid Mechanics* [117]. The analysis of slip flow through a channel with varying elliptic cross section presented in Chapter 3 has been published in the *IMA Journal of Applied Mathematics* [118]. The analysis and numerical solution in both these papers were carried out by Z. M. Wilmott under the supervision of C. J. W. Breward and S. J. Chapman. Imperial College London provided the Micro-CT data extracted from a sample of Berea sandstone used in Chapter 3, and this is acknowledged. The work in Chapter 4 is original, however the homogenisation of Stokes flow subject to a slip boundary condition in §4.2 is similar to the work by Skjetne & Auriault [97]. In Chapter 5, §5.2 onwards is original work. The work in Chapter 6 is all original, however the homogenisation of the one-dimensional network model of single phase flow presented in §6.2 is similar to the homogenisation of the one-dimensional diffusion equation by Chapman & Shabala [21].

Chapter 2

The effect of ions on the motion of an oil slug through a capillary

2.1 Introduction

One of the main difficulties in determining the dominant mechanism causing the low salinity effect is that the proposed mechanisms, which are typically reaction-based, occur on the molecular scale, whereas the low salinity effect is usually observed during centimetre-scale experiments. In order to accurately interpret the experimental data, and determine the dominant mechanism, the results need to be compared to appropriate, centimetre-scale models for the different mechanisms. In this chapter, we will perform the first steps in deriving such a model using an upscaling process. We will study the two-dimensional steady motion of a charged oil slug through a brine-filled clay pore throat, assuming that multicomponent ionic exchange (MIE) reactions occur on the oil and clay surfaces. Through this model, we will determine how the molecular-scale surface reactions affect the movement of oil on the pore scale. This will form the basis for the models in subsequent chapters, since, by translating the molecular-scale information into the pore-scale model, we can determine the effect of the salinity on the fluid dynamics directly. This eliminates the need to include the surface reactions at each stage of the modelling process, which simplifies the mathematics, and makes it easier to model alternative reaction-based mechanisms.

Our aim in this chapter is to determine the speed at which the oil slug moves through the pore throat as a function of the salinity of the surrounding brine for a given applied pressure difference across the throat. An increase in the velocity of the oil slug is equivalent to an increase in the effective conductivity of the throat, averaged across the two fluid phases. We anticipate that, on a larger scale, an increase in the conductivity of the pore throats can lead to a greater oil recovery, since this results

in an increase in the relative permeability of the oil phase, which leads to a reduction in the residual oil. However, before we determine the effect of salinity on the larger scale, which is the subject of later chapters, we must first determine the effect of salinity on the pore scale. Since variations in the residual oil are not observed on this scale, we will use the velocity of the oil slug as a proxy for the macroscopic oil recovery, with an increase in the velocity representing a greater recovery.

We will present a mathematical model to describe the motion of the oil slug, which includes a simple model for the reactions occurring between the ions and the oil and clay surfaces. The reactions affect the surface charge densities of the oil-water and clay-water interfaces which, in turn, affect the electrical component of the force acting between them. We focus on the MIE mechanism to highlight the method used to upscale the model from the molecular-scale reactions to the pore-scale motion of the oil slug. However, to show how the method may be applied to alternative reaction-based mechanisms, we will also present a model for the pH increase mechanism, and derive expressions for the surface charge densities in this case.

Using the expressions for the surface charge densities, we will determine the thickness of the water film separating the oil slug from the clay surface, as well as the radii of curvature of the front and rear ends of the oil slug, as functions of the salinity of the surrounding brine. We will then study the macroscopic flow problem to derive an expression for the velocity at which the oil slug moves given a pressure difference along the length of the pore throat. On this scale, the water film is very thin and supplies an effective slip boundary condition for the oil at the clay interface, with the slip length determined by the film thickness. The front and rear menisci radii affect the pressure drop felt by the oil slug, and thus the speed at which it moves through the pore throat. We will solve the model for the velocity of the oil slug, assuming that the ratio of the pressure drop to the disjoining pressure due to the charged surfaces is $O(1)$, and we will compare the results with the asymptotic solution in the limit in which this term tends to zero.

2.1.1 Previous work

Numerous authors have studied the electrostatic interaction between two charged bodies across a thin film [9, 71, 79, 80, 81]. Ben-Yaakov & Andelman [9], and Parsegian & Gingell [81] study the interaction between two charged plates across symmetric electrolytes. They use Poisson-Boltzmann theory to determine the disjoining pressure, considering the cases of prescribed surface charges and surface potentials separately. McCormack *et al.* [71] use a similar approach to determine the interaction

force between differently charged surfaces. Ohshima [79, 80] studies the electrostatic interaction resulting from the overlapping electric field between two charged plates with finite thickness. He considers similarly charged and dissimilarly charged plates, as well as the limits in which the plates have zero and infinite thickness.

Theoretical predictions for the thickness of the thin layer of water between the clay and the oil have been made by balancing the capillary pressure and electro-osmotic pressure [39, 55, 119]. Hirasaki [39] determines the film thickness by assuming that the disjoining pressure, Π, is the same as between two flat plates. He computes Π as sum of the pressure components resulting from electrostatic interactions, van der Waals forces, and structural forces, which he derives using the Derjaguin-Landau-Verwey-Overbeek (DLVO) theory of colloidal stability [26, 108]. Kovscek *et al.* [55] use a similar method to determine the film thickness below an oil droplet, and show that the film thickness can be related to the effective contact angle by integrating the disjoining pressure over the length of the oil-water interface. Wong *et al.* [119] use a similar approach to determine the film thickness and effective contact angle for a three-dimensional menisci.

The expressions often stated for the film thickness are for static models [39, 55, 119, 58, 59]; however, as can be seen by studing the motion of bubbles through capillary tubes [15, 120, 121], or by studying the spreading of droplets on surfaces [102], the film thickness below a moving droplet is dependent on the velocity at which the droplet moves. Bretherton [15] studies the motion of a bubble through a horizontal tube, in which a thin film of fluid separates the bubble from the tube walls. He uses lubrication theory to determine a third-order ODE for the film profile, as well as the speed at which the bubble moves through the tube. Wong *et al.* [120, 121] extend this model to polygonal capillaries, and conclude that, because drag in the capillary arises due to the thin film, corners in capillary do not affect the scaling relationship between the pressure difference and the bubble velocity. Tanner [102] studies the spreading of a droplet on a horizontal surface, assuming a thin film between the droplet and the surface, and derives an equation for the droplet interface.

In our model for the motion of an oil slug, we will combine the effects of the viscous motion with the electrostatic interaction. Hodges and Jensen [40] study a similar problem in the context of the viscous spreading of a biological cell on an adhesive surface. However, the attractive force between the cell and the surface in their model is of a different form from the electrostatic ion-exchange reactions we are concerned with. Egorov *et al.* [28] study the motion of a fluid through a prewetted capillary in the presence of a disjoining pressure, neglecting electrostatic effects due

to the surfaces being charged. They derive a Bretherton-type equation to determine the film profile of the moving interface, as well as the effective contact angle. Starov *et al.* [99] use a similar approach to determine the film profile and velocity of a long oil drop moving through a thin capillary, neglecting electrostatic effects. In contrast, Kuchin *et al.* [58, 59] study the profile of a capillary meniscus with the inclusion of electrostatic effects. In their model, the meniscus is static, and so they do not consider Bretherton effects which will influence the motion of the oil slug.

2.2 Model Formulation

We wish to describe the motion of an oil slug through a clay pore throat filled with saline water, subject to a constant pressure difference, P, across the ends of the pore. We suppose that the pore throat can be represented by a two-dimensional constant-radius tube of length L and height $2R$, and that at each end of the capillary there is a bulk region of water. In this chapter, we suppose that the walls of the tube are straight in order to simplify the mathematics and focus on understanding the chemical and fluid dynamic processes occurring in the pore throat. We will study the effect of uneven surfaces and irregular geometries later in the thesis. We label the oil region by Ω_o, the surrounding water region by Ω_w, and the clay regions bounding either side of the capillary tube by Ω_c, as shown in Figure 2.1. We assume that there is a thin film of water separating the oil from the clay surface along the upper and lower surfaces of the oil slug. The thickness of this water layer is unknown *a priori*; however, we assume that it is thin enough such that, from a macroscopic perspective, there appears to be contact between the oil and the clay. We denote the length of the oil droplet, measured from the apparent contact line at the rear meniscus to the apparent contact line at the front meniscus, by L_o. Taking the origin of our coordinate system to be the lower left corner of the tube, we suppose that the rear apparent contact point has horizontal coordinate x_c, with the extremal positions of the front and rear menisci being x_f and x_r, as shown in Figure 2.2.

In order to capture the effect of the salinity of the water on the motion of the oil slug, we assume that the water phase contains solvated positively and negatively charged ions, with the concentrations of the monovalent and divalent species being $c^{\pm}$ and $c^{2\pm}$ respectively. For simplicity, we assume that the oil phase does not contain any charged particles. We also assume that the capillary wall and the oil-water interfaces contain a number of negatively charged exchange sites at which reactions are allowed to occur.

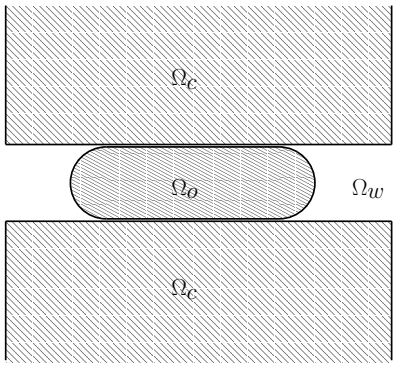


Figure 2.1: Schematic diagram of the macroscopic motion of an oil slug through a capillary between two bulk phases of water.

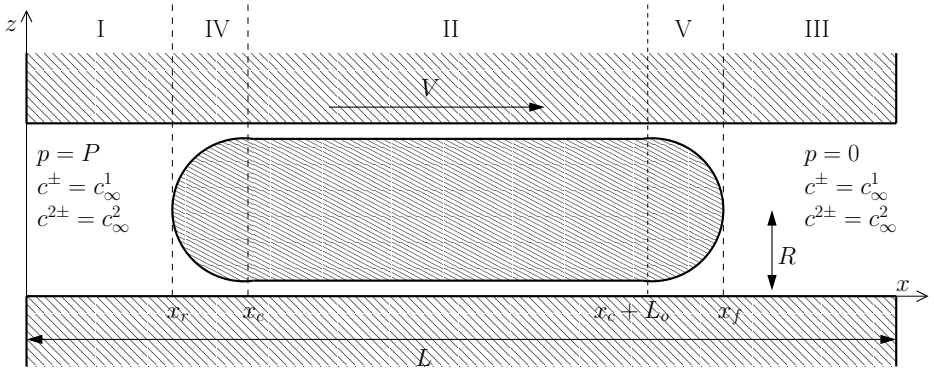


Figure 2.2: Schematic diagram of the problem. The thickness of the water layer below the oil slug has been exaggerated for illustrative purposes.

2.2.1 Governing Equations

Our building blocks for describing the flow of oil and water are the Navier-Stokes equations. Since the capillary and oil surfaces are charged, there is an electric field, $-\nabla\phi$, which induces a body force on the fluid phases, given by the electric field multiplied by the net charge density. Due to the presence of the ions, the net charge density in the water phase is given by the sum of the charge of each ion multiplied by its concentration, $q(c^+ - c^- + 2c^{2+} - 2c^{2-})$, where q is the (absolute) charge of an electron. Since there are no charged particles present in the oil phase, the net charge density in the oil is zero and consequently there is no electrical body force acting on this phase. By including the body force in the equations for the water phase [110, 123], we obtain the modified Navier-Stokes equations, which read

$$\boldsymbol{\nabla} \cdot \boldsymbol{u}_w = 0, \qquad \text{in } \Omega_w, \tag{2.1}$$

$$\rho_w \frac{\mathrm{D}\boldsymbol{u}_w}{\mathrm{D}t} = -\nabla p_w + \mu_w \nabla^2 \boldsymbol{u}_w - q(c^+ - c^- + 2c^{2+} - 2c^{2-})\nabla\phi \qquad \text{in } \Omega_w, \tag{2.2}$$

$$\boldsymbol{\nabla} \cdot \boldsymbol{u}_o = 0, \qquad \text{in } \Omega_o, \tag{2.3}$$

$$\rho_o \frac{\mathrm{D}\boldsymbol{u}_o}{\mathrm{D}t} = -\nabla p_o + \mu_o \nabla^2 \boldsymbol{u}_o, \qquad \text{in } \Omega_o, \tag{2.4}$$

where $\boldsymbol{u}_w = (u_w, w_w)$ is the velocity in the water phase, $\boldsymbol{u}_o = (u_o, w_o)$ is the velocity in the oil phase, p_w, ρ_w, and μ_w are the pressure, density, and viscosity of the water, respectively, while p_o, ρ_o, and μ_o are the pressure, density, and viscosity of the oil, respectively, ϕ is the electric potential, and $\frac{D}{Dt} = \frac{\partial}{\partial t} + \boldsymbol{u}\cdot\nabla$ is the convective derivative.

We assume that the ion concentrations are governed by the Nernst-Planck (drift-diffusion) equations, which represent conservation of mass, and read

$$\frac{\partial c^{\pm,2\pm}}{\partial t} = -\nabla \cdot \boldsymbol{J}^{\pm,2\pm}, \qquad \text{in } \Omega_w, \tag{2.5}$$

$$\boldsymbol{J}^{\pm} = -\left(D^{\pm}\nabla c^{\pm} - \boldsymbol{u}_w c^{\pm} \pm D^{\pm}\frac{q}{k_B T} c^{\pm}\nabla\phi \right), \qquad \text{in } \Omega_w, \tag{2.6}$$

$$\boldsymbol{J}^{2\pm} = -\left(D^{2\pm}\nabla c^{2\pm} - \boldsymbol{u}_w c^{2\pm} \pm D^{2\pm}\frac{2q}{k_B T} c^{2\pm}\nabla\phi \right), \qquad \text{in } \Omega_w, \tag{2.7}$$

where $\boldsymbol{J}^{\pm}$, $\boldsymbol{J}^{2\pm}$, $D^{\pm}$, $D^{2\pm}$, k_B, and T denote the flux of the monovalent and divalent ions, the diffusivities of the monovalent and divalent ions, Boltzmann's constant, and the temperature, respectively. Finally, we assume that the electric potential satisfies Poisson's equation, which reads

$$\nabla^2\phi = \begin{cases} -\frac{q}{\varepsilon_w}(c^+ - c^- + 2c^{2+} - 2c^{2-}) & \text{in } \Omega_w, \\ 0 & \text{in } \Omega_o \cup \Omega_c, \end{cases} \tag{2.8}$$

where ε_w is the permittivity of the water phase. We note that, although we only need to solve the fluid equations inside the capillary, we need to solve Poisson's equation everywhere in order to determine ϕ.

2.2.2 Boundary Conditions

We prescribe a pressure drop of size P along the tube. We also assume that the concentration of monovalent ions is the same at either end of the tube, and make an equivalent assumption for the divalent ions. We denote these concentrations by c^1_∞ and c^2_∞, respectively. We assume that the net current over the cross section of the capillary at the inlet is zero [22, 29]. In addition, we fix the arbitrary constant in ϕ by setting $\phi = 0$ at the inlet. Thus we have the boundary conditions

$$p_w = P, \qquad \text{at } x = 0, \tag{2.9}$$

$$p_w = 0, \qquad \text{at } x = L, \tag{2.10}$$

$$c^{\pm} = c^1_\infty, \qquad c^{2\pm} = c^2_\infty, \qquad \text{at } x = 0, L, \tag{2.11}$$

$$\int_0^R \boldsymbol{e}_x \cdot \left(\boldsymbol{J}^+ - \boldsymbol{J}^- + 2\boldsymbol{J}^{2+} - 2\boldsymbol{J}^{2-}\right) \mathrm{d}z = 0, \qquad \text{at } x = 0, \tag{2.12}$$

where $\boldsymbol{e}_x$ is the unit vector in the direction of the applied pressure drop.

We restrict our attention to the lower half of the capillary by imposing symmetry conditions on the plane $z = R$, which read

$$\frac{\partial u_w}{\partial z} = \frac{\partial u_o}{\partial z} = w_w = w_o = \frac{\partial p_w}{\partial z} = \frac{\partial p_o}{\partial z} = \frac{\partial c^{\pm,2\pm}}{\partial z} = \frac{\partial \phi}{\partial z} = 0, \qquad \text{on } z = R. \tag{2.13}$$

One of the advantages of considering only the lower half plane is that the oil-water interface becomes a single valued function in x. We denote this interface by $z = h(x,t)$. On the capillary wall we impose the no slip condition

$$\boldsymbol{u}_w = 0, \qquad \text{at } z = 0, \tag{2.14}$$

and on $z = h$ we impose continuity of velocity across the interface, the kinematic condition, and a balance of normal and tangential stresses. These conditions read

$$\boldsymbol{u}_w = \boldsymbol{u}_o, \qquad \text{at } z = h, \tag{2.16}$$

$$w_w = h_t + u_w h_x, \qquad \text{at } z = h, \tag{2.17}$$

$$\boldsymbol{n} \cdot \boldsymbol{T}_w \cdot \boldsymbol{t} = \boldsymbol{n} \cdot \boldsymbol{T}_o \cdot \boldsymbol{t}, \qquad \text{at } z = h, \tag{2.18}$$

$$\boldsymbol{n} \cdot \boldsymbol{T}_w \cdot \boldsymbol{n} = \boldsymbol{n} \cdot \boldsymbol{T}_o \cdot \boldsymbol{n} + \frac{\gamma h_{xx}}{(1 + h_x^2)^{3/2}}, \qquad \text{at } z = h, \tag{2.19}$$

where γ is the (constant) surface tension of the oil-water interface, and the unit normal and tangential vectors are given by

$$\boldsymbol{n} = \frac{1}{\sqrt{1+h_x^2}} \begin{pmatrix} h_x \\ -1 \end{pmatrix}, \qquad \boldsymbol{t} = \frac{1}{\sqrt{1+h_x^2}} \begin{pmatrix} 1 \\ h_x \end{pmatrix}, \tag{2.20}$$

where we choose the sign of $\boldsymbol{n}$ to point out of the oil. The stress tensors for the water and oil, $\boldsymbol{T}_w$ and $\boldsymbol{T}_o$ respectively, are given by

$$\boldsymbol{T}_w = -p_w \boldsymbol{I} + \mu_w \left[\nabla \boldsymbol{u}_w + (\nabla \boldsymbol{u}_w)^T\right] + \varepsilon_w (\nabla\phi)(\nabla\phi)^T - \frac{\varepsilon_w}{2}|\nabla\phi|^2 \boldsymbol{I}, \tag{2.21}$$

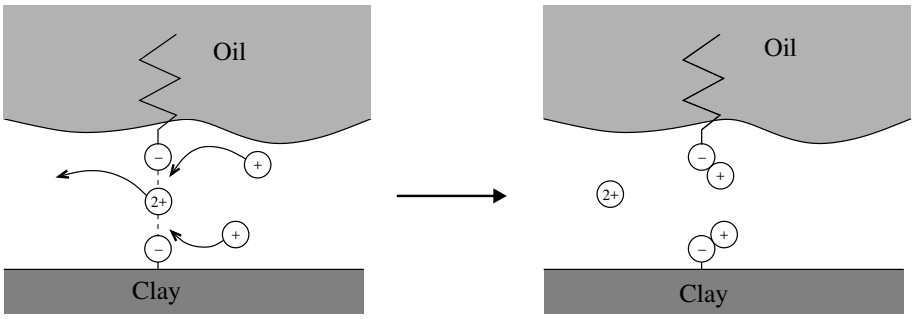
$$\boldsymbol{T}_o = -p_o \boldsymbol{I} + \mu_o \left[\nabla \boldsymbol{u}_o + (\nabla \boldsymbol{u}_o)^T\right] + \varepsilon_o (\nabla\phi)(\nabla\phi)^T - \frac{\varepsilon_o}{2}|\nabla\phi|^2 \boldsymbol{I}, \tag{2.22}$$

where the last two terms in (2.21) and (2.22) correspond to the Maxwell stress tensor [107, 122]. We note that even though there is no electrical body force acting on the oil phase in (2.4), we still need to include the Maxwell term in the expression for the stress tensor. This is consistent, since the body force can be derived by taking the divergence of the stress tensor, and the divergence of the Maxwell terms is proportional to $\nabla^2\phi$ which is zero in the oil phase by Poisson's equation, (2.8).

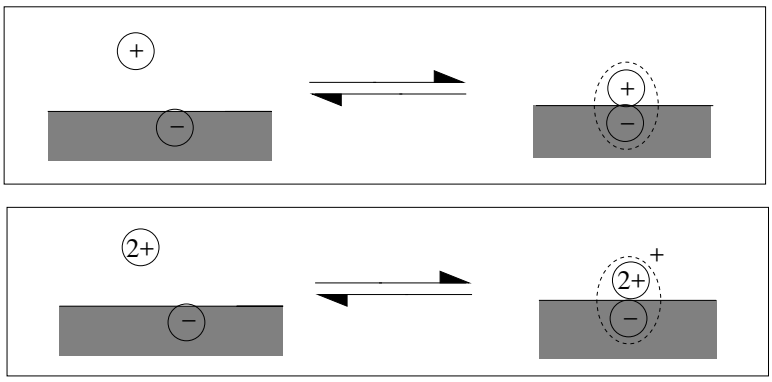
2.2.3 Modelling surface reactions

In the multicomponent ionic exchange (MIE) mechanism, shown in Figure 2.3a, the divalent cations initially bind the charged sites on the surface of the oil, resulting from deprotonated carboxylic acid groups, to the cation exchange sites along the surface of the clay. This bond, known as a ligand bridge, is a three-particle interaction, $\mathrm{RCOO^-} - \mathrm{Ca^{2+}} - \mathrm{Clay^-}$, and in order to accurately model this bond we need to introduce three-particle correlations into the electrical model [63]. However, this significantly complicates the mathematics, since the existence of the electric potential, ϕ, and the equation which governs it, (2.8), depend heavily on the mean-field approximation in which the effect of higher-order correlations are neglected. In order to be able to make the mean-field approximation, and therefore retain the simplicity of the model presented in §2.2.1 and §2.2.2, we choose to model the reactions on the oil and clay surfaces as two separate two-particle interactions, as shown in Figure 2.3b. This results in an effective charge at each ion-exchange site, from which we derive the effective surface charge densities along the oil and clay surfaces. We assume that the multiple bonds formed by ligand bridging between the oil and clay surfaces can be approximated by the attraction between the two charged surfaces.

At the clay-water interface, we suppose that there are a number of negatively charged exchange sites which can either be occupied by a monovalent cation to create



(a)



(b)

Figure 2.3: (a) Schematic diagram of the MIE mechanism as described by Lager *et al.* [60]. (b) Diagram of the proposed model for the reactions occuring on each surface. The first reaction represents the adsorption of a monovalent cation to create a neutral site, the second reaction represents the adsorption of a divalent cation to create a positively charged site.

a neutrally charged site, a divalent cation to create a positively charged site, or remain unoccupied. We let S_c and S_c^+ denote sites on the surface occupied by monovalent and divalent cations, respectively. The subscript c denotes 'clay'. We suppose the following reactions occur on the surface,

$$(\text{hole})^- + \text{Na}^+ \underset{K^1_{c_r}}{\overset{K^1_{c_f}}{\rightleftharpoons}} S_c, \qquad (\text{hole})^- + \text{Ca}^{2+} \underset{K^2_{c_r}}{\overset{K^2_{c_f}}{\rightleftharpoons}} S_c^+. \tag{2.23}$$

The first reaction describes the adsorption of monovalent sodium ions to create neutrally charged sites, and the second describes the adsorption of divalent calcium ions to create positively charged sites. The rate parameters $K^i_{c_f}$ and $K^i_{c_r}$ are the forward and reverse reaction rates, respectively, for the reaction involving the ion of valence i, which we take to be constant. We let s_c and s_c^+ denote the concentrations of adsorbed monovalent and divalent cations respectively, and let s_c^* be the saturation concentration, which we assume is constant along the capillary wall. Using the law of mass action, we obtain the following equations on the capillary surface,

$$\frac{\partial s_c}{\partial t} = K^1_{c_f}\, c^+\big|_{z=0}\,(s_c^* - s_c - s_c^+) - K^1_{c_r} s_c, \tag{2.24}$$

$$\frac{\partial s_c^+}{\partial t} = K^2_{c_f}\, c^{2+}\big|_{z=0}\,(s_c^* - s_c - s_c^+) - K^2_{c_r} s_c^+. \tag{2.25}$$

We assume that the flux of ions onto the surfaces is governed by drift diffusion, and so we also write

$$D^+\left(\frac{\partial c^+}{\partial z} + \frac{q}{k_B T} c^+ \frac{\partial \phi}{\partial z}\right)\bigg|_{z=0} = \frac{\partial s_c}{\partial t}, \qquad D^{2+}\left(\frac{\partial c^{2+}}{\partial z} + \frac{2q}{k_B T} c^{2+} \frac{\partial \phi}{\partial z}\right)\bigg|_{z=0} = \frac{\partial s_c^+}{\partial t}. \tag{2.26}$$

By representing carboxylic acid groups on the oil surface by negatively charged exchange sites, and assuming that similar reactions occur on the oil-water interface, we derive a similar set of boundary conditions on the surface of the oil,

$$\frac{\mathrm{D}s_o}{\mathrm{D}t} = K^1_{o_f}\, c^+\big|_{z=h}\,(s_o^* - s_o - s_o^+) - K^1_{o_r} s_o = -\boldsymbol{n}\cdot\boldsymbol{J}^+\big|_{z=h}\,, \tag{2.27}$$

$$\frac{\mathrm{D}s_o^+}{\mathrm{D}t} = K^2_{o_f}\, c^{2+}\big|_{z=h}\,(s_o^* - s_o - s_o^+) - K^2_{o_r} s_o^+ = -\boldsymbol{n}\cdot\boldsymbol{J}^{2+}\big|_{z=h}\,, \tag{2.28}$$

where the subscript o denotes 'oil'. Note that partial derivatives are used in (2.26) since the interface at $z = 0$ is stationary, whereas the convective derivative is required in (2.27) and (2.28). We assume that s_o^* is constant along the oil-water interface. As the negatively charged ions do not react with the surfaces, we impose zero flux conditions,

$$\boldsymbol{n}\cdot\boldsymbol{J}^-\big|_{z=0,h} = 0, \qquad \boldsymbol{n}\cdot\boldsymbol{J}^{2-}\big|_{z=0,h} = 0. \tag{2.29}$$

We suppose that the presence of the charged surfaces causes a discontinuity in the electric field across the clay-water and oil-water interfaces. Since the surface concentration of negatively charged, unoccupied sites is given by $s_c^* - s_c - s_c^+$ on the clay-water interface, and $s_o^* - s_o - s_o^+$ on the oil-water interface, the surface charge densities are given by $\sigma_c = q(2s_c^+ + s_c - s_c^*)$, and $\sigma_o = q(2s_o^+ + s_o - s_o^*)$, for the clay and oil surfaces respectively. We impose that the electric field is zero at infinity, since we assume that the system is globally neutral. These conditions read

$$[\varepsilon\phi_z]_{z=0^-}^{z=0^+} = q(2s_c^+ + s_c - s_c^*), \qquad [\varepsilon \boldsymbol{n}\cdot\nabla\phi]_{z=h^-}^{z=h^+} = q(2s_o^+ + s_o - s_o^*), \tag{2.30}$$

$$\nabla\phi \to 0 \qquad \text{as } x^2 + z^2 \to \infty, \tag{2.31}$$

where the permittivity is given by $\varepsilon = \varepsilon_w$ in the water phase, $\varepsilon = \varepsilon_o$ in the oil phase, and $\varepsilon = \varepsilon_c$ in the clay phase.

Finally, we also assume that the electric potential is continuous across these interfaces, so we write

$$[\phi]_{z=0^-}^{z=0^+} = [\phi]_{z=h^-}^{z=h^+} = 0. \tag{2.32}$$

2.2.4 Capturing salinity variations

In many experiments designed to study the low salinity effect the concentration of monovalent and divalent ions varies simultaneously between the low salinity and high salinity regimes. In order to compare the theoretical model with experimental data, we introduce the parameter τ such that

$$c_\infty^{1,2} = c_{low}^{1,2} + 10^\tau \left(c_{high}^{1,2} - c_{low}^{1,2}\right), \tag{2.33}$$

where $c_{low}^{1,2}$ are the concentration of monovalent and divalent ions, respectively, in the low salinity regime, and $c_{high}^{1,2}$ are the concentration of monovalent and divalent ions, respectively, in the high salinity regime. By varying τ from $-\infty$ to 0 we can study the model continuously between the low salinity and high salinity regimes using a single parameter. We note that we can study the effect of varying the concentration of a single ion species by setting the low-salinity and high-salinity concentrations of the other species to be identical. We choose a power law for τ as typically the salinities span multiple orders of magnitude. A summary of the parameter values used in this chapter is given in Table 2.1.

Parameter	Value	Reference/Notes
R	$1\ \mu\mathrm{m}$	[76]
L	$10\ \mu\mathrm{m}$	[76]
γ	$0.02\ \mathrm{J\,m^{-2}}$	[18]
μ_o	$0.01\ \mathrm{kg\,m^{-1}\,s^{-1}}$	[18]
μ_w	$8.9 \times 10^{-4}\ \mathrm{kg\,m^{-1}\,s^{-1}}$	[18]
ρ_o	$850\ \mathrm{kg\,m^{-3}}$	[18]
ρ_w	$1000\ \mathrm{kg\,m^{-3}}$	[18]
c^1_{low}	$17\ \mathrm{mol\,m^{-3}}$	[7]
c^1_{high}	$1.7 \times 10^3\ \mathrm{mol\,m^{-3}}$	[7]
c^2_{low}	$5\ \mathrm{mol\,m^{-3}}$	[7]
c^2_{high}	$90\ \mathrm{mol\,m^{-3}}$	[7]
$D^{\pm,2\pm}$	$7.9 \times 10^{-10} - 2 \times 10^{-9}\ \mathrm{m^2\,s^{-1}}$	[87]
s^*_c	$10^{16}\ \mathrm{m^{-2}}$	[66]
s^*_o	$7.5 \times 10^{17}\ \mathrm{m^{-2}}$	[64]
$K^1_{c_f}/K^1_{c_r}$	$10^{-3}\ \mathrm{m^3\,mol^{-1}}$	[31]
$K^2_{c_f}/K^2_{c_r}$	$0.2\ \mathrm{m^3\,mol^{-1}}$	[31]
$K^1_{o_f}/K^1_{o_r}$	$6 \times 10^{-4}\ \mathrm{m^3\,mol^{-1}}$	[32]
$K^2_{o_f}/K^2_{o_r}$	$3 \times 10^{-4}\ \mathrm{m^3\,mol^{-1}}$	[48]
ε_{wr}	56	[69]
ε_0	$8.9 \times 10^{-12}\ \mathrm{C^2J^{-1}\,m^{-1}}$	
q	$1.6 \times 10^{-19}\ \mathrm{C}$	
k_B	$1.4 \times 10^{-23}\ \mathrm{J\,K^{-1}}$	
T	$375°\mathrm{K}$	[60]
V_p	$1.5 \times 10^{-5}\ \mathrm{m\,s^{-1}}$	[43]
K/ψ	$3 \times 10^3\ \mathrm{mD}$	[67]
λ	$1.5 \times 10^{-9} - 2 \times 10^{-10}\ \mathrm{m}$	$\lambda = \left(\frac{\varepsilon_w k_B T}{2(c^1_\infty + 4c^2_\infty)q^2}\right)^{\frac{1}{2}}$
P	$0.045\ \mathrm{N\,m^{-2}}$	$P \sim \mu_w L V_p \psi / K$

Table 2.1: Dimensional parameters

2.2.5 Dimensionless system of equations

We non-dimensionalise the problem using the following scalings,

$$
\begin{gathered}
x = L\hat{x}, \qquad z = R\hat{z}, \qquad h = R\hat{h}, \\
u_w = U\hat{u}_w, \qquad u_o = U\hat{u}_o, \qquad w_w = \epsilon_1 U\hat{w}_w, \qquad w_o = \epsilon_1 U\hat{w}_o, \\
p_w = P\hat{p_w}, \qquad p_o = P\hat{p_o}, \qquad t = \frac{L}{U}\hat{t}, \\
c^{\pm} = c^1_{low}\hat{c}^{\pm}, \qquad c^{2\pm} = c^2_{low}\hat{c}^{2\pm}, \qquad \phi = \frac{k_B T}{q}\hat{\phi}, \qquad \varepsilon = \varepsilon_w\hat{\varepsilon}, \\
s_c = s^*_c\hat{s}_c, \qquad s^+_c = s^*_c\hat{s}^+_c, \qquad s_o = s^*_o\hat{s}_o, \qquad s^+_o = s^*_o\hat{s}^+_o,
\end{gathered}
\tag{2.34}
$$

where we choose $U = \frac{PR^2}{\mu_w L}$ in order to get a balance in (2.2), and $\epsilon_1 = R/L$ is the aspect ratio of the tube. We substitute scalings (2.34) into (2.1) – (2.33), and, dropping the hats, the dimensionless equations read

$$
\begin{aligned}
\epsilon_1^2 Re\frac{\mathrm{D}u_w}{\mathrm{D}t} &= -p_{wx} + \left(\epsilon_1^2 u_{wxx} + u_{wzz}\right) \\
&\quad - \frac{\xi}{\delta P^*}(c^+ - c^- + 2c^* c^{2+} - 2c^* c^{2-})\phi_x, && \text{in } \Omega_w, && (2.35)\\
\epsilon_1^4 Re\frac{\mathrm{D}w_w}{\mathrm{D}t} &= -p_{wz} + \epsilon_1^2(\epsilon_1^2 w_{wxx} + w_{wzz}) \\
&\quad - \frac{\xi}{\delta P^*}(c^+ - c^- + 2c^* c^{2+} - 2c^* c^{2-})\phi_z, && \text{in } \Omega_w, && (2.36)\\
u_{wx} + w_{wz} &= 0 && \text{in } \Omega_w, && (2.37)\\
\epsilon_1^2 Pe^{\pm}\frac{\mathrm{D}c^{\pm}}{\mathrm{D}t} &= \epsilon_1^2\left(c^{\pm}_x \pm c^{\pm}\phi_x\right)_x + \left(c^{\pm}_z \pm c^{\pm}\phi_z\right)_z, && \text{in } \Omega_w && (2.38)\\
\epsilon_1^2 Pe^{2\pm}\frac{\mathrm{D}c^{2\pm}}{\mathrm{D}t} &= \epsilon_1^2\left(c^{2\pm}_x \pm 2c^{2\pm}\phi_x\right)_x + \left(c^{2\pm}_z \pm 2c^{2\pm}\phi_z\right)_z, && \text{in } \Omega_w, && (2.39)\\
\delta\xi\left(\epsilon_1^2\phi_{xx} + \phi_{zz}\right) &= -\left(c^+ - c^- + 2c^* c^{2+} - 2c^* c^{2-}\right) && \text{in } \Omega_w, && (2.40)\\
\epsilon_1^2\rho^* Re\frac{\mathrm{D}u_o}{\mathrm{D}t} &= -p_{ox} + \mu^*\left(\epsilon_1^2 u_{oxx} + u_{ozz}\right), && \text{in } \Omega_o, && (2.41)\\
\epsilon_1^4\rho^* Re\frac{\mathrm{D}w_o}{\mathrm{D}t} &= -p_{oz} + \epsilon_1^2\mu^*\left(\epsilon_1^2 w_{oxx} + w_{ozz}\right), && \text{in } \Omega_o, && (2.42)\\
u_{ox} + w_{oz} &= 0, && \text{in } \Omega_o, && (2.43)\\
\epsilon_1^2\phi_{xx} + \phi_{zz} &= 0 && \text{in } \Omega_o \cup \Omega_c, && (2.44)
\end{aligned}
$$

$$
\varepsilon = 1 \quad \text{in } \Omega_w, \qquad \varepsilon = \varepsilon_1 \quad \text{in } \Omega_o, \qquad \varepsilon = \varepsilon_2 \quad \text{in } \Omega_c, \tag{2.45}
$$

By non-dimensionalising (2.9) – (2.12), we find that equations (2.35) – (2.45) are subject to the axial boundary conditions

$$
\begin{aligned}
p_w &= 1, \qquad c^{\pm,2\pm} = 1 + 10^{\tau}\left(\bar{c}^{1,2} - 1\right), && \text{at } x = 0, && (2.46)\\
p_w &= 0, \qquad c^{\pm,2\pm} = 1 + 10^{\tau}\left(\bar{c}^{1,2} - 1\right), && \text{at } x = 1, && (2.47)
\end{aligned}
$$

as well as the zero net current constraint

$$\int_0^1 \left\{ \frac{c_x^+ + c^+\phi_x}{Pe^+} - \frac{c_x^- - c^-\phi_x}{Pe^-} + 2c^* \left[\frac{c_x^{2+} + 2c^{2+}\phi_x}{Pe^{2+}} - \frac{c_x^{2-} - 2c^{2-}\phi_x}{Pe^{2-}} \right] \right\} \mathrm{d}z = 0, \tag{2.48}$$

at $x = 0$, where we have substituted (2.6) and (2.7) into (2.12). We also have that,

$$\left.\begin{aligned} \boldsymbol{u}_w = 0, \qquad \xi \left[\varepsilon\phi_z\right]_{z=0^-}^{z=0^+} = 2s_c^+ + s_c - 1, \qquad [\phi]_{z=0^-}^{z=0^+} = 0, \\ \Lambda_c^1 \frac{\partial s_c}{\partial t} = \mathcal{K}_c^1 c^+ (1 - s_c - s_c^+) - s_c, \\ \Lambda_c^2 \frac{\partial s_c^+}{\partial t} = \mathcal{K}_c^2 c^{2+} (1 - s_c - s_c^+) - s_c^+, \\ c_z^+ + c^+\phi_z = \epsilon_1^2 \delta Pe^+ \frac{\partial s_c}{\partial t}, \qquad c_z^- - c^-\phi_z = 0, \\ c_z^{2+} + 2c^{2+}\phi_z = \frac{\epsilon_1^2 \delta Pe^{2+}}{c^*} \frac{\partial s_c^+}{\partial t}, \qquad c_z^{2-} - 2c^{2-}\phi_z = 0, \end{aligned}\right\} \quad z = 0, \tag{2.49}$$

$$\left.\begin{aligned} \boldsymbol{u}_w = \boldsymbol{u}_o \qquad w_w = h_t + u_w h_x, \qquad [\phi]_{z=h^-}^{z=h^+} = 0, \\ \frac{\xi}{(1+\epsilon_1^2 h_x^2)^{1/2}} \left[\varepsilon \left(\phi_z - \epsilon_1^2 h_x \phi_x\right)\right]_{z=h^-}^{z=h^+} = s^*(2s_o^+ + s_o - 1), \\ \Lambda_o^1 \frac{\mathrm{D}s_o}{\mathrm{D}t} = \mathcal{K}_o^1 c^+ (1 - s_o - s_o^+) - s_o, \\ \Lambda_o^2 \frac{\mathrm{D}s_o^+}{\mathrm{D}t} = \mathcal{K}_o^2 c^{2+} (1 - s_o - s_o^+) - s_o^+, \\ c_z^+ + c^+\phi_z - \epsilon_1^2 h_x \left(c_x^+ + c^+\phi_x\right) \\ \qquad = \epsilon_1^2 Pe^+ \left(\delta s^* \frac{\mathrm{D}s_o}{\mathrm{D}t} + w_w c^+ - h_x u_w c^+ \right), \\ c_z^{2+} + 2c^{2+}\phi_z - \epsilon_1^2 h_x \left(c_x^{2+} + 2c^{2+}\phi_x\right) \\ \qquad = \epsilon_1^2 Pe^{2+} \left(\frac{\delta s^*}{c^*} \frac{\mathrm{D}s_o^+}{\mathrm{D}t} + w_w c^{2+} - h_x u_w c^{2+} \right), \\ c_z^- - c^-\phi_z - \epsilon_1^2 h_x \left(c_x^- - c^-\phi_x\right) = \epsilon_1^2 Pe^- \left(w_w c^- - h_x u_w c^-\right), \\ c_z^{2-} - 2c^{2-}\phi_z - \epsilon_1^2 h_x \left(c_x^{2-} - 2c^{2-}\phi_x\right) \\ \qquad = \epsilon_1^2 Pe^{2-} \left(w_w c^{2-} - h_x u_w c^{2-}\right), \end{aligned}\right\} \quad z = h, \tag{2.50}$$

$$\begin{aligned} \mu^* \left[(u_{oz} + \epsilon_1 w_{oz})(1 - \epsilon_1^2 h_x^2) + 2\epsilon_1^2 h_x (w_{oz} - u_{ox})\right] \\ = (u_{wz} + \epsilon_1 w_{wz})(1 - \epsilon_1^2 h_x^2) + 2\epsilon_1^2 h_x (w_{wz} - u_{wx}) \\ - \frac{\epsilon_1}{P^*} \left[h_x(\epsilon_1^2 \phi_x^2 - \phi_z^2) + (1 - \epsilon_1^2 h_x^2)\phi_x \phi_z\right]_{z=h^-}^{z=h^+}, \end{aligned} \quad z = h, \tag{2.51}$$

$$\begin{aligned} \epsilon_1^2 \mu^* \frac{\left[w_{oz} - h_x u_{oz} + \epsilon_1^2 h_x (h_x u_{ox} - w_{ox})\right]}{1 + \epsilon_1^2 h_x^2} = \epsilon_1^2 \frac{\left[w_{wz} - h_x u_{wz} + \epsilon_1^2 h_x (h_x u_{wx} - w_{wx})\right]}{1 + \epsilon_1^2 h_x^2} \\ + \frac{1}{2}(p_o - p_w) + \frac{\xi^2}{P^*} \left[\frac{\epsilon_1^2 h_x \phi_x \phi_z}{1 + \epsilon_1^2 h_x^2} + \frac{1}{4}(\epsilon_1^2 \phi_x^2 - \phi_z^2) \right]_{z=h^-}^{z=h^+} - \frac{\Gamma h_{xx}}{4P^*(1 + \epsilon_1^2 h_x^2)^{3/2}}, \end{aligned} \quad z = h, \tag{2.52}$$

$$u_{wz} = u_{oz} = w_w = w_o = p_{wz} = p_{oz} = c_z^{\pm} = c_z^{2\pm} = \phi_z = 0, \qquad \text{at } z = 1, \quad (2.53)$$

$$\nabla\phi \to \mathbf{0}, \qquad \text{as } x^2 + z^2 \to \infty, \quad (2.54)$$

where we have substituted in the expressions (2.21) and (2.22) for the stress tensors into the boundary conditions on the oil-water interface, (2.18) and (2.19), to obtain (2.51) and (2.52).

2.2.6 Dimensionless parameters

We have introduced dimensionless parameters ϵ_1, Re, $Pe^{\pm,2\pm}$, Γ, P^*, ξ, δ, ρ^*, μ^*, s^*, ε_1, ε_2, $\bar{c}^{1,2}$, c^*, $\Lambda_c^{1,2}$, $\Lambda_o^{1,2}$, $\mathcal{K}_c^{1,2}$, and $\mathcal{K}_o^{1,2}$, as summarised in Table 2.2. These are as follows: $\epsilon_1 = R/L$ is the aspect ratio of the tube, $Re = \rho_w P R^2/\mu_w^2$ is the Reynolds number, $Pe^{\pm,2\pm} = PR^2/D^{\pm,2\pm}\mu_w$ are the Péclet numbers for the different ionic species, $\Gamma = 2\gamma\varepsilon_w R/L^2 q^2 s_c^{*2}$ is the ratio of the surface tension forces to the electrostatic forces, and $P^* = \varepsilon_w P/q^2 s_c^{*2}$ is the ratio of the pressure drop across the capillary to the electrostatic pressure due to the charged surfaces. It is through P^* and Γ that we measure the influence of the electrostatic forces in the model, since these are the dimensionless pressure and surface tension, respectively.

The ratio of the thermal voltage to the potential due to the charged surfaces is given by $\xi = \varepsilon_w k_B T/q^2 s_c^* R$. We can think of ξ^{-1} as a dimensionless measure of how far through the water phase the electrostatic effects propagate as a result of the magnitude and density of the surface charges. The ratio of the density of exchange sites on the clay surface to the concentration of ions in the bulk water regions is given by $\delta = s_c^*/c_{low}^1 R$. This is a dimensionless measure of how many ions are removed from the bulk regions of water due to adsorption at the surface exchange sites.

Relative properties of the different materials are as follows: $\rho^* = \rho_o/\rho_w$ is the ratio of the density of the oil to the density of the water, $\mu^* = \mu_o/\mu_w$ is the ratio of the viscosity of the oil to the viscosity of the water, $s^* = s_o^*/s_c^*$ is the ratio of the saturation concentration of the oil surface to the saturation concentration of the clay surface, and the dimensionless permittivity is $\varepsilon_1 = \varepsilon_o/\varepsilon_w$ in the oil phase, and $\varepsilon_2 = \varepsilon_c/\varepsilon_w$ in the clay phase. The ratios of the ion concentrations in the high-salinity and low-salinity regimes are given by $\bar{c}^{1,2} = c_{high}^{1,2}/c_{low}^{1,2}$, and the ratio of the bulk concentration of divalent ions to the bulk concentration of monovalent ions in the low salinity regime is given by $c^* = c_{low}^2/c_{low}^1$.

The ratios of the timescales of the surface reactions to the flow timescale are given by $\Lambda_c^{1,2} = PR^2/\mu_w L^2 K_{c_r}^{1,2}$ and $\Lambda_o^{1,2} = PR^2/\mu_w L^2 K_{o_r}^{1,2}$, and the dimensionless equilibrium constants are $\mathcal{K}_c^{1,2} = {K_c}_f^{1,2} c_{low}^{1,2}/{K_c}_r^{1,2}$ and $\mathcal{K}_o^{1,2} = {K_o}_f^{1,2} c_{low}^{1,2}/{K_o}_r^{1,2}$.

Parameter	Expression	Value
ϵ_1	R/L	0.1
ϵ_2	λ/R	$1.5 \times 10^{-3} - 2 \times 10^{-4}$
Re	$\rho_w P R^2/\mu_w^2$	5.7×10^{-5}
$Pe^{\pm,2\pm}$	$PR^2/D^{\pm,2\pm}\mu_w$	$0.025 - 0.064$
Γ	$2\gamma\varepsilon_w R/L^2 q^2 s_c^{*2}$	0.08
P^*	$\varepsilon_w P/q^2 s_c^{*2}$	9×10^{-6}
ξ	$\varepsilon_w k_B T/q^2 s_c^* R$	0.01
δ	$s_c^*/c_{low}^1 R$	10^{-3}
ρ^*	ρ_o/ρ_w	0.85
μ^*	μ_o/μ_w	11
s^*	s_o^*/s_c^*	75
ε_1	$\varepsilon_o/\varepsilon_w$	
ε_2	$\varepsilon_c/\varepsilon_w$	
$\bar{c}^1$	c_{high}^1/c_{low}^1	100
$\bar{c}^2$	c_{high}^2/c_{low}^2	18
c^*	c_{low}^2/c_{low}^1	0.3
$\Lambda_c^{1,2}$	$PR^2/\mu_w L^2 K_{c_r}^{1,2}$	$\ll 1$
$\Lambda_o^{1,2}$	$PR^2/\mu_w L^2 K_{o_r}^{1,2}$	$\ll 1$
$\mathcal{K}_c^1$	$K_{c_f}^1 c_{low}^1/K_{c_r}^1$	1.7×10^{-2}
$\mathcal{K}_c^2$	$K_{c_f}^2 c_{low}^2/K_{c_r}^2$	0.99
$\mathcal{K}_o^1$	$K_{o_f}^1 c_{low}^1/K_{o_r}^1$	0.01
$\mathcal{K}_o^2$	$K_{o_f}^2 c_{low}^2/K_{o_r}^2$	1.5×10^{-3}
L_o^*	L_o/L	0.5

Table 2.2: Dimensionless parameters

2.2.7 Typical non-dimensional parameter sizes

Injection rates used in core experiments vary considerably [43], so for the purposes of this thesis we assume that the flow velocity within the pores of a reservoir is $V_p = 1.5 \times 10^{-5}\ \mathrm{m\,s^{-1}}$ ($\approx 4\ \mathrm{ft\,day^{-1}}$). We estimate the pressure using Darcy's law, $\psi V_p = KP/\mu_w L$, where ψ is the porosity of the reservoir rock, K is the permeability, P is the pressure drop across a pore throat, μ_w is the viscosity of the fluid (which we take to be water for simplicity), and L is the length of the pore throat. For $K/\psi = 3000$ mD [67], this gives $P \approx 0.045\ \mathrm{N\,m^{-2}}$. We use this value for the applied pressure, as well as the parameter values given in Table 2.1, to obtain the typical values for the dimensionless parameters given in Table 2.2.

We find that aspect ratio of the channel is $\epsilon_1 \approx 0.1 \ll 1$, and the Reynolds number is $Re \approx 5.7 \times 10^{-5} \ll 1$. Therefore, we will exploit the thin nature of the capillary, and we will also neglect the inertial terms in the Navier-Stokes equations. The Péclet numbers are $Pe^+ \approx 0.039$, $Pe^- \approx 0.025$, $Pe^{2+} \approx 0.064$, $Pe^{2-} \approx 0.046$. It would be reasonable to take these to be $\ll 1$, however for generality we will retain these terms in the subsequent analysis.

We find that the ratio of the density of exchange sites on the clay surface to the concentration of ions in the bulk is given by $\delta \approx 10^{-3}$, and the ratio of the thermal voltage to the potential due to charged surfaces is $\xi \approx 0.01$. We suppose that $\delta \ll 1$, and, for generality, we will treat ξ as $O(1)$. We find that $\Gamma \approx 0.08$, which we take to be $O(1)$ for generality, and $P^* \approx 9 \times 10^{-6}$. We will find later that viscous effects become important for $P^* \approx 10^{-5}$, hence we will not neglect terms proportional to P^* at this stage. In §2.4.12, we will consider the limit $P^* \to 0$.

We also assume that the ions react quickly at the surfaces by comparison to the flow timescale so that instantaneous adsorption occurs, that is, we assume that $\Lambda_c^{1,2} \ll 1$ and $\Lambda_o^{1,2} \ll 1$.

2.2.8 Dimensionless system, neglecting small terms

We exploit the small aspect ratio of the system by performing an expansion in ϵ_1 and solving the leading-order system. This is equivalent to considering the limit $\epsilon_1 \to 0$. We will later use the fact that $\delta \ll 1$ in order to perform an expansion in δ. However, this expansion will be used to simplify and solve the leading-order (in ϵ_1) system, and consequently find the leading-order solution in both ϵ_1 *and* δ simultaneously. In order to perform the multiple expansions rigorously, we will, for the moment, retain all terms proportional to δ.

In addition to neglecting terms proportional to ϵ_1, we simplify the system further by neglecting terms proportional to Re, $\Lambda_c^{1,2}$, and $\Lambda_o^{1,2}$, while treating all other variables as $O(1)$. With these simplifications, equations (2.35) – (2.54) read

$$\left.\begin{aligned} u_{wzz} &= p_{wx} + \frac{\xi}{\delta P^*}(c^+ - c^- + 2c^*c^{2+} - 2c^*c^{2-})\phi_x, \\ p_{wz} &= \frac{\xi}{\delta P^*}(c^+ - c^- + 2c^*c^{2+} - 2c^*c^{2-})\phi_z, \\ u_{wx} + w_{wz} &= 0, \end{aligned}\right\} \qquad \text{in } \Omega_w, \tag{2.55}$$

$$\mu^* u_{ozz} = p_{ox}, \qquad p_{oz} = 0, \qquad u_{ox} + w_{oz} = 0, \qquad \text{in } \Omega_o, \tag{2.56}$$

$$\left(c_z^{\pm} \pm c^{\pm}\phi_z\right)_z = 0, \qquad \left(c_z^{2\pm} \pm 2c^{2\pm}\phi_z\right)_z = 0, \qquad \text{in } \Omega_w, \tag{2.57}$$

$$\phi_{zz} = \begin{cases} -\frac{1}{\delta\xi}\left(c^+ - c^- + 2c^*c^{2+} - 2c^*c^{2-}\right) & \text{in } \Omega_w, \\ 0 & \text{in } \Omega_o \cup \Omega_c, \end{cases} \tag{2.58}$$

$$\varepsilon = 1 \quad \text{in } \Omega_w, \qquad \varepsilon = \varepsilon_1 \quad \text{in } \Omega_o, \qquad \varepsilon = \varepsilon_2 \quad \text{in } \Omega_c, \tag{2.59}$$

subject to

$$p_w = 1, \qquad c^{\pm,2\pm} = 1 + 10^{\tau}\left(\bar{c}^{1,2} - 1\right), \qquad x = 0, \tag{2.60}$$

$$p_w = 0, \qquad c^{\pm,2\pm} = 1 + 10^{\tau}\left(\bar{c}^{1,2} - 1\right), \qquad x = 1, \tag{2.61}$$

$$\int_0^1 \left\{ \frac{c_x^+ + c^+\phi_x}{Pe^+} - \frac{c_x^- - c^-\phi_x}{Pe^-} + 2c^*\left[\frac{c_x^{2+} + 2c^{2+}\phi_x}{Pe^{2+}} - \frac{c_x^{2-} - 2c^{2-}\phi_x}{Pe^{2-}}\right]\right\} \mathrm{d}z = 0, \qquad x = 0 \tag{2.62}$$

$$\left.\begin{aligned} &\boldsymbol{u}_w = 0, \quad \xi\left[\varepsilon\phi_z\right]_{z=0^-}^{z=0^+} = 2s_c^+ + s_c - 1, \quad [\phi]_{z=0^-}^{z=0^+} = 0, \\ &\mathcal{K}_c^1 c^+(1 - s_c - s_c^+) - s_c = 0, \\ &\mathcal{K}_c^2 c^{2+}(1 - s_c - s_c^+) - s_c^+ = 0, \\ &c_z^{\pm} \pm c^{\pm}\phi_z = 0, \qquad c_z^{2\pm} \pm 2c^{2\pm}\phi_z = 0, \end{aligned}\right\} \qquad z = 0, \tag{2.63}$$

$$\left.\begin{aligned} &\boldsymbol{u}_w = \boldsymbol{u}_o, \quad \xi\left[\varepsilon\phi_z\right]_-^+ = s^*(2s_o^+ + s_o - 1), \quad [\phi]_{z=h^-}^{z=h^+} = 0, \\ &\mathcal{K}_o^1 c^+(1 - s_o - s_o^+) - s_o = 0, \\ &\mathcal{K}_o^2 c^{2+}(1 - s_o - s_o^+) - s_o^+ = 0, \\ &c_z^{\pm} \pm c^{\pm}\phi_z = 0, \qquad c_z^{2\pm} \pm 2c^{2\pm}\phi_z = 0, \\ &w_w = h_t + u_w h_x, \qquad \mu^* u_{oz} = u_{wz}, \\ &p_w = p_o - \frac{\xi^2}{2P^*}\left[\phi_z^2\right]_{z=h^-}^{z=h^+} - \frac{\Gamma h_{xx}}{2P^*}, \end{aligned}\right\} \qquad z = h, \tag{2.64}$$

$$u_{wz} = u_{oz} = w_w = w_o = p_{wz} = p_{oz} = c_z^{\pm} = c_z^{2\pm} = \phi_z = 0, \qquad z = 1, \tag{2.65}$$

$$\nabla\phi \to \mathbf{0}, \qquad x^2 + z^2 \to \infty. \tag{2.66}$$

Taking the limit $\epsilon_1 \to 0$ has resulted in a system which is not closed, since the solution to the homogeneous problem, (2.57) subject to (2.63), (2.64) and (2.65), is given by any $c^{\pm,2\pm}$ such that $c_z^{\pm} \pm c^{\pm}\phi_z$ and $c_z^{2\pm} \pm 2c^{2\pm}\phi_z$ are some arbitrary functions of x. The extra information we need arises from solvability conditions on higher-order terms in the expansion when substituted into (2.38) and (2.39). However, we can find these conditions directly by integrating (2.38) and (2.39). We separate the water phase into five regions as shown in Figure 2.2; the bulk region of water to the left of the oil slug (region I), the thin layer of water separating the oil from the capillary walls (region II), the bulk region of water to the right of the oil slug (region III), and the meniscus regions at each end of the oil slug (regions IV and V). In regions I and III, imposing (2.49), (2.50), and (2.53) gives

$$Pe^{+}\int_0^1 \frac{\mathrm{D}c^{+}}{\mathrm{D}t}\,\mathrm{d}z = \frac{\partial}{\partial x}\int_0^1 \left(\frac{\partial c^{+}}{\partial x} + c^{+}\frac{\partial \phi}{\partial x}\right)\mathrm{d}z - \delta Pe^{+}\frac{\partial s_c}{\partial t}, \tag{2.67}$$

$$Pe^{2+}\int_0^1 \frac{\mathrm{D}c^{2+}}{\mathrm{D}t}\,\mathrm{d}z = \frac{\partial}{\partial x}\int_0^1 \left(\frac{\partial c^{2+}}{\partial x} + 2c^{2+}\frac{\partial \phi}{\partial x}\right)\mathrm{d}z - \frac{\delta Pe^{2+}}{c^*}\frac{\partial s_c^{+}}{\partial t}, \tag{2.68}$$

$$Pe^{k-}\int_0^1 \frac{\mathrm{D}c^{k-}}{\mathrm{D}t}\,\mathrm{d}z = \frac{\partial}{\partial x}\int_0^1 \left(\frac{\partial c^{2-}}{\partial x} - kc^{k-}\frac{\partial \phi}{\partial x}\right)\mathrm{d}z, \qquad \text{for } k = 1, 2, \tag{2.69}$$

while, in regions II, IV and V, we have

$$\begin{aligned} Pe^{+}\int_0^h \frac{\mathrm{D}c^{+}}{\mathrm{D}t}\,\mathrm{d}z = \frac{\partial}{\partial x}\int_0^h \left(\frac{\partial c^{+}}{\partial x} + c^{+}\frac{\partial \phi}{\partial x}\right)\mathrm{d}z \\ + \delta Pe^{+}\left(s^*\frac{\mathrm{D}s_o}{\mathrm{D}t} - \frac{\partial s_c}{\partial t}\right) + Pe^{+}\frac{\partial h}{\partial t}c^{+}|^{z=h}, \end{aligned} \tag{2.70}$$

$$\begin{aligned} Pe^{2+}\int_0^h \frac{\mathrm{D}c^{2+}}{\mathrm{D}t}\,\mathrm{d}z = \frac{\partial}{\partial x}\int_0^h \left(\frac{\partial c^{2+}}{\partial x} + 2c^{2+}\frac{\partial \phi}{\partial x}\right)\mathrm{d}z \\ + \frac{\delta Pe^{2+}}{c^*}\left(s^*\frac{\mathrm{D}s_o^{+}}{\mathrm{D}t} - \frac{\partial s_c^{+}}{\partial t}\right) + Pe^{2+}\frac{\partial h}{\partial t}c^{2+}|^{z=h}, \end{aligned} \tag{2.71}$$

$$Pe^{k-}\int_0^h \frac{\mathrm{D}c^{k-}}{\mathrm{D}t}\,\mathrm{d}z = \frac{\partial}{\partial x}\int_0^h \left(\frac{\partial c^{k-}}{\partial x} - kc^{k-}\frac{\partial \phi}{\partial x}\right)\mathrm{d}z + Pe^{k-}\frac{\partial h}{\partial t}c^{k-}|^{z=h}, \tag{2.72}$$

for $k = 1, 2$. Note that we have swapped the order of integration and differentiation in (2.70) – (2.72) by applying the kinematic and flux boundary conditions in (2.50). Equations (2.55) – (2.72) form a closed system of equations and boundary conditions for the 15 variables u_w, u_o, w_w, w_o, p_w, p_o, $c^{\pm}$, $c^{2\pm}$, ϕ, s_c, s_c^{+}, s_o and s_o^{+}, which we will solve in §2.3 and §2.4.

2.3 Solution to the electrical probem

Since the oil and clay surfaces are charged, there is a net force acting between them; this force can be attractive or repulsive, depending on the relative signs of the two surface charge densities. The magnitude of the attraction or repulsion varies as a function of the salinity, and affects the thickness of the water layer separating the two charged surfaces, which in turn affects the fluid dynamics. Hence, in order to solve the fluid dynamics problem, and consequently the velocity of the oil slug, we must first determine the electric potential, ϕ, resulting from the charged surfaces. We solve the electrical problem (2.57) – (2.72) to determine ϕ, considering the oil, clay, and water phases separately.

2.3.1 In the oil phase

In the oil phase, Ω_o, we solve (2.58) subject to (2.65) to get that $\phi_z \equiv 0$. This is sufficient for our needs, however to find $\phi(x,t)$ we could first solve for ϕ in the water phase, and then impose (2.64).

2.3.2 In the clay phase

In the clay phase, Ω_c, we solve (2.58) subject to (2.66) to find that $\phi_z \equiv 0$. Again, this is sufficient for our needs. However we could find $\phi(x,t)$ by solving for ϕ in the water phase and applying (2.63).

2.3.3 In the water phase

In the water phase, Ω_w, integrating (2.57) twice and applying (2.63) yields

$$c^{\pm} = d^{\pm}\mathrm{e}^{\mp\phi}, \qquad\qquad c^{2\pm} = d^{2\pm}\mathrm{e}^{\mp 2\phi}, \tag{2.73}$$

for some functions $d^{\pm,2\pm}(x,t)$. By substituting (2.73) into (2.58), (2.67) – (2.72), we find that, throughout the water phase,

$$\delta\xi\phi_{zz} = d^{-}\mathrm{e}^{\phi} - d^{+}\mathrm{e}^{-\phi} + 2c^{*}(d^{2-}\mathrm{e}^{2\phi} - d^{2+}\mathrm{e}^{-2\phi}), \tag{2.74}$$

in regions I and III,

$$Pe^{+}\left[\frac{\partial}{\partial t}\int_0^1 d^{+}\mathrm{e}^{-\phi}\mathrm{d}z + \int_0^1 (\boldsymbol{u}_w\cdot\boldsymbol{\nabla})d^{+}\mathrm{e}^{-\phi}\,\mathrm{d}z\right] = \left[\int_0^1 d_x^{+}\mathrm{e}^{-\phi}\mathrm{d}z\right]_x - \delta Pe^{+}\frac{\partial s_c}{\partial t}, \tag{2.75}$$

$$Pe^{2+}\left[\frac{\partial}{\partial t}\int_0^1 d^{2+}\mathrm{e}^{-2\phi}\mathrm{d}z + \int_0^1 (\boldsymbol{u}_w\cdot\boldsymbol{\nabla})d^{2+}\mathrm{e}^{-2\phi}\,\mathrm{d}z\right] = \left[\int_0^1 d_x^{2+}\mathrm{e}^{-2\phi}\mathrm{d}z\right]_x - \frac{\delta Pe^{2+}}{c^{*}}\frac{\partial s_c^{+}}{\partial t}, \tag{2.76}$$

$$Pe^{k-}\left[\frac{\partial}{\partial t}\int_0^1 d^{k-}\mathrm{e}^{k\phi}\mathrm{d}z + \int_0^1 (\boldsymbol{u}_w\cdot\boldsymbol{\nabla})d^{k-}\mathrm{e}^{k\phi}\,\mathrm{d}z\right] = \left[\int_0^1 d_x^{k-}\mathrm{e}^{k\phi}\mathrm{d}z\right]_x, \tag{2.77}$$

and, in regions II IV and V,

$$Pe^{+}\left[\int_0^h \frac{\partial}{\partial t}\left(d^{+}\mathrm{e}^{-\phi}\right)\mathrm{d}z + \int_0^h (\boldsymbol{u}_w\cdot\boldsymbol{\nabla})d^{+}\mathrm{e}^{-\phi}\,\mathrm{d}z\right] = \left[\int_0^h d_x^{+}\mathrm{e}^{-\phi}\mathrm{d}z\right]_x + \delta Pe^{+}\left(s^{*}\frac{\mathrm{D}s_o}{\mathrm{D}t} - \frac{\partial s_c}{\partial t}\right), \tag{2.78}$$

$$Pe^{2+}\left[\int_0^h \frac{\partial}{\partial t}\left(d^{2+}\mathrm{e}^{-2\phi}\right)\mathrm{d}z + \int_0^h (\boldsymbol{u}_w\cdot\boldsymbol{\nabla})d^{2+}\mathrm{e}^{-2\phi}\,\mathrm{d}z\right] = \left[\int_0^h d_x^{2+}\mathrm{e}^{-2\phi}\mathrm{d}z\right]_x + \frac{\delta Pe^{2+}}{c^{*}}\left(s^{*}\frac{\mathrm{D}s_o^{+}}{\mathrm{D}t} - \frac{\partial s_c^{+}}{\partial t}\right), \tag{2.79}$$

$$Pe^{k-}\left[\int_0^h \frac{\partial}{\partial t}\left(d^{k-}\mathrm{e}^{k\phi}\right)\mathrm{d}z + \int_0^h (\boldsymbol{u}_w\cdot\boldsymbol{\nabla})d^{k-}\mathrm{e}^{k\phi}\,\mathrm{d}z+\right] = \left[\int_0^h d_x^{k-}\mathrm{e}^{k\phi}\mathrm{d}z\right]_x, \tag{2.80}$$

for $k = 1, 2$. To solve these equations for ϕ and $d^{\pm,2\pm}$, we consider the bulk regions of water, regions I and III, the thin film of water below the oil slug, region II, and the transition regions, regions IV and V, separately.

2.3.4 In the water phase: Regions I and III

In regions I and III, we expand ϕ and $d^{\pm,2\pm}$ in powers of δ to find that the leading order contributions, ϕ_0 and $d_0^{\pm,2\pm}$, satisfy

$$d_0^{-}\mathrm{e}^{\phi_0} - d_0^{+}\mathrm{e}^{-\phi_0} + 2c^{*}(d_0^{2-}\mathrm{e}^{2\phi_0} - d_0^{2+}\mathrm{e}^{-2\phi_0}) = 0. \tag{2.81}$$

Since (2.81) is an algebraic expression relating ϕ_0 and $d_0^{\pm,2\pm}(x,t)$, it follows that $\phi_0 = \phi_0(x,t)$, and therefore (2.75) – (2.77) become

$$Pe^{\pm}\left[\left(d_0^{\pm}\mathrm{e}^{\mp\phi_0}\right)_t + (d_0^{\pm}\mathrm{e}^{\mp\phi_0})_x\int_0^1 u_w\,\mathrm{d}z\right] = (d_{0_x}^{\pm}\mathrm{e}^{\mp\phi_0})_x, \tag{2.82}$$

$$Pe^{2\pm}\left[\left(d_0^{2\pm}\mathrm{e}^{\mp2\phi_0}\right)_t + (d_0^{2\pm}\mathrm{e}^{\mp2\phi_0})_x\int_0^1 u_w\,\mathrm{d}z\right] = (d_{0_x}^{2\pm}\mathrm{e}^{\mp2\phi_0})_x, \tag{2.83}$$

for $0 < x < x_r^{*}$ and $x_f^{*} < x < 1$, where $x_r^{*} = x_r/L$ and $x_f^{*} = x_f/L$. Equations (2.82) and (2.83) are subject to

$$d_0^{\pm,2\pm}(1,t) = d_0^{\pm,2\pm}(0,t) = 1 + 10^{\tau}\left(\bar{c}^{1,2} - 1\right), \tag{2.84}$$

and

$$\frac{\left(d_0^{+}\right)_x e^{-\phi_0}}{Pe^{+}} - \frac{\left(d_0^{-}\right)_x e^{\phi_0}}{Pe^{-}} + 2c^{*}\left[\frac{\left(d_0^{2+}\right)_x e^{-2\phi_0}}{Pe^{2+}} - \frac{\left(d_0^{2-}\right)_x e^{2\phi_0}}{Pe^{2-}}\right] = 0, \tag{2.85}$$

at $x = 0$, by substituting (2.73) into (2.60) – (2.62). In §2.3.6, we will find that the relevant solutions to (2.82) and (2.83) are ϕ_0 constant, which we take to be zero

without loss of generality, and $d_0^{\pm,2\pm} \equiv 1+10^{\tau}\,(\bar{c}^{1,2}-1)$ by matching with the solutions in regions IV and V.

However, after solving $\phi_{zz}=0$ in the clay phase subject to (2.63), we find that ϕ_z becomes unbounded as $z\to-\infty$, which contradicts (2.66). Hence, there is a boundary layer at the capillary wall of size ϵ_2 (to be determined). We rescale $z=\epsilon_2 Z$, and, from (2.63) and (2.64), we observe that the rescaling $\phi=\epsilon_2\xi^{-1}\Phi$ is required to balance the terms in the boundary conditions. Writing (2.74) in terms of the rescaled parameters, and expanding the exponential terms (assuming that $\epsilon_2 \ll 1$), yields

$$\frac{\delta}{\epsilon_2}\Phi_{ZZ} = d^- - d^+ + 2c^*(d^{2+}-d^{2+}) + \frac{\epsilon_2}{\xi}\left[d^+ + d^- + 4c^*\left(d^{2+}+d^{2-}\right)\right]\Phi + O\left(\epsilon_2^2\right). \tag{2.86}$$

By rescaling $\phi=\epsilon_2\xi^{-1}\Phi$, and expanding the exponential terms, we have introduced $O(\epsilon_2)$ terms into (2.86). Consequently, we must expand $d^{\pm,2\pm}$ in powers of ϵ_2 near the boundary (and wherever else this scaling is used). This is in contrast to the solution away from the boundary, where we performed the expansion in powers of δ, since this was the small parameter in the governing equations, (2.74) – (2.77). In order to match the two solutions, we make the additional assumption that $\delta \ll \epsilon_2$. This allows us to impose the constraint that the leading-order solution to the ϵ_2 expansion must match the leading-order solution of the δ expansion in the limit $Z\to\infty$.

We use the tilde notation to denote an expansion in powers of ϵ_2. We write $d^{\pm,2\pm} \sim \tilde{d_0}^{\pm,2\pm} + \epsilon_2 \tilde{d_1}^{\pm,2\pm} + O\left(\epsilon_2^2\right)$ and substitute into (2.86) to get

$$\frac{\delta\xi}{\epsilon_2^2}\Phi_{ZZ} = \left[d_0^+ + d_0^- + 4c^*\left(d_0^{2+}+d_0^{2-}\right)\right]\Phi + \xi\left[\tilde{d_1}^{-} - \tilde{d_1}^{+} + 2c^*\left(\tilde{d_1}^{2-} - \tilde{d_1}^{2+}\right)\right] + O\left(\epsilon_2\right), \tag{2.87}$$

where we have used the fact that $\tilde{d_0}^{\pm,2\pm} = d_0^{\pm,2\pm}$ by matching with the solution for $d^{\pm,2\pm}$ in the outer region. To balance the leading-order terms in (2.87), we substitute $d_0^{-,2-} = d_0^{+,2+}$ and set

$$\epsilon_2 = \left(\frac{\delta\xi}{2(d_0^+ + 4c^* d_0^{2+})}\right)^{1/2} = \frac{\lambda}{R}, \tag{2.88}$$

where

$$\lambda = \left(\frac{\varepsilon_w k_B T}{2(c_\infty^1 + 4c_\infty^2)q^2}\right)^{1/2}, \tag{2.89}$$

is the Debye length. From (2.88) we see that $\epsilon_2 = O\left(\delta^{1/2}\right)$. Since $\delta \ll 1$, the assumption we made that $\delta \ll \epsilon_2 \ll 1$ is valid, so our asymptotic analysis is consistent.

Since $\epsilon_2 \gg \delta$, and the next non-zero terms in the expansions for $d^{\pm,2\pm}$ in the outer region away from the capillary wall are $O(\delta)$, it follows that the $O\left(\epsilon_2\right)$ terms, $\tilde{d_1}^{\pm,2\pm}$,

in the expansion for $d^{\pm,2\pm}$ near the capillary wall are zero. Hence, with this definition of ϵ_2, equation (2.87) reads

$$\Phi_{ZZ} = \Phi, \tag{2.90}$$

for $0 < x < x_r^*$, $0 < z < \infty$, and $x_f^* < x < 1$, $0 < z < \infty$ at leading order in ϵ_2, subject to

$$\Phi_Z \to 0, \qquad \text{as } Z \to \infty, \tag{2.91}$$

$$[\Phi]_{Z=0^-}^{Z=0^+} = 0, \quad \Phi_Z = 2s_{c0}^+ + s_{c0} - 1, \qquad \text{at } Z = 0, \tag{2.92}$$

where (2.91) is the matching condition required to ensure that the potential in the boundary layer, Φ, matches with the outer solution, $\phi_0 = 0$, and we have used the fact that $\phi_z = 0$ in the clay phase to derive (2.92). We solve (2.90) subject to (2.91) and (2.92) to get

$$\Phi = -\left(2s_{c0}^+ + s_{c0} - 1\right) \mathrm{e}^{-Z}. \tag{2.93}$$

We see from (2.93) that the electric potential decays exponentially in the boundary layer due to screening from counter-ions in the water phase.

2.3.5 In the water phase: Region II

We now turn our attention to finding the potential in region II. Since we expect the thickness of the wetting film to be partly determined by the electrostatic forces occurring between the two charged surfaces, we suppose that $h^* = O(\epsilon_2)$[1]. Therefore, we rescale $h = \epsilon_2 H$. To balance the terms in (2.55) and (2.64), we rescale $u_w = \epsilon_2 \xi U_w$, $w_w = \epsilon_2^2 \xi W_w$, and $t = \epsilon_2^{-1}\xi^{-1} T$. In terms of Z, H, Φ, U_w, W_w, and T, equations (2.74), (2.78) – (2.80) read

$$\Phi_{ZZ} = \left(\frac{\xi}{\epsilon_2}\right)\left(\frac{d^- - d^+ + 2c^*(d^{2-} - d^{2+})}{2(d_0^+ + 4c^* d_0^{2+})}\right) + \frac{d^+ + d^- + 4c^*(d^{2+} + d^{2-})}{2(d_0^+ + 4c^* d_0^{2+})}\Phi + O(\epsilon_2), \tag{2.94}$$

$$\begin{aligned}\xi\epsilon_2 Pe^+ \left[H d_T^+ + d_x^+ \int_0^H U_w \,\mathrm{d}Z\right] = \left[d_x^+ \int_0^H \left(1 - \frac{\epsilon_2}{\xi}\Phi\right) \mathrm{d}Z\right]_x \\ + \frac{\delta\xi Pe^{2+}}{c^*}\left(s^* \frac{\mathrm{D}s_o^+}{\mathrm{D}T} - \frac{\partial s_c^+}{\partial T}\right) + O\left(\epsilon_2^2\right),\end{aligned} \tag{2.95}$$

$$\begin{aligned}\xi\epsilon_2 Pe^{2+} \left[H d_T^{2+} + d_x^{2+} \int_0^H U_w \,\mathrm{d}Z\right] = \left[d_x^{2+} \int_0^H \left(1 - \frac{2\epsilon_2}{\xi}\Phi\right) \mathrm{d}Z\right]_x \\ + \frac{\delta\xi Pe^{2+}}{c^*}\left(s^* \frac{\mathrm{D}s_o^+}{\mathrm{D}T} - \frac{\partial s_c^+}{\partial T}\right) + O\left(\epsilon_2^2\right),\end{aligned} \tag{2.96}$$

$$\xi\epsilon_2 Pe^{k-} \left[H d_T^{k-} + d_x^{k-} \int_0^H U_w \,\mathrm{d}Z\right] = \left[d_x^{k-} \int_0^H \left(1 + \frac{k\epsilon_2}{\xi}\Phi\right) \mathrm{d}Z\right]_x + O\left(\epsilon_2^2\right), \tag{2.97}$$

[1]This is the canonical scaling. If h^* is larger than $O(\epsilon_2)$ then there is a bulk region between the surfaces in which $\phi = 0$, and therefore there is no electrical interaction between them.

for $k = 1, 2$. Since we are using the boundary-layer scalings, we expand Φ and $d^{\pm,2\pm}$ in powers of ϵ_2 to find that, at leading order, equations (2.94) – (2.97) read

$$\tilde{d_0}^{-} - \tilde{d_0}^{+} + 2c^*(\tilde{d_0}^{2-} - \tilde{d_0}^{2+}) = 0, \tag{2.98}$$

$$\left(\tilde{d_0}_x^{\pm} H\right)_x = 0, \qquad \left(\tilde{d_0}_x^{2\pm} H\right)_x = 0. \tag{2.99}$$

We have used the fact that that $\delta = O(\epsilon_2^2)$, so that the terms involving the surface concentrations in (2.95) and (2.96) are neglected at leading order. In §2.3.6, we will find that the relevant solutions to (2.98) and (2.99) are the constant solutions $\tilde{d_0}^{\pm,2\pm} \equiv 1 + 10^{\tau}(\bar{c}^{1,2} - 1)$, by matching with the solutions in regions IV and V.

At the next order in ϵ_2, equation (2.94) reads

$$\Phi_{0ZZ} = \Phi_0 + \xi \left[\frac{\tilde{d_1}^{-} - \tilde{d_1}^{+} + 2c^*(\tilde{d_1}^{2-} - \tilde{d_1}^{2+})}{2(\tilde{d_0}^{+} + 4c^*\tilde{d_0}^{2+})} \right], \tag{2.100}$$

By writing (2.63) and (2.64) in terms of the rescaled variables, and using the fact that $\phi_z = 0$ in the oil and clay phases, we derive the boundary conditions

$$[\Phi_0]_{Z=0^-}^{Z=0^+} = 0, \qquad \Phi_{0Z} = 2s_{c0}^{+} + s_{c0} - 1, \qquad \text{at } Z = 0, \tag{2.101}$$

$$[\Phi_0]_{Z=H^-}^{Z=H^+} = 0, \qquad \Phi_{0Z}|^{Z=H^-} = -s^*(2s_{o0}^{+} + s_{o0} - 1), \qquad \text{at } Z = H. \tag{2.102}$$

We solve (2.100) subject to (2.101) and (2.102) to find

$$\Phi_0 = -\xi \left[\frac{\tilde{d_1}^{-} - \tilde{d_1}^{+} + 2c^*(\tilde{d_1}^{2-} - \tilde{d_1}^{2+})}{2(\tilde{d_0}^{+} + 4c^*\tilde{d_0}^{2+})} \right] + \left(2s_{c0}^{+} + s_{c0} - 1\right)\sinh Z - \frac{\left(2s_{c0}^{+} + s_{c0} - 1\right)\cosh H + s^*(2s_{o0}^{+} + s_{o0} - 1)}{\sinh H}\cosh Z. \tag{2.103}$$

We determine $\tilde{d_1}^{\pm,2\pm}$ by solving the first-order (in ϵ_2) terms in (2.95) – (2.97), which read

$$\left[\left(\tilde{d_1}^{\pm}\right)_x H\right]_x = 0, \qquad \left[\left(\tilde{d_1}^{2\pm}\right)_x H\right]_x = 0. \tag{2.104}$$

We integrate (2.104) twice and match with the solutions in regions IV and V to determine $\tilde{d_1}^{\pm,2\pm}$. In §2.3.6 we will show that the relevant solutions are $\tilde{d_1}^{\pm,2\pm} \equiv 0$.

2.3.6 In the water phase: Regions IV and V

In order to verify the solution $d_0^{\pm,2\pm} \equiv \tilde{d_0}^{\pm,2\pm} \equiv 1 + 10^{\tau}(\bar{c}^{1,2} - 1)$ throughout the water phase, and $\tilde{d_1}^{\pm,2\pm} \equiv 0$ in the thin film, we must match together the solutions in regions I, II, and III via regions IV and V. A schematic diagram of the matching

process is shown in Figure 2.4. We assume that, in region IV, the shape of the meniscus is approximately circular which, dimensionally, reads $h \sim (x - x_c)^2 / 2R$. Non-dimensionalised in terms of the rescaled variables, this gives us $H \sim \frac{1}{2}\epsilon_1^{-2}\epsilon_2^{-1}(x - x_c^*)^2$, where $x_c^* = x_c/L$ is the dimensionless apparent contact point. Thus, towards the left of the region, for $|x - x_c^*| \gg \epsilon_1\epsilon_2^{1/2}$, we find that $H \gg 1$ and therefore the oil and clay surfaces are far enough apart for the bulk water solution $\phi_0 \equiv 0$ and $d_0^{\pm,2\pm} \equiv 1+10^{\tau}(\bar{c}^{1,2} - 1)$ to be valid, with a boundary layer on the clay surface in which Φ is given by (2.93) and the constant solutions $\tilde{d_0}^{\pm,2\pm} = d_0^{\pm,2\pm} \equiv 1 + 10^{\tau}(\bar{c}^{1,2} - 1)$ and $\tilde{d_1}^{\pm,2\pm} \equiv 0$ are permitted.

Towards the right of region IV, the gradient of the oil-water interface is small so (2.103) applies. This solution is valid provided $H_x \ll \epsilon_1^{-1}\epsilon_2^{-1}$, which holds for $|x - x_c^*| \ll \epsilon_1$ assuming the circular shape of the meniscus. Hence, for $|x - x_c^*| \ll \epsilon_1$, Φ is given by (2.103), $\tilde{d_0}^{\pm,2\pm}$ satisfy (2.99), and $\tilde{d_1}^{\pm,2\pm}$ satisfy (2.104).

The two regimes ($H \gg 1$ and $H_x \ll \epsilon_1^{-1}\epsilon_2^{-1}$) overlap for $\epsilon_1\epsilon_2^{1/2} \ll |x - x_c^*| \ll \epsilon_1$. By applying a similar analysis to region V, we deduce that constant solutions for $d_0^{\pm,2\pm} = \tilde{d_0}^{\pm,2\pm}$ are applicable *throughout* the water region. Thus, our previous assertion that $d_0^{\pm,2\pm} \equiv 1 + 10^{\tau}(\bar{c}^{1,2} - 1)$ is justified. Furthermore, by solving (2.104) subject to the matching conditions that $\tilde{d_1}^{\pm,2\pm} = 0$ in regions I and III, we find that $\tilde{d_1}^{\pm,2\pm} \equiv 0$ throughout the water region. Finally, as (2.103) is asymptotically equivalent to (2.93) as $H \to \infty$, equation (2.103) is valid near the clay wall throughout region IV and V.

It is worth noting that the electric potential is the same at both ends of the tube, $\phi_0 = 0$ at $x = 0, 1$. Since positively charged ions are attracted to the negatively charged surfaces, one may expect that the negatively charged counter-ions are advected with the faster-moving bulk of the fluid to create an electric current. This is known as a 'streaming current', and the difference in the electric potential caused by the build up of ions at either end of the tube is known as the 'streaming potential'. In our model, a streaming potential does not develop in the leading-order solution for ϕ_0 since we have assumed that $Pe^{\pm,2\pm} = O(1)$. Therefore, the terms relating to ionic advection are $O(\epsilon_2)$ in equations (2.95) – (2.97), and consequently affect the potential at $O(\epsilon_2^2)$; this result is observed by Schnitzer *et al.* [90].

2.3.7 Expressions for the surface charge densities

To write ϕ as a function of the salinity, we must first find expressions for s_{c0}, s_{c0}^+, s_{o0}, and s_{o0}^+ in terms of τ. From (2.63) and (2.64), we obtain the following expressions

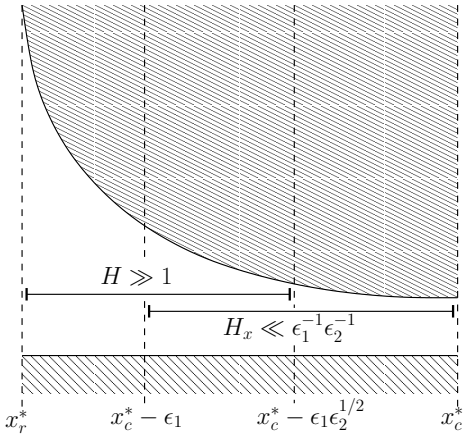


Figure 2.4: Schematic diagram of region IV. For $|x - x_c^*| \gg \epsilon_1\epsilon_2^{1/2}$ the bulk water solution is valid, as $H \gg 1$. For $|x - x_c^*| \ll \epsilon_1$ the thin film solution is valid, as $H_x \gg \epsilon_1^{-1}\epsilon_2^{-1}$.

for the surface concentrations:

$$s_{c0} = \frac{\mathcal{K}_c^1 c_0^+}{1 + \mathcal{K}_c^1 c_0^+ + \mathcal{K}_c^2 c_0^{2+}}, \qquad s_{c0}^+ = \frac{\mathcal{K}_c^2 c_0^{2+}}{1 + \mathcal{K}_c^1 c_0^+ + \mathcal{K}_c^2 c_0^{2+}}, \tag{2.105}$$

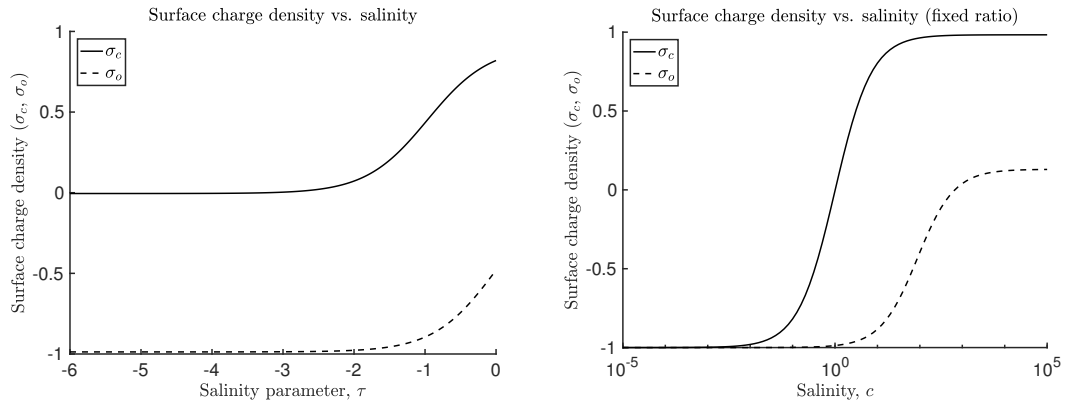
$$s_{o0} = \frac{\mathcal{K}_o^1 c_0^+}{1 + \mathcal{K}_o^1 c_0^+ + \mathcal{K}_o^2 c_0^{2+}}, \qquad s_{o0}^+ = \frac{\mathcal{K}_o^2 c_0^{2+}}{1 + \mathcal{K}_o^1 c_0^+ + \mathcal{K}_o^2 c_0^{2+}}, \tag{2.106}$$

where $c_0^{\pm,2\pm} = 1 + 10^\tau\,(\bar{c}^{1,2} - 1)$. We observe that as the concentration of divalent ions, c_0^{2+}, decreases, the number of exchange sites occupied by monovalent ions on the clay and oil surfaces, s_{c0} and s_{o0} respectively, increases. This supports the claim made by Lager *et al.* [60] that as the concentration of divalent ions in the injected water decreases, the divalent ions attracting the oil to the clay migrate into the bulk and are replaced by monovalent ions.

Using the relations for the surface charge densities, $\sigma_c = 2s_c^+ + s_c - 1$, and $\sigma_o = 2s_o^+ + s_o - 1$, we find that

$$\sigma_{c0} = \frac{\mathcal{K}_c^2 c_0^{2+} - 1}{1 + \mathcal{K}_c^1 c_0^+ + \mathcal{K}_c^2 c_0^{2+}}, \qquad \sigma_{o0} = \frac{\mathcal{K}_o^2 c_0^{2+} - 1}{1 + \mathcal{K}_o^1 c_0^+ + \mathcal{K}_o^2 c_0^{2+}}. \tag{2.107}$$

Note that σ_{c0} and σ_{o0} are constant along the capillary surface and oil-water interface, since, at leading order, the ion concentrations are constant. This is a result of the fact that $\phi = O(\epsilon_2)$, so the exponential factors in (2.73) are near unity. In Figure 2.5a, we plot the surface charge densities of the two surfaces against the salinity parameter, τ. In the high salinity regime (near $\tau = 0$) the clay surface is positively charged and the oil surface is negatively charged, resulting in attraction between the surfaces. As the salinity is reduced, the oil surface becomes more negatively charged and the



(a) (b)

Figure 2.5: Plots of the surface charge densities of the oil-water and clay-water interfaces as functions of the salinity. In Figure (a), the salinity varies between the high salinity ($\tau \approx 0$) and low salinity ($\tau \approx -6$) regimes used for low salinity waterflooding experiments. In Figure (b), the salinity ratio is kept constant, and the dimensionless concentration is defined to be $c := c^{\pm,2\pm}$. The values of the dimensionless parameters, given in Table 2.2, are $\bar{c}^1 = 100$, $\bar{c}^2 = 18$, $\mathcal{K}_c^1 = 1.7 \times 10^{-2}$, $\mathcal{K}_c^2 = 0.99$, $\mathcal{K}_o^1 = 0.01$, and $\mathcal{K}_o^2 = 1.5 \times 10^{-3}$.

clay surface becomes slightly negatively charged, resulting in repulsion between the surfaces. The clay surface charge reversal occurs when $\mathcal{K}_c^2 c_0^{2+} - 1$ changes sign. Since c_0^{2+} typically spans multiple orders of magnitude, we expect the sign change to occur as the salinity varies for a wide range of values of $\mathcal{K}_c^2$. The reduction in the attraction between the surfaces as the salinity decreases may aid the oil recovery process by increasing the mobility of oil within the reservoir, as the oil becomes 'unstuck' from the surface of the pore throat; this is consistent with the MIE proposal. The repulsion between the two surfaces is enhanced by the fact that the Debye length is greater in the low salinity regime, so the repulsion is greater as a result of the reduced screening from the counter-ions.

In Figure 2.5b, we plot the surface charge density against the salinity, keeping the ratio of divalent ions to monovalent ions constant (given by the ratio in the low salinity regime), so that, dimensionally, the concentration of each ion species is given by $c_0^{\pm} = c c_{low}^1$, and $c_0^{2\pm} = c c_{low}^2$, for some dimensionless parameter c. In dimensionless variables, the concentration of each ion species reads $c_0^{\pm} = c_0^{2\pm} = c$. In the limit $c \to 0$, we see that both surfaces have the same surface charge density, -1, and therefore repel each other in the low salinity regime. As $c \to \infty$, the surface charge density on each surface approaches a limiting value determined by the reaction rates, given by $\sigma_{c0} \to \mathcal{K}_c^2/(\mathcal{K}_c^1 + \mathcal{K}_c^2)$ and $\sigma_{o0} \to \mathcal{K}_o^2/(\mathcal{K}_o^1 + \mathcal{K}_o^2)$.

2.3.8 Electric potential near the capillary wall

To understand how variations in the surface charge densities affect the motion of the oil slug, we write (2.93) and (2.103) in terms of the surface charge densities, which reads

$$\Phi = \begin{cases} -\sigma_{c0} \mathrm{e}^{-Z} & \text{I, III,} \\ \sigma_{c0} \sinh Z - \frac{\sigma_{c0} \cosh H + s^* \sigma_{o0}}{\sinh H} \cosh Z, & \text{II, IV, V,} \end{cases} \tag{2.108}$$

where σ_{c0} and σ_{o0} are given by (2.107), and we have simplified (2.103) using the fact that $\tilde{d}_1^{\,\pm,2\pm} = 0$. The electric potential affects the macroscopic flow through equations (2.55) and the boundary condition (2.64).

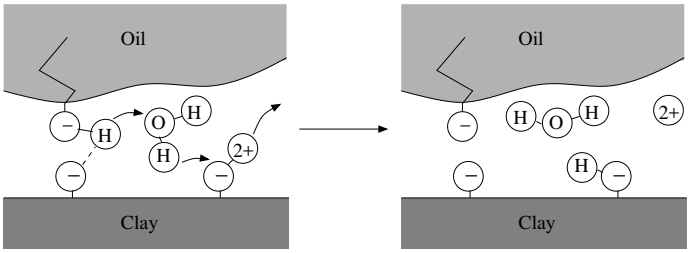
Having found an expression for the electric potential in the water phase, we are now in a position to find the thickness of the water film, the profile of the oil-water interface, and consequently the speed at which the oil slug moves through the capillary. However, before studying the macroscopic fluid dynamics problem, we will first briefly discuss how to model alternative mechanisms for the low salinity process. We observe that all of the information relating to the MIE model is contained in the expressions for the surface charge densities, (2.107). Hence, we can model alternative reaction-based mechanisms by considering a different set of reactions in place of (2.23), and applying the same methodology to obtain alternative expressions for the surface charge densities. As an example, we model the pH increase mechanism proposed by Austad *et al.* [7].

2.3.9 Modelling the pH increase mechanism

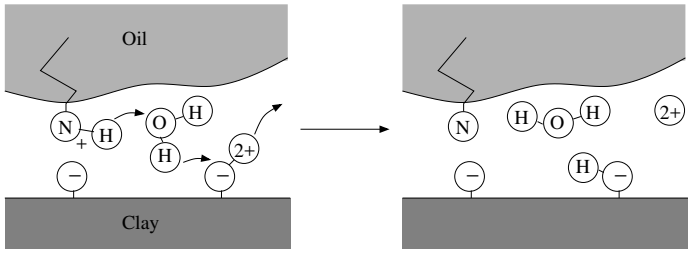
As the number of vacant exchange sites on the clay surface increases due to the net desorption of cations, Austad *et al.* [7] assert that H^+ ions from the water adsorb onto the clay surface. This increases the pH in the wetting film between the oil and the clay, which enables the release of acidic and basic compounds in the oil which are adsorbed to the clay surface. In Figure 2.6a, we show a schematic diagram of the acidic release mechanism, and in Figure 2.6b we present a schematic diagram of the basic release mechanism.

We model the three-particle reactions using separate reactions on the oil and clay surfaces. We assume that the reactions on the clay surface are given by

$$(\text{hole})^- + \mathrm{Ca}^{2+} \underset{K_{cr}^2}{\overset{K_{cf}^2}{\rightleftharpoons}} S_c^+, \qquad (\text{hole})^- + \mathrm{H}^+ \underset{K_{cr}^3}{\overset{K_{cf}^3}{\rightleftharpoons}} S_c, \tag{2.109}$$



(a) Acidic reaction



(b) Basic reaction

Figure 2.6: Diagram of the pH increase mechanism as described by [7], for the (a) acidic (negatively charged), and (b) basic (positively charged) compounds on the oil surface.

where $K^2_{c\,f}$ and $K^2_{c\,r}$ are the same as for the MIE mechanism described in §2.2.3, and $K^3_{c\,f}$ and $K^3_{c\,r}$ are the forward and reverse reaction rates, respectively, for the reaction involving the monovalent hydrogen ion.

Denoting the unoccupied acidic and basic sites on the oil surface by S^-_A and S_B, respectively, and the occupied acidic and basic sites by S_A and S^+_B, respectively, the reactions on the oil surface read

$$S^-_A + \mathrm{H}^+ \underset{K^A_{o\,r}}{\overset{K^A_{o\,f}}{\rightleftharpoons}} S_A, \qquad S_B + \mathrm{H}^+ \underset{K^B_{o\,r}}{\overset{K^B_{o\,f}}{\rightleftharpoons}} S^+_B, \tag{2.110}$$

where $K^A_{c\,f}$ and $K^A_{c\,r}$ are the forward and reverse reaction rates, respectively, for the acidic reaction, and $K^B_{c\,f}$ and $K^B_{c\,r}$ are the forward and reverse reaction rates, respectively, for the basic reaction. By following the same law-of-mass-action approach as for the MIE mechanism, we find that the adsorption isotherm expressions at the clay surface are given by

$$s_{c0} = \frac{c_0^{\mathrm{H}^+}\mathcal{K}_c^3}{1 + c_0^{\mathrm{H}^+}\mathcal{K}_c^3 + c_0^{2+}\mathcal{K}_c^2}, \qquad s_{c0}^{+} = \frac{c_0^{2+}\mathcal{K}_c^2}{1 + c_0^{\mathrm{H}^+}\mathcal{K}_c^3 + c_0^{2+}\mathcal{K}_c^2}, \tag{2.111}$$

where c_0^{2+} and $\mathcal{K}_c^2$ are the same as for the MIE mechanism, $c_0^{\mathrm{H}^+}$ denotes the leading-order concentration of monovalent H^+ ions, and $\mathcal{K}_c^3 = K^3_{c\,f} c^{\mathrm{H}^+}_{\mathrm{low}}/K^3_{c\,r}$, where $c^{\mathrm{H}^+}_{\mathrm{low}}$ is the

concentration of H^+ ions in the low salinity regime. On the oil surface, the isotherm expressions are

$$s_A^- = \frac{s_A^*}{1 + c_0^{H^+} \mathcal{K}_o^A}, \qquad s_B^+ = \frac{s_B^* c_0^{H^+} \mathcal{K}_o^B}{1 + c_0^{H^+} \mathcal{K}_o^B}, \tag{2.112}$$

where s_A^* is the surface saturation concentration of acidic compounds, s_B^* is the surface saturation concentration of basic compounds (so that $s_A^* + s_B^* = 1$ is the total surface saturation concentration of exchange sites on the oil surface), $\mathcal{K}_o^A = K_{o\,f}^A c_{\text{low}}^{H^+} / K_{o\,r}^A$, and $\mathcal{K}_o^B = K_{o\,f}^B c_{\text{low}}^{H^+} / K_{o\,r}^B$.

Substituting (2.111) and (2.112) into the expressions for the surface charge densities of the clay and oil surfaces, $\sigma_c = q(2s_c^+ + s_c - 1)$ and $\sigma_o = q(s_B^+ - s_A^-)$ respectively, we find that

$$\sigma_{c0} = \frac{\mathcal{K}_c^2 c_0^{2+} - 1}{1 + \mathcal{K}_c^3 c_0^{H^+} + \mathcal{K}_c^2 c_0^{2+}}, \qquad \sigma_{o0} = \frac{s_B^* c_0^{H^+} \mathcal{K}_o^B}{1 + c_0^{H^+} \mathcal{K}_o^B} - \frac{s_A^*}{1 + c_0^{H^+} \mathcal{K}_o^A}. \tag{2.113}$$

We observe that the expression for the surface charge density of the clay surface is of the same form as the expression in (2.107) that determines the surface charge of the clay in the MIE model, providing we associate the concentration of monovalent hydrogen ions in (2.113) with the concentration of monovalent sodium ions in (2.107). However, the expression for the surface charge of the oil in the pH increase mechanism is not of the same form as the corresponding expression in the MIE model. By applying the same asymptotic analysis as for the MIE mechanism, we conclude that $c^{H^+} \sim 1 + O(\delta)$. However, unlike in the MIE case the concentration of monovalent ions is now determined from the pH of the fluid in the thin film, rather than the salinity of the brine. Since $c_0^{H^+} \equiv 1$, the pH is unaffected by the salinity. This contradicts the idea behind the mechanism, but may partly explain why the low salinity effect can be observed without an increase in the pH [60, 98].

The pH remains constant as the salinity varies because the surface charge densities of the oil and clay surfaces are not large enough to induce a noticeable variation in the ion concentrations within the water layer for the parameter values used in this thesis. This is a consequence of the assumption that $\delta = s_c^* / c_{\text{low}}^{H^+} R \ll 1$. Some types of clays and oils may have greater surface exchange site densities, s_c^* and s_o^* respectively, leading to greater surface charge densities, and may therefore react as suggested by Austad *et al.* [7]. However, the asymptotic analysis presented in this section is not applicable in the case $\delta = O(1)$, and therefore studying this case is beyond the scope of this thesis.

Despite the pH being independent of the salinity, the surface charge density of the clay, σ_{c0}, *does* vary with the concentration of Ca^{2+}. As the salinity decreases in

(2.113), σ_{c0} goes from being positively charged to negatively charged, and σ_{o0} remains constant. This results in oil becoming less attracted to the clay surface as the salinity of the surrounding brine is reduced, which may produce the low salinity effect. The variation in σ_{c0} is due to calcium desorbing from the clay surface, in exactly the same way as in the MIE mechanism. Since the two mechanisms work using a similar process, we will focus on the effect of the MIE mechanism for the remainder of this thesis.

2.4 Solution to the fluid dynamics problem

As the shape of the oil slug is unknown *a priori*, it must be found as part of the solution. We solve for the profile of the oil-water interface at the front and rear (downstream and upstream) ends of the oil slug separately, noting that the shape of the oil slug may be different at each end due to the fluid motion. We will first find the shape of the meniscus at the front end, assuming that the oil-water interface here can be split into three distinct regions as shown in Figure 2.7. These are: (i) a flat region with constant thickness h^* (to be determined) along the base of the oil slug, in which the electrostatic forces balance the viscous forces, (ii) a meniscus region with constant curvature r^+ (to be determined) in which the capillary forces balance the viscous forces, and (iii) a transition region matching regions (i) and (ii), in which we balance the capillary forces and the electrostatic forces with the viscous forces.

Once we have found the shape of the front end of the oil slug, we will find the shape of the rear end by assuming that the rear end recedes at the same speed that the front end advances, and using the transformation $V \mapsto -V$, where V is the velocity of the oil slug. We must find V as part of the solution, but in order to do so we must first determine the film thickness below the oil slug and the menisci radii at the front and rear ends. We will then consider the macroscopic flow problem, in which the water film allows the oil to slip along the clay interface, and the corrections to the front and rear curvatures affect the pressure drop felt by the oil slug. We will determine V from this macroscopic problem.

2.4.1 Shape of the oil-water interface at the front end of the oil slug

We study the neighbourhood of the point near $x = x_c + L_o$ where, from the macroscopic perspective, there appears to be a three phase contact. We examine how the

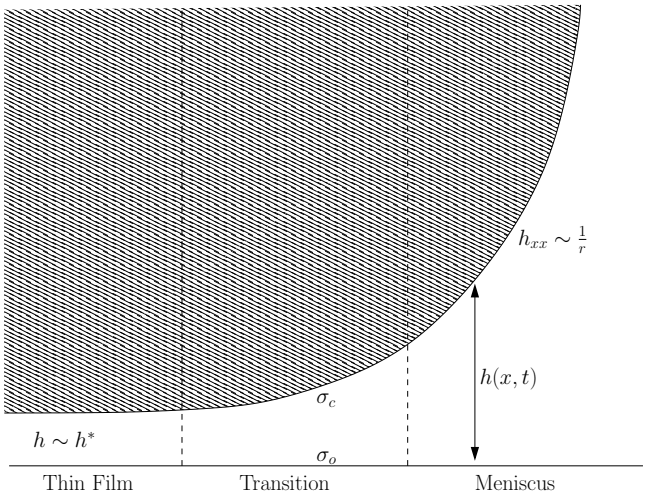


Figure 2.7: Schematic diagram of the three regions at the front meniscus.

region of constant thickness underneath the slug matches with the region of constant curvature, and this will allow us to determine h^* and r^+.

In the transition region between the thin film and the meniscus, we expect the electrostatic, capillary, and viscous forces to balance. We determine the correct scalings for the transition region by writing (2.55), (2.56), (2.63), and (2.64) in terms of the thin-film electric potential, $\Phi = \epsilon_2^{-1}\xi\phi$, and balancing the terms. This yields the rescalings

$$x - (x_c^* + L_o^*) = \epsilon_2^{1/2}\bar{X}, \qquad z = \epsilon_2 Z, \qquad h = \epsilon_2 H, \tag{2.114}$$

$$u_w = \epsilon_2^{3/2}\bar{U}_w, \quad u_o = \epsilon_2^{3/2}\bar{U}_o, \quad w_w = \epsilon_2^2\bar{W}_w, \quad w_o = \epsilon_2^2\bar{W}_o, \quad t = \epsilon_2^{-1}\bar{T}, \tag{2.115}$$

where $L_o^* = L_o/L$ is the dimensionless length of the oil slug. We write (2.55), (2.56), (2.63), and (2.64) in terms of the transition region variables, (2.114) and (2.115), and neglect terms proportional to $\epsilon_2^{1/2}$ to obtain the leading order (in $\epsilon_2^{1/2}$) system, which reads

$$\bar{U}_{w_{ZZ}} = p_{w\bar{X}} - \frac{1}{P^*}\Phi_{\bar{X}}\Phi_{ZZ}, \qquad \bar{U}_{w_{\bar{X}}} + \bar{W}_{w_Z} = 0, \tag{2.116 a,b}$$

$$\mu^*\bar{U}_{o_{ZZ}} = p_{o\bar{X}}, \qquad \bar{U}_{o_{\bar{X}}} + \bar{W}_{o_Z} = 0, \tag{2.117 a,b}$$

$$p_{wZ} = \frac{1}{P^*}\Phi_Z\Phi_{ZZ}, \qquad p_{oZ} = 0, \tag{2.118 a,b}$$

subject to

$$\bar{U}_w = \bar{W}_w = 0, \qquad Z = 0, \tag{2.119}$$

$$\bar{U}_w = \bar{U}_o, \qquad \bar{W}_w = \bar{W}_o = \bar{U}H_{\bar{X}} + H_{\bar{T}}, \qquad \bar{U}_{wZ} = \mu^* \bar{U}_{oZ}, \qquad Z = H, \tag{2.120}$$

$$p_w = p_o + \frac{1}{2P^*}\Phi_Z^2|_{Z=H^-} - \frac{\Gamma}{2P^*}H_{\bar{X}\bar{X}}, \qquad Z = H, \tag{2.121}$$

$$U_{oZ} \to 0, \qquad W_{oZ} \to 0, \qquad Z \to \infty, \tag{2.122}$$

where we have used the fact that $\Phi_Z = 0$ in the oil phase in writing down (2.121). We note that (2.122) is the constraint that the velocity is bounded in the bulk of the oil.

Integrating (2.118b) in the oil phase yields $p_o = p_o(\bar{X}, \bar{T})$. By substituting this into (2.117a) and applying (2.122), we find that $\bar{U}_{oZ} = 0$, and $p_{o_{\bar{X}}} = 0$. Hence, $\bar{U}_o = \bar{U}_o(\bar{X}, \bar{T})$, and $p_o = p_o(\bar{T})$. By integrating (2.118a) and applying (2.121) we find that the pressure in the water layer is given by

$$p_w = p_o + \frac{1}{2P^*}\Phi_Z^2 - \frac{\Gamma}{2P^*}H_{\bar{X}\bar{X}}. \tag{2.123}$$

We substitute (2.123) into (2.116a), and apply (2.119) and (2.120), to find that the horizontal component of the velocity in the transition region is given by

$$\bar{U}_w = \frac{1}{4P^*}(2HZ - Z^2)\left(\Gamma H_{\bar{X}\bar{X}} + \frac{\sigma_{c0}^2 + 2s^*\sigma_{c0}\sigma_{o0}\cosh H + s^{*2}\sigma_{o0}^2}{\sinh^2 H}\right)_{\bar{X}}, \tag{2.124}$$

where we have used the expression for Φ given in (2.108). Using (2.124) for $\bar{U}_w$, integrating (2.116b) from $Z = 0$ to $Z = H$, and applying (2.119) and (2.120), we obtain the following thin-film equation describing the thickness of the water layer, $H(\bar{X}, \bar{T})$, in the transition region,

$$H_{\bar{T}} + \left[\frac{H^3}{6P^*}\left(\Gamma H_{\bar{X}\bar{X}} + \frac{\sigma_{c0}^2 + 2s^*\sigma_{c0}\sigma_{o0}\cosh H + s^{*2}\sigma_{o0}^2}{\sinh^2 H}\right)_{\bar{X}}\right]_{\bar{X}} = 0. \tag{2.125}$$

This is a lubrication type equation [75] combining the effects of capillarity and electrostatics. In the limit $\bar{X} \to -\infty$ we impose the condition that the solution approaches a constant value, H^*, to be determined. As $\bar{X} \to \infty$ we require the solution to match with the meniscus region. We assume that the radius of the meniscus is approximately the radius of the capillary tube and that the leading-order correction, r_1^+, is of the order of the thickness of the wetting layer i.e. $r^+ = 1 - \epsilon_2 r_1^+ + O(\epsilon_2^2)$ (the $+$ superscripts denote the front meniscus). Hence, the boundary conditions we impose on H are $H \to H^*$ as $\bar{X} \to -\infty$, and $H_{\bar{X}\bar{X}} \to 1$ as $\bar{X} \to \infty$.

2.4.2 Travelling wave solution

Since this chapter is the first stage in the upscaling process, in which we investigate how the salinity affects the macroscopic flow through a porous structure, we are primarily interested in the steady-state fluid motion on the microscopic, pore scale, rather than inertial effects. Therefore, we solve (2.125) by assuming that there exists a quasi-static travelling wave solution, $H(\bar{X},\bar{T}) = H(Y)$, where we define $Y = \bar{X} - \bar{X}_R(\bar{T})$, and $\bar{X}_R$ corresponds with the origin in the reference frame moving with the oil slug, which can be chosen arbitrarily. In the travelling wave coordinate, equation (2.125) becomes

$$\epsilon_2^{-3/2} P^* V H_Y = \left[\frac{H^3}{6} \left(\Gamma H_{YY} + \frac{\sigma_{c0}^2 + 2s^*\sigma_{c0}\sigma_{o0}\cosh H + s^{*2}\sigma_{o0}^2}{\sinh^2 H} \right)_Y \right]_Y, \tag{2.126}$$

subject to[2]

$$H \to H^* \qquad \text{as } Y \to -\infty, \tag{2.127}$$

$$H_{YY} \to 1 \qquad \text{as } Y \to \infty, \tag{2.128}$$

where $V = \mathrm{d}x_r/\mathrm{d}t = \epsilon_2^{3/2}\mathrm{d}\bar{X}_R/\mathrm{d}\bar{T}$ is the velocity at which the oil slug moves, scaled with the macroscopic variables, x_r and t. We have chosen this scaling as we expect the velocity to be $O(1)$ on the macroscopic scale, as the flow is driven by the pressure gradient. The factor of $\epsilon_2^{3/2}$ arises because we have defined (2.126) in terms of the transition region variables, $Y = \epsilon_2^{-1/2}(x - x_r(t))$ and $T = \epsilon_2 t$.

We integrate (2.126) once to arrive at

$$6\epsilon_2^{-3/2} P^* V \frac{(H - H^*)}{H^3} = \Gamma H_{YYY} + \left(\frac{\sigma_{c0}^2 + 2s^*\sigma_{c0}\sigma_{o0}\cosh H + s^{*2}\sigma_{o0}^2}{\sinh^2 H} \right)_Y. \tag{2.129}$$

We would like to be able to determine H^* for a given P^*, however at this stage the velocity, V, is still unknown. To better understand (2.129) we will, for the moment, treat P^*V as an independent parameter. In §2.4.6 we will find V by solving the macroscopic flow problem in combination with (2.129).

To solve (2.129) subject to (2.127) and (2.128) for a given P^*V, we use a shooting method. We treat (2.129) as an initial value problem with H^* as the initial parameter, and vary H^* until $H(Y)$ satisfies (2.128) in the limit $Y \to \infty$. This gives us the correct value of the film thickness, H^*, and the shape of the film thickness in the transition region.

[2] In Appendix A, we show that (2.127) and (2.128) impose the required number of constraints on (2.126) to be able to find both $H(Y)$ and H^*.

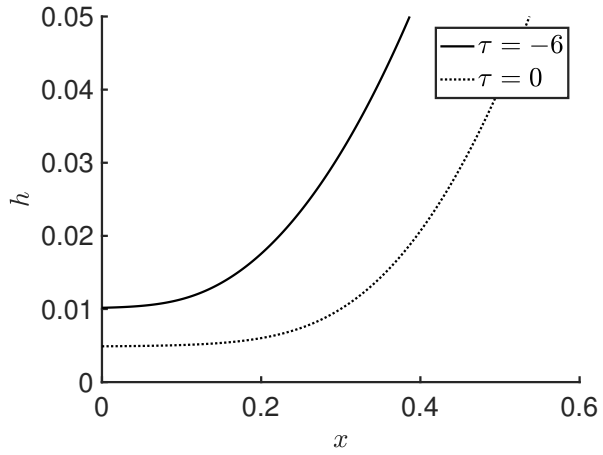


Figure 2.8: Plots of the front transition region profiles, $h(x)$, in the low ($\tau = -6$) and high ($\tau = 0$) salinity regimes, for $P^*V = 9 \times 10^{-6}$.

In Figure 2.8 we plot $h(x) = \epsilon_2 H(Y)$ in the high salinity ($\tau = 0$) and low salinity ($\tau = -6$) regimes, for $P^*V = 9 \times 10^{-6}$, where P^* is determined by the values in Table 2.1, and we have chosen $V = 1$. Values for the other parameters used are given in Table 2.2. In the numerical computations we use a fourth-order Runge-Kutta method to solve (2.129). We observe that the film is thicker in the low salinity regime than in the high salinity regime. This is consistent with the MIE proposal that reducing the salinity of the brine increases the film thickness, thus aiding the release of oil.

2.4.3 Correction to the radius of curvature

To determine the leading-order correction to the radius of curvature in the meniscus region, r_1^+, we consider the behaviour of $H(Y)$ as Y approaches the meniscus region. Since $H_{YY} \sim 1$ as $Y \to \infty$, at leading order

$$H \sim \frac{1}{2}(Y + \alpha^+)^2 + \beta^+, \qquad \text{as } Y \to \infty, \tag{2.130}$$

for some constants α^+ and β^+. Using the leading-order translational invariance of the problem, α^+ can be chosen arbitrarily, so we take it to be zero without loss of generality. To determine β^+ we match (2.130) with the film thickness in the meniscus region. In the meniscus region the oil-water interface is circular, which, in terms of the macroscopic variables x and h, gives

$$(1-h)^2 + (x - x^*)^2 = \left(r^+\right)^2 \sim \left(1 - \epsilon_2 r_1^+\right)^2, \tag{2.131}$$

where $(x^*, 1)$ is the centre of the circle with the same tangent and curvature as the extremal point of the oil-water interface, as shown in Figure 2.9. As $x \to x^*$ (i.e. as

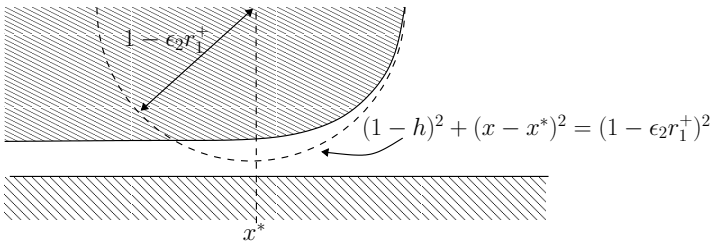


Figure 2.9: Schematic diagram of the circular solution the oil-water interface approaches.

x approaches the transition region), expanding (2.131) in $(x-x^*)$ and ϵ_2 yields,

$$h \sim \frac{1}{2}\left(x-x^*\right)^2 + \epsilon_2 r_1^+ + O\left((x-x^*)^4, \epsilon_2(x-x^*)^2\right). \tag{2.132}$$

Matching the inner solution (2.130) with the outer solution (2.132) gives $\beta^+ = r_1^+$. Differentiating (2.130) yields $H_Y \sim Y + \alpha^+$ as $Y \to \infty$, which we substitute back into (2.130) (using the fact that $\beta^+ = r_1^+$) and rearrange to give the first correction to the radius of the meniscus as

$$r_1^+ = \lim_{Y\to\infty} H - \frac{1}{2}H_Y^2. \tag{2.133}$$

By substituting the solution for $H(Y)$ found in §2.4.2 into (2.133), we can therefore compute the correction to the curvature in the front meniscus region.

2.4.4 Shape of the oil-water interface in the transition region

We study the rear end of the oil slug advancing with speed V by considering the equivalent problem of the front end *receding* with speed V. Thus, to find the shape of the oil-water interface at the rear end of the oil slug, we make the substitution $V \mapsto -V$ and solve (2.129) subject to (2.127) and (2.128) using a shooting method. However, since we have already determined H^* by considering the shape of the front transition region, we can no longer use this as a shooting parameter. To determine the correct parameter to vary, we examine the behaviour of $H(Y)$ as $Y \to -\infty$ (towards the thin film region). In this limit, we assume that $H \sim H^* + \bar{H}$, where $\bar{H}$ is small. By substituting this into (2.129), applying $\bar{H} \to 0$ as $Y \to -\infty$, and using the translational invariance of the problem to eliminate one constant of integration, we find that

$$H \sim H^* + \mathrm{e}^{k_1 Y} + A\mathrm{e}^{k_2 Y}. \tag{2.134}$$

The constants k_1 and k_2 are roots of the characteristic equation associated with the linear ODE satisfied by $\bar{H}$, and A is an unknown constant; the details of this

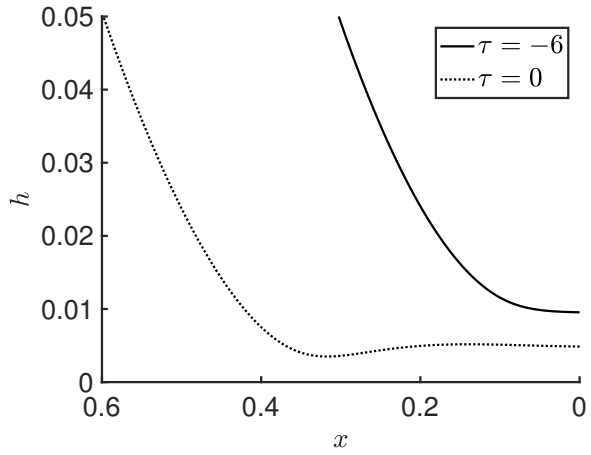


Figure 2.10: Plots of the rear transition region profiles, $h(x)$, in the low ($\tau = -6$) and high ($\tau = 0$) salinity regimes, for $P^*V = 9 \times 10^{-6}$.

calculation are given in Appendix A. We determine the shape of the rear transition region, $H(Y)$, by solving (2.129) (with the substitution $V \mapsto -V$) subject to (2.128) in the limit $Y \to \infty$ and (2.134) in the limit $Y \to -\infty$, with A as a shooting parameter.

In Figure 2.10 we plot $h(x) = \epsilon_2 H(Y)$ in the high salinity ($\tau = 0$) and low salinity ($\tau = -6$) regimes, with $P^*V = 9 \times 10^{-6}$. We observe that the profile of the rear of the oil slug is non-monotonic in the high salinity regime. This in contrast to the profile of the front of the oil slug, shown in Figure 2.8, which is monotonic in both regimes. This is consistent with Bretherton [15], who studied the motion of a bubble though a capillary and found that the front meniscus is monotonic, whereas the rear meniscus exhibits sinusoidal behaviour in the absence of electrostatic forces.

2.4.5 Correction to the radius of curvature

At the rear of the oil slug we find that, similarly to the front of the oil slug, the leading-order correction to the radius of curvature of the meniscus is given by

$$r_1^- = \lim_{Y \to \infty} H - \frac{1}{2} H_Y^2, \tag{2.135}$$

where the radius of curvature is $r^- \sim 1 - \epsilon_2 r_1^- + O(\epsilon_2^2)$, and $H(Y)$ is the solution found in §2.4.4.

2.4.6 Macroscopic capillary problem

We now consider the macroscopic flow problem to determine the velocity, V, at which the oil slug moves through the capillary, using the solutions for the shape of the oil

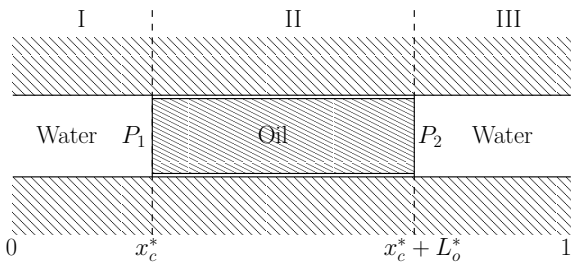


Figure 2.11: Schematic diagram of the macroscopic flow problem.

slug found in §2.4.2 and §2.4.4. On the macroscopic scale, the thin wetting film will be felt by the oil through an effective boundary condition on the oil-clay interface. The corrections to the menisci radii will affect the pressure difference at the oil-water interface at each end of the oil slug, and hence the speed at which the oil slug moves.

Returning to the macroscopic variables x, z, u_w, u_o, w_w, and w_o, the leading-order equations governing the fluid dynamics, (2.55) and (2.56), read

$$u_{wzz} = p_{wx}, \qquad p_{wz} = 0, \qquad u_{wx} + w_{wz} = 0, \tag{2.136 a,b,c}$$

$$\mu^* u_{ozz} = p_{ox}, \qquad p_{oz} = 0, \qquad u_{ox} + w_{oz} = 0. \tag{2.137 a,b,c}$$

We have previously separated the problem into the five regions (recall Figure 2.2). However, when considering the macroscopic problem we can neglect meniscus regions IV and V as x is scaled with the length of the capillary, L, and these regions have length $O(R)$. Hence, $x_c^* - x_r^* = O(\epsilon_1)$ and $x_f^* - x_c^* - L_o^* = O(\epsilon_1)$, where $x_r^* = x_r/L$ and $x_f^* = x_f/L$ are the dimensionless positions of the rear and front end of the oil slug, respectively. We impose the Laplace-Young boundary condition in (2.64) on the oil slug at the positions $x = x_c^*$ and $x = x_c^* + L_o^*$. In Figure 2.11, we present a schematic diagram of the the regions involved in the macroscopic problem.

We let P_1 and P_2 correspond to the unknown pressures on the water side of the water-oil interfaces at $x = x_c^*$ and $x = x_c^* + L_o^*$ respectively. The boundary conditions

(2.60) – (2.66) read

$$p_w = 1, \qquad \text{at } x = 0, \tag{2.138}$$

$$p_w = P_1, \qquad p_o = P_1 + \frac{\Gamma}{2P^*(1-\epsilon_2 r_1^-)}, \qquad \text{at } x = x_c^*, \tag{2.139}$$

$$p_w = P_2, \qquad p_o = P_2 + \frac{\Gamma}{2P^*(1-\epsilon_2 r_1^+)}, \qquad \text{at } x = x_c^* + L_o^*, \tag{2.140}$$

$$p_w = 0, \qquad \text{at } x = 1, \tag{2.141}$$

$$\boldsymbol{u}_w = 0, \qquad \text{at } z = 0, \tag{2.142}$$

$$\boldsymbol{u}_w = \boldsymbol{u}_o, \qquad \mu^* u_{oz} = u_{wz}, \qquad p_w = p_o, \qquad \text{at } z = \epsilon_2 H^* \tag{2.143}$$

$$p_z = u_{wz} = u_{oz} = w_w = w_o = 0, \qquad \text{at } z = 1. \tag{2.144}$$

We will solve (2.136) – (2.144) to determine the water flux in regions I and III and the oil flux in region II separately, in terms of P_1 and P_2. We will then use conservation of flux between the three regions to eliminate the unknown pressures and find the macroscopic flux through the capillary.

2.4.7 Macroscopic capillary problem: Regions I and III

From (2.136b), we see that $p_w = p_w(x)$. By integrating (2.136a) twice and applying (2.142) and (2.144), we find that, in regions I and III,

$$u_w = p_{wx}\left(\frac{1}{2}z^2 - z\right). \tag{2.145}$$

By integrating (2.136c) from $z = 0$ to $z = 1$ and applying (2.142) and (2.144), we find that

$$\frac{\partial}{\partial x}\left[\int_0^1 u_w \mathrm{d}z\right] = 0. \tag{2.146}$$

It follows that $p_{wxx} = 0$, i.e. the pressure gradient is constant. Integrating (2.146) and substituting (2.145) yields

$$Q_w := \int_0^1 u_w \,\mathrm{d}z = -\frac{1}{3}p_{wx}, \tag{2.147}$$

where Q_w is the volumetric flow rate of water in the lower half of the capillary tube. By applying (2.138) – (2.141), we find that

$$Q_w = \frac{1}{3x_c^*}(1 - P_1), \qquad \text{in region I,} \tag{2.148}$$

$$Q_w = \frac{1}{3(1 - x_c^* - L_o^*)}P_2, \qquad \text{in region III.} \tag{2.149}$$

2.4.8 Macroscopic capillary problem: Region II

From (2.137b), we see that $p_o = p_o(x)$. Integrating (2.136a) and (2.137a) subject to (2.142) – (2.144) yields (to $O(\epsilon_2)$),

$$u_w = p_{wx}\left(\frac{1}{2}z^2 - z\right) \qquad 0 < z < \epsilon_2 H^*, \tag{2.150}$$

$$u_o = \frac{1}{\mu^*}p_{ox}\left(\frac{1}{2}z^2 - z + \epsilon_2 H^*(1-\mu^*)\right) \qquad \epsilon_2 H^* < z < 1. \tag{2.151}$$

By integrating (2.136c) from $z = 0$ to $z = \epsilon_2 H^*$, (2.137c) from $z = \epsilon_2 H^*$ to $z = 1$, and applying (2.142) – (2.144), we find that

$$\frac{\partial}{\partial x}\left[\int_0^{\epsilon_2 H^*} u_w \mathrm{d}z + \int_{\epsilon_2 H^*}^1 u_o \mathrm{d}z\right] = 0, \qquad \text{in region II.} \tag{2.152}$$

By substituting (2.150) into (2.152), we find that the water flux makes an $O(\epsilon_2^2)$ contribution to the overall flux, since the water layer is thin and has low velocity near the capillary surface; it can thus be neglected. Hence, by substituting (2.151) into (2.152), it follows that that $p_{oxx} = 0$. Integrating (2.152) yields

$$Q_o := \int_{\epsilon_2 H}^1 u_o \,\mathrm{d}z = -\frac{1}{\mu^*}p_{ox}\left(\frac{1}{3} - \epsilon_2(1-\mu^*)H^*\right), \qquad \text{in region II,} \tag{2.153}$$

where Q_o is the volumetric flow rate of oil in the lower half of the capillary tube. By integrating p_{oxx} and imposing (2.139) and (2.140), we find that

$$p_o = \left[\frac{P_2 - P_1}{L_o^*} + \frac{\epsilon_2\Gamma}{2P^*L_o^*}\left(r_1^+ - r_1^-\right)\right]x + \frac{P_1(L_o^* + x_c^*) - x_c^* P_2}{L_o^*} + \frac{\Gamma}{2P^*} + \frac{\epsilon_2\Gamma}{2P^*L_o^*}\left[(L_o^* + x_c^*)r_1^- - x_c^* r_1^+\right] + O\left(\epsilon_2^2\right). \tag{2.154}$$

Substituting (2.154) into (2.153) yields

$$Q_o = \frac{1}{\mu^* L_o^*}\left\{\frac{P_1 - P_2}{3} + \epsilon_2\left[\frac{\Gamma}{6P^*}(r_1^- - r_1^+) - (P_1 - P_2)(1-\mu^*)H^*\right]\right\} + O(\epsilon_2^2). \tag{2.155}$$

2.4.9 Effective slip

An alternative way to interpret how the water film affects the flow of oil is to take the limit in which the water layer thickness tends to zero and derive an effective boundary condition at the capillary surface. By evaluating u_o and u_{oz} on $z = 0$ using (2.151), and eliminating p_{ox}, we find that

$$u_o = \epsilon_2 H^*\left(\mu^* - 1\right)u_{oz}, \qquad \text{on } z = 0, \tag{2.156}$$

which is equivalent to applying a slip boundary condition [25, 109] at the bottom of the oil slug. We observe that, since the oil is more viscous than the water, $\mu^* > 1$, the presence of the thin water film below the oil slug results in slip along the capillary surface, with the slip length being proportional to the width of the water film.

2.4.10 Macroscopic flux

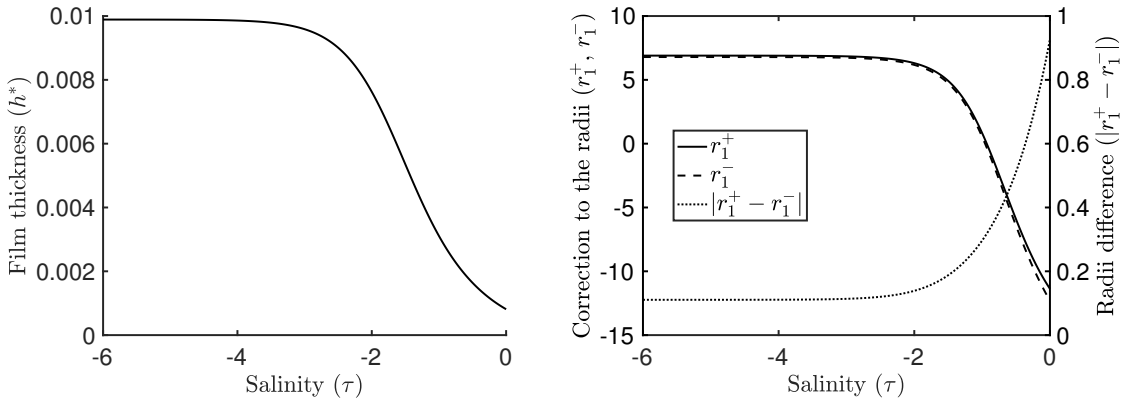
Since we assume that the slug fills almost the whole width of the channel ($\epsilon_2 H^*$ is small), conservation of volume imposes that $Q := Q_o \sim Q_w$. Hence, by solving the three equations, (2.148), (2.149), and (2.155), for the three unknowns, P_1, P_2, and Q, we find that

$$Q \sim \frac{1}{1+(\mu^*-1)L_o^*}\left\{\frac{1}{3}+\epsilon_2\left[\underbrace{\frac{\Gamma}{6P^*}(r_1^- - r_1^+)}_{\text{capillary}} + \underbrace{\frac{\mu^* L_o^*}{1+(\mu^*-1)L_o^*}(\mu^*-1)H^*}_{\text{slip due to thin water film}}\right]\right\}. \tag{2.157}$$

We see from (2.157) that the volumetric flow rate consists of a leading-order term, plus a capillary contribution resulting from a difference between the droplet shape at the front and rear of the slug, and a slip term resulting from the finite film thickness. In order to make use of this expression, we need to use the solutions for $r_1^{\pm}$ and H^* found in §2.4.2, §2.4.3, §2.4.4 and §2.4.5 by solving (2.129) subject to (2.127) and (2.128). However, since the volumetric flow rate is the velocity of the oil slug multiplied by the channel width, $Q = V$, the solution for H given by solving (2.129) is dependent on Q. Thus, we must solve (2.129) and (2.157) simultaneously to determine the velocity.

In Figure 2.12a, we plot the film thickness, $h^* = \epsilon_2 H^*$, against the salinity, τ. The film thickness is approximately ten times smaller in the high salinity regime by comparison with the low salinity regime. This percentage decrease is larger than found experimentally by Lee *et al.* [62]. This is likely due to the fact that we have neglected structural and van der Waals forces from our model. As discussed in Hirasaki [39], the structural forces due to the finite size of the ions dominate for thin films (such as in our high salinity regime) which prevents the film thickness from reducing further. Furthermore, as the thickness of the film becomes comparable with the size of the ions in the model, the continuum assumption breaks down and the model presented here is no longer applicable.

In Figure 2.12b we plot the corrections to the menisci radii, $r_1^{\pm}$, and the magnitude of the difference between them, $|r_1^+ - r_1^-|$, against the salinity. The corrections to the menisci radii increase as the salinity decreases, and therefore the menisci radii



(a) Film thickness vs salinity

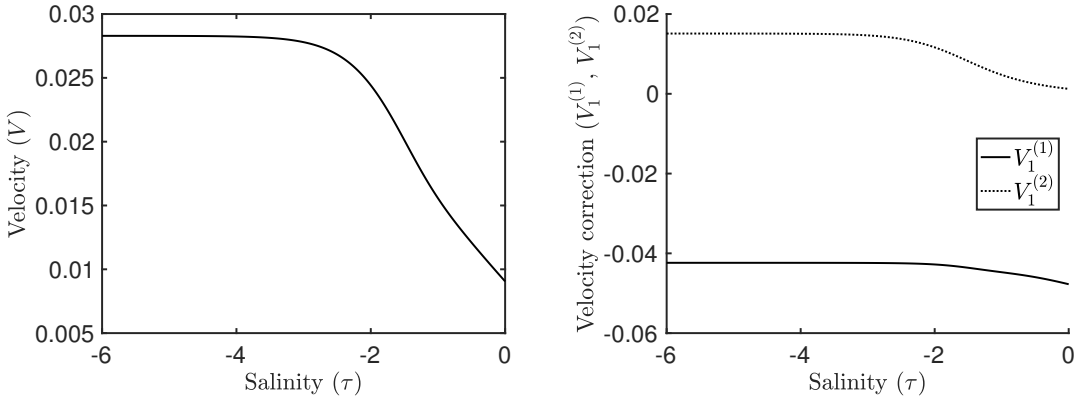
(b) Radii corrections vs salinity

Figure 2.12: (a) Film thickness, h^* against the salinity, τ. (b) Corrections to the menisci radii, $r_1^{\pm}$, and the difference, $|r_1^+ - r_1^-|$, against the salinity, τ.

decrease. The difference between the front and rear corrections is an order of magnitude smaller than the corrections themselves, suggesting that the asymmetrical fluid motion contributes a small perturbation to the menisci radii. This difference is approximately 8.4 times larger in the high salinity regime than in the low salinity regime.

In Figure 2.13a, we plot the velocity of the oil slug, V, against the salinity, τ. We choose $L_o^* = 0.5$ for this calculation and for subsequent computations. We observe that the velocity decreases as the salinity increases, with the velocity being approximately 3.1 times larger in the low salinity regime than in the high salinity regime.

In Figure 2.13b, we plot the components of the velocity corresponding to (i) the difference in the menisci radii, $V_1^{(1)} = \epsilon_2 \Gamma \left(r_1^- - r_1^+\right) / 6P^* \left(1 + (\mu^* - 1)\, L_o^*\right)$, and (ii) the slip resulting from the thin water layer, $V_1^{(2)} = \epsilon_2 \mu^* L_o^* \left(\mu^* - 1\right) H^* / \left(1 + (\mu^* - 1)\, L_o^*\right)^2$. We observe that $V_1^{(1)}$ and $V_1^{(2)}$ have opposite signs and are of a similar magnitude to the first term in (2.157), $V_0 := 1/3 \left(1 + (\mu^* - 1)\, L_o^*\right) \approx 0.056$. This is a result of the fact that $P^* \ll \epsilon_2$ for the values of the parameters used (given in Table 2.1), and implies that $V_1^{(1)}$ and $V_1^{(2)}$ (which depend on V through (2.129)) contribute to the dominant balance in (2.157). This is in contrast with the $P^* \gg \epsilon_2$ regime, in which $V_1^{(1)}$ and $V_1^{(2)}$ are perturbations to the leading-order velocity, V_0. Although $P^* \ll \epsilon_2$ for the values used in this thesis, it is worth noting that due to the diversity of reservoir conditions there will likely be applications in which $P^* \gg \epsilon_2$. Since we are able to make further analytical progress in this regime, we will briefly discuss the case $P^* \gg \epsilon_2$ in §2.4.11.



(a) Velocity vs salinity

(b) Components of the velocity correction, V_1 vs salinity

Figure 2.13: Plots of the velocity of the oil slug, given by equation (2.157), as a function of the salinity, τ. Figure (a) is the total velocity, and Figure (b) shows the two corrections to the velocity. These are $V_1^{(1)} = \frac{\epsilon_2 \Gamma}{6P^*(1+(\mu^*-1)L_o^*)}\left(r_1^- - r_1^+\right)$, and $V_1^{(2)} = \frac{\epsilon_2 \mu^* L_o^*}{(1+(\mu^*-1)L_o^*)^2}\left(\mu^* - 1\right)H^*$.

2.4.11 Solution when $P^* \gg \epsilon_2$

For $P^* \gg \epsilon_2$, we expand $Q \sim Q_0 + \epsilon_2 Q_1 + O(\epsilon_2^2)$ and $V \sim V_0 + \epsilon_2 V_1 + O(\epsilon_2^2)$. By expanding in ϵ_2, we are able to solve (2.129) and (2.157) independently, since at leading order (2.157) reduces to

$$Q_0 = V_0 = \frac{1}{3}\left[\frac{1}{1+(\mu^*-1)L_o^*}\right], \tag{2.158}$$

which does not depend on the shape of the oil slug. Using this leading-order expression for the velocity, we determine H^* and $r_1^{\pm}$ using the method described in §2.4.2, §2.4.3, §2.4.4 and §2.4.5 with $V = V_0$. We substitute the resulting solutions into (2.157) to get the correction to the velocity. This is in contrast to the $P^* \ll \epsilon_2$ case, in which we are not able to solve (2.129) and (2.157) independently, since the velocity correction due to the difference in the menisci radii can no longer be neglected at leading order. However, for $P^* \ll \epsilon_2^{3/2}$ we can simplify (2.129), enabling us to make further analytical progress.

2.4.12 Solution when $P^* \ll \epsilon_2^{3/2}$

The limit $P^* \ll \epsilon_2^{3/2}$ corresponds to the quasi-static limit in which the pressure difference across the capillary tube is negligible in comparison with the electrostatic pressure between the charged interfaces. For the values used in this thesis, $\epsilon_2^{-3/2} P^* \approx 0.15$

in the low salinity regime which justifies considering this limit. However, different reservoirs will contain different clays, oils, and pore geometries, so the quasi-static limit in which $P^* \to 0$ may not always be applicable. Furthermore, in the high salinity regime, $\epsilon_2^{-3/2} P^* \approx 3.2$, so this approximation does not apply.

To determine the film thickness, we return to (2.129) and integrate once to find that

$$\Gamma H_{YY} + \frac{\sigma_{c0}^2 + 2s^*\sigma_{c0}\sigma_{o0}\cosh H + s^{*2}\sigma_{o0}^2}{\sinh^2 H} + 6\epsilon_2^{-3/2} P^* V \int_Y^\infty \frac{H - H^*}{H^3} \mathrm{d}Y' = \Gamma. \quad (2.159)$$

By expanding H and H^* in powers of $\epsilon_2^{-3/2}P^*$, $H \sim H_0 + \epsilon_2^{-3/2} P^* H_1 + O(\epsilon_2^{-3} P^{*2})$ and $H^* \sim H_0^* + \epsilon_2^{-3/2} P^* H_1^* + O(\epsilon_2^{-3} P^{*2})$, we find that, at leading order,

$$\Gamma H_{0YY} + \frac{\sigma_{c0}^2 + 2s^*\sigma_{c0}\sigma_{o0}\cosh H_0 + s^{*2}\sigma_{o0}^2}{\sinh^2 H_0} = \Gamma. \quad (2.160)$$

We determine H_0 by solving (2.160) subject to $H_0 \to H_0^*$ as $Y \to -\infty$ and $H_{0YY} \to 1$ as $Y \to \infty$. However, by considering (2.160) in the limit $Y \to -\infty$, we can immediately determine the film thickness,

$$H_0^* = \cosh^{-1}\left(\frac{s^*\sigma_{c0}\sigma_{o0} + \sqrt{(\sigma_{c0}^2 + \Gamma)(s^{*2}\sigma_{o0}^2 + \Gamma)}}{\Gamma}\right). \quad (2.161)$$

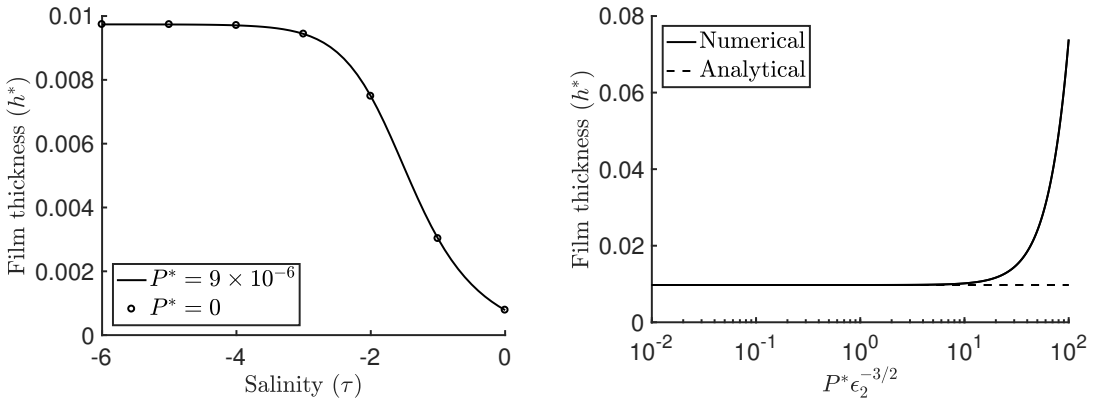
Furthermore, by substituting (2.161) into (2.156), we find that the effective slip length along the oil-clay interface is given by

$$\lambda_s = \left(\frac{\mu_o}{\mu_w} - 1\right)\cosh^{-1}\left(\frac{s^*\sigma_{c0}\sigma_{o0} + \sqrt{(\sigma_{c0}^2 + \Gamma)(s^{*2}\sigma_{o0}^2 + \Gamma)}}{\Gamma}\right). \quad (2.162)$$

In Figure 2.14a, we plot the film thickness, (2.161), against the salinity, for $-6 < \tau < 0$. We compare the numerical solution found in §2.4.10, using $P^* = 9 \times 10^{-6}$, with the asymptotic solution in the limit $\epsilon_2^{-3/2} P^* \to 0$, (2.161). There is excellent agreement between the two solutions. In Figure 2.14b we plot the film thickness, $h^* = \epsilon_2 H^*$, found numerically in §2.4.10 against $\epsilon_2^{-3/2} P^*$ in the low salinity regime, for $10^{-2} < \epsilon_2^{-3/2} P^* < 10^2$. We compare the result with the film thickness found in the asymptotic limit $\epsilon_2^{-3/2} P^* \to 0$. The asymptotic solution agrees with the numerical solution to within 4.4%, for $\epsilon_2^{-3/2} P^* < 10$.

To determine $r_1^{\pm}$, we integrate (2.159) to get

$$\frac{\Gamma}{2} H_Y^2 + \frac{2s^*\sigma_{c0}\sigma_{o0} + (\sigma_{c0}^2 + s^{*2}\sigma_{o0}^2)\cosh H^*}{\sinh H^*} - \frac{2s^*\sigma_{c0}\sigma_{o0} + (\sigma_{c0}^2 + s^{*2}\sigma_{o0}^2)\cosh H}{\sinh H} + 6\epsilon_2^{-3/2} P^* V \int_{-\infty}^{Y} H_Y \int_{Y'}^\infty \frac{H - H^*}{H^3} \mathrm{d}Y'' \mathrm{d}Y' = \Gamma(H - H^*). \quad (2.163)$$



(a) (b)

Figure 2.14: (a) Film thickness as a function of the salinity, comparing the numerical solution for $P^* = 9 \times 10^{-6}$ with the asymptotic solution in the limit $\epsilon_2^{-3/2} P^* \to 0$. (b) Film thickness as a function of the dimensionless pressure, $\epsilon_2^{-3/2} P^*$, in the low salinity regime, comparing the numerical solution with the analytic solution in the limit $\epsilon_2^{-3/2} P^* \to 0$.

We have retained the $O(\epsilon_2^{-3/2} P^*)$ terms, as we will need to solve the first-order system in order to determine the effect of the fluid motion on the corrections to the menisci radii.

We substitute the expansion $H \sim H_0 + \epsilon_2^{-3/2} P^* H_1 + O\left(\epsilon_2^{-3} P^{*2}\right)$ and consider the leading-order terms in the limit $Y \to \infty$ to get

$$\frac{\Gamma}{2} H_{0Y}^2 + \frac{2 s^* \sigma_{c0} \sigma_{o0} + (\sigma_{c0}^2 + s^{*2} \sigma_{o0}^2) \cosh H_0^*}{\sinh H_0^*} - (\sigma_{c0}^2 + s^{*2} \sigma_{o0}^2) = \Gamma (H_0 - H_0^*). \quad (2.164)$$

Integrating once yields

$$H_0 \sim \frac{1}{2} \left(Y + \alpha^+\right)^2 + \left\{ H_0^* + \frac{\left(\sigma_{c0}^2 + s^{*2} \sigma_{o0}^2\right)}{\Gamma} \left(\coth H_0^* - 1\right) + \frac{2 s^* \sigma_{c0} \sigma_{o0}}{\Gamma \sinh H_0^*} \right\}. \quad (2.165)$$

By matching terms with (2.130), and using the fact that $\beta^+ = r_1^+$, we find that the bracketed term in (2.165) must be the first-order (in ϵ_2) correction to the radius of the meniscus,

$$r_1^+ \sim H_0^* + \frac{\left(\sigma_{c0}^2 + s^{*2} \sigma_{o0}^2\right)}{\Gamma} \left(\coth H_0^* - 1\right) + \frac{2 s^* \sigma_{c0} \sigma_{o0}}{\Gamma \sinh H_0^*} + O(\epsilon_2^{-3/2} P^*). \quad (2.166)$$

To find the correction to the meniscus radius at the rear end of the oil slug, we make the substitution $V \mapsto -V$. However, as the leading-order correction to the radius of curvature (2.166) is independent of V, the first-order correction is required in order to find the leading-order *difference* between the radii of the two menisci.

The $O(\epsilon_2^{-3/2}P^*)$ terms in equation (2.163) read

$$\Gamma H_{0Y}H_{1Y} + H_1\frac{2s^*\sigma_{c0}\sigma_{o0}\cosh H_0 + \sigma_{c0}^2 + s^{*2}\sigma_{o0}^2}{\sinh^2 H_0} + 6V\int_{-\infty}^{Y} H_{0Y}\int_{Y'}^{\infty}\frac{H_0 - H_0^*}{H_0^3}\mathrm{d}Y''\mathrm{d}Y' = \Gamma H_1, \quad (2.167)$$

where we have made use of (2.161) in eliminating some of the terms. We find that

$$H_1 \sim \frac{6V}{\Gamma}\int_{-\infty}^{\infty}\frac{\left(H_0 - H_0^*\right)^2}{H_0^3}\mathrm{d}Y', \quad (2.168)$$

as $Y \to \infty$, which provides the $O(\epsilon_2^{-3/2}P^*)$ term in the expression for r_1^+. By making the substitution $V \mapsto -V$ we find that the $O(\epsilon_2)$ corrections to the front (r^+) and back (r^-) radii are

$$r_1^{\pm} \sim H_0^* + \frac{\left(\sigma_{c0}^2 + s^{*2}\sigma_{o0}^2\right)}{\Gamma}\left(\coth H_0^* - 1\right) + \frac{2s^*\sigma_{c0}\sigma_{o0}}{\Gamma\sinh H_0^*} \pm \frac{6P^*V}{\epsilon_2^{3/2}\Gamma}\int_{-\infty}^{\infty}\frac{\left(H_0 - H_0^*\right)^2}{H_0^3}\mathrm{d}Y'. \quad (2.169)$$

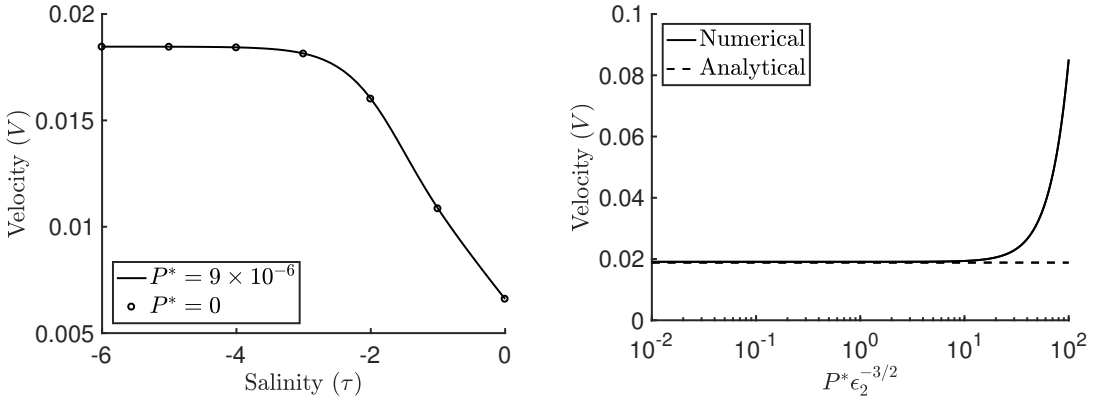
To determine the velocity of the oil slug in the limit $P^* \ll \epsilon_2^{3/2}$, we substitute (2.169) into (2.157) and rearrange (using the fact that $Q = V$) to find

$$Q = V \sim \frac{\frac{1+(\mu^*-1)L_o^*}{3} + \epsilon_2\left[L_o^*\mu^*(\mu^*-1)H_0^*\right]}{\left[1+(\mu^*-1)L_o^*\right]^2 + 2\epsilon_2^{-1/2}\left(1+(\mu^*-1)L_o^*\right)\int_{-\infty}^{\infty}\frac{(H_0-H_0^*)^2}{H_0^3}\mathrm{d}Y'}, \quad (2.170)$$

where H_0^* is given by (2.161), and H_0 is found by solving (2.160) subject to $H_0 \to H_0^*$ as $Y \to -\infty$, and $H_{0YY} \to 1$ as $Y \to \infty$.

It should be noted that (2.160) needs to be solved numerically to evaluate the integral term in (2.170), even in this asymptotic limit. However, this computation can be made simpler by integrating (2.160) once, subject to $H_0 \to H_0^*$ as $Y \to -\infty$, to obtain (2.163) (with P^* set to zero). Thus, we only need to solve a first-order ODE. Furthermore, since we have an expression for the film thickness, (2.161), we can solve (2.163) as a boundary value problem, whereas for the $\epsilon_2^{-3/2}P^* = O(1)$ problem we need to use a shooting method as this boundary condition is unknown.

In Figure 2.15a we plot the velocity of the oil slug against the salinity, τ, for $-6 < \tau < 0$. We compare the numerical solution found in §2.4.10 using $P^* = 9 \times 10^{-6}$, with the asymptotic solution in the limit $\epsilon_2^{-3/2}P^* \to 0$, (2.170). There is good agreement between the two solutions. The velocity is approximately three times greater in the low salinity regime, for $P^* = 0$, which suggests that the MIE mechanism, as described by the model presented here, contributes to the low salinity effect.



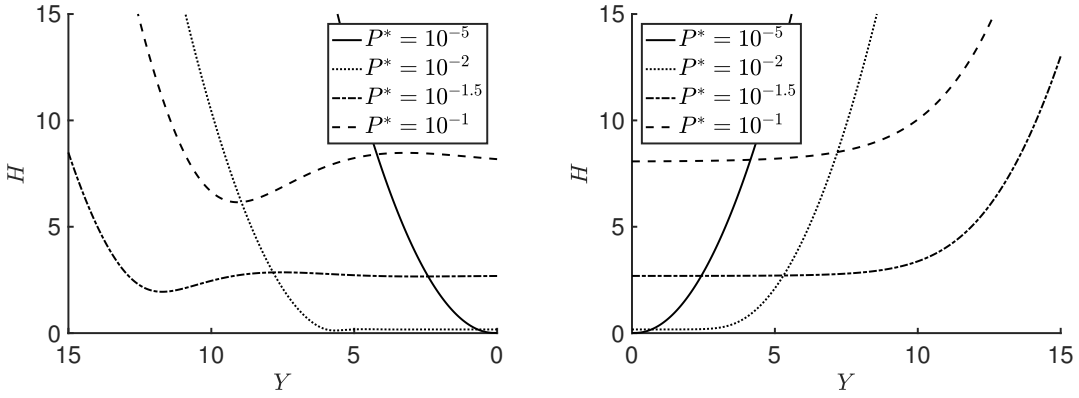
(a) (b)

Figure 2.15: (a) Velocity of the oil slug as a function of the salinity, comparing numerical solution for $P^* = 9 \times 10^{-6}$ with the asymptotic solution in the limit $\epsilon_2^{-3/2} P^* \to 0$. (b) Velocity as a function of the dimensionless pressure, $\epsilon_2^{-3/2} P^*$, in the low salinity regime, comparing the numerical solution with the analytic solution in the limit $\epsilon_2^{-3/2} P^* \to 0$.

In Figure 2.15b we plot the velocity as a function of $\epsilon_2^{-3/2} P^*$ in the low salinity regime, comparing the numerical and asymptotic solutions. The solutions agree to within 2.8% for $\epsilon_2^{-3/2} P^* < 10$. We expect that $\epsilon_2^{-3/2} P^* < 10$ for most reservoir conditions, and consequently that the quasi-static limit can usually be applied. However, in other applications where the applied pressure is much larger, P^* can no longer be considered small. We briefly study how larger pressures affect the shape and velocity of the oil slug.

2.4.13 Shape of the oil-water interface for large $\epsilon_2^{-3/2} P^*$

In Figure 2.16, we plot the profiles of the front and rear transition regions, $H(Y)$, found by solving (2.129) subject to $H \to H^*$ as $Y \to -\infty$ and $H_{YY} \to 1$ as $Y \to \infty$, for $P^* = 10^{-5}, 10^{-2}, 10^{-1.5}, 10^{-1}$ in the low salinity regime, $\tau = -6$. We see that the front meniscus is always monotonic, but that non-monotonic solutions are possible for the rear meniscus. This is because the characteristic equation of (2.129) under a perturbation, $H = H^* + \bar{H}$, only admits real-valued solutions when $V > 0$ for all P^*, but admits complex-valued solutions when $V < 0$ for $P^* > 1.6 \times 10^{-3}$ in the low salinity regime; the details of this calculation are given in Appendix A. Hence, the front profile is monotonic for all pressures, the rear profile is monotonic at lower pressures ($P^* = 10^{-5}$), but for higher pressures ($P^* = 10^{-2}, 10^{-1.5}, 10^{-1}$) the rear profile has a sinusoidal component. We also observe that the film thickness increases



(a) Rear transition region profile

(b) Front transition region profile

Figure 2.16: Plots of the rear and front oil-water interface profiles in the low salinity regime, $\tau = -6$, for $P^* = 10^{-5}, 10^{-2}, 10^{-1.5}, 10^{-1}$.

as P^* increases. This is because at higher pressures the oil slug moves more quickly, so more water is forced between the oil and the clay surface.

2.4.14 Velocity of the oil slug for large $\epsilon_2^{-3/2} P^*$

In Figure 2.17 we plot the velocity of the oil slug against the salinity for $-6 < \tau < 0$, comparing the solutions in which $P^* = 10^{-2}, 10^{-1.5}, 10^{-1}$. For all of the applied pressures, P^*, the speed increases as the salinity decreases. This is consistent with the MIE proposal, and suggests that MIE mechanism contributes to the low salinity effect. We observe that, as P^* increases, the percentage increase in the velocity also increases. The percentages are 130%, 330%, and 390%, for $P^* = 10^{-2}, 10^{-1.5}, 10^{-1}$, respectively.

2.5 Conclusions

In this chapter, we have presented a model for the steady motion of an oil slug through a clay pore throat, assuming that multicomponent ionic exchange (MIE) reactions involving monovalent Na^+ ions and divalent Ca^{2+} ions occur on the surfaces of the oil and the pore throat. We assumed that the pore throat could be represented by a tube with small aspect ratio, for which lubrication theory is applicable. We treated the oil and clay surfaces as charged surfaces, separated by a thin layer of salt water, and we assumed that the rates at which the ions in the water react with the surfaces are fast in comparison to the typical relaxation time of the surfaces in the viscous fluid.

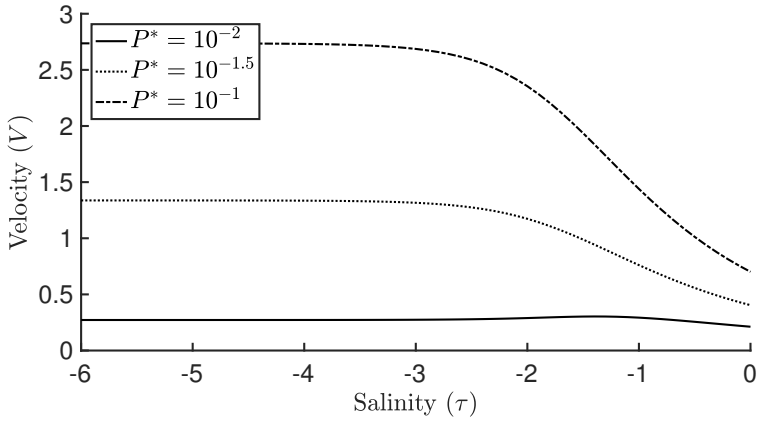


Figure 2.17: Velocity of the oil slug, V, as a function of the salinity, for $P^* = 10^{-2}, 10^{-1.5}, 10^{-1}$.

We derived expressions (2.107) for the surface charge densities on the oil-water and clay-water interface resulting from the MIE reactions. These were determined as functions of the salinity of the surrounding fluid. As the salinity of the brine decreases, the surfaces become more negatively charged. This is consistent with theoretical and experimental studies of the MIE mechanism.

We derived an equation (2.129) describing the shape of the water film separating the oil and the clay surfaces which depends on the surface charges, and therefore the salinity of the surrounding fluid. This equation is solved numerically using a shooting method, since the constant film thickness below the oil slug is unknown *a priori*. We find that the profile of the front of the oil slug is always monotonic, whereas the rear profile permits sinusoidal solutions. This is consistent with the Bretherton model [15], which studies the motion of a bubble through a capillary in the absence of electrostatic forces.

We determined the thickness of the water film below the oil slug, h^*, by solving (2.129). We find that, as the salinity of the surrounding fluid decreases, h^* increases, which is consistent with theoretical and experimental studies of the MIE mechanism [60, 62].

We solved the macroscopic flow model to obtain an expression for the velocity of the oil slug, (2.157). We found that, on this scale, the thin water film acts as a slip layer, with the slip length proportional to the film thickness: which, in turn, depends on the salinity. As the salinity of the water reduces, the slip length increases, so the speed of the oil slug increases. We found that the menisci at the front and rear of the oil slug were roughly the same, with the corrections affecting the pressure drop felt by the oil, and also the speed at which it moves.

For $P^* \gg \epsilon_2$, we found that the velocity of the oil slug is given by Poiseuille flow at leading order in ϵ_2, with first-order corrections resulting from the difference between the front and rear menisci radii, $V_1^{(1)}$, and the slip due to the thin water film, $V_1^{(2)}$. For $P^* \ll \epsilon_2$, the velocity is determined by balancing the change in velocity due to the difference between the front and rear menisci with the the increase in the velocity due to slip, that is, by balancing $V_1^{(1)}$ with $V_0 + V_1^{(2)}$. Hence, the velocity of the oil slug is an order magnitude less than might be expected, since at slow speeds the free interfaces at either end of the oil slug act to resist the flow. We derived analytical expressions for the film thickness and macroscopic velocity in the limit $P^* \ll \epsilon_2^{3/2}$. The asymptotic solution agrees with the numerical solution in the limit $\epsilon_2^{-3/2} P^* \to 0$.

In summary, we have shown that decreasing the salinity increases the thickness of the thin film of water residing between an oil slug and a pore throat, which results in an increase in the velocity at which the oil slug can move, given an applied pressure. In Chapter 3, we investigate one of the key results from this chapter that the salinity affects the slip length, by studying slip flow through an irregular channel. We develop this further in Chapter 4 by studying slip flow through a porous structure consisting of a network of throats. In Chapter 5, we will return to the two-phase oil slug model presented in this chapter in order to develop a network model for low salinity waterflooding, by assuming that the two-phase flow through the network can be represented by the locally homogenised motion of multiple oil slugs.

Chapter 3

Slip flow through a channel with varying elliptical cross section

3.1 Introduction

In Chapter 2, we studied the motion of an oil slug through a water-filled pore throat. We found that the thin film of water separating the oil slug from the throat wall acts as a slip layer, with the magnitude of the slip determined by the thickness of the water layer, which, in turn, depends on the salinity of the water. For simplicity, we assumed that the pore throat could be modelled by a straight-walled capillary. However, since the throats in an oil reservoir are irregularly shaped, it is important to understand the effect of the throat geometry on the model. We investigate this issue by studying oil flow through an irregular channel in the presence of a thin water layer which manifests itself as an effective slip condition between the oil and the pore walls, By computing the flux through the throat as a function of the slip length (i.e. the salinity) for an arbitrary shape, we can apply the results of the previous chapter to a general throat. This will enable us to apply the slip model to real rock geometries extracted from a sample of porous rock, and consequently compute the responsiveness of the sample to variations in the salinity. We choose to restrict our attention to single-phase oil flow since we are primarily interested in the effect of the geometry on the motion of oil, and this simplifies the model considerably.

Due to the complexity of the problem, the only way to accurately compute the low Reynolds number flow through an irregular channel is to numerically solve the Stokes equations inside the channel, typically using a finite element or lattice Boltzmann method. This can be time consuming and computationally expensive, particularly if we wish to model the flow through numerous throats as part of a network model of a porous rock.

A common approach used to estimate the flow, without having to resort to expensive computations, is to suppose that there is an equivalent circularly cylindrical channel, with a radius to be determined, such that the flux through the cylindrical channel behaves similarly to the flux through the irregular channel. However, estimates for the effective radius are typically quite crude, such as taking the radius of the largest sphere which passes through the channel [104], or choosing the radius to be such that the volume of the cylindrical channel is the same as the volume of the irregular channel [4]. Crude methods such as these are prone to systematic errors. For example, taking the effective radius to be given by the radius of the largest sphere which passes through the channel will consistently underestimate the flux. For large systems of channels, as might be used to model a porous medium, this leads to significant errors in estimating the permeability.

A more sophisticated approach is to estimate the flow by considering a channel with varying circular cross section, with the radius at each point along the length of the channel given by the largest inscribed sphere at that point along the length [33]. Since the radius at each point needs to be calculated anyway in order to find the radius at the most constricted point, this method requires negligible extra computational effort to extract the relevant data. However, more work is required to determine the flux through a channel with varying circular cross section than a channel with uniform cross section.

One disadvantage of assuming that the irregular geometry can be approximated by a channel with varying circular cross section is that, at each point along the length of the channel, there is only a single degree of freedom, the radius of the circle. Therefore the circumference and area of the cross section cannot be varied independently. This makes estimating the flux particularly difficult for problems involving slip along the fluid-solid interface, since the flux depends primarily on the cross-sectional area whereas the effect of slip is intimately related to the circumference of the cross section of the channel.

In this chapter, we study the problem of slip flow through a channel of varying elliptic cross section. For simplicity, we assume that the channel has a straight central axis. By considering an elliptical cross section, as opposed to a circular cross section, we introduce two degrees of freedom and are therefore able to vary the area and circumference of the channel independently. Our aim is to determine the flux through the channel as a function of the slip length, assuming that the slip length is small in comparison to the dimensions of the channel. Furthermore, we assume that the

channel is slender, and that the cross section varies slowly by comparison to its diameter.

In §3.2, we present a model for the velocity of the fluid in the channel. We assume that the velocity on the surface of the channel is proportional to the shear stress, with the constant of proportionality given by the slip length. In §3.3.1 we determine the flux through the channel to first order in the slip length. In §3.3.2 we determine the flux in the limit in which the eccentricity of the elliptic cross section is small. In §3.3.3 we compute the flux through three example channels and compare the equations for the flux given in §3.3.1 and 3.3.2 with the finite element solution. We compare the results with the estimations given by the minimum radius and volume matching methods. In §3.4 we discuss popular methods for estimating the flux through irregular channels. We compare these methods with the elliptic approximation approach by computing the flux through a pore throat extracted from a sample of Berea sandstone using X-ray microtomography. Finally, in §3.5 we discuss our findings.

3.1.1 Previous work

Similar problems have been considered in the literature. Bahrami *et al.* [8] study slip flow through channels with uniform circular, rectangular, trapezoidal, and double-trapezoidal cross sections. They consider an averaged slip boundary condition, so that the velocity of the fluid at the boundary is proportional to the average of the shear stress over the perimeter of the channel. The difference between the bulk velocity and the boundary velocity satisfies Stokes' equations with homogeneous boundary conditions. They express the average channel velocity in terms of the Fanning friction coefficient (the ratio between the shear stress and the kinetic energy density), and they determine a relationship between the coefficient in the slip regime and the no-slip regime. By numerically computing the Fanning friction coefficient in the no-slip regime for a particular geometry, they are able to determine an approximation for the flux with slip included. Ghosal [33] studies flow through channels with slowly varying cross section, including slip due to electro-osmotic effects, assuming that the slip length is small in comparison to the dimensions of the channel. He solves the problem for an arbitrary cross section in terms of the Green's function, and finds expressions for the particular cases of slowly varying circular cross section and slowly varying rectangular cross section. He assumes that the slip length is proportional to the electric field, and is independent of the shear stress at the boundary. Duan & Muzychka [27] study slip flow through an elliptical pipe with uniform cross section. They assume that the slip length is $O(1)$, and they use a binomial series expansion to

approximate the metric (assuming that the eccentricity is small) in order to evaluate the flux. Since we assume that the slip length is small in our model, we use this as our small parameter, and make no such assumption about the eccentricity of the channel. Sisavath *et al.* [95] study flow through a circular pipe with slowly-varying radius. They perform an expansion in terms of a small parameter characterizing the slowly varying nature of the pipe, and they determine the leading-order and first-order velocity and pressure profiles. By including the first-order term, they observe an improvement in the accuracy of their solution in comparison to the leading-order integrated Hagen-Poiseuille equation. They find that their model is able to predict effects such as flow reversal, which the parabolic Hagen-Poiseuille equation cannot reproduce. For simplicity, we will only consider the leading-order terms (with respect to the aspect ratio of the pipe) in our solution, since our primary focus is on the effect of slip.

3.2 Model formulation

We consider flow through a channel of varying elliptic cross section with a straight central axis, denoting the interior domain of the channel by Ω, and the boundary by $\partial\Omega$. We suppose that the channel has length L, and that R is the largest value of the major radius. The fluid is subject to a pressure difference, P, along the channel, and the surface allows slip, with slip length λ_s, such that $\lambda_s \ll R \ll L$.

We suppose that the origin of our coordinate system is at the mid point of one end of the channel, with the central axis of the channel lying along the z axis, and we further suppose that the semi-major axis of the elliptic cross section in the (x, y) plane for a given z is at an angle $\phi(z)$ to the x axis, as shown in Figure 3.1. We suppose that ϕ varies slowly along the length of the channel, that is, $\phi_z = O(1/L)$. For rapidly varying ϕ, the torsion of the channel needs to be considered, however this is beyond the scope of this thesis.

3.2.1 Governing equations

We model the flow in the channel using the incompressible Stokes equations,

$$\mu\nabla^2\mathbf{u} = \nabla p, \qquad \nabla\cdot\mathbf{u} = 0, \tag{3.1}$$

where $\mathbf{u}$ is the velocity of the fluid, p is the pressure, and μ is the viscosity of the fluid.

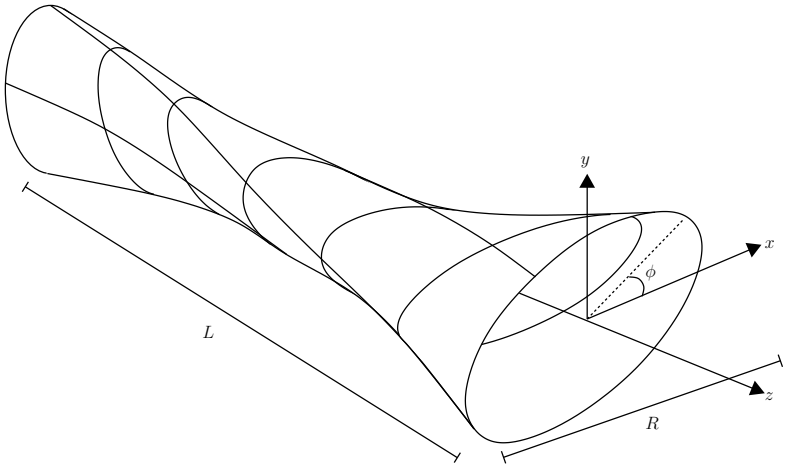


Figure 3.1: Schematic diagram of the channel with varying elliptic cross section.

We prescribe a pressure difference, P, across the ends of the channel, and we suppose that the fluid satisfies a slip boundary condition on the fluid-solid interface, so that the tangential velocity of the fluid on the surface is proportional to the shear stress. Thus, $\mathbf{u}$ and p satisfy the boundary conditions

$$p = P, \qquad \text{at } z = 0, \tag{3.2}$$

$$p = 0, \qquad \text{at } z = L, \tag{3.3}$$

$$\mathbf{u} \cdot \mathbf{t}_{1,2} = \lambda_s \mathbf{n} \cdot \left(\nabla \mathbf{u} + (\nabla \mathbf{u})^T \right) \cdot \mathbf{t}_{1,2}, \qquad \mathbf{u} \cdot \mathbf{n} = 0, \qquad \text{on } \partial\Omega, \tag{3.4}$$

where $\mathbf{t}_1$, $\mathbf{t}_2$ and $\mathbf{n}$ are two tangential vectors and the normal vector, respectively, on the surface of the tube, $\partial\Omega$, and λ_s is the slip length. In general, the slip length varies with the salinity according to (2.162), which, in dimensional form, reads

$$\lambda_s = \left(\frac{\varepsilon_w k_B T}{2(c_\infty^1 + 4c_\infty^2)q^2} \right)^{1/2} (\mu^* - 1) \cosh^{-1} \left(\frac{s^* \sigma_{c0} \sigma_{o0} + \sqrt{(\sigma_{c0}^2 + \Gamma)\left(s^{*2}\sigma_{o0}^2 + \Gamma\right)}}{\Gamma} \right), \tag{3.5}$$

where c_∞^1 and c_∞^2 are the concentrations of the monovalent and divalent ions, respectively, σ_{c0} and σ_{o0} are the surface charge densities on the clay and oil surfaces, respectively, which depend on c_∞^1 and c_∞^2 according to (2.107), and the parameters ε_w, k_B, T, q, μ^*, s^*, and Γ are defined in Chapter 2. However, in this chapter, we treat λ_s as an independent parameter for simplicity.

We define the surface of the channel by $f(x, y, z) = 0$, so that the tangential and

normal vectors on the surface are given by

$$\mathbf{t}_1 = \frac{1}{\sqrt{\left(f_x^2+f_y^2\right)\left(f_x^2+f_y^2+f_z^2\right)}}\left[-f_x f_z\mathbf{i} - f_y f_z\mathbf{j} + \mathbf{k}\left(f_x^2+f_y^2\right)\right], \tag{3.6}$$

$$\mathbf{t}_2 = \frac{1}{\sqrt{f_x^2+f_y^2}}\left[f_y\mathbf{i} - f_x\mathbf{j}\right], \tag{3.7}$$

$$\mathbf{n} = \frac{1}{\sqrt{f_x^2+f_y^2+f_z^2}}\left[f_x\mathbf{i} + f_y\mathbf{j} + f_z\mathbf{k}\right], \tag{3.8}$$

where $\mathbf{i}$, $\mathbf{j}$, $\mathbf{k}$ are the basis vectors of the cartesian coordinate system.

3.2.2 Nondimensionalisation

We nondimensionalise our model with the following scalings,

$$x = R\hat{x}, \qquad y = R\hat{y}, \qquad z = L\hat{z}, \tag{3.9}$$

$$p = P\hat{p}, \qquad u^* = \epsilon_1 U\hat{u}^*, \qquad v^* = \epsilon_1 U\hat{v}^*, \qquad w^* = U\hat{w}^*, \tag{3.10}$$

where we pick $U = PR^2/\mu L$ to balance the terms in (3.1), we define $\epsilon_1 = R/L$ to be the aspect ratio of the channel, $\mathbf{u} = u^*\mathbf{i} + v^*\mathbf{j} + w^*\mathbf{k}$ (the star superscript denotes cartesian coordinates), and the hat denotes the dimensionless variable.

We define the dimensionless slip length to be $\epsilon_2 = \lambda_s/R \ll 1$. For a typical pore throat, $L \sim 10^{-5}$ m, $R \sim 10^{-6}$ m, and $\lambda_s \sim 10^{-8}$ m, and thus $\epsilon_1 = 10^{-1}$ and $\epsilon_2 = 10^{-2}$. We find that, neglecting quadratic terms in ϵ_1 and ϵ_2, equations (3.1) - (3.4) read

$$w^*_{xx} + w^*_{yy} = p_z, \qquad p_x = 0, \qquad p_y = 0, \tag{3.11}$$

$$u^*_x + v^*_y + w^*_z = 0, \tag{3.12}$$

subject to

$$p = 1, \qquad \text{at } z = 0, \tag{3.13}$$

$$p = 0, \qquad \text{at } z = 1, \tag{3.14}$$

$$w^* = \frac{\epsilon_2}{\sqrt{f_x^2+f_y^2}}\left(w^*_x f_x + w^*_y f_y\right), \qquad \text{at } f = 0, \tag{3.15}$$

$$\begin{aligned} u^* f_y - v^* f_x = \frac{\epsilon_2}{\sqrt{f_x^2+f_y^2}}\big[&\left(f_y^2 - f_x^2\right)\left(u^*_y + v^*_x\right) \\ &+2f_x f_y\left(u^*_x - v^*_y\right) + f_z\left(w^*_x f_y - w^*_y f_x\right)\big], \end{aligned} \qquad \text{at } f = 0, \tag{3.16}$$

$$f_x u^* + f_y v^* + f_z w^* = 0, \qquad \text{at } f = 0, \tag{3.17}$$

where we have dropped the hat notation for convenience.

3.2.3 Elliptic coordinates

We assume that, for each value of z, the cross section of the channel in the (x, y) plane is an ellipse, with semi-major and semi-minor radii given by $r_a(z)$ and $r_b(z)$ respectively. Hence, the surface of the channel is given by

$$f(x, y, z) = 1 - \left(\frac{x\cos\phi + y\sin\phi}{r_a}\right)^2 - \left(\frac{y\cos\phi - x\sin\phi}{r_b}\right)^2 = 0. \tag{3.18}$$

In order to simplify the boundary conditions (3.15) – (3.17), we formulate the problem in terms of elliptic coordinates (η, ξ, z) using the change of variables

$$x = a(z)\cosh\eta\cos\xi\cos\phi - a(z)\sinh\eta\sin\xi\sin\phi, \tag{3.19}$$

$$y = a(z)\cosh\eta\cos\xi\sin\phi + a(z)\sinh\eta\sin\xi\cos\phi, \tag{3.20}$$

where $\eta \in [0, \infty)$, $\xi \in [0, 2\pi)$, and $a = \sqrt{r_a^2 - r_b^2}$. The foci of the ellipse in the (x, y) plane passing through z are given by $x = \pm a(z)\cos\phi(z)$, $y = \pm a(z)\sin\phi(z)$. In the (η, ξ, z) coordinate system, the boundary of the tube is given by $\eta = N(z)$, where $N = \tanh^{-1}(r_b/r_a)$.

We define $\mathbf{u} = u^*\mathbf{i} + v^*\mathbf{j} + w^*\mathbf{k} = u\mathbf{e}_\eta + v\mathbf{e}_\xi + w\mathbf{e}_z$, where $(\mathbf{e}_\eta, \mathbf{e}_\xi, \mathbf{e}_z)$ are the basis vectors in the elliptic coordinate system. In the (η, ξ, z) coordinate system, equations (3.11) – (3.17), read

$$\frac{\partial^2 w}{\partial\eta^2} + \frac{\partial^2 w}{\partial\xi^2} = a^2h^2\frac{\partial p}{\partial z}, \qquad \frac{\partial p}{\partial\eta} = 0, \qquad \frac{\partial p}{\partial\xi} = 0, \tag{3.21}$$

$$\frac{1}{a^2h^2}\left[\frac{\partial}{\partial\eta}(ahu) + \frac{\partial}{\partial\xi}(ahv)\right] + \frac{1}{a^2}\frac{\partial}{\partial z}\left(a^2w\right) = 0, \tag{3.22}$$

subject to

$$p = 1, \qquad \text{at } z = 0, \tag{3.23}$$

$$p = 0, \qquad \text{at } z = 1, \tag{3.24}$$

$$w = \frac{-\epsilon_2}{ah}\frac{\partial w}{\partial\eta}, \qquad \text{at } \eta = N, \tag{3.25}$$

$$ah\frac{\mathrm{d}N}{\mathrm{d}z}w - u = 0, \qquad \text{at } \eta = N, \tag{3.26}$$

where

$$h = \sqrt{\frac{1}{2}(\cosh 2\eta - \cos 2\xi)}. \tag{3.27}$$

We have omitted the elliptic form of (3.16) since we only need to determine w in order to compute the flux through the channel, and this boundary condition is only required to determine u and v.

Since $\eta = 0$ corresponds the the central axis of the channel, and the problem is symmetric under a rotation of π, we require that the solution satisfies

$$\frac{\partial w}{\partial \eta} = 0, \qquad \text{at } \eta = 0. \tag{3.28}$$

3.3 Solution

3.3.1 Flux through the channel

Integrating (3.22) over the cross section of the channel yields

$$\int_0^{2\pi}\int_0^{N(z)} \left[\frac{\partial}{\partial \eta}\left(ahu\right) + \frac{\partial}{\partial \xi}\left(ahv\right) + \frac{\partial}{\partial z}\left(a^2h^2w\right)\right] \mathrm{d}\eta\mathrm{d}\xi = 0. \tag{3.29}$$

By Leibniz's integral rule,

$$\int_0^{2\pi}\int_0^{N(z)} \frac{\partial}{\partial z}\left(a^2h^2w\right)\mathrm{d}\eta\mathrm{d}\xi = \frac{\mathrm{d}}{\mathrm{d}z}\int_0^{2\pi}\int_0^{N(z)} a^2h^2w\,\mathrm{d}\eta\mathrm{d}\xi - \int_0^{2\pi}\frac{\mathrm{d}N}{\mathrm{d}z}\left[a^2h^2w\right]_{\eta=N}\mathrm{d}\xi, \tag{3.30}$$

$$= \frac{\mathrm{d}}{\mathrm{d}z}\iint_A w\,\mathrm{d}A - \int_0^{2\pi}\frac{\mathrm{d}N}{\mathrm{d}z}\left[a^2h^2w\right]_{\eta=N}\mathrm{d}\xi, \tag{3.31}$$

where we have used that $\mathrm{d}A := \mathrm{d}x\mathrm{d}y = a^2h^2\mathrm{d}\eta\mathrm{d}\xi$.

Substituting (3.31) into (3.29) and applying Green's Theorem yields

$$\frac{\mathrm{d}}{\mathrm{d}z}\iint_A w\,\mathrm{d}A - \int_0^{2\pi}\frac{\mathrm{d}N}{\mathrm{d}z}\left[a^2h^2w\right]_{\eta=N}\mathrm{d}\xi + \int_{\partial A} ah\left[u\frac{\mathrm{d}\xi}{\mathrm{d}s} - v\frac{\mathrm{d}\eta}{\mathrm{d}s}\right]\mathrm{d}s = 0, \tag{3.32}$$

where s is arc length along the circumference of the ellipse, and therefore we define $\mathrm{d}s := \sqrt{\mathrm{d}x^2 + \mathrm{d}y^2}$. Since $\eta = N$ corresponds to the boundary of the ellipse, we find that $\mathrm{d}\eta/\mathrm{d}s = 0$, and thus (3.32) reads

$$\frac{\mathrm{d}}{\mathrm{d}z}\iint_A w\,\mathrm{d}A + \int_0^{2\pi}\left[ahu - a^2h^2w\frac{\mathrm{d}N}{\mathrm{d}z}\right]_{\eta=N}\mathrm{d}\xi = 0. \tag{3.33}$$

By substituting (3.26) into (3.33), we obtain the conservation of flux equation

$$\frac{\mathrm{d}Q}{\mathrm{d}z} = 0, \qquad \text{where} \qquad Q = \iint_A w\,\mathrm{d}A. \tag{3.34}$$

To compute the flux, we must find w by solving (3.21) and (3.22) subject to (3.25) – (3.28). From (3.21) we see that $p = p(z)$. We expand w and p in powers of ϵ_2, to find that, at leading order, equations (3.21) and (3.25) read

$$\frac{\partial^2 w^{(0)}}{\partial \eta^2} + \frac{\partial^2 w^{(0)}}{\partial \xi^2} = \frac{a^2}{2}\frac{\mathrm{d}p^{(0)}}{\mathrm{d}z}\left(\cosh 2\eta - \cos 2\xi\right), \tag{3.35}$$

subject to $w^{(0)} = 0$ on $\eta = N$. A particular solution to the inhomogeneous equation (3.35) is

$$w_P^{(0)} = \frac{a^2}{8}\frac{\mathrm{d}p^{(0)}}{\mathrm{d}z}\left(\cosh 2\eta + \cos 2\xi\right). \tag{3.36}$$

However, this does not satisfy the boundary condition $w^{(0)} = 0$ on $\eta = N$. In order to rectify this issue, we use separation of variables to solve the complimentary homogeneous equation

$$\frac{\partial^2 w_H^{(0)}}{\partial \eta^2} + \frac{\partial^2 w_H^{(0)}}{\partial \xi^2} = 0, \tag{3.37}$$

observing that, by linearity, $w^{(0)} = w_P^{(0)} + w_H^{(0)}$ satisfies (3.35). By imposing (3.28), we find that $w_H^{(0)}$ is of the form

$$w_H^{(0)} = \frac{1}{2}\alpha_0^{(0)} + \sum_{k=1}^{\infty}\left(\alpha_k^{(0)}\cos k\xi + \beta_k^{(0)}\sin k\xi\right)\cosh k\eta. \tag{3.38}$$

By evaluating $w^{(0)} = w_P^{(0)} + w_H^{(0)} = 0$ on $\eta = N$ using the expressions for $w_P^{(0)}$ and $w_H^{(0)}$ given by (3.36) and (3.38), respectively, and computing the coefficients $\alpha_k^{(0)}$ and $\beta_k^{(0)}$, we find that

$$w^{(0)} = \frac{a^2}{8}\frac{\mathrm{d}p^{(0)}}{\mathrm{d}z}\left[\cosh 2\eta - \cosh 2N + \cos 2\xi - \frac{\cos 2\xi \cosh 2\eta}{\cosh 2N}\right]. \tag{3.39}$$

By writing this expression in cartesian coordinates, we find that

$$w^{(0)} = -\frac{r_a^2 r_b^2}{2(r_a^2 + r_b^2)}\frac{\mathrm{d}p^{(0)}}{\mathrm{d}z}\left[1 - \frac{\left(x\cos\phi + y\sin\phi\right)^2}{r_a^2} - \frac{\left(y\cos\phi - x\sin\phi\right)^2}{r_b^2}\right], \tag{3.40}$$

which is the expression for quasi-Poiseuille flow through a channel with elliptic cross section [74]. The leading-order flux is given by

$$Q^{(0)} = -\frac{r_a^2 r_b^2}{2(r_a^2 + r_b^2)}\frac{\mathrm{d}p^{(0)}}{\mathrm{d}z}\iint_A\left(1 - \frac{\left(x\cos\phi + y\sin\phi\right)^2}{r_a^2} - \frac{\left(y\cos\phi - x\sin\phi\right)^2}{r_b^2}\right)\mathrm{d}x\mathrm{d}y. \tag{3.41}$$

To evaluate this integral, we make the change of variables $x\cos\phi + y\sin\phi = r_a r\cos\theta$, $y\cos\phi - x\sin\phi = r_b r\sin\theta$, which yields

$$Q^{(0)} = -\frac{r_a^3 r_b^3}{2(r_a^2 + r_b^2)}\frac{\mathrm{d}p^{(0)}}{\mathrm{d}z}\int_0^{2\pi}\int_0^1 (1 - r^2) r\mathrm{d}r\mathrm{d}\theta = -\frac{\pi r_a^3 r_b^3}{4(r_a^2 + r_b^2)}\frac{\mathrm{d}p}{\mathrm{d}z}. \tag{3.42}$$

Substituting (3.42) into (3.34), and applying (3.23) and (3.24), yields

$$\frac{\mathrm{d}p^{(0)}}{\mathrm{d}z} = -\frac{r_a^2 + r_b^2}{r_a^3 r_b^3}\left[\int_0^1 \frac{r_a^2 + r_b^2}{r_a^3 r_b^3}\mathrm{d}z\right]^{-1}, \tag{3.43}$$

and thus

$$Q^{(0)} = \left\{ \int_0^1 \left[\frac{\pi r_a^3 r_b^3}{4\left(r_a^2 + r_b^2\right)} \right]^{-1} \mathrm{d}z \right\}^{-1}. \tag{3.44}$$

The term inside the square brackets is the expression for the flux through a pipe with uniform elliptic cross section. Hence, the conductivity of the pipe with varying elliptic cross section is given by the harmonic mean of the conductivites of each cross section along the length of the pipe.

To find the contribution to the flux resulting from the slip along the surface, $Q^{(1)}$, we require the solution for the fluid velocity at the next order, $w^{(1)}$. From (3.21), we obtain the governing equation for $w^{(1)}$, which reads

$$\frac{\partial^2 w^{(1)}}{\partial \eta^2} + \frac{\partial^2 w^{(1)}}{\partial \xi^2} = \frac{a^2}{2} \frac{\mathrm{d}p^{(1)}}{\mathrm{d}z} \left(\cosh 2\eta - \cos 2\xi\right). \tag{3.45}$$

We separate the fluid velocity into a particular solution and a solution to the homogeneous problem, given by

$$w_P^{(1)} = \frac{a^2}{8} \frac{\mathrm{d}p^{(1)}}{\mathrm{d}z} \left(\cosh 2\eta + \cos 2\xi\right), \tag{3.46}$$

$$w_H^{(1)} = \frac{1}{2}\alpha_0^{(1)} + \sum_{k=1}^{\infty} \left(\alpha_k^{(1)} \cos k\xi + \beta_k^{(1)} \sin k\xi \right) \cosh k\eta. \tag{3.47}$$

Substituting $w^{(1)} = w_P^{(1)} + w_H^{(1)}$ into (3.25) and gathering the first-order terms yields

$$\begin{aligned} \frac{a^2}{8} \frac{\mathrm{d}p^{(1)}}{\mathrm{d}z} \left(\cosh 2N + \cos 2\xi\right) + \frac{1}{2}\alpha_0^{(1)} + \sum_{k=1}^{\infty} \left(\alpha_k^{(1)} \cos k\xi + \beta_k^{(1)} \sin k\xi \right) \cosh kN \\ = -\frac{a \sinh 2N}{2\sqrt{2} \cosh 2N} \frac{\mathrm{d}p^{(0)}}{\mathrm{d}z} \sqrt{\cosh 2N - \cos 2\xi}. \end{aligned} \tag{3.48}$$

From (3.48), we compute the Fourier coefficients to be $\beta_k^{(1)} = 0$, and

$$\alpha_0^{(1)} = -\frac{a^2}{4} \cosh 2N \frac{\mathrm{d}p^{(1)}}{\mathrm{d}z} - \frac{a \sinh 2N}{2\sqrt{2}\pi \cosh 2N} \frac{\mathrm{d}p^{(0)}}{\mathrm{d}z} \int_0^{2\pi} \sqrt{\cosh 2N - \cos 2\xi} \mathrm{d}\xi, \tag{3.49}$$

$$\alpha_2^{(1)} = -\frac{a^2}{8 \cosh 2N} \frac{\mathrm{d}p^{(1)}}{\mathrm{d}z} - \frac{a \sinh 2N}{2\sqrt{2}\pi \cosh^2 2N} \frac{\mathrm{d}p^{(0)}}{\mathrm{d}z} \int_0^{2\pi} \cos 2\xi \sqrt{\cosh 2N - \cos 2\xi} \mathrm{d}\xi, \tag{3.50}$$

$$\alpha_k^{(1)} = -\frac{a \sinh 2N}{2\sqrt{2}\pi \cosh 2N \cosh kN} \frac{\mathrm{d}p^{(0)}}{\mathrm{d}z} \int_0^{2\pi} \cos k\xi \sqrt{\cosh 2N - \cos 2\xi} \mathrm{d}\xi, \tag{3.51}$$

for $k \neq 0, 2$. By substituting (3.49) – (3.51) into (3.47), and summing (3.46) and (3.47), we are able to write $w^{(1)} = w_P^{(1)} + w_H^{(1)}$ in terms of an infinite series of integrals.

However, we can make further analytical progress with the first-order flux, and we find that

$$Q^{(1)} = \frac{a^2}{2}\int_0^N \int_0^{2\pi} \left(w_P^{(1)} + w_H^{(1)}\right)(\cosh 2\eta - \cos 2\xi)\,\mathrm{d}\xi\mathrm{d}\eta \tag{3.52}$$

$$= \frac{a^4\pi}{32}\sinh 2N \cosh 2N \frac{\mathrm{d}p^{(1)}}{\mathrm{d}z} + \frac{a^2\pi}{4}\sinh 2N\left(\alpha_0^{(1)} - \alpha_2^{(1)}\right). \tag{3.53}$$

Substituting (3.49) and (3.50) into (3.53) yields

$$Q^{(1)} = -\frac{a^4\pi}{32}\tanh 2N \sinh^2 2N \frac{\mathrm{d}p^{(1)}}{\mathrm{d}z} - \frac{a^3}{8\sqrt{2}}\tanh^2 2N \frac{\mathrm{d}p^{(0)}}{\mathrm{d}z}\int_0^{2\pi}(\cosh 2N - \cos 2\xi)^{3/2}\,\mathrm{d}\xi. \tag{3.54}$$

We write (3.54) in terms of r_a and r_b, and substitute (3.43) to obtain

$$Q^{(1)} = -\frac{\pi r_a^3 r_b^3}{4\left(r_a^2 + r_b^2\right)}\frac{\mathrm{d}p^{(1)}}{\mathrm{d}z} + \frac{4\int_0^{2\pi}\left(r_a^2\sin^2\theta + r_b^2\cos^2\theta\right)^{3/2}\mathrm{d}\theta}{\pi r_a r_b\left(r_a^2 + r_b^2\right)}\left[\int_0^1\left(\frac{\pi r_a^3 r_b^3}{4\left(r_a^2+r_b^2\right)}\right)^{-1}\right]^{-1}. \tag{3.55}$$

From (3.34), we find that $Q^{(1)}$ is constant, so, by integrating (3.55) from $z = 0$ to $z = 1$ and imposing (3.23) and (3.24), we find that the first-order component of the flux is given by

$$Q^{(1)} = \frac{\int_0^1\left[\left(\frac{\pi^2}{16}r_a^4 r_b^4\right)^{-1}\int_0^{2\pi}\left(r_a^2\sin^2\theta + r_b^2\cos^2\theta\right)^{3/2}\mathrm{d}\theta\right]\mathrm{d}z}{\left(\int_0^1\left[\frac{\pi r_a^3 r_b^3}{4\left(r_a^2+r_b^2\right)}\right]^{-1}\mathrm{d}z\right)^2}. \tag{3.56}$$

Combining equations (3.44) and (3.56) yields the total flux to order ϵ_2, which reads

$$Q = \left\{\int_0^1\left[\frac{\pi r_a^3 r_b^3}{4\left(r_a^2+r_b^2\right)}\left(1 + \frac{4\epsilon_2}{\pi r_a r_b\left(r_a^2+r_b^2\right)}\int_0^{2\pi}\left(r_a^2\sin^2\theta + r_b^2\cos^2\theta\right)^{3/2}\mathrm{d}\theta\right)\right]^{-1}\mathrm{d}z\right\}^{-1}. \tag{3.57}$$

As for the leading-order flux, the total flux is the harmonic mean of the equivalent flux through each cross section of the channel. Note that, since we assumed that the rotation of the elliptical cross section varies slowly along the length of the channel, ϕ does not appear in (3.57). In Figure 3.2, we plot the the flux, Q, given by (3.57), through a uniform elliptical channel with cross-sectional area $\pi r_a r_b = 1$ against the eccentricity, $e = \sqrt{1 - r_b^2/r_a^2}$, where we have taken $\epsilon_2 = 0.1$. As the eccentricity increases, the total flux through the channel decreases due to stagnant flow near the outermost edges of the ellipse.

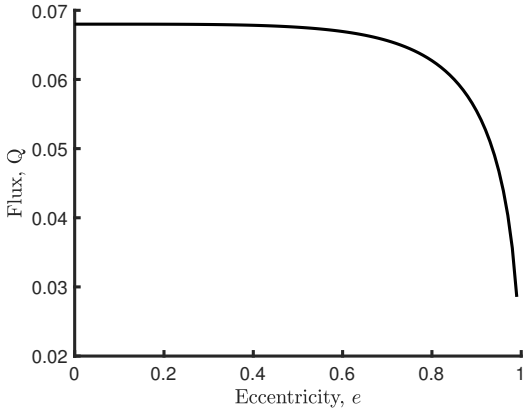


Figure 3.2: Plot of the flux, given by (3.57), through a uniform channel of elliptic cross section against the eccentricity.

3.3.2 Solution for small eccentricity

It is possible to write the integral in θ in (3.57) in terms of elliptic integrals of the first and second kind. However, for certain applications it may be impractical to compute these for each cross section. In the case where $\delta = \left(r_a^2 - r_b^2\right) / \left(r_a^2 + r_b^2\right) \ll 1$, which corresponds the eccentricity of the ellipse being small, we are able to simplify the integral. To exploit this small parameter, we make the change of variable

$$\cos^2\theta = \frac{1+\zeta}{2}, \qquad \sin^2\theta = \frac{1-\zeta}{2}, \tag{3.58}$$

so that the integral reads

$$\int_0^{2\pi} \left(r_a^2 \sin^2\theta + r_b^2 \cos^2\theta\right)^{3/2} \mathrm{d}\theta = \frac{\left(r_a^2 + r_b^2\right)^{3/2}}{\sqrt{2}} \int_{-1}^{1} \frac{(1-\delta\zeta)^{3/2}}{\sqrt{1-\zeta^2}} \mathrm{d}\zeta. \tag{3.59}$$

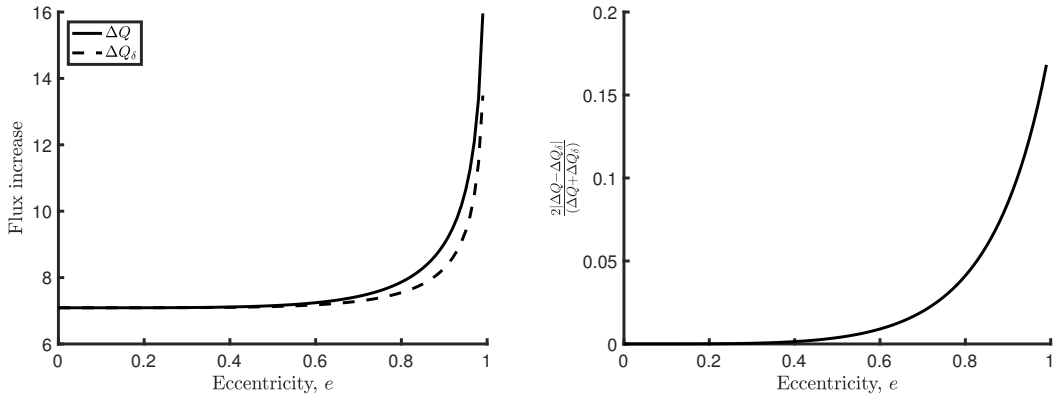
We expand the integrand in powers of δ and perform the integration to find that

$$\int_0^{2\pi} \left(r_a^2 \sin^2\theta + r_b^2 \cos^2\theta\right)^{3/2} \mathrm{d}\theta \sim \frac{\pi\left(r_a^2 + r_b^2\right)^{3/2}}{\sqrt{2}} + O\left(\delta^2\right). \tag{3.60}$$

By substituting (3.60) into (3.57), we find that the flux through the channel can be approximated by

$$Q_\delta \sim Q_\delta^{(0)} + \epsilon_2 Q_\delta^{(1)} \sim \left\{ \int_0^1 \left[\frac{\pi r_a^3 r_b^3}{4\left(r_a^2 + r_b^2\right)} \left(1 + \frac{2\sqrt{2}\epsilon_2 \sqrt{r_a^2 + r_b^2}}{r_a r_b}\right) \right]^{-1} \mathrm{d}z \right\}^{-1}. \tag{3.61}$$

In Figure 3.3a, we compare the relative flux increase due to slip given by the full expression, $\Delta Q := Q^{(1)}/Q^{(0)}$, and the approximation, $\Delta Q_\delta := {Q^{(1)}}_\delta / {Q^{(0)}}_\delta$, against



(a) Relative flux increase due to slip (b) Difference between ΔQ and ΔQ_δ

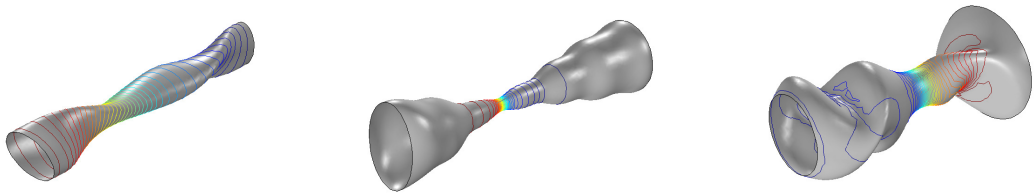
Figure 3.3: Comparison between the flux increase due to slip for Q, given by (3.57), and Q_δ, given by (3.61), showing a) the relative flux increase for the two solutions as a function of the eccentricity, and b) the difference in the relative flux increase between the two solutions as a function of the eccentricity, where $\Delta Q = Q_1/Q_0$, and $\Delta Q_\delta = Q_{1\delta}/Q_{0\delta}$.

the eccentricity, e. We plot the solution for a uniform elliptic channel with cross-sectional area given by $\pi r_a r_b = 1$. As the eccentricity increases, we see that the relative flux increase due to slip also increases. This is because the circumference to area ratio of the elliptic cross section increases, and channels with a greater surface area are more greatly affected by slip along the boundary.

In Figure 3.3b, we plot the difference between the relative flux increase given by the two expressions, ΔQ and ΔQ_δ, calculated using $2|\Delta Q - \Delta Q_\delta|/(\Delta Q + \Delta Q_\delta)$. We see that the difference is greatest (16.8%) for $e = 1$, and decreases to zero as $e \to 0$, with the error less than 1% for $e < 0.62$.

3.3.3 Comparison between flux estimation methods

A common method used to estimate the flux through a non-uniform channel is to assume that the channel can be approximated by a circular cylinder with some 'hydraulic radius'. Two popular estimates for the hydraulic radius are the radius of the inscribed circle at the most constricted point along the channel, which we will call the 'minimum radius' method, and the radius such that the volume of the cylinder is the same as the volume of the channel, which we will call the 'volume matching' method. We will compare the flux computed using these approximations with the fluxes given by (3.57) and (3.61) for three channels with varying elliptic cross section, shown in Figure 3.4. The geometries of the three channels are chosen to study how accurately



(a) Channel 1 (b) Channel 2 (c) Channel 3

Figure 3.4: Diagrams of the three channels used to compare the flux estimation methods.

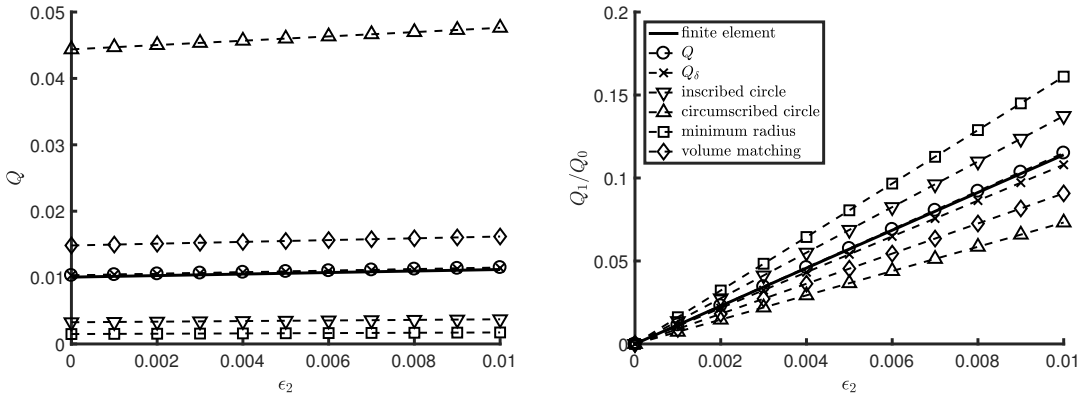
	ϵ_1	$e_{\min}$	$e_{\max}$	$\delta_{\min}$	$\delta_{\min}$
Channel 1	0.073	0.75	0.92	0.39	0.72
Channel 2	0.14	0	0.71	0	0.34
Channel 3	0.28	0	0.95	0	0.83

Table 3.1: Dimensionless parameter values for the three pore channels.

the different methods estimate the flux through a channel with i) high eccentricity, ii) a bottleneck region, and iii) high torsion. For each channel, the aspect ratio, ϵ_1, the minimum and maximum eccentricity along the length of the channel, $e_{\min}$ and $e_{\max}$, respectively, and the minimum and maximum value of $\delta = e^2/(2-e^2)$ along the length of the channel, $\delta_{\min}$ and $\delta_{\max}$, respectively, are given in Table 3.1.

We will also consider two 'intermediate' approaches in which the flux is estimated by approximating the geometry of the channel with a channel of varying *circular* cross section. The first involves computing the flux using (3.57), with $r_a = r_b = r$ being the radius of the maximum inscribed circle at each cross section, and the second involves computing the flux using (3.57), with $r_a = r_b = r$ being the radius of the minimum circumscribed circle at each cross section. We call these the 'inscribed circle' and 'circumscribed circle' methods, respectively. Both of these approximations improve on the minimum radius and volume matching methods because they take into consideration the variation of the channel cross section along its length, but they are easier to compute than the elliptic approximation because only one length needs to be found at each cross section.

We compare the flux calculated using the different methods with the numerical finite element solution to (3.1) – (3.4), which we take to be our 'reference' solution, for each of the three channel shapes. In Figure 3.5a, we plot the total flux through channel 1 against the slip length. The 'minimum radius', 'volume matching', 'inscribed circle', and 'circumscribed circle' methods are labelled accordingly, and we



(a) Total flux

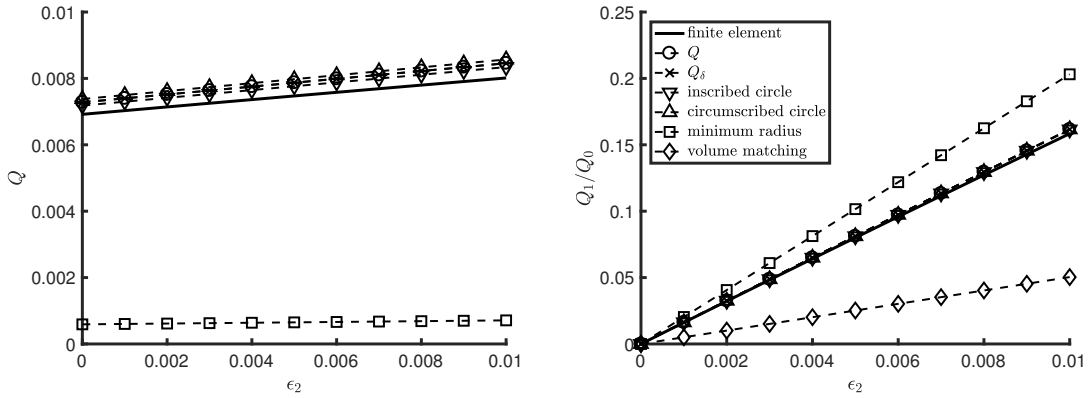
(b) Relative flux increase due to slip

Figure 3.5: Comparison between the different flux estimation methods for channel 1, showing a) the total flux through channel 1, and b) the relative flux increase in the presence of slip along the surface of the channel.

also plot Q and Q_δ, given by (3.57) and (3.61), respectively. Since the elliptical cross section is rotating slowly, the effects of torsion are minimal and thus we see that there is good agreement between Q and the finite element solution. The elliptical solution with small eccentricity, Q_δ is nearly indistinguishable from Q, despite the eccentricity of the channel being relatively high, since the error for this solution is $O(\epsilon_2\delta^2)$. The volume matching method is the next most accurate model, but overestimates the total flux. The circumscribed circle solution significantly overestimates the flux, and the inscribed circle and minimum radius method significantly underestimate the flux.

In Figure 3.5b, we plot the relative flux increase due to slip, Q_1/Q_0, against the slip length for channel 1. We observe that there is excellent agreement between Q and the finite element solution, with Q_δ being the next most accurate. The volume matching method and inscribed circle method slightly underestimate and overestimate, respectively, the flux increase. As for the total flux, the minimum radius and circumscribed circle methods are the least accurate.

In Figure 3.6a we plot the total flux through channel 2 against the slip length. The flux calculated by the volume matching method is 20 times larger than the finite element solution, and so is not shown on the plot. We see that Q, Q_δ, and the inscribed and circumscribed circle solutions provide excellent estimations for the flux. However, all of these methods slightly overestimate the flux due to the torsion of the channel reducing the flow rate in the finite element solution. The minimum radius significantly underestimates the flux. In Figure 3.6b we plot the relative flux increase due to slip against the slip length. Again, Q, Q_δ, and the inscribed and circumscribed circle



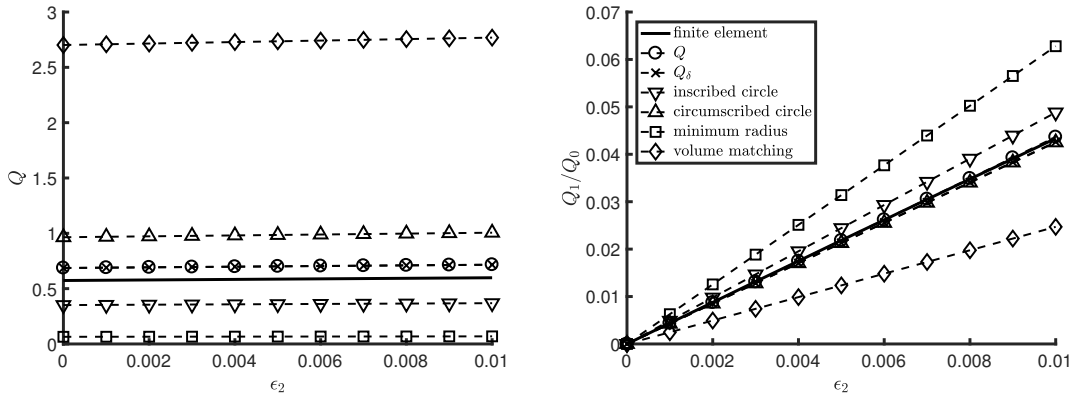
(a) Total flux (b) Relative flux increase due to slip

Figure 3.6: Comparison between the different flux estimation methods for channel 2, showing a) the total flux through channel 2 (the volume-matching method is not shown), and b) the relative flux increase in the presence of slip along the surface of the channel.

solutions are in excellent agreement with the finite element solution, and the minimum radius and volume matching methods significantly overestimate and underestimate, respectively, the flux increase.

In Figure 3.7a, we plot the total flux against the slip length for channel 3, and in Figure 3.7b we plot the relative increase in flux due to slip against the slip length. As for the other examples, the elliptic solutions, Q and Q_δ, provide the best estimate for the total flux, but overestimate the flux due to the torsion of the channel decreasing the flow rate. These methods also provide the best estimate for the flux increase. The two methods often used in practice, the volume matching and minimum radius method, significantly overestimate and underestimate the flux, respectively.

These examples demonstrate the care that needs to be taken when applying the minimum radius or volume matching methods. The minimum radius method appears to consistently underestimate the total flux and overestimate the relative flux increase as the slip increases, and the volume matching method appears to consistently overestimate the total flux and underestimate the relative flux increase. We see that, across the three channels, Q and Q_δ typically give the best fit to the finite element solution. This is to be expected, since the channels considered have an elliptic cross section. In §3.4, we compare the different methods on an irregular channel by computing the flow through a pore throat extracted from a rock sample using X-ray microtomography.



(a) Total flux (b) Relative flux increase due to slip

Figure 3.7: Comparison between the different flux estimation methods for channel 3, showing a) the total flux through channel 3, and b) the relative flux increase in the presence of slip along the surface of the channel.

3.4 Flow through irregularly-shaped channels

It is common practice for the flux through an irregularly shaped throat to be estimated by assuming that the throat can be represented by a circular cylindrical tube, with an effective radius determined by the complex geometry of the throat, and various methods can be used to estimate the effective radius of the cylinder [4, 11, 104]. Al-Kharusi & Blunt [4] define the radius using the volume matching method described in §3.3.3. Bentz & Martys [11] and Thovert *et al.* [104] define the radius to be given by the largest sphere which could pass through the throat, which is equivalent to the minimum radius method described in §3.3.3. Two alternative approaches are the Aissen approximation [2] and the hydraulic radius approximation [115] methods, which we will discuss further in §3.4.1 and §3.4.2, respectively.

As an alternative approach, Koplik *et al.* [54] approximate irregular throat shapes using uniform *elliptical* channels, with the area and the ratio of the maximum to minimum span matching that of the pore cross section. One of the benefits of studying slip flow through elliptical channels as opposed to circular channels is the ability to vary the circumference and the area of the channel independently. This is useful when trying to estimate the flux through an irregularly shaped channel, as it is important to be able to determine both the total flux through the channel and the relative increase in flux due to slip. By introducing two degrees of freedom, r_a and r_b (the semi-major and semi-minor axes of the ellipse, respectively), we are able to determine an elliptic cross section which agrees with both the leading-order and first-order flux through

the irregularly shaped channel.

In §3.4.1 and §3.4.2, we discuss how the results obtained in §3.3 can be used to extend current approximations of flow through irregular channels to include slip and varying cross section. We then compare the different approaches with the numerically computed solution for flow through an irregularly-shaped channel with varying cross section taken from a sample of porous rock.

3.4.1 Aissen approximation

The Aissen approximation [2] is a method used to estimate the flux through a uniform channel with non-circular cross section, assuming that there is no slip along the surface. If we define R_a and R_b to be the radii of the smallest circumscribed circle and largest inscribed circle, respectively, of the channel, and A to be the cross-sectional area, then the Aissen approximation for the flux is

$$Q_{Ai} = \frac{A^2}{4\pi} \frac{R_a R_b}{R_a^2 + R_b^2}. \tag{3.62}$$

We can extend the Aissen approximation, (3.62), to include the effect of slip on the surface of a non-uniform channel using our model for slip-flow through a channel with varying elliptical cross section, (3.61). By choosing the semi-major and semi-minor axes, r_a and r_b respectively, in our elliptical model, (3.61), to be equal to R_a and R_b, respectively, at each point along the length of the channel, and using the fact that the cross-sectional area is given by $A = \pi R_a R_b$ at each point along the length of channel, we find that (3.61) reads

$$Q_{Ai} = \left\{ \int_0^1 \left[\frac{A^2}{4\pi} \frac{R_a R_b}{(R_a^2 + R_b^2)} \left(1 + \frac{2\sqrt{2}\epsilon_2 \sqrt{R_a^2 + R_b^2}}{R_a R_b} \right) \right]^{-1} \mathrm{d}z \right\}^{-1}, \tag{3.63}$$

which we define to be our extension to the Aissen approximation for the flux. For a uniform channel (R_a and R_b independent of z) in the limit $\epsilon_2 \to 0$ (i.e. no slip), our model (3.63) reduces to the standard Aissen approximation (3.62).

The Aissen approximation has been shown to be exact for circular and elliptical channels, and accurate to within 10% for square, triangular, rectangular, and semi-circular channels [96]. However, a disadvantage of this method is that calculating R_a and R_b requires some computational effort for irregularly shaped channels.

3.4.2 Hydraulic radius approximation

Another method used to estimate the flux through an irregularly shaped channel in the absence of slip is the hydraulic radius approximation [115], in which the flux is assumed to satisfy

$$Q \approx \frac{1}{2} A R_H^2, \tag{3.64}$$

where A is the area of the cross section, and R_H is the hydraulic radius, defined to be $R_H := A/C$ where C is the circumference of the cross section.

We can extend the standard hydraulic radius approximation, (3.64), to include the effect of slip on the surface of a non-uniform channel using our model for slip-flow through a channel with varying elliptical cross section, (3.61), using a similar method to the one we used to extend the Aissen approximation in §3.4.1. Given an irregularly-shaped channel with spatially varying cross-sectional area and circumference, $A(z)$ and $C(z)$ respectively, we define the semi-major and semi-minor axes, r_a and r_b, of our elliptical approximation to the channel, (3.61), to be such that $\pi r_a r_b = A$ and $\pi\sqrt{2(r_a^2 + r_b^2} = C$ at each point along the length of the channel, i.e. we ensure that the area and circumference[1] of our elliptical model agree with the irregular channel. By writing (3.61) in terms of A and C, we define

$$Q_H = \left\{ \int_0^1 \left[\frac{A R_H^2}{2} \left(1 + \frac{2\epsilon_2}{R_H} \right) \right]^{-1} \mathrm{d}z \right\}^{-1}, \tag{3.65}$$

to be our extension to the hydraulic radius approximation for the flux. For a uniform channel in the limit $\epsilon_2 \to 0$ (i.e. no slip), (3.65) reduces to the standard hydraulic radius approximation, (3.64). Although it is usually easier to implement, the hydraulic radius approximation is often less accurate than the Aissen approximation [96].

3.4.3 Comparing methods

To compare the accuracy of the different methods on an irregular channel, we compare the flux estimated by each method with the finite element solution for flow through a pore throat. We use an example extracted from a Micro CT image of a Berea sandstone provided by Imperial College London. We have smoothed the voxels of the pore throat to reduce the effect of flow trapping in the corners. In Figure 3.8a, we show the extracted pore throat after smoothing.

[1]For simplicity, we have used Euler's series expansion for the circumference of an ellipse, $C \sim \pi\sqrt{2\left(r_a^2 + r_b^2\right)}\left(1 + O\left(\delta^2\right)\right)$ in order to approximate the circumference of the ellipse using a simple algebraic expression.

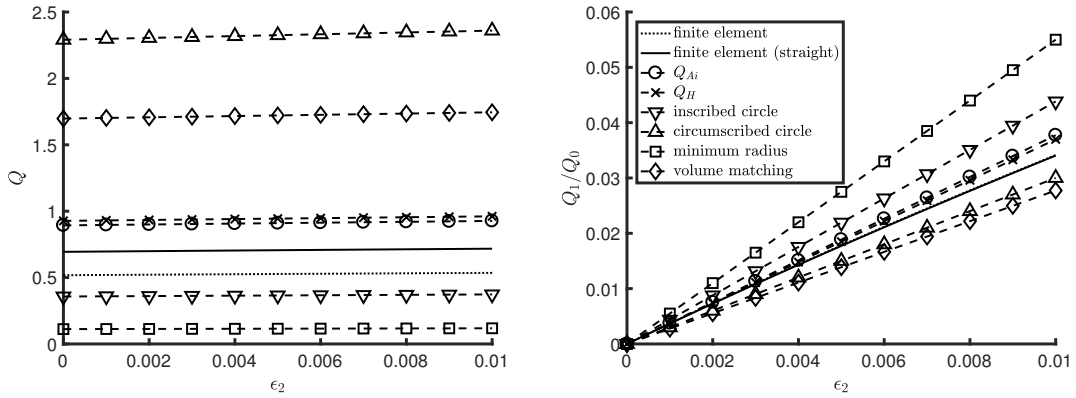


(a) Pore throat extracted from sample (b) 'Straightened' pore throat

Figure 3.8: Data extracted from a Berea sandstone sample using X-ray microtomography, provided by Imperial College London. Figure (a) depicts the pore throat extracted from the sample, and Figure (b) depicts the pore throat with the shape modified such that the central axis is straight.

To find the minimum circumscribed circle, maximum inscribed circle, area, and circumference at each cross section along the length of the throat, we suppose that the central axis of the throat lies along the z axis, and we extract the properties from the data in the (x, y) plane at each z. This will introduce some error, since the central axis of the throat is curved. To investigate the extent of this error, we also consider a 'straightened' version of the pore throat, depicted in Figure 3.8b, for which the cross section at each z has been shifted such that the centroid of the cross section lies at $(x, y) = \mathbf{0}$. The central axis of the straightened pore throat is a straight line, with the cross section at each z being identical to the unaltered pore throat. The aspect ratio of the throat is $\epsilon_1 = 0.36$, the minimum and maximum eccentricity, as measured by the inscribed and circumscribed circle at each point along its length, are $e_{\min} = 0.56$ and $e_{\max} = 0.93$, respectively, and the minimum and maximum value of δ along the length of the throat are $\delta_{\min} = 0.19$ and $\delta_{\max} = 0.76$, respectively.

In Figure 3.9a we plot the total flux through the throat for the different methods. In terms of the percentage error relative to the finite element solution, which we take to be our 'reference' solution, the inscribed circle solution is the most accurate, followed by the extended Aissen approximation and extended hydraulic radius approximation. However, the extended Aissen approximation and extended hydraulic radius approximation methods are closest to the straightened pore throat solution. This suggests that the torsion of the pore throat has a significant affect on the total flux, and introduces noticeable error. In order to correct this issue, a method such



(a) Total flux (b) Relative flux increase due to slip

Figure 3.9: Comparison between the different flux estimation methods for a) the total flux through the Berea throat, and b) the relative flux increase in the presence of slip along the surface of the throat.

as the medial axis method [68] needs to be applied to find the correct central axis, and the cross section perpendicular to that axis should be considered. Additionally, a mathematical model for the elliptic channel in which the central axis is curved needs to be developed. However, these considerations are beyond the scope of this thesis.

We see that the difference between the extended Aissen approximation and extended hydraulic radius approximation is small, and, given the typical error observed in estimating the flux using the different methods, the two approaches can likely be used interchangeably. The approach to use for a particular application will depend on the available data. It is not surprising that the two approaches produce a similar result given that both assume that the channel can be approximated by a varying elliptical cross section. The only difference between the two approaches is that the extended Aissen approximation estimates the semi-major and semi-minor axes using the minimum circumscribed circle and maximum inscribed circle, respectively, whereas the extended hydraulic radius approximation calculates the axes such that the area and circumference of the ellipse match that of the irregular cross section. The circumscribed circle solution significantly overestimates the total flux. The two methods currently used in practice, minimum radius and volume matching, are the least accurate.

In Figure 3.9b we plot the relative flux increase due to slip. The extended hydraulic radius method is the most accurate, followed by the extended Aissen approximation. The inscribed radius method and circumscribed radius method overestimate and underestimate, respectively, the relative flux increase. The two methods currently used

in practice, minimum radius and volume matching, overestimate and underestimate, respectively, the relative flux increase by the greatest amount. The relative flux increase for the unaltered pore and straightened pore are nearly identical, suggesting that tortuosity primarily affects the leading-order flux. For both the total flux and the relative flux increase, the extended Aissen approximation and extended hydraulic radius methods are significantly more accurate than the methods used currently, the volume matching and minimum radius methods.

3.5 Conclusions

In this chapter, we have presented a model for low-Reynolds number slip flow through a channel of varying elliptic cross section. We solved the system of equations using elliptical coordinates, and we assumed that the aspect ratio of the channel was small. We included slip in the model by supposing that the velocity on the surface of the channel was proportional to the shear stress on the boundary. We assumed that the slip length was small in comparison to the width of the channel, so that the problem could be solved asymptotically in terms of the dimensionless slip length.

In §3.3.1, we derived an expression for the flux through the channel, (3.57). We found that, since the shape of the cross section varies along its length, the flux is given by the harmonic mean of the equivalent flux through a uniform channel at each cross section. The leading-order (in ϵ_2) flux is the harmonic mean of the standard result for quasi-Poiseuille flow through an elliptic channel, and the first-order flux is written in terms of an elliptic integral, which, to solve numerically, needs to be computed at each cross section along the length of the channel.

In §3.3.2, we expanded the elliptic integral in the case where the small parameter $\delta = (r_a^2 - r_b^2) / (r_a^2 + r_b^2) \ll 1$, to find a simplified expression for the flux, (3.61). We compared the relative flux increase due to slip given by the simplified expression for the flux, $Q_\delta^{(1)}/Q_\delta^{(0)}$, with the full expression, $Q^{(1)}/Q^{(0)}$, and found that there is agreement to within 16.8%, even for very eccentric ellipses. The difference is within 5% for $\delta < 0.55$, which corresponds to $r_b < r_a < 1.8 r_b$, and within 1% for $\delta < 0.24$, which corresponds to $r_b < r_a < 1.3 r_b$.

In §3.3.3, we computed the flux through three elliptic channels. We compared the flux calculated by two existing methods, the 'volume matching' and 'minimum radius' methods, with Q, Q_δ, the 'inscribed circle' and 'circumscribed circle' methods, and the numerical finite element solution. We found that Q and Q_δ are in excellent agreement with the finite element solution, the volume matching method consistently

overestimates the total flux, and the minimum radius method consistently underestimates the total flux. Furthermore, the volume matching method consistently underestimates the relative flux increase due to slip, and the minimum radius method consistently overestimates the relative flux increase.

In §3.4.3, we computed the flux through a pore throat extracted from a Micro-CT image of a Berea sandstone, as calculated by the different methods. We conclude that the methods which approximate the pore throat using a channel with varying elliptic cross section, which we derived as extensions to the Aissen approximation and hydraulic radius approximation (equations (3.63) and (3.65), respectively), are typically the most accurate methods. More importantly, our elliptic approaches are less susceptible to the systematic errors observed when applying the other methods. In particular, the methods currently used in practice, the minimum radius method and volume matching method, consistently underestimate and overestimate, respectively, the total flux. Additionally, the minimum radius method consistently overestimates the relative flux increase due to slip, and the volume matching method consistently underestimates the flux increase due to slip. Applying either of these methods to a network of pore throats is likely to lead to an inaccurate estimation of the permeability of the porous structure due to the cumulative effect of consistently overestimating or underestimating the flux. Furthermore, network models constructed using one of these methods is likely to miscalculate the effect of the slip length (i.e. the salinity) on the flow through the structure. We conclude that, by using our extensions to the Aissen or hydraulic radius methods, we can estimate the flux through the throat with reasonable accuracy. In particular, we can use this method to model a pore throat extracted from image data of a rock sample. Furthermore, by including the first-order extensions to these methods presented in this chapter, we can estimate the effect of the slip length, and therefore the salinity, on the flux through the throat. In Chapter 4, we will discuss how to apply these results to a periodic network of throats, and consequently determine the effect of slip on the permeability of a porous structure.

The main limitation of the model presented in this chapter is the assumption that the central axis is straight, which will lead to errors when estimating the flux through a curved throat. We observe that the elliptic approximations overestimate the flux through the pore throat extracted from the Berea sandstone. This is partly due to the fact that the flux through the throat is reduced as a result of the central axis being curved, since the error is reduced when comparing the elliptic approximations with the straightened pore. Further work needs to be done to generalise the model for curved channels.

Chapter 4

Slip flow through a periodic porous structure

4.1 Introduction

In Chapters 2 and 3, we investigated the effect of salinity on the motion of oil through a pore throat. We determined the flux as a function of the salinity for an oil slug moving through a two-dimensional straight-walled capillary, as well as for a continuous oil phase in a three-dimensional irregularly-shaped capillary. Our observations were driven by the result that the salinity affects the flow of oil by changing the thickness of the thin layer of water residing between the oil and the wall. In the limit of interest, the presence of this water layer provides slip to the oil, with the slip length dependent on the salinity. In order to be able to use this knowledge to study the effect of salinity on oil-flow through a reservoir rock, we need to understand how the slip-length affects flow through a porous structure in which multiple flow paths interact. In this chapter, we will study slip-flow through periodic porous structures constructed from repeated unit cells, with the aim of determining the permeability as a function of the slip length. We will use a homogenisation method to derive the permeability tensor for a periodic structure constructed from a unit cell, and study the simple case of a cell containing a single inclusion. We will then estimate the permeability of a complex periodic pore structure constructed from a repeated unit cell containing multiple inclusions by modelling it as a network of pores and throats.

Throughout this chapter, we restrict out attention to the case where water is only present in a thin layer adjacent to the rock so that we can concentrate on the single-phase flow of oil in order to understand the effect of the salinity on the oil phase, without the additional complications introduced by the two-phase flow of oil and water. While it is possible to use volume averaging techniques to derive equations

for two-phase flow through porous media [61, 70, 113, 114], numerous issues arise as a result of the unknown location of the fluid-fluid interface, and such approaches require a number of simplifications in order to make the resulting system tractable. Hilfer [38] discusses this issue further, and proposes an alternative approach based on macroscopic mixture theory, by applying conservation of mass, energy, and momentum on the macroscopic scale. However, the disadvantage with this approach is that it ignores the microscopic system entirely. Since determining the flow of each phase independently is problematic, two phase flow through porous media is typically described using the Buckley-Leverett model [20], in which the locally averaged saturation is determined using a non-linear advection equation. Two of the key functional inputs into the model are the saturation-dependent 'relative permeabilities' of the two phases. Whilst these functions are often determined experimentally, one of the widely-accepted theoretical models is the Brooks-Corey model [17, 23, 65], in which the relative permeability of each phase is given by the single-phase permeability multiplied by a power law for the saturation. We expect the model to depend on the salinity through the single-phase permeability of the oil. Therefore, in this chapter, we focus on determining the single-phase salinity-dependent permeability of an oil-filled porous structure with the view that this can be applied to a two-phase Buckley-Leverett model.

In §4.2, we will use the method of multiple scales to derive a 'cell problem' for the slip-dependent permeability of a periodic porous structure, starting from the incompressible Stokes equations subject to a slip boundary condition. In §4.2.4, we will use COMSOL's in-built finite element method solver to solve the cell problem for a unit cell containing a simple circular inclusion to demonstrate the effect of the slip length on the permeability. Due to the complexity of the cell problem, it is impractical to numerically solve the full model on complex geometries. In §4.3, we will attempt to determine an easily-computable geometrical property of two-dimensional simply-connected unit cells which we can use as a reasonable estimate for the permeability of the macroscale periodic structure, without having to solve the full cell problem. In §4.3.1 we will test two simple properties, the area of the inclusion and the minimum pore width. We choose these two properties as they are the two-dimensional equivalents of the volume-matching and minimum radius methods introduced in Chapter 3. In §4.3.2, we will redefine the boundaries of the periodic unit cell to pass through the centre of the inclusion, in order to present the fluid domain as a single channel. We will calculate the flux through a thin, irregular channel, and use the resulting geometrical expression to estimate the flux through the unit cell. In §4.3.3, we will

discuss how to relate the flux through the unit cell to the permeability of the periodic porous structure constructed from the cell, and therefore how to use the expression derived in §4.3.2 to estimate the permeability. In §4.3.4, we will test the validity of this estimate by comparing the permeabilities of periodic structures constructed from repeated unit cells containing square, diamond, cross-shaped, and circular inclusions.

In §4.4 we will study the permeability of a periodic porous structure constructed from a unit cell containing multiple inclusions. We will treat the multiply-connected domain as a network of channels, in which we estimate the conductivities using the geometrical expression derived in §4.3.2. In §4.4.1 and §4.4.2, we will present a method for extracting the channel network from an image of a porous structure in order to uniquely define the pore spaces and channels for a given fluid domain. We will present the network as a conductivity-weighted adjacency matrix. In §4.4.3, we will derive an expression for the flux through the network, which we will use to estimate the permeability of the multiply-connected domain. We will compare the network model estimation with the finite element solution for two examples in §4.4.4. Finally, in §4.5, we will discuss our findings.

4.1.1 Previous work

There have been a number of theoretical studies investigating slip flow through porous media. Valdes-Parada *et al.* [105] use a volume-averaging method to homogenise slip-flow through a porous structure. They retain a viscous term in their microscale model, and derive a Darcy-Brinkman type equation [16] on the macroscopic scale. They observe that the slip length affects the effective viscosity on the macroscopic scale, and that the macroscopic viscosity is equal to the microscopic viscosity in the no-slip limit. However, they find that the computation of the permeability tensor and effective viscosity involves the numerical solution of non-homogeneous boundary-value problems for various closure variables, which is equivalent to numerically solving a cell problem. Skjetne & Auriault [97] use the method of multiple scales to homogenise wall-slip gas flow through porous media. They perform a double-scale homogenisation by assuming that the slip length and the ratio of the pore length scale to the macroscopic length scale are both small. They find that the lowest-order slip effect is given by the Darcy-Klinkenberg equation [51], in which the slip-dependent permeability is given by the permeability in the no-slip limit multiplied by a linear function of the reciprocal of the mean pressure. Wang [111] studies slip-flow through square and triangular arrays of circular cylinders, and determines the permeability using eigenfunction expansions. This approach improves upon direct numerical integration when dealing

with small cylinder radii, since scaling issues which may arise using finite difference or finite element methods do not occur. However, it is not clear that the method can be generalised to arbitrarily-shaped geometries.

There are two main approaches commonly used for extracting a simplified network model from voxel data of a rock sample. Lindquist *et al.* [68] propose the 'medial axis' algorithm for generating the central axis of a porous structure. In this method, the normal lines are computed at each point on the surface of the rock. The points at which the normals intersect form a number of connected two-dimensional surfaces throughout the structure. The central axes of the pore throats are defined to be the lines passing through the centre of the surfaces, and pore spaces are defined to be the points where the central axes intersect. We will use a similar algorithm in two dimensions in this chapter. An alternative algorithm for extracting an appropriate network from voxel data of a rock sample was first proposed by Silin & Patzek [94]. They find the maximal inscribed ball at each voxel in the fluid domain, and, by constructing a hierarchy of balls based on their radii, are able to distinguish the pore spaces from the pore throats. Whilst this method is straightforward to implement, and provides a lot of information about the rock structure, it can be computationally demanding. However, Arand & Hesser [6] recently developed an algorithm to improve the efficiency of this method.

Turning our attention to network models for fluid flow, the conductivity of each channel is typically given by Poiseuille's law [100], which, when combined with conservation of mass at each node, leads to a set of simultaneous equations to be solved for the pressures at each node. Koplik & Lasseter [53], and O'Carrol & Sorbie [78], generate and solve such systems to study single-phase and two-phase flow through randomly-generated network structures. They observe that the problem is equivalent to a random electrical resistor problem, and use effective medium theory to determine the permeability of the network. The equivalence of the flow network to a resistor network is well known, and is a problem that has been widely studied in the context of percolation theory [50, 91].

4.2 Darcy flow with slip boundary condition

We consider a two-dimensional rigid periodic porous medium of length L filled with oil, in which a thin layer of water, thickness h^*, coats the walls of the pores. We denote the fluid-filled pore space by Ω, and the fluid-solid boundary by $\partial\Omega$. We assume that the porous structure is constructed from a repeated cell with side-length r_p, and that

the ratio of the pore length scale to the macroscopic length scale, $\epsilon_p := r_p/L \ll 1$, is small. We suppose that the fluid is subject to a pressure difference, P, across the ends of the porous medium.

4.2.1 Governing Equations

We model the oil flow using the steady incompressible Stokes equations,

$$\mu_o \nabla^2 \mathbf{u} = \nabla p, \qquad \nabla \cdot \mathbf{u} = 0, \tag{4.1}$$

where $\mathbf{u}$ is the fluid velocity, p is the pressure, and μ_o is the viscosity of the oil.

We model the thin water film using an effective slip boundary condition at the oil-solid interface. Using the result (2.156), we suppose that the normal velocity of the fluid at the surface is zero, and the tangential velocity of the fluid is proportional to the shear stress, with the constant of proportionality given by $h^* (\mu^* - 1)$, where $\mu^* = \mu_o/\mu_w > 1$ is the viscosity ratio of the oil to the water. Separating the slip condition into the tangential and normal components yields

$$\left.\begin{aligned} \mathbf{u} \cdot \mathbf{t} &= h^* (\mu^* - 1)\, \mathbf{n} \cdot \nabla(\mathbf{u} \cdot \mathbf{t}), \\ \mathbf{u} \cdot \mathbf{n} &= 0, \end{aligned}\right\} \quad \text{on } \partial\Omega, \tag{4.2}$$

where $\mathbf{n}$ and $\mathbf{t}$ are the normal and tangent vectors, respectively, to the fluid-solid interface.

We suppose that the fluid is subject to a pressure difference, P, so that

$$p(0, Y) = \tilde{p} + P, \qquad p(L, Y) = \tilde{p}, \tag{4.3}$$

where $\tilde{p}$ is an arbitrary reference pressure.

4.2.2 Non-dimensionalisation

We expect that viscous dissipation occurs on the length scale of the pores, r_p, whereas the pressure varies over the macroscopic length scale, L. From (4.1), this implies that the typical flow speed is $U \sim r_p^2 P/\mu_o L$. We therefore non-dimensionalise the problem by setting

$$\mathbf{u} = \frac{r_p^2 P}{\mu_o L}\hat{\mathbf{u}}, \qquad p = p_0 + P\hat{p}, \qquad X = L\hat{X}, \qquad Y = L\hat{Y}, \tag{4.4}$$

which, dropping the hats for convenience, yields the dimensionless system,

$$\epsilon_p^2 \nabla^2 \mathbf{u} = \nabla p, \qquad \nabla \cdot \mathbf{u} = 0, \tag{4.5}$$

subject to

$$\left.\begin{aligned} \mathbf{u}\cdot\mathbf{t} &= \epsilon_p \lambda_s \mathbf{n}\cdot\nabla(\mathbf{u}\cdot\mathbf{t}), \\ \mathbf{u}\cdot\mathbf{n} &= 0, \end{aligned}\right\} \quad \text{on } \partial\Omega, \tag{4.6}$$

$$p(0,Y) = 1, \qquad p(1,Y) = 0, \tag{4.7}$$

where $\lambda_s = h^* (\mu^* - 1)/r_p$ is the dimensionless slip length.

4.2.3 Multiple-scales solution

We are primarily interested in the macroscopic behaviour, rather than the local variation, so we use the method of multiple scales to determine the equations governing the locally homogenised velocity and pressure. We capture the variation over the two separate length scales by introducing the microscopic variable, $\mathbf{x} = (x, y)$, such that

$$\mathbf{x} = \frac{1}{\epsilon_p}\mathbf{X}, \tag{4.8}$$

where $\mathbf{X} = (X, Y)$. We suppose that $\mathbf{u}$ and p are functions of both $\mathbf{x}$ and $\mathbf{X}$, which we assume can be treated as *independent* variables. The extra degree of freedom this introduces enables us to exploit the periodic nature of the porous structure by imposing that both functions are periodic with respect to the small length scale, $\mathbf{x}$, that is

$$\mathbf{u}(\mathbf{x} + \mathbf{e}_k, \mathbf{X}) = \mathbf{u}(\mathbf{x}, \mathbf{X}), \qquad p(\mathbf{x} + \mathbf{e}_k, \mathbf{X}) = p(\mathbf{x}, \mathbf{X}), \tag{4.9}$$

where $\mathbf{e}_k$ are the basis vectors in each spatial direction. By treating these two variables as independent, we can impose periodicity on the pore scale, $\mathbf{x}$, whilst still allowing $\mathbf{u}$ and p to vary on the macroscopic scale, $\mathbf{X}$.

We expand $\mathbf{u}$ and p in powers of ϵ_p,

$$\mathbf{u}(\mathbf{x}, \mathbf{X}) \sim \mathbf{u}^{(0)}(\mathbf{x}, \mathbf{X}) + \epsilon_p \mathbf{u}^{(1)}(\mathbf{x}, \mathbf{X}) + \epsilon_p^2 \mathbf{u}^{(2)}(\mathbf{x}, \mathbf{X}) + \cdots, \tag{4.10}$$

$$p(\mathbf{x}, \mathbf{X}) \sim p^{(0)}(\mathbf{x}, \mathbf{X}) + \epsilon_p p^{(1)}(\mathbf{x}, \mathbf{X}) + \epsilon_p^2 p^{(2)}(\mathbf{x}, \mathbf{X}) + \cdots, \tag{4.11}$$

and, by the chain rule, we write

$$\nabla = \nabla_{\mathbf{X}} + \frac{1}{\epsilon_p}\nabla_{\mathbf{x}}. \tag{4.12}$$

We use this change of variables to write (4.5) – (4.7) and (4.9) as

$$\nabla_{\mathbf{x}}^2 \mathbf{u}^{(0)} \sim \frac{1}{\epsilon_p}\nabla_{\mathbf{x}} p^{(0)} + \nabla_{\mathbf{X}} p^{(0)} + \nabla_{\mathbf{x}} p^{(1)}, \tag{4.13}$$

$$\nabla_{\mathbf{x}}\cdot\mathbf{u}^{(0)} + \epsilon_p \nabla_{\mathbf{X}}\cdot\mathbf{u}^{(0)} + \epsilon_p \nabla_{\mathbf{x}}\cdot\mathbf{u}^{(1)} \sim 0, \tag{4.14}$$

subject to

$$\left.\begin{aligned} \mathbf{u}^{(0)}\cdot\mathbf{t} &\sim \lambda_s \mathbf{n}\cdot\nabla_{\mathbf{x}}(\mathbf{u}^{(0)}\cdot\mathbf{t}),\\ \mathbf{u}^{(0)}\cdot\mathbf{n}+\epsilon_p\mathbf{u}^{(1)}\cdot\mathbf{n} &\sim 0, \end{aligned}\right\} \quad \text{on } \partial\Omega, \tag{4.15}$$

$$\frac{1}{\epsilon_p}p^{(0)}+p^{(1)} \sim \frac{1}{\epsilon_p}, \qquad \text{on } X=0, \tag{4.16}$$

$$\frac{1}{\epsilon_p}p^{(0)}+p^{(1)} \sim 0, \qquad \text{on } X=1, \tag{4.17}$$

$$\mathbf{u}^{(0)}(\mathbf{x}+\mathbf{e}_k,\mathbf{X})+\epsilon_p\mathbf{u}^{(1)}(\mathbf{x}+\mathbf{e}_k,\mathbf{X}) \sim \mathbf{u}^{(0)}(\mathbf{x},\mathbf{X})+\epsilon_p\mathbf{u}^{(1)}(\mathbf{x},\mathbf{X}), \tag{4.18}$$

$$\frac{1}{\epsilon_p}p^{(0)}(\mathbf{x}+\mathbf{e}_k,\mathbf{X})+p^{(1)}(\mathbf{x}+\mathbf{e}_k,\mathbf{X}) \sim \frac{1}{\epsilon_p}p^{(0)}(\mathbf{x},\mathbf{X})+p^{(1)}(\mathbf{x},\mathbf{X}). \tag{4.19}$$

We have multiplied (4.16), (4.17), and (4.19) by a factor of ϵ_p^{-1}, as we will find that this gives us the appropriate order for these equations when we equate terms at each order in ϵ_p.

The $O(\epsilon_p^{-1})$ terms in (4.13) read

$$\nabla_{\mathbf{x}}p^{(0)}=0, \tag{4.20}$$

which implies that $p^{(0)}=p^{(0)}(\mathbf{X})$. This automatically satisfies the $O(\epsilon_p^{-1})$ terms in (4.19), and, by (4.16) and (4.17), we find that $p^{(0)}$ is subject to the boundary conditions

$$p^{(0)}(0,Y)=1, \qquad p^{(0)}(1,Y)=0. \tag{4.21}$$

We must proceed to higher orders in order to determine the functional dependence of $p^{(0)}$ with respect to $\mathbf{X}$.

The $O(1)$ terms in (4.13) – (4.19), read

$$\nabla_{\mathbf{x}}^2\mathbf{u}^{(0)}-\nabla_{\mathbf{x}}p^{(1)}=\nabla_{\mathbf{X}}p^{(0)}, \qquad \nabla_{\mathbf{x}}\cdot\mathbf{u}^{(0)}=0, \tag{4.22}$$

subject to

$$\left.\begin{aligned} \mathbf{u}^{(0)}\cdot\mathbf{t} &= \lambda_s\mathbf{n}\cdot\nabla_{\mathbf{x}}(\mathbf{u}^{(0)}\cdot\mathbf{t}),\\ \mathbf{u}^{(0)}\cdot\mathbf{n} &= 0, \end{aligned}\right\} \quad \text{on } \partial\Omega, \tag{4.23}$$

$$\mathbf{u}^{(0)}(\mathbf{x}+\mathbf{e}_k,\mathbf{X})=\mathbf{u}^{(0)}(\mathbf{x},\mathbf{X}), \tag{4.24}$$

$$p^{(1)}(\mathbf{x}+\mathbf{e}_k,\mathbf{X})=p^{(1)}(\mathbf{x},\mathbf{X}). \tag{4.25}$$

Since (4.22) – (4.25) is a linear inhomogeneous system of PDEs with respect to $\mathbf{x}$, we seek a solution in which $\mathbf{u}^{(0)}$ and $p^{(1)}$ are linear functions of $\nabla_{\mathbf{X}} p^{(0)}$. Thus, we make the ansatz

$$u_i^{(0)} = -K_{ij}(\mathbf{x})\frac{\partial p^{(0)}}{\partial \mathbf{X}_j}, \qquad p^{(1)} = -A_j(\mathbf{x})\frac{\partial p^{(0)}}{\partial \mathbf{X}_j} + c^{(1)}(\mathbf{X}), \tag{4.26}$$

where the tensors K_{ij} and A_j are to be determined, $c^{(1)}$ is an arbitrary function of $\mathbf{X}$ resulting from the gauge invariance of $p^{(1)}$, and we have written the equations using the summation convention.

Substituting (4.26) into (4.22) yields

$$\left(\frac{\partial^2 K_{11}}{\partial x^2} + \frac{\partial^2 K_{11}}{\partial y^2} - \frac{\partial A_1}{\partial x} + 1\right)\frac{\partial p^{(0)}}{\partial X} + \left(\frac{\partial^2 K_{12}}{\partial x^2} + \frac{\partial^2 K_{12}}{\partial y^2} - \frac{\partial A_2}{\partial x}\right)\frac{\partial p^{(0)}}{\partial Y} = 0, \tag{4.27}$$

$$\left(\frac{\partial^2 K_{21}}{\partial x^2} + \frac{\partial^2 K_{21}}{\partial y^2} - \frac{\partial A_1}{\partial y}\right)\frac{\partial p^{(0)}}{\partial X} + \left(\frac{\partial^2 K_{22}}{\partial x^2} + \frac{\partial^2 K_{22}}{\partial y^2} - \frac{\partial A_2}{\partial y} + 1\right)\frac{\partial p^{(0)}}{\partial Y} = 0, \tag{4.28}$$

$$\left(\frac{\partial K_{11}}{\partial x} + \frac{\partial K_{21}}{\partial y}\right)\frac{\partial p^{(0)}}{\partial X} + \left(\frac{\partial K_{12}}{\partial x} + \frac{\partial K_{22}}{\partial y}\right)\frac{\partial p^{(0)}}{\partial Y} = 0. \tag{4.29}$$

Since the terms in brackets depend only on $\mathbf{x}$, and $p^{(0)}$ depends on $\mathbf{X}$, we find that, in order for the equations to be valid for all $\mathbf{X}$, each of the bracketed expressions must be equal to zero, that is,

$$\nabla^2 K_{ij} - \frac{\partial A_j}{\partial x_i} + \delta_{ij} = 0, \qquad \frac{\partial K_{ij}}{\partial x_i} = 0, \qquad \text{in } \Omega. \tag{4.30}$$

Substituting (4.26) into (4.23) – (4.25) yields the boundary conditions

$$t_i K_{ij} = \lambda_s n_i \frac{\partial}{\partial x_i}\left(K_{kj} t_k\right), \qquad n_i K_{ij} = 0, \qquad \text{on } \partial\Omega, \tag{4.31}$$

$$K_{ij}(x+1, y) = K_{ij}(x, y) \qquad K_{ij}(x, y+1) = K_{ij}(x, y), \tag{4.32}$$

$$A_i(x+1, y) = A_i(x, y) \qquad A_i(x, y+1) = A_i(x, y). \tag{4.33}$$

The system of equations, (4.30) – (4.33) is known as a 'cell problem' for K_{ij} and A_j. We can think of this system as multiple sets of Stokes equations with a forcing term, given by δ_{ij}, acting in each direction. In solving these equations, we determine how the fluid moves through the geometry in each direction, with K_{ij} acting as the fluid velocity, and A_j acting as the pressure.

Equation (4.26) relates the leading-order velocity, $u_i^{(0)}$, to the leading-order pressure, $p_i^{(0)}$, through K_{ij}. However, we have yet to determine the equations which govern $u_i^{(0)}$ and $p_i^{(0)}$. Since we are primarily interested in the overall behaviour of the fluid on the macroscopic scale, we formulate the problem in terms of the locally homogenised

variables found by taking the average of the fluid properties over the unit cell. We define the notation

$$\langle F \rangle = \frac{1}{V} \int_{V_f} F \, \mathrm{d}\mathbf{x}, \tag{4.34}$$

where V is the volume of a unit cell, and V_f is the volume of fluid within the unit cell, so that $\phi = V_f/V$ is the porosity of the saturated material. By integrating (4.26) over the unit cell, we find that the locally averaged velocity is given by

$$\langle u_i^{(0)} \rangle = -\langle K_{ij} \rangle \frac{\partial p^{(0)}}{\partial \mathbf{X}_j}. \tag{4.35}$$

This is known as the Darcy velocity, which is proportional to the leading-order pressure gradient, $\nabla_{\mathbf{X}} p^{(0)}$. To determine the governing equation for $p^{(0)}$ (and therefore $\langle u_i^{(0)} \rangle$), we consider the $O(\epsilon_p)$ terms in (4.14) and (4.15), which read

$$\nabla_{\mathbf{X}} \cdot \mathbf{u}^{(0)} + \nabla_{\mathbf{x}} \cdot \mathbf{u}^{(1)} = 0, \tag{4.36}$$

and

$$\mathbf{u}^{(1)} \cdot \mathbf{n} = 0, \qquad \text{on } \partial\Omega, \tag{4.37}$$

respectively. Now,

$$\begin{aligned}
\nabla_{\mathbf{X}} \cdot \langle \mathbf{u}^{(0)} \rangle &= \nabla_{\mathbf{X}} \cdot \left(\frac{1}{V} \int_{V_f} \mathbf{u}^{(0)} \, \mathrm{d}\mathbf{x} \right) \\
&= \frac{1}{V} \int_{V_f} \nabla_{\mathbf{X}} \cdot \mathbf{u}^{(0)} \, \mathrm{d}\mathbf{x} \\
&= -\frac{1}{V} \int_{V_f} \nabla_{\mathbf{x}} \cdot \mathbf{u}^{(1)} \, \mathrm{d}\mathbf{x} \qquad \text{(From (4.36))} \\
&= -\frac{1}{V} \int_{\partial V_f} \mathbf{u}^{(1)} \cdot \mathbf{n} \, \mathrm{d}s \qquad \text{(Divergence theorem)} \\
&= -\frac{1}{V} \int_{\partial V_f \cap \partial\Omega} \mathbf{u}^{(1)} \cdot \mathbf{n} \, \mathrm{d}s - \frac{1}{V} \int_{\partial V_f \setminus \partial\Omega} \mathbf{u}^{(1)} \cdot \mathbf{n} \, \mathrm{d}s.
\end{aligned} \tag{4.38}$$

The last line in (4.38) is derived by separating the boundary integral into the two components given by the solid boundaries in the interior of the unit cell, $\partial V_f \cap \partial\Omega$, and the fluid boundaries at the inlets and outlets of the cell, $\partial V_f \setminus \partial\Omega$. The first integral is zero since the velocity normal to the fluid-solid interface is zero by (4.37). For the second integral, we use the fact that, by periodicity, the normal velocity of the fluid entering one side of the unit cell is equal and opposite to the normal velocity of the fluid exiting the cell at the opposite edge. Hence, the net velocity normal to the cell surface is zero, and therefore

$$\nabla_{\mathbf{X}} \cdot \langle \mathbf{u}^{(0)} \rangle = 0. \tag{4.39}$$

To simplify the notation, we write $\bar{\mathbf{U}} = \langle \mathbf{u}^{(0)} \rangle$, $\bar{P} = p^{(0)}$, and let $\boldsymbol{K}$ denote the tensor form of $\langle K_{ij} \rangle$, so that (4.35) and (4.39) read

$$\bar{\mathbf{U}} = -\boldsymbol{K} \nabla_{\mathbf{X}} \bar{P}, \qquad \nabla_{\mathbf{X}} \cdot \bar{\mathbf{U}} = 0. \tag{4.40}$$

Equations (4.40) are Darcy's law for flow through porous media, with permeability tensor $\boldsymbol{K}$, which are valid throughout the porous structure. Since we assumed that the structure is periodic, we only need to solve the cell problem in a single cell in order to determine the permeability for the entire porous medium.

It is worth noting that our cell problem differs from traditional cell problems for Darcy flow, since the boundary condition (4.31) involves slip along the fluid-solid interface. Hence, not only must we solve this problem for each geometry we are considering, we must also solve a different cell problem for every slip length. Consequently, the permeability tensor, $\boldsymbol{K}$, is a function of the slip length, λ_s, which in turn is a function of the salinity.

Formulating the problem in terms of the two length-scales has resulted in a separation between the calculations for the local behaviour of the fluid, which is found by solving the pore-scale cell problem to determine $\boldsymbol{K}$, and the macroscopic behaviour, which is then found by solving (4.40) (with $\boldsymbol{K}$ as an input) for $\bar{\mathbf{U}}$ and $\bar{P}$.

4.2.4 Example: Unit cell with simple circular inclusion

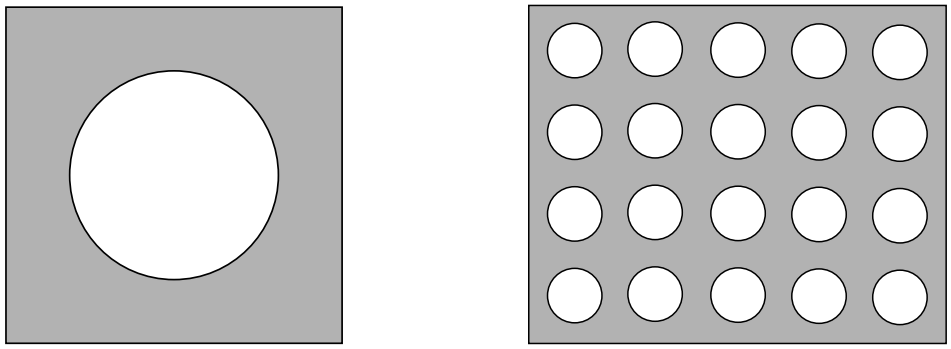
To demonstrate the effect of the slip length (i.e. the salinity) on the permeability, we consider the simple example of a square unit cell containing a circular inclusion with radius of 0.25 with centre at the middle of the square. In Figure 4.1a, we show the geometry in which we need to solve the cell problem to determine the macroscale permeability tensor, $\boldsymbol{K}(\lambda_s)$, and, in Figure 4.1b, we show the porous structure, constructed from the repeated unit cell, over which Darcy's law applies.

For our simple example, we only need to solve (4.30) – (4.33) to determine K_{11}, K_{21}, and A_1, since, by symmetry, $K_{22} = K_{11}$, $K_{12} = K_{21}$, and $A_2 = A_1$. Defining $\mathcal{K} := (K_{11}, K_{21})$, and recalling that $\mathbf{e}_x := (1, 0)^T$, the system of equations (4.30) – (4.33) for the case $j = 1$ read

$$\nabla^2 \mathcal{K} - \nabla A_1 + \mathbf{e}_x = 0, \qquad \nabla \cdot \mathcal{K} = 0, \tag{4.41}$$

subject to

$$\mathbf{n} \cdot \mathcal{K} = 0, \qquad \mathbf{t} \cdot \mathcal{K} = \lambda_s \mathbf{n} \cdot \nabla(\mathbf{t} \cdot \mathcal{K}), \tag{4.42}$$



(a) (b)

Figure 4.1: Diagram of a periodic porous material with simple circular inclusion: (a) the unit cell; (b) the porous structure generated from the repeated cell.

on the boundary of the circular inclusion, and the periodicity conditions,

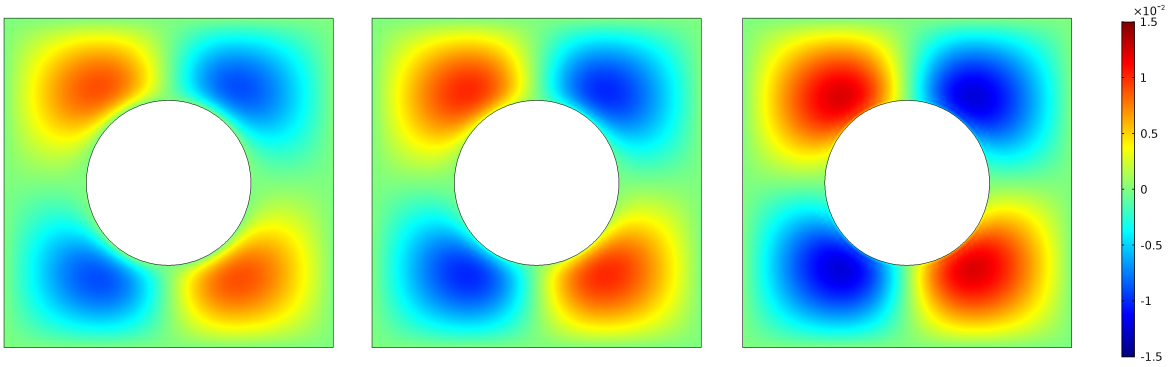
$$\mathcal{K}(0,y) = \mathcal{K}(1,y), \qquad \mathcal{K}(x,0) = \mathcal{K}(x,1), \tag{4.43}$$

$$A_1(0,y) = A_1(1,y), \qquad A_1(x,0) = A_1(x,1), \tag{4.44}$$

on the edges of the unit cell.

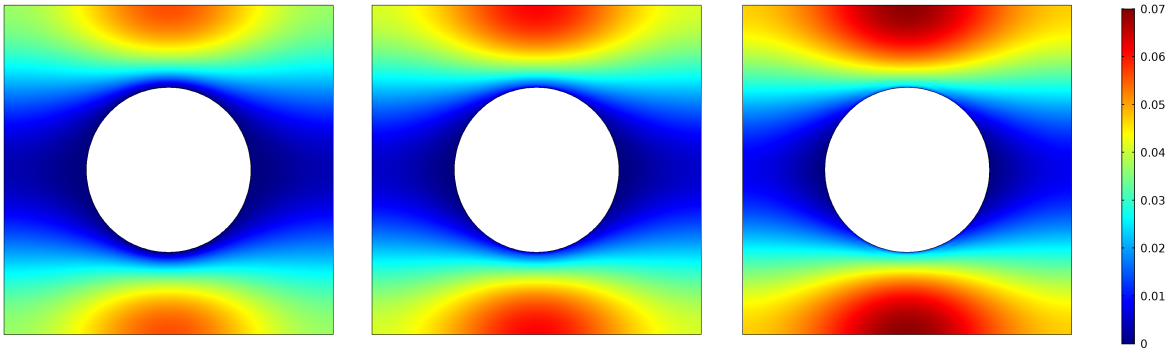
In Figure 4.2, we plot the numerical solution for K_{12}, found by solving (4.41) – (4.44) using a finite element method in COMSOL. We plot the solution for three values of the dimensionless slip length, given by $\lambda_s = 0$, $\lambda_s = 0.005$, and $\lambda_s = 0.01$ in Figures 4.2a, 4.2b, and 4.2c, respectively. We observe that, due to the symmetry of the circular inclusion, the values of K_{12} in the upper half of the unit cell are equal and opposite to the values of K_{12} in the lower half of the unit cell, and therefore K_{12} integrates to zero over the domain. This makes intuitive sense, since, by the symmetry of the circular inclusion, we expect the off-diagonal components of the permeability tensor to vanish, $\langle K_{12} \rangle = \langle K_{21} \rangle = 0$.

In Figure 4.3, we plot the numerical solution for K_{11} for the three values of the slip length. We observe that K_{11} increases throughout the fluid domain as the slip length increases, and consequently the diagonal component of the permeability tensor, $\langle K_{11} \rangle$, also increases. Furthermore, by symmetry, we know that $\langle K_{11} \rangle = \langle K_{22} \rangle =: K$, and therefore the permeability tensor is proportional to the identity matrix, $\boldsymbol{K}(\lambda_s) = K(\lambda_s)\boldsymbol{I}$. In Figure 4.4, we plot the permeability 'scalar', $K(\lambda_s)$, against the slip length. The permeability increases by 37.8% as the slip length increases from 0 to 0.01.



(a) (b) (c)

Figure 4.2: Numerical solution for K_{12}, found by solving (4.41) – (4.44): (a) $\lambda_s = 0$; (b) $\lambda_s = 0.005$; (c) $\lambda_s = 0.01$.



(a) (b) (c)

Figure 4.3: Numerical solution for K_{11}, found by solving (4.41) – (4.44): (a) $\lambda_s = 0$; (b) $\lambda_s = 0.005$; (c) $\lambda_s = 0.01$.

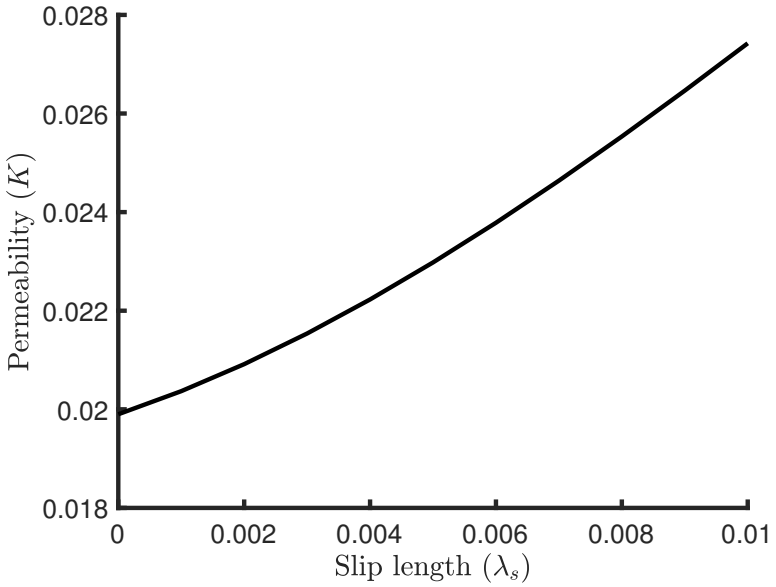


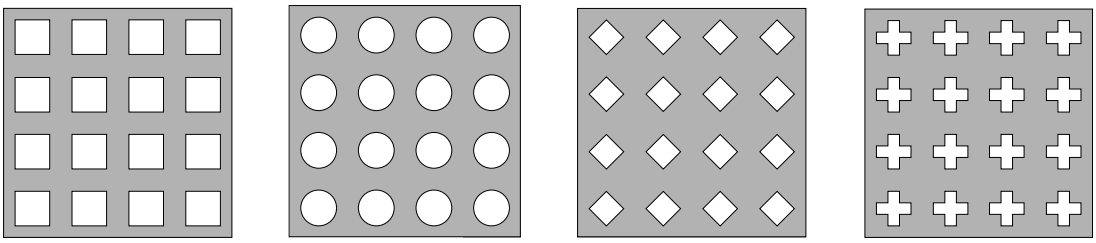
Figure 4.4: Plot of the permeability against the slip length for the square unit cell containing a circular inclusion with radius 0.25.

4.3 Simply-connected periodic domains

While the example in the previous section demonstrates that the slip length, and therefore the salinity, affects the permeability, the simplified geometry is of limited use when trying to quantitatively estimate the permeability of a sample of porous rock. In this section, we investigate how the geometry of the pore structure affects the permeability, and determine a simple estimate for the permeability which does not require us to numerically solve (4.30) – (4.33).

4.3.1 Simple permeability estimates

The numerical solution to (4.30) – (4.33) can be easily computed for the simple inclusions shown in Figure 4.5. However, it becomes impractical for complex structures, such as those containing multiple inclusions. In order to be able to study more complex structures, and to gain a greater insight into the dependence of the permeability on the geometry of unit cell, our aim in this section is to determine an easily-calculated geometrical quantity of the unit cell, such as the area of the inclusion, from which we can estimate the permeability. This geometry-based approach is similar to the approaches used by various authors to estimate the flux through an irregularly-shaped pore throat, such as volume-matching or minimum pore radius methods, which we described in Chapter 3.

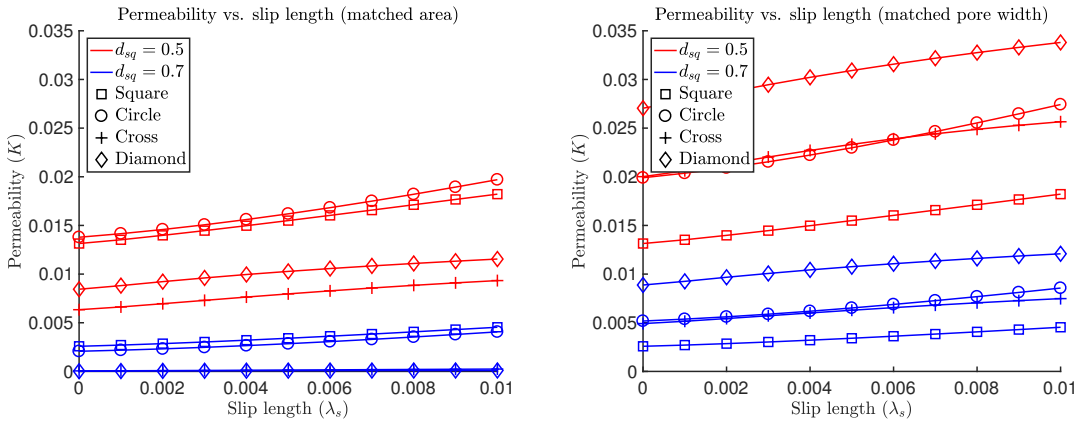


(a) (b) (c) (d)

Figure 4.5: Periodic porous structure constructed from a unit cell with a simple inclusion given by a (a) square (b) circle (c) diamond (d) cross. The shaded region represents the fluid domain, and the white region represents the solid inclusion.

Since computing a geometrical quantity does not provide us with an estimate for the permeability in itself, we test the viability of a particular quantity by checking that the permeability is independent of the shape of the inclusion, provided that the quantity we are testing is held constant. We test each geometrical quantity we consider on the four periodic structures with simple inclusions constructed from unit cells with square, circular, diamond, and cross-shaped simple inclusions, as shown in Figure 4.5. We do this by constructing a unit cell containing a square inclusion with side length d_{sq}, and calculating the value of the particular geometrical quantity we are testing. We then determine the size of the circular, diamond, and cross-shaped inclusions such that the geometrical quantity is consistent across all of the shapes. Finally, we numerically compute the permeabilities of each of the periodic structures constructed from the repeated unit cells containing the different inclusions, and, by checking whether the permeabilities are in agreement, determine whether the geometrical quantity is an appropriate predictor for the permeability.

As a first step towards understanding the relationship between the geometry of the inclusion and the permeability of the porous structure, we consider the area and the minimum pore width as our test quantities since these are the two-dimensional equivalent to the volume matching and minimum radius methods, respectively, discussed in Chapter 3. By testing these easily-computed quantities, we reveal some of the issues which arise when trying to estimate the permeability using a simple geometrical measure, and determine where these basic quantities fall short. For each quantity, we test the two cases in which the length of the sides of the square inclusion are given by $d_{sq} = 0.5$ and $d_{sq} = 0.7$. The results in this section are found by solving (4.30) – (4.33) for the appropriate geometries using a finite element method in COMSOL.



(a) (b)

Figure 4.6: Permeability as a function of slip length, computed using a finite element method to solve (4.30) – (4.33), for the periodic structures constructed from repeated unit cells containing square, circular, cross, and diamond shaped inclusions. The marker shape corresponds to the appropriate geometry. The sizes of the circular, diamond, and cross-shaped inclusions are chosen to match the (a) area, and (b) minimum pore width, of the square-shaped inclusion for two test cases, $d_{sq} = 0.5$ and $d_{sq} = 0.7$.

Since the horizontal and vertical directions are identical and symmetric along the central axis for the four geometries we are considering, the permeability tensors are isometric, $\boldsymbol{K}(\lambda_s) = K(\lambda_s)\boldsymbol{I}$. In Figure 4.6a, we plot the scalar permeability, $K(\lambda_s)$, for the four geometries, keeping the area the same between the different geometries. There is reasonable agreement between the permeability of the circular inclusion and the square inclusion for both $d_{sq} = 0.5$ and $d_{sq} = 0.7$. We observe that for the $d_{sq} = 0.5$ case, there is a large discrepancy between the permeabilities of the cross-shaped, diamond-shaped, and square geometries, which suggests that knowing the area of the inclusion is not sufficient to estimate the permeability. In the $d_{sq} = 0.7$ case, the permeabilities of the diamond-shaped and cross-shaped geometries are an order of magnitude smaller than for the square-shaped geometry. This is a result of the fact that the diamond-shaped and cross-shaped inclusions touch the cell boundary, and a flow path ceases to exist, for $d_{sq} = 1/\sqrt{2} \approx 0.707$ and $d_{sq} = \sqrt{5/9} \approx 0.745$, respectively. Hence, $d_{sq} = 0.7$ is near the critical value at which the area can no longer be matched for the two geometries, and therefore the channels are extremely restricted for both of these geometries in this case. The area-matching method ignores critical aspects of the geometry, such as the shape of the region where the flow is most restricted, and is therefore susceptible to significant errors, as demonstrated by these examples.

As an alternative to matching the area, we match the minimum pore width (twice the shortest distance between the bottom of the unit cell and the inclusion) between the different geometries, since we expect that the permeability will depend significantly on the most constricted point along the flow path. In Figure 4.6b, we plot $K(\lambda_s)$ for the four geometries. We observe that there is poor agreement between all geometries for both $d_{sq} = 0.5$ and $d_{sq} = 0.7$, suggesting that the minimum pore width is a poor measure for estimating the permeability. This is due to the fact that the flow past the inclusion depends not only on the vertical width of the most constricted point, but also the horizontal distance that the constricted region spans. For example, since the lower edge of the square inclusion lies parallel to the edge of the unit cell, the fluid must pass through a long constricted region. Since the pressure gradient is fixed across the unit cell, the pressure decreases gradually across the thin region. Hence, the total flux through the unit cell, and therefore the macroscale permeability, is low. In contrast, the constricted region is much shorter for the diamond shaped inclusion. Therefore, the regions either side of the minimum pore width act as bulk regions of fluid at near-constant pressure. This results in a large pressure gradient across the constricted region, and consequently a much greater flux.

We conclude that neither of these measures is useful for predicting the permeability. In §4.3.2, we compute the flux of fluid for slip-flow through a thin, irregularly-shaped channel in order to estimate the flux through the unit cell. In §4.3.3, we discuss how to relate the flux through the cell to the permeability of the periodic structure in order to define a new geometrical measure for the permeability.

4.3.2 Slip flow through an irregular channel

In order to understand the relationship between the shape of the constricted region and the flux, we study low-Reynolds flow through a thin, irregular channel, as shown in Figure 4.7. We suppose that the channel has length L, and that the lower and upper walls of the channel are given by $f(x)$ and $g(x)$, respectively, and we set $R(x) = g(x) - f(x)$ to be the width of the channel at each point along its length. We model the flow through the channel using the incompressible Stokes equations (4.1) subject to the slip boundary conditions (4.2). The model is

$$\mu_o \nabla^2 \mathbf{u} = \nabla p, \qquad \nabla \cdot \mathbf{u} = 0, \tag{4.45}$$

$$\left.\begin{aligned} \mathbf{u}\cdot\mathbf{t} &= h^*\left(\mu^* - 1\right)\mathbf{n}\cdot\nabla(\mathbf{u}\cdot\mathbf{t}), \\ \mathbf{u}\cdot\mathbf{n} &= 0, \end{aligned}\right\} \quad \text{on } z = f(x),\ z = g(x), \tag{4.46}$$

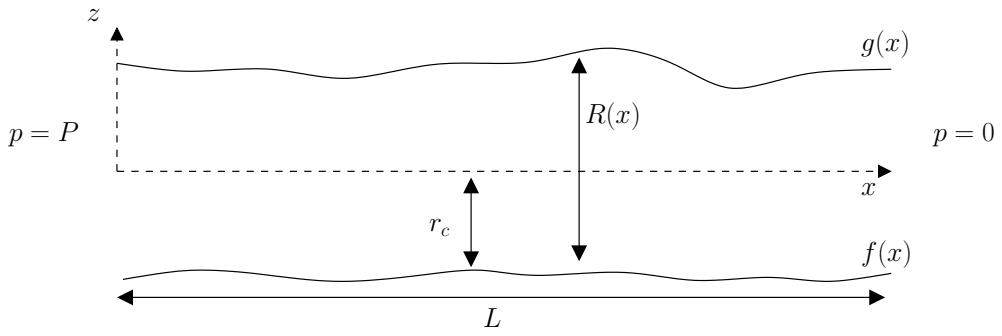


Figure 4.7: Schematic diagram of the channel with varying width.

where the inward-pointing normal and tangential vectors are given by

$$\mathbf{n} = \frac{1}{\sqrt{1+f_x^2}}\begin{pmatrix}-f_x\\1\end{pmatrix}, \qquad \mathbf{t} = \frac{1}{\sqrt{1+f_x^2}}\begin{pmatrix}1\\f_x\end{pmatrix}, \qquad \text{on } z = f(x), \tag{4.47}$$

$$\mathbf{n} = \frac{1}{\sqrt{1+g_x^2}}\begin{pmatrix}g_x\\-1\end{pmatrix}, \qquad \mathbf{t} = \frac{1}{\sqrt{1+g_x^2}}\begin{pmatrix}1\\g_x\end{pmatrix}, \qquad \text{on } z = g(x). \tag{4.48}$$

We use the subscript notation $f_x := \partial f/\partial x$ for clarity. We suppose that the flow is subject to a pressure difference, P, across the ends of the channel,

$$p(x=0) = \tilde{p} + P, \qquad p(x=L) = \tilde{p}, \tag{4.49}$$

where $\tilde{p}$ is an arbitrary reference pressure.

We write the velocity in terms of its horizontal and vertical components, $\mathbf{u} = (u, w)$, and non-dimensionalise the problem by setting

$$\begin{gathered} x = L\hat{x}, \qquad z = r_c\hat{z}, \qquad f = r_c\hat{f}, \qquad g = r_c\hat{g}, \qquad h = r_c\hat{h}, \\ u = U\hat{u}, \qquad w = \epsilon_c U\hat{w}, \qquad p = \tilde{p} + P\hat{p}, \end{gathered} \tag{4.50}$$

where $2r_c$ is the vertical length scale given by the minimum width of the channel, $U = r_c^2 P/\mu_o L$ is the typical horizontal velocity scale, and $\epsilon_c = r_c/L$ is the aspect ratio of the channel, which we assume is small.

Dropping the hat notation, and neglecting terms proportional to ϵ_c^2, the dimensionless system reads

$$u_{zz} = p_x, \qquad p_z = 0, \qquad u_x + w_z = 0, \tag{4.51}$$

subject to

$$u = \lambda_s u_z, \qquad w = uf_x, \qquad \text{on } z = f, \tag{4.52}$$

$$u = -\lambda_s u_z, \qquad w = ug_x, \qquad \text{on } z = g, \tag{4.53}$$

$$p = 1, \qquad x = 0, \tag{4.54}$$

$$p = 0, \qquad x = 1. \tag{4.55}$$

We integrate (4.51b) to find that $p = p(x)$. Integrating (4.51a) twice with respect to z and applying (4.52) and (4.53) yields

$$u = \frac{1}{2} p_x \left[z^2 - (f+g)z + fg + \lambda_s (f-g) \right]. \tag{4.56}$$

We integrate (4.51c) across the width of the channel and substitute (4.56) to find that

$$\begin{aligned} 0 &= \int_f^g u_x + w_z \, \mathrm{d}z && (4.57) \\ &= \frac{\partial}{\partial x} \left(\int_f^g u \, \mathrm{d}z \right) - g_x u|_{z=g} + f_x u|_{z=f} + \int_f^g w_z \, \mathrm{d}z && (4.58) \\ &= - \left(\frac{1}{2} p_x \left[\frac{1}{6} (g-f)^3 + \lambda_s (g-f)^2 \right] \right)_x - g_x u|_{z=g} + f_x u|_{z=f} + [w]_f^g . && (4.59) \end{aligned}$$

Applying (4.52) and (4.53) yields

$$\left(p_x \left[\frac{1}{6} R^3 + \lambda_s R^2 \right] \right)_x = 0. \tag{4.60}$$

Integrating (4.60) twice and applying (4.54) and (4.55) yields

$$p = Q \int_x^1 \frac{1}{\frac{1}{6} R^3 + \lambda_s R^2} \, \mathrm{d}x, \tag{4.61}$$

where

$$Q = \left[\int_0^1 \left(\frac{1}{6} R^3 + \lambda_s R^2 \right)^{-1} \mathrm{d}x \right]^{-1}, \tag{4.62}$$

is the total flux. Equation (4.62) is the two-dimensional equivalent of the equation for the flux through a three-dimensional channel with varying elliptic cross section given in Chapter 3. It is worth noting, however, that we assumed that the slip length was small in Chapter 3 in order to solve the flow equations in the elliptic geometry, but we made no such assumption in deriving (4.62). We observe that, like in the three-dimensional case, the flux (4.62) is given by the harmonic mean of the conductivites of each cross section along the length of the channel.

In §4.3.3 we show how the flux (4.62) may be used to estimate the permeability of a periodic porous structure constructed from a repeated unit cell containing a single inclusion, and, in §4.3.4, we compare the estimate for the square, circular, diamond, and cross-shaped geometries shown in Figure 4.5.

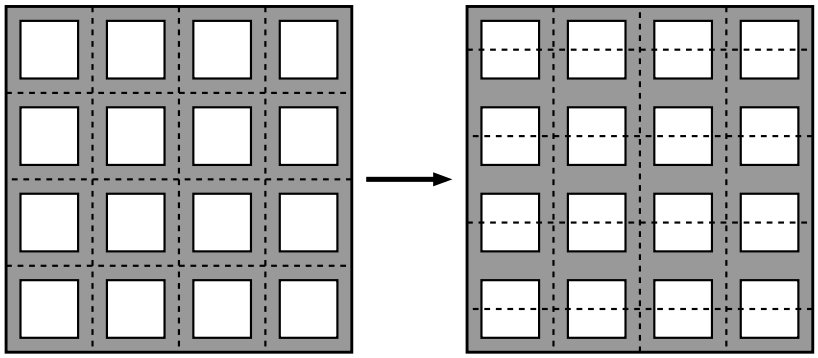


Figure 4.8: Redefining the boundaries of the unit cell such that the fluid domain forms a single path spanning the width of the cell.

4.3.3 Estimating the permeability using the flux

We use (4.62) to estimate the flux through the unit cell by redefining the boundaries of the unit cell to pass through the centre of the inclusion, as shown in Figure 4.8, and treating the fluid domain as a thin channel with varying cross section. It is worth noting that, in practice, the channel may not be thin along the full length. However, we observe from (4.62) that the regions in which the channel is widest (i.e. R is largest) contribute the least to the integral since these are the regions in which the integrand (which is proportional to R^{-3} for large R) is smallest. Hence, the flux is primarily determined by the thin regions along the length of the channel where the assumptions we have made in deriving (4.62) are applicable.

To relate the flux through the cell to the permeability of the periodic porous structure, we make use of the observation that the cell problem, (4.30) – (4.33), is equivalent to multiple sets of Stokes equations in the unit cell subject to a forcing term. Hence, computing K_{11} and K_{21} for a particular cell is equivalent to computing the components of the flow velocity through the cell when subjected to a pressure gradient in the horizontal direction. The first component of the permeability tensor, $\langle K_{11} \rangle$, is proportional to the flux in the horizontal direction, with the constant of proportionality is given by the pressure difference divided by the viscosity. We set this to be unity throughout this chapter since we are considering a dimensionless system. We therefore use (4.62) as our estimate for $\langle K_{11} \rangle$. Furthermore, since the geometries we are considering are symmetric[1], we find that $\boldsymbol{K} = K\boldsymbol{I}$ with $K = \langle K_{11} \rangle = \langle K_{22} \rangle$, and therefore we use (4.62) to estimate the scalar permeability, K.

[1]For non-symmetric unit cells, separate estimates for the flux in the horizontal and vertical directions need to be considered to determine $\langle K_{11} \rangle$ and $\langle K_{22} \rangle$. To determine the off-diagonal components of the permeability tensor, the flux in the direction perpendicular to the pressure gradient needs to be determined.

4.3.4 Comparison between the different geometries

Using the approach outlined in §4.3.1, we test this permeability estimate by scaling the size of the inclusions such that the fluxes, as computed by (4.62), match between the different geometries. For simplicity, we match the fluxes in the no-slip limit, given by (4.62) with λ_s set to zero. We define Q_{sq}, Q_{ci}, Q_{di} and Q_{cr} to be the fluxes through the square, circle, diamond, and cross-shaped geometries, respectively. It is straightforward to find explicit formulae for Q_{sq}, Q_{di} and Q_{cr},

$$Q_{sq} = \frac{(1-d_{sq})^3}{6d_{sq}}, \tag{4.63}$$

$$Q_{di} = \frac{(1-\sqrt{2}d_{di})^2}{6d_{di}(\sqrt{2}-d_{di})}, \tag{4.64}$$

$$Q_{cr} = \frac{1}{6d_{cr}}\left(\frac{2}{(1-d_{cr})^3} + \frac{1}{(1-3d_{cr})^3}\right)^{-1}, \tag{4.65}$$

where d_{sq}, d_{di} and d_{cr} are the lengths of the sides of the square, diamond, and cross, respectively. To compute the flux for the circular geometry, we rearrange the equation for the circle,

$$\frac{1}{4}(R-1)^2 + \left(x-\frac{1}{2}\right)^2 = d_{ci}^2, \tag{4.66}$$

where d_{ci} is the radius of the circle, to obtain the equation for the channel width,

$$R = 1 - 2d_{ci}\sqrt{1-\frac{\left(x-\frac{1}{2}\right)^2}{d_{ci}^2}}. \tag{4.67}$$

Since the main contribution to the expression for the flux comes from the region near $x = 1/2$ where the channel is thinnest, we expand (4.67) in powers of $(x-1/2)/d_{ci}$. Neglecting fourth-order terms and higher, this yields the parabolic approximation to the circle,

$$R \sim 1 - 2d_{ci} + \frac{\left(x-\frac{1}{2}\right)^2}{d_{ci}}. \tag{4.68}$$

Substituting (4.68) into (4.62) (with λ_s set to zero), and setting the integration limits to $\pm\infty$ (since this is the appropriate far-field limit for the parabolic approximation) yields

$$Q_{ci} = \frac{1}{6}\left(\int_{-\infty}^{\infty}\left[1 - 2d_{ci} + \frac{\left(x-\frac{1}{2}\right)^2}{d_{ci}}\right]^{-3}\,\mathrm{d}x\right)^{-1}. \tag{4.69}$$

We perform the change of variables, $x - 1/2 = d_{ci}^{1/2} u$, to obtain

$$Q_{ci} = \frac{1}{6d_{ci}^{1/2}} \left(\int_{-\infty}^{\infty} \left[1 - 2d_{ci} + u^2 \right]^{-3} \, \mathrm{d}u \right)^{-1} \tag{4.70}$$

$$= \frac{4(1 - 2d_{ci})^{5/2}}{9\pi d_{ci}^{1/2}}. \tag{4.71}$$

For a given square size, defined by d_{sq}, we use equations (4.63), (4.64), (4.65), and (4.71), to determine the values of d_{di}, d_{cr} and d_{ci} such that $Q_{sq} = Q_{di} = Q_{cr} = Q_{ci}$. Since the flux is equal to the permeability, as discussed in section 4.3.3, this gives us the size of the diamond, cross-shaped, and circular inclusions which should have the same permeability as the square geometry. In Figure 4.9, we plot the scalar permeabilities, K, of the different geometries against the slip length, computed numerically by solving (4.30) – (4.33) for K_{11} and evaluating $K = \langle K_{11} \rangle$. We consider the two cases given by $d_{sq} = 0.5$ and $d_{sq} = 0.7$. We see that there is excellent agreement between the different geometries in the $d_{sq} = 0.7$ case, demonstrating a significant improvement over the area and minimum pore radius matching methods. The $d_{sq} = 0.5$ case does not perform quite as well since the thin-channel approximation is not as applicable in this case as for $d_{sq} = 0.7$. However, there is still reasonable agreement, and, more importantly, this method does not appear to be susceptible to the systematic errors observed using the other methods, such as flow being blocked (as observed using the area matching method) or the square geometry consistently generating a lower permeability due to the sides being parallel to the cell boundary (as observed using the minimum pore width matching method).

In this section, we have used (4.62) to estimate the permeability of a periodic porous structure constructed from a repeated unit cell containing a single inclusion. However, this is not a realistic representation of a reservoir rock, since a representative sample typically contains many thousands of pores. In the next section, we investigate how to compute the flux through a unit cell containing multiple inclusions, and consequently compute the permeability of a periodic structure constructed from such a cell. We restrict ourselves to two dimensions for simplicity, however many aspects of the approach will be applicable to three dimensions.

4.4 Multiply-connected periodic domains

In the previous section, we developed a method for estimating the flux through a cell containing a single inclusion by treating the fluid region as a thin channel with varying

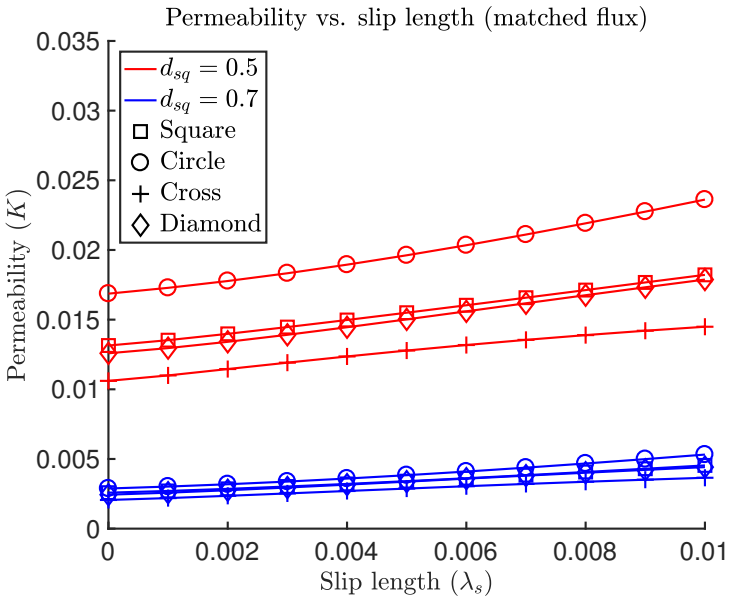


Figure 4.9: Permeability as a function of slip length, computed using a finite element method to solve (4.30) – (4.33), for the periodic structures constructed from repeated unit cells containing square, circular, cross, and diamond shaped inclusions. The marker shape corresponds to the appropriate geometry. The sizes of the circular, diamond, and cross-shaped inclusions are chosen such that $Q_{sq} = Q_{di} = Q_{cr} = Q_{ci}$, given by (4.63), (4.64), (4.65), and (4.71), respectively. Two test cases are displayed, $d_{sq} = 0.5$ and $d_{sq} = 0.7$.

width. We were able to do this by defining the edge of the unit cell to pass through the centre of the inclusion in order to ensure that the fluid domain comprises a single path connecting one side of the cell to the other. One of the issues which arises when trying to use a similar approach for a cell containing multiple inclusions is that there may be multiple fluid paths across any given cross-section, regardless of where we place the boundaries of the unit cell. To overcome this issue, we will now explore treating the fluid region in the multiply-connected domain as a network of channels. We will estimate the conductivity of each channel using (4.62), and compute the total flux through the network by solving a simple network flow problem, which we define in §4.4.3.

4.4.1 Determining the neighbouring inclusions from an image

Before we can compute the conductivities of the channels in a unit cell, we must first *find* each channel. Since we cannot assume that we always know the network structure *a priori*, we present an automated method to find the network structure from an image of a multiply-connected domain. We demonstrate the method on an example image which we have constructed, shown in Figure 4.10a. We assume that, initially, we know the locations of the boundaries of the inclusions in the cell, which have been highlighted in red. In our computations, we have used MATLAB's in-built boundary tracing tool. We determine the neighbouring inclusions by numerically computing the normal direction at each point along the boundaries, and incrementally expanding each boundary uniformly in the normal direction, as shown in Figure 4.10b. In our computations, we choose the size of the expansion increment to be equal to the pixel width in the image. Once a point along an expanded boundary reaches another inclusion, we register it as a neighbour and store the distance between the two inclusions (i.e. the distance the boundary has been expanded normal to the surface). We repeat this process until all of the points along the expanded boundaries have either reached another inclusion or the edge of the unit cell. From this we can construct an initial map of the neighbouring inclusions, shown in Figure 4.10c, in which we have shown the shortest distances between each neighbouring pair. We observe that this process yields many non-nearest neighbouring pairs, indicated with yellow lines, in the cases where two inclusions lie at opposite ends of a throat. We find the nearest neighbours, indicated with blue lines, by only keeping the shortest line every time two or more lines cross. In Figure 4.10d, we show the graph of the

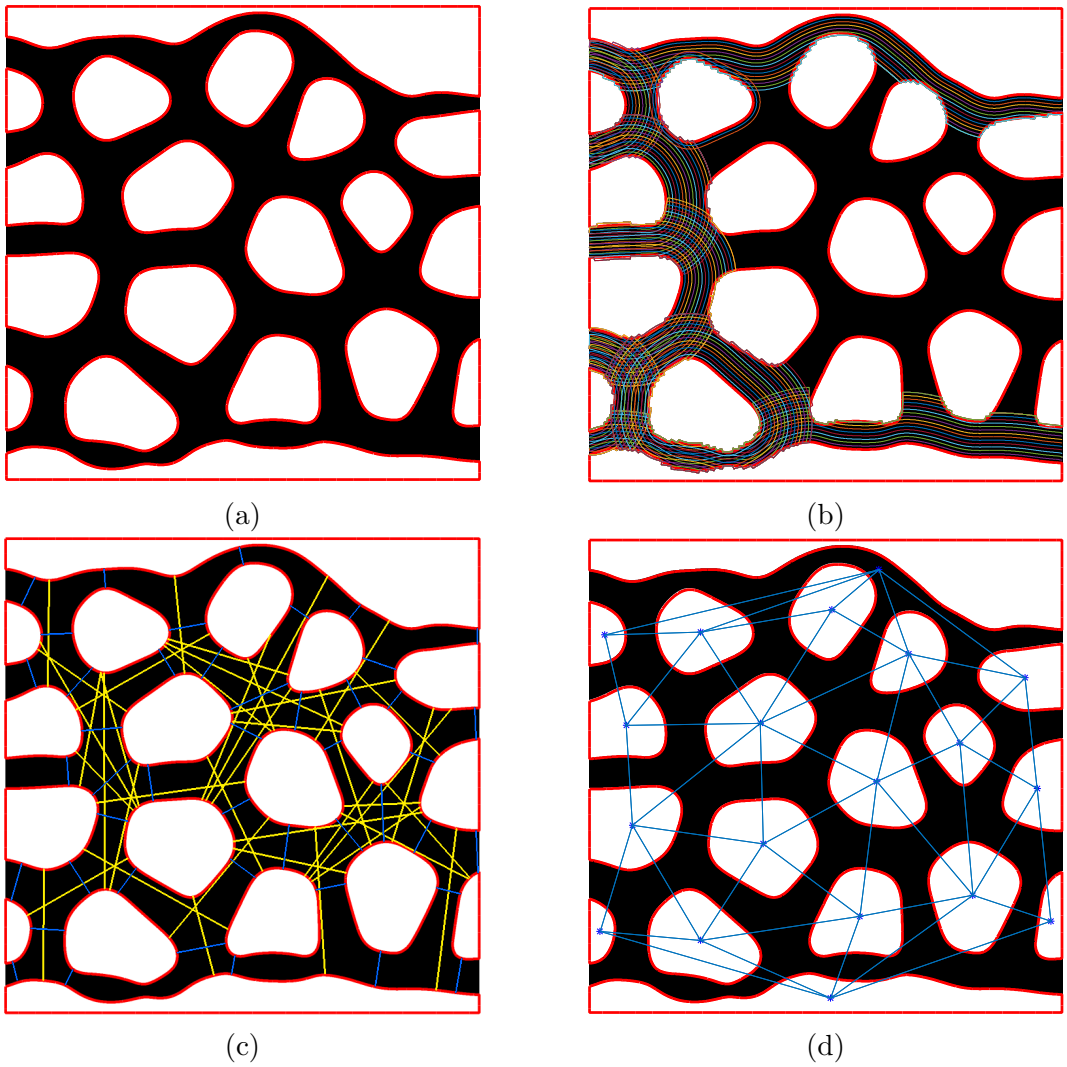


Figure 4.10: Figures showing the automated method to determine the neighbouring inclusions from an image of a multiply-connected domain: (a) the initial image, with the solid boundaries shown in red; (b) the boundary-expansion method to determine the neighbouring pairs; (c) the shortest path between each pair of boundaries with a clear fluid path between them. Nearest-neighbours are shown in blue, non-nearest neighbours are shown in yellow; (d) the network of nearest-neighbour inclusions.

nearest-neighbours, represented by lines between the centre of masses of the solid regions.

4.4.2 Extracting the channel network from an image

Having determined the neighbouring inclusion network, we wish to find the central axis of the channel between each neighbouring pair. We consider a neighbouring pair of inclusions with boundaries defined by $f(\mathbf{x}) = 0$ and $g(\mathbf{x}) = 0$, respectively. We

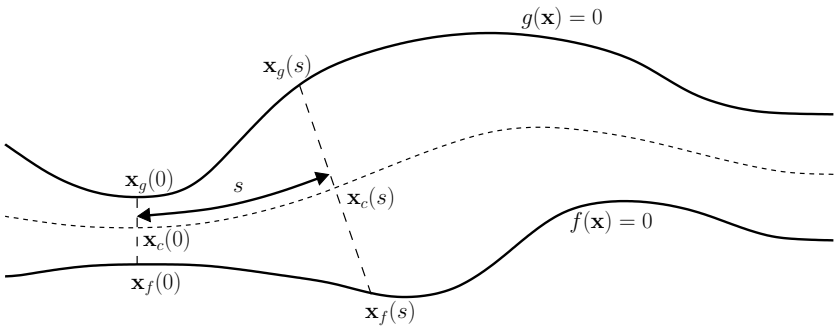


Figure 4.11: Schematic diagram of the channel between a neighbouring pair of inclusions.

define s to be arc length along the central axis between the inclusions, $\mathbf{x}_c(s)$, and we denote the points where the normal to the central axis intersects the two surfaces by $\mathbf{x}_f(s)$ and $\mathbf{x}_g(s)$, respectively. A schematic diagram of this setup is shown in Figure 4.11.

We determine $\mathbf{x}_c(s)$, $\mathbf{x}_f(s)$, and $\mathbf{x}_g(s)$ iteratively along the central axis, by choosing an appropriately small increment, $\mathrm{d}s$. Given $\mathbf{x}_c(s)$, $\mathbf{x}_f(s)$, and $\mathbf{x}_g(s)$, we define the direction of the central axis at $\mathbf{x}_c(s)$ to be the average of the tangents to the two surfaces at $\mathbf{x}_f(s)$, and $\mathbf{x}_g(s)$. Hence, the position of the central axis at $s + \mathrm{d}s$ is given by

$$\mathbf{x}_c(s+\mathrm{d}s) = \mathbf{x}_c(s) + \frac{\mathrm{d}s}{2}\left\{\left[\frac{1}{\sqrt{f_x^2+f_y^2}}\begin{pmatrix} f_y \\ -f_x\end{pmatrix}\right]_{\mathbf{x}_f(s)} + \left[\frac{1}{\sqrt{g_x^2+g_y^2}}\begin{pmatrix} g_y \\ -g_x\end{pmatrix}\right]_{\mathbf{x}_g(s)}\right\}. \quad (4.72)$$

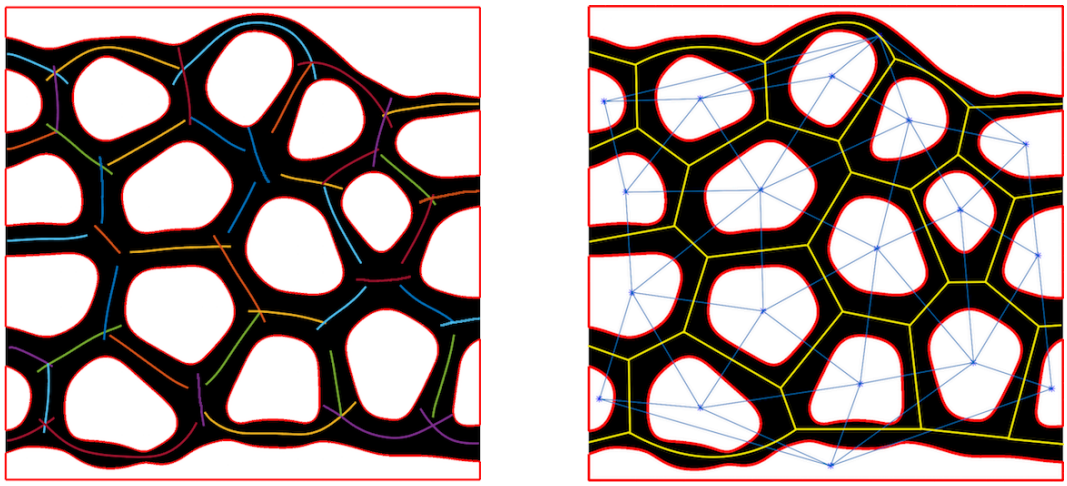
We define the direction of the normal to the central axis at $\mathbf{x}_c(s + \mathrm{d}s)$ to be the average of the normals to the surfaces at $\mathbf{x}_f(s)$ and $\mathbf{x}_g(s)$. Hence, the line in the direction normal to the central axis at $s + \mathrm{d}s$ is given by

$$\mathbf{x}_c(s+\mathrm{d}s) + t\left\{\left[\frac{1}{\sqrt{f_x^2+f_y^2}}\begin{pmatrix} f_x \\ f_y\end{pmatrix}\right]_{\mathbf{x}_f(s)} + \left[\frac{1}{\sqrt{g_x^2+g_y^2}}\begin{pmatrix} g_x \\ g_y\end{pmatrix}\right]_{\mathbf{x}_g(s)}\right\} = 0, \quad (4.73)$$

where $t \in (-\infty, \infty)$ parameterises the line. We define $\mathbf{x}_f(s + \mathrm{d}s)$, and $\mathbf{x}_g(s + \mathrm{d}s)$ to be the points where this line intersects $f(\mathbf{x}) = 0$ and $g(\mathbf{x}) = 0$, respectively.

We define $\mathbf{x}_c(0)$ to be the midpoint of the shortest line between the two surfaces. This line is found during the boundary-expansion process, and is normal to both surfaces[2]. The points $\mathbf{x}_f(0)$, and $\mathbf{x}_g(0)$ are given by the intersection between this line and $f(\mathbf{x}) = 0$ and $g(\mathbf{x}) = 0$, respectively.

[2]Exceptions may occur near the boundary of the unit cell.



(a) (b)

Figure 4.12: Figures showing the automated method to determine the channel network from an image of a multiply-connected domain, having previously determined the neighbouring inclusions network: (a) the central axis between each pair of neighbouring inclusions; (b) the structure of the channel network is shown in yellow, the neighbouring inclusions network is shown in blue.

We perform this iterative procedure for each pair of neighbouring inclusions. In Figure 4.12a, we show the central axis computed for each channel in the example image. During this process, we compute the conductivity of each channel using (4.62), replacing x with arc length, s, and computing the width of the channel in the direction normal to the central axis, that is, we define $R(s) = \|\mathbf{x}_f(s) - \mathbf{x}_g(s)\|$. It is worth pointing out that we assumed that the central axis was straight in order to derive (4.62), and therefore there will be some error due to the tortuosity of the channels in the image. This error could be reduced by solving a similar model in which the central axis is curved, however this is beyond the scope of this thesis.

Having computed the conductivity of each channel individually, we now determine the structure of the channel network. In Figure 4.12b, we show the graph of the neighbouring inclusions using blue lines, and we show the channel graph using yellow lines. Each node in the channel graph represents a pore space, and each edge corresponds to a channel. We see that the neighbouring inclusion graph is made up of a number of triangular 'faces', and that the channel graph can be constructed by treating the faces as nodes, and joining two nodes when the corresponding faces share an edge. Consequently, there is a one-to-one correspondence between edges in the inclusion graph and edges in the channel graph. The graph constructed in this manner from a planar graph embedded in two-dimensional space is known as the

dual graph. In general, the dual graph is not uniquely defined, as it is dependent on the particular embedding in the two-dimensional plane. However, by Whitney [116], the embedding, and therefore the dual graph, is unique up to reflection and choice of the external boundary in our case, since the inclusion graph is three-connected. Hence, it is possible to determine the channel network adjacency matrix, $\boldsymbol{G}$, from the adjacency matrix for the inclusions, $\boldsymbol{H}$, where $(\boldsymbol{H})_{ij} = 1$ if the i^{th} and j^{th} inclusions are nearest neighbours, and $(\boldsymbol{H})_{ij} = 0$ otherwise.

We initially set the dimensions of the square adjacency matrix $\boldsymbol{G}$ to be equal to the number of unique 3-cycles in $\boldsymbol{H}$, since each 3-cycle corresponds to a triangular face of the inclusion graph, i.e. a node of the channel network. If the i^{th} and j^{th} 3-cycles in $\boldsymbol{H}$ share an edge, then the i^{th} and j^{th} nodes are connected by the channel which corresponds to that edge. In this case, we set $(\boldsymbol{G})_{ij}$ to be equal to the conductivity of this channel. Otherwise, we set $(\boldsymbol{G})_{ij} = 0$. Each edge which has not been counted in two of the 3-cycles must correspond to a channel connected to the boundary. Hence, we add an additional row and column to $\boldsymbol{G}$ for each of these remaining edges, representing the inlet and outlet nodes, and set the non-zero entries of $\boldsymbol{G}$ as appropriate to indicate the conductivities of the channels connected to these nodes. This process yields the adjacency matrix for the pore spaces, weighted by the conductivities of the channels connecting the pores.

4.4.3 Flux through a network of channels

Having determined the network structure of the multiply-connected domain, and computed the conductivites of the channels connecting the pore spaces within the domain, we are now in a position to determine the flux through the cell. We number the pore spaces from 1 to n, as shown in Figure 4.13, and we define p_i to be the pressure at the i^{th} node. We assume that the flux from the i^{th} node to the j^{th} node, Q_{ij}, is given by the conductivity, $g_{ij} := (\boldsymbol{G})_{ij}$, multiplied by the pressure difference between the nodes. We also assume that the sum of the fluxes at each node is zero, representing conservation of flux. Hence, the equations governing the flow through the network read

$$Q_{ij} = g_{ij}(p_i - p_j), \qquad \sum_j Q_{ij} = 0. \tag{4.74}$$

We assume that pores 1 to a are connected to the inlet, and pores $n - b + 1$ to n are connected to the outlet. We suppose that the cell is subject to a unit pressure drop,

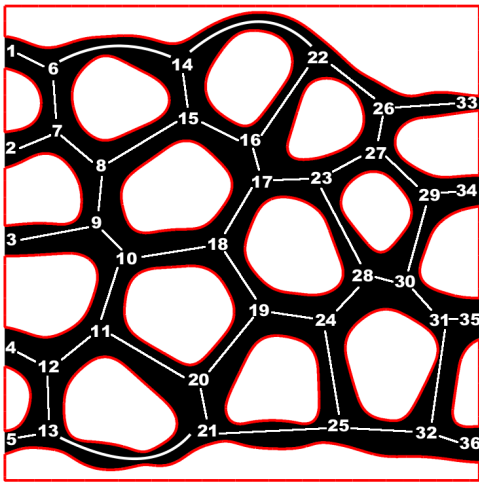


Figure 4.13: Numbering of the pore spaces within the example image.

so that

$$p_i = 1 \qquad 1 \leq i \leq a, \tag{4.75}$$

$$p_i = 0 \qquad n - b < i \leq n. \tag{4.76}$$

Substituting (4.74a) into (4.74b) yields the system of equations for p_i,

$$\sum_j g_{ij}(p_i - p_j) = 0, \qquad \text{for } a < i \leq n - b, \tag{4.77}$$

where we have neglected equations $1 \leq i \leq a$ and $n - b < i \leq n$, since the pressures at the inlet and outlet are known from (4.75) and (4.76). To simplify the notation, we write this system in matrix form,

$$\boldsymbol{L}\mathbf{p} = \mathbf{0}, \tag{4.78}$$

where

$$(\boldsymbol{L})_{i-a,j} = \delta_{i-a,j} \sum_k g_{i-a,k} - g_{i-a,j}, \qquad \text{for } a < i \leq n - b, \tag{4.79}$$

$$\mathbf{p} = (1, \cdots, 1, p_a, \cdots, p_{n-b}, 0, \cdots, 0)^T, \tag{4.80}$$

and δ_{ij} is the Kronecker delta function, $\delta_{ij} = 1$ if $i = j$, $\delta_{ij} = 0$ otherwise.

It is worth noting that $\boldsymbol{L}$ is a non-square $(n - a - b) \times n$ matrix, since we already know the pressure at the inlet and outlet nodes, and consequently we cannot simply invert (4.78) to find the pressure vector. Instead, we define

$$\boldsymbol{L} = (\underbrace{\boldsymbol{L}_1}_{a} \mid \underbrace{\boldsymbol{L}_2}_{n-a-b} \mid \underbrace{\boldsymbol{L}_3}_{b})\}_{n-a-b}, \qquad \mathbf{p}_M = (p_a, \cdots, p_{n-b})^T, \tag{4.81}$$

where the dimensions of the matrices $\boldsymbol{L}_1, \boldsymbol{L}_2$, and $\boldsymbol{L}_3$ have been shown, and we substitute (4.81) into (4.78), to find that

$$\mathbf{p}_M = -\boldsymbol{L}_2^{-1}\boldsymbol{L}_1 \left(1, \cdots, 1\right)^T. \tag{4.82}$$

Finally, in order to determine the total flux through the network, Q, we compute the sum of the fluxes passing through the channels connected to the inlet nodes, which reads

$$Q = \sum_{i=1}^{a} \sum_{j} Q_{ij} = \sum_{i=1}^{a} \sum_{j} g_{ij} \left(1 - p_j\right). \tag{4.83}$$

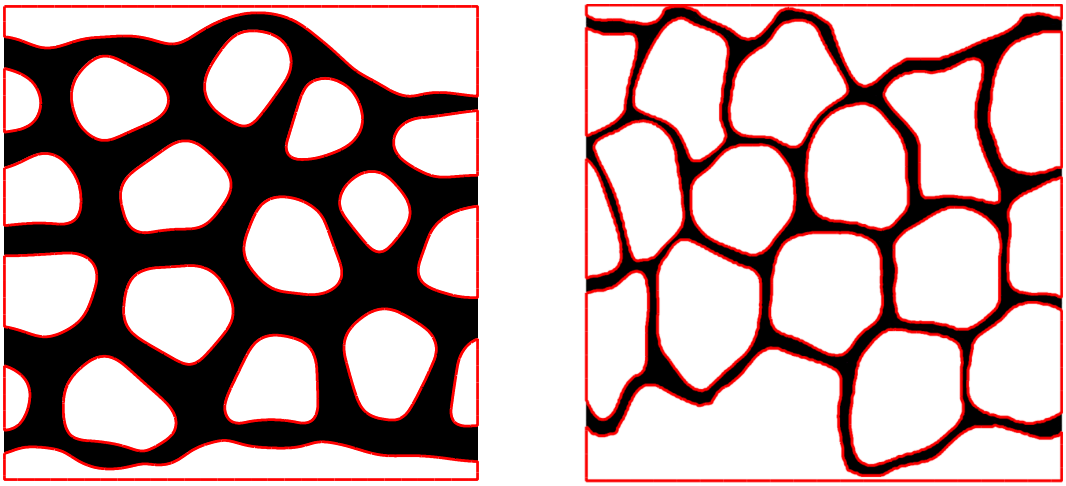
In practice, we check that our numerical scheme conserves mass by also computing the flux through the outlet nodes and checking that the two solutions are in agreement.

By the argument given in (4.3.3), we use (4.83) to estimate the scalar permeability of the network, K, since the first component of the permeability tensor, $\langle K_{11} \rangle$, is equal to the horizontal flux through the cell subject to a unit pressure difference in the horizontal direction. In our example, since there are no inlet or outlet nodes in the vertical direction, the permeability is defined only in the horizontal direction. However, for a general network, the additional components of the permeability tensor can be determined by computing the flux through the network in the both the horizontal and vertical directions for the two cases in which the network is subjected to a unit pressure difference horizontally and vertically.

4.4.4 Comparison between the network model and the finite element solution

We test the accuracy of the network model by considering two example unit cell problems, shown in Figure 4.14. Example A, shown in Figure 4.14a, consists of a network of reasonably straight, wide channels. Example B, shown in Figure 4.14b, consists of a network of thin channels with curved central axes. For both examples, we have chosen not to include any outlets along the top or bottom boundaries of the cell. This avoids us having to impose periodicity in the vertical direction, which requires the fluid outlets at the top and bottom to match. This will rarely be the case naturally, but can be imposed by reflecting the image vertically. However, this doubles the size of the network, so we have chosen to avoid this complication and focus on the horizontal component of the permeability.

In Figure 4.15 we show the magnitude of the flux and pressure distribution for example A, computed by solving (4.41) – (4.44) using a finite element method on the geometry depicted in Figure 4.14a. We see that the flux through each channel is close



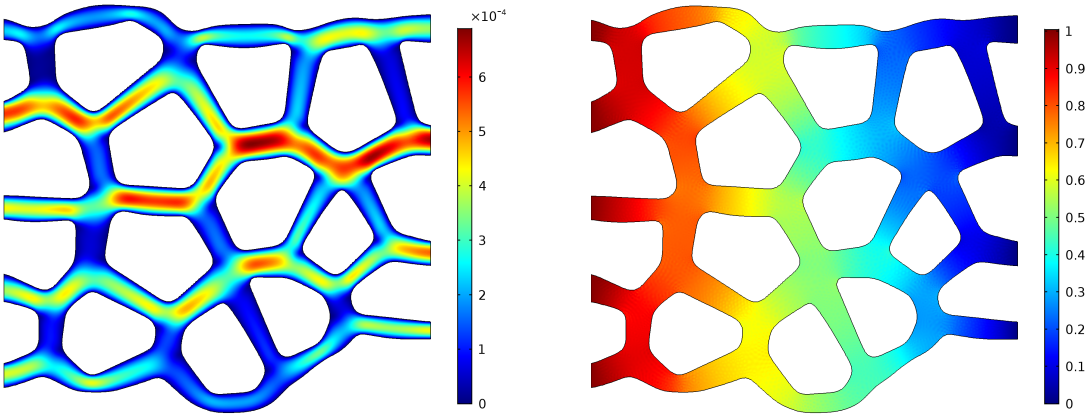
(a) Example A (b) Example B

Figure 4.14: Test images for the network model. Image (a) consists of a network with reasonably straight, wide channels. Image (b) consists of a network of thin channels with curved central axis.

to uniform along the length of the channel, due to the fact the channels are nearly straight. However, since the channels are wide, the pore spaces are of a similar size to the channels, resulting in a non-uniform pressure distribution within the pores. This will likely cause some issues when trying to estimate the flux using our network model, since we assumed that the pressure at each node could be represented by a single value.

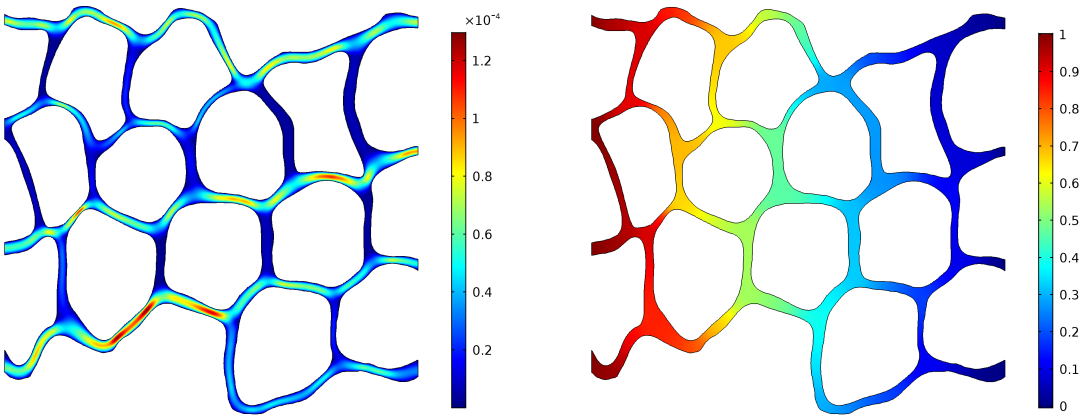
In Figure 4.16, we show the magnitude of the flux and pressure distribution for example B, computed by solving (4.41) – (4.44) using a finite element method on the geometry depicted in Figure 4.14b. Since the channels are much thinner, we see that, in contrast to the first example, the pressure is uniform within the pore spaces. Hence, the network model for the pressures appears to be more applicable in this case. However, we still expect some error due to the curved nature of the channels.

In Figure 4.17, we plot the permeability, K, for the two examples against the slip length. We compare the numerical solutions, found by solving (4.41) – (4.44) using a finite element method, which we take to be our 'true' solutions, with our network model estimate, (4.83). For example A, shown in Figure 4.17a, the network model overestimates the permeability by 18% for $\lambda_s = 0$. This is likely due to the fact that the pore spaces are of a comparable size to the channels, and therefore modelling the pressure within the pore using a single value is not appropriate. The relative flux increase due to slip is 90% for the finite element solution, and 103% for the network model, and therefore there is reasonable agreement between the two



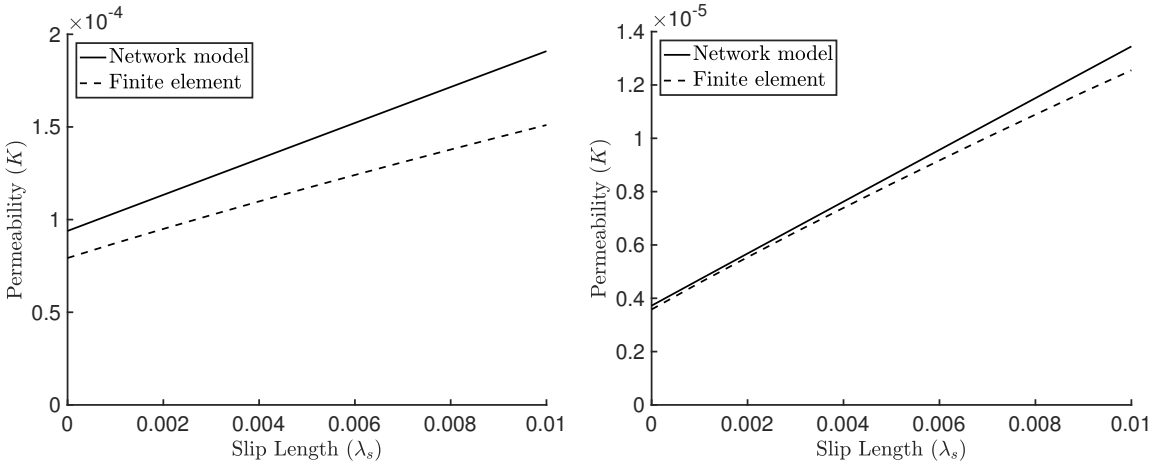
(a) (b)

Figure 4.15: Plots of (a) the magnitude of the flux, and (b) the pressure distribution, through the fluid domain extracted from example A, found by solving (4.41) – (4.44) using a finite element method.



(a) (b)

Figure 4.16: Plots of (a) the magnitude of the flux, and (b) the pressure distribution, through the fluid domain extracted from example B, found by solving (4.41) – (4.44) using a finite element method.



(a) Example A

(b) Example B

Figure 4.17: Plots of the permeability as a function of the slip length, comparing the network model with the finite element solution.

solutions. Hence, whilst the network model may slightly overestimate the total flux, it captures the effect of the salinity on the permeability with reasonable accuracy. For example B, shown in Figure 4.17b, the network model overestimates the permeability by 4% for $\lambda_s = 0$. The relative flux increase due to slip is 251% for the finite element solution, and 261% for the network model. There is excellent agreement between the network solution and the finite element solution, for both the total flux and the relative flux increase, despite the central axes of the channels being curved.

The two examples studied in this section suggest that the network model is best-suited to pore networks consisting of thin channels connecting small pore spaces. The error introduced by neglecting tortuosity in the channel model appears to be small in comparison to the error introduced by assuming that the pore spaces can be represented by single points. However, the effect of slip (i.e. the salinity) is captured with reasonable accuracy for both cases. Hence, if a network model of a pore sample is calibrated by computing the permeability in the high salinity regime ($\lambda_s \approx 0$), it may be possible to estimate the effect of a reduction in the salinity even if the network model itself is slightly inaccurate.

4.5 Conclusions

In this chapter, we studied single-phase slip flow through a periodic porous structure constructed from a repeated unit cell. In §4.2, we used the method of multiple scales to derive a cell problem for the permeability. We found that the cell problem is

equivalent to multiple sets of Stokes equations on the unit cell subject to a forcing term. In §4.2.4, we used a finite element method to solve the cell problem (4.41) – (4.44) for a unit cell containing a circular inclusion. We found that the permeability increases as the slip length increases.

In §4.3, we studied the flow through periodic porous structures constructed from unit cells containing a single inclusion. In order to avoid having to numerically solve the computationally-expensive cell problem, we looked for an easily computed geometrical quantity which would provide us with a reasonable estimate for the permeability. As a first step, in §4.3.1 we tested the viability of the area of the inclusion and the minimum pore width as predictors for the permeability, since these are the two-dimensional equivalents of the volume matching and minimum radius methods presented in Chapter 3. Since these quantities do not intrinsically provide us with an estimate for the permeability, we tested the viability of each predictor by checking that the permeability of the periodic structure constructed from the unit cell is independent of the shape of the inclusion, provided that the geometrical quantity being considered is held constant. We found that the area is a poor predictor of the permeability, and that the area-matching method is extremely limited since it ignores critical aspects of the geometry, such as the shape of the region where the flow is most restricted. We found that the minimum pore width is also a poor predictor of the permeability, since it does not take into consideration the length of the restricted region.

In order to find an appropriate estimate for the permeability, we redefined the boundaries of the periodic unit cell in such a way that the fluid domain comprises a single channel spanning the width of the cell. In §4.3.2, we derived an expression for the flux through a thin, irregularly-shaped channel (4.62), which is given by the harmonic mean of the conductivites of each cross section along the length of the channel. In §4.3.3, we showed how to relate the flux through the cell to the permeability, in order to use (4.62) as our new estimate for the permeability. In §4.3.4, we used this measure to match the permeabilities of different-shaped inclusions. We found that this measure gives an improvement over the area and minimum pore width measures, with excellent agreement for unit cells containing large inclusions, i.e. thin flow paths.

In §4.4, we studied the flow through periodic porous structures constructed from unit cells containing multiple inclusions. To efficiently estimate the permeability, we modelled the multiply-connected unit cell as a network of channels, with the conductivity of each channel given by the expression for the flux (4.62) derived in §4.3.2. In order to be able to use this approach, we presented an algorithm for

extracting the appropriate channel network from an image of a multiply-connected fluid domain. In §4.4.1 and §4.4.2, we determined the graph of the neighbouring inclusions network, $\boldsymbol{H}$, using a boundary-expansion method similar to the medial axis method proposed by Lindquist *et al.* [68]. We observed that the channel network can be constructed by connecting the faces of the neighbouring inclusions network, and consequently we constructed the conductivity-weighted channel adjacency matrix, $\boldsymbol{G}$, by computing the dual graph of $\boldsymbol{H}$. In §4.4.3, we presented a simple model for the flow through the network, which we solved to find the pressure at each node (4.82). We used (4.82) to determine the flux through the network, (4.83), which, in turn, we used to estimate the permeability. We restricted our attention to two-dimensional domains for simplicity, however the work presented may be easily extended to higher dimensions by extracting the network using existing methods [68, 94], and estimating the conductivity through the three-dimensional pore using the approach presented in Chapter 3.

In §4.4.4, we compared the numerical solution for the permeability, found by solving (4.41) – (4.44) using a finite element method, with the estimation for the permeability found using the network model for two example domains. The first example consists of a network of straight, wide channels, and there is reasonable agreement between the two solutions. However, there is some error due to the non-uniform pressure across the large pore spaces, which is not captured by the network model. The second example consists of a network of thin, curved channels. There is excellent agreement between the two solutions, since the thin-channel model for the conductivity is appropriate in this case, and the pressure is approximately uniform in the pore spaces. There is some error due to the curved central axes of the channels, which is not modelled in the derivation of (4.62), however this seems to have little impact on the solution.

In summary, we have shown that the slip-dependent permeability of a periodic porous structure can be estimated with reasonable accuracy using a network model for single-phase flow. We have presented an algorithm for extracting the appropriate network from an image of the pores, as well as a geometrical expression which can be used to estimate the conductivity of each channel. This method is significantly more computationally efficient than solving the full cell problem. In Chapter 5, we will develop this approach further by presenting a network model for two-phase flow, in which the oil phase is subject to a slip boundary condition. In Chapter 6, we will use the homogenisation techniques introduced in this chapter to derive a simple, macroscopic continuum model for the network model presented in Chapter 5.

Chapter 5

Network models of two-phase flow

5.1 Introduction

In Chapter 4, we used a network model to study two-phase flow through a multiply-connected domain, in which the wetting phase acts as a thin slip layer on the solid surface. Since we assumed that the thickness of the wetting layer was small in comparison to the pore width, we were able to use a single-phase flow model with an effective slip boundary condition in place of the wetting phase. We found that the network model accurately estimated the permeability of the pore structure.

We wish to utilise the efficiency of the network modelling approach to study two-phase flow through a pore structure, in which both phases occupy the bulk regions of the pore spaces. However, there are a number of issues which arise when modelling two-phase flow which need to be addressed. First, we must present a mechanism for determining the position of each phase within the pores and throats, since, unlike in the single-phase model, this is unknown *a priori*. We must also specify an appropriate function for the local capillary pressure within the pores and throats, which may depend on the geometry of the pore/throat, as well as the volume fraction of each phase [46, 93]. We must specify the equations governing the microscale fluid dynamics, ensuring that mass is conserved [24], and, finally, we must ensure that our solution procedure is computationally efficient since two-phase flow is significantly more complex than single-phase flow.

There are numerous modelling approaches used to study two-phase flow through a network, which can typically be separated into three classes; quasi-static, semi-dynamic, and dynamic models. Dynamic models can be further split into the classes of 'Washburn equation' and 'annular flow' models. In §5.1.1 – §5.1.5, we will discuss each of these approaches and review the appropriate literature.

In §5.2, we will present our network model for two phase flow. We will assume that both phases occupy the throats and pores simultaneously, and we will suppose that each phase forms a number of slugs within the throats. Rather than keep track of the numerous interfaces separating the phases within the throats [52], we will determine the saturation of each phase, and determine the effective conductivity of the throat as a function of the saturation. We will define the phase-weighted pressure throughout the network, and formulate our model in terms of the phase-weighted pressure and saturation using conservation of mass for each fluid. Formulating our model in this way will enable us to solve a single set of pressure equations, reducing the computational effort required. We will include the advection of ions in our model in order to study the effect of the salinity on the flow.

In §5.3, we will non-dimensionalise our model and present the system of equations in vector format. We will describe a numerical scheme to solve the system subject to appropriate initial and boundary conditions. In §5.4 we will solve our model numerically to simulate a waterflood. We will separate the waterflooding process into two stages. First, we will model a 'drainage' stage, in which oil invades an initially water-filled network through the action of capillary forces. Second, we will model a 'waterflood' stage, in which water is injected into the oil-filled network, and the oil recovered is measured. We will compare the results for a high-salinity and low-salinity waterflood on a 30×30 lattice. We will also simulate a tertiary low-salinity waterflood, in which the network is initially flooded with high salinity brine before a low-salinity injection is performed. Finally, in §5.5, we will discuss our findings.

Before presenting our network model, we briefly review alternative methods which have been presented in the literature.

5.1.1 Quasi-static network models

Numerous authors model two-phase flow through a network using a quasi-static approach [36, 37, 47, 106], in which the pressure in each phase is assumed to be constant, and the invading fluid advances through the pores discretely, one pore at a time. To model drainage, in which oil invades a water-filled porous structure by the action of capillary forces, the network is initially assumed to be saturated with water held at constant zero pressure. Oil is connected to the inlet nodes of the network, and the pressure in the oil phase is also assumed to be zero initially. The pressure in the oil phase is increased until the capillary pressure is large enough for the oil to enter one of the throats connected to the water phase. This pressure is known as the 'entry pressure' of that particular throat, which depends on the geometry of the

throat. Once the capillary pressure exceeds the entry pressure of a particular throat, oil invades the connected pore. Since the fluids are assumed to be incompressible, oil cannot invade a water-filled pore which has become disconnected from the network outlet. The process is repeated until the oil phase spans the network, at which point properties such as the relative permeability of each phase (the permeability of the network with respect to each phase as a function of the total water saturation), may be computed.

To model imbibition, in which water is injected into the network to displace the oil, the initial state of the network is assumed to be the final state of the network given by the drainage model described above. Most of the pores in this initial state are filled with oil, and the constant pressure in the oil phase is greater than the constant pressure in the water phase (which is equal to zero). Water is connected to the inlet nodes of the network, and the pressure in the water phase is increased until the capillary pressure is lower than the entry pressure a throat connecting the oil to the water. Water then invades the throat and partially fills the connected pore until the capillary pressure in the pore is equal to the prescribed pressure difference between the two phases. The capillary pressure in the pore is evaluated using a local capillary-pressure-saturation function which depends on the geometry of the pore.

A global capillary-pressure-saturation function can be determined by computing the total volume fraction of each phase in the network as a function of the prescribed pressure difference, which may be different for the drainage and imbibiton processes. Held & Celia [36] use a quasi-static model to determine the relationship between the global capillary pressure, saturation, and interfacial area in a pore network. They demonstrate that the hysteresis between the capillary pressure and the saturation during drainage and imbibition can be essentially eliminated by supposing that the capillary pressure depends on the interfacial area, in contrast to more typical models in which it only depends on the saturation. Helland & Skjaeveland [37] study a similar problem for a network constructed from triangular tubes, and demonstrate that hysteresis is observed when contact angle hysteresis is assumed. Joekar-Niasar *et al.* [47] also investigate the relationship between capillary pressure, saturation, and interfacial area, considering both a throat-only model, and a model which includes both pores and throats. They find that the throat-only model cannot reproduce hysteresis, and they show that the interfacial-area-saturation relationship largely depends on the trapping assumptions made. Valvatne & Blunt [106] generate a network representation of a Berea sandstone, and use a quasi-static model to determine single and multi-phase properties of the network for water-wet, oil-wet, and mixed-wet

conditions. They find that their model is able to successfully predict the oil recovery and relative permeability curves for the Berea sample by comparing their results with experimental data.

5.1.2 Semi-dynamic network models

An alternative approach, which retains many features of the quasi-static method, is to model the two-phase flow through the network semi-dynamically [41, 42, 77, 126]. Semi-dynamic models are similar to quasi-static models in the sense that the displacement of the defending phase occurs discretely, a single pore/throat at a time. However, in a semi-dynamic model, the pressure field, and therefore the fluid flow, is computed at each time step, and the next pore in the network that would fill is determined by calculating the flux of the invading phase into each pore. The capillary pressure across the fluid-fluid interface is taken into consideration by assuming that there is a pressure difference at the throat-pore boundaries where the two phases meet. Semi-dynamic models retain much of the computational efficiency of quasi-static models since interfaces are not tracked, and pore filling occurs instantaneously.

Hughes & Blunt [41] study imbibition on a square lattice of pores using a semi-dynamic network model. They assume that a small amount of water is present in the pores and throats, and solve a set of pressure equations for each phase. They compute the relative permeability curves of the two phases, as well as the residual oil saturation after a steady-state is reached, in two and three dimensions, and identify five different flow regimes. Yiotis *et al.* [126] use a semi-dynamic drainage model to study evaporation within a water-saturated porous medium. They model evaporation by including phase changes in the pressure equations, and they suppose that the water-air interface advances quasi-statically. Nguyen *et al.* [77] study imbibition semi-dynamically, assuming that the water phase fills the pores behind the displacement front and is contained in corner films in the pores and throats filled with oil. They include the effects of film swelling and snap-off, in which a pore ahead of the displacement front may still be filled due to a combination film swelling and rupture of the oil-water interface, in their model. In contrast to traditional snap-off models, in which the criterion for snap-off is given by the contact angle alone, they include displacement rate as an additional component of the mechanism. They use their model to predict relative permeability curves for a water-wet Berea sandstone, and find good agreement with experimental data. Idowu & Blunt [42] study a semi-dynamic network model, solving for the pressure in each phase separately. They allow wetting-layer swelling near an advancing flood front, and include a mechanism for partial-filling of

pores depending on whether the filling mechanism is due to the advancement of the displacement front or snap-off.

5.1.3 Dynamic network models

A more accurate, but computationally demanding, approach is to model the network dynamically using a system of time-dependent equations for the pressure and fluid flow. Dynamic models allow partial filling of the pores or throats, and therefore require a process for tracking the saturation of each phase within the network. Some dynamic models attempt to track the interface between the fluids within the throats [3, 24, 52, 53], whereas others assume that each phase is present throughout the network and require the pressure to be calculated in each phase at each node [46, 93, 103]. We will briefly review these two approaches and discuss their relative advantages and disadvantages.

5.1.4 Washburn equation

One approach to dynamic network modelling used by numerous authors [3, 24, 52, 53] is to suppose that each phase spans the width of the pores and throats, and to track the interface separating the two phases, as shown in Figure 5.1. Once an interface reaches the pore at a throat outlet, the pore is partially filled with the invading phase according to a local capillary-pressure-saturation relationship. Once the saturation in the pore reaches a certain threshold value, new interfaces are formed at each of the throats connected to that pore. The rate at which the interface advances through the throat connecting pores i and j is determined from the flux through the throat, Q_{ij}. The model is governed by Washburn's equation [112] and conservation of flux, which read

$$Q_{ij} = \frac{g_{ij}}{\mu^{\text{eff}} L_{ij}} \left(p_i - p_j + P^c_{ij} \right), \qquad \sum_j Q_{ij} = 0, \tag{5.1}$$

respectively, where L_{ij} is the length of the throat connecting pores i and j, p_i is the pressure in pore i, and P^c_{ij} is the capillary pressure across the oil-water interface in the throat connecting pores i and j. The capillary pressure is zero if the throat contains a single phase (since there is no interface in this case), and can be positive or negative depending on the direction of flow of the invading fluid when two phases are present. We assume that g_{ij} is zero if there is no throat connecting pores i and j, and that otherwise g_{ij} is the conductance of the throat connecting the two pores, which depends on the geometry of the throat and is typically given by Poiseuille's law [74]. The effective viscosity, μ^{eff}, is given by the weighted average of the viscosity of

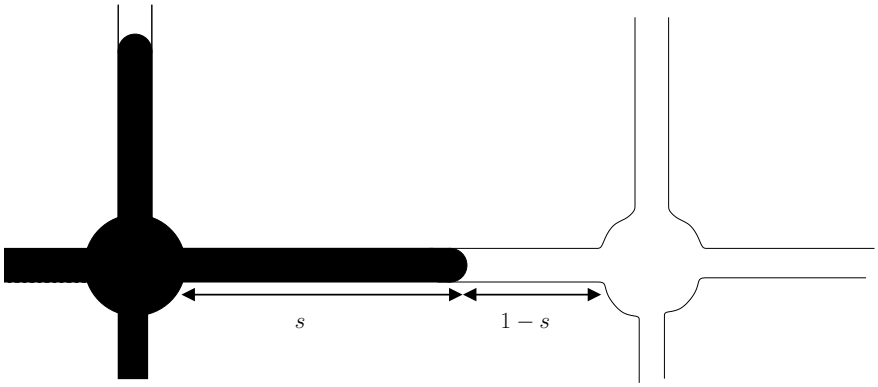


Figure 5.1: Schematic diagram of the Washburn equation network model.

the two phases, $\mu^{\text{eff}} = s\mu_o + (1-s)\mu_w$, where s is the proportion of the throat filled with the oil phase, as shown in Figure 5.1.

Only a single set of pressure equations is required in order to solve the Washburn equation model due to the fact that only a single phase occupies each pore at any given time. Since solving the pressure field equation is often the most computationally expensive part of dynamic network modelling, this approach retains some of the computational efficiency of the semi-dynamic models.

However, different issues can arise depending on how the interface tracking process is implemented. If an interface is formed at the entrance to a throat which already contains an interface somewhere along its length, one of two approaches must be taken:

- The interface is prevented from advancing (so that only a single interface may advance in a throat at a given time). This approach may cause unphysical blocking within the throat since the movement of fluid is artificially restricted.

- The interface is allowed to advance (so that multiple interfaces may advance in a single throat, i.e. slugs of fluid). This approach may be cumbersome to implement, and keeping track of multiple interfaces may cause computational issues if the number of interfaces within each throat isn't limited.

Koplik & Lasseter [53] use the Washburn equation to model two-phase flow in a network, and show that the problem is equivalent to current flow in an electrical resistor network. Dahle & Celia [24] also model two-phase flow using an interface-tracking model. They restrict their model by only allowing a single interface in a throat at a time, and define a set of displacement rules at the nodes for when an interface reaches a throat entrance. They find that, in order to maintain a global

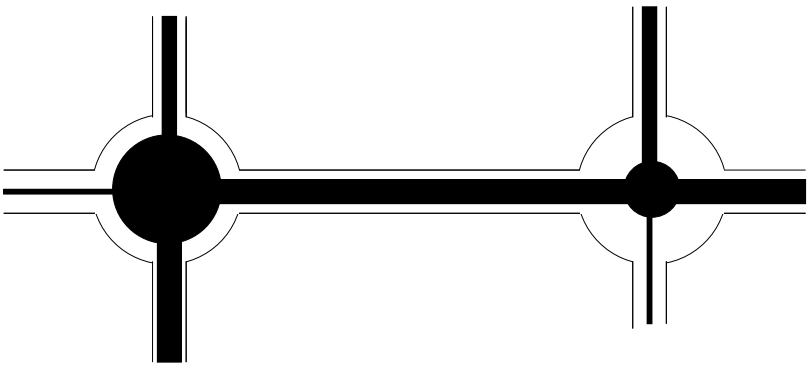


Figure 5.2: Schematic diagram of the annular flow network model.

mass balance, they require a correction step in their algorithm. Knudsen *et al.* [52] present a two-phase dynamic network model in which the two phases form bubbles which can separate and merge together. They assume that the network is periodic, so that the volume of each fluid is conserved, in order to compute fractional flow properties of the system. Al-Gharbi & Blunt [3] develop a dynamic interface-tracking model in which the pores and throats have triangular cross section. They track the interfaces using the effective hydraulic resistance of the throats, and include a mechanism for snap-off in their model.

5.1.5 Annular flow

An alternative approach to the Washburn equation model is to assume that both phases are present throughout the network [46, 93, 103]. Typically, this is done by assuming an 'annular flow' model, in which the non-wetting phase moves through the centre of the pores and throats, and the wetting phase is restricted to the annular region between the non-wetting phase and the pore/throat walls. For oil/water systems it is generally assumed that water is the wetting phase. A schematic diagram of this model is shown in Figure 5.2.

Since both phases are present throughout the network, a separate set of equations exists for the pressure field in each phase. This is in contrast to the Washburn equation model, in which we only needed to solve a single set of equations. This results in the annular flow model being more computationally demanding, since solving for the pressure field is usually the most computationally expensive part of the process.

The model is governed by Poiseuille's law and conservation of mass for each phase,

which read

$$Q_{ij}^o = \frac{g_{ij}^o}{\mu^o}\left(p_j^o - p_i^o\right), \qquad V_i \frac{\mathrm{d}S_i^o}{\mathrm{d}t} = -\sum_j Q_{ij}^o, \tag{5.2}$$

$$Q_{ij}^w = \frac{g_{ij}^w}{\mu^w}\left(p_j^w - p_i^w\right), \qquad V_i \frac{\mathrm{d}S_i^w}{\mathrm{d}t} = -\sum_j Q_{ij}^w, \tag{5.3}$$

where Q_{ij}^o and Q_{ij}^w are the fluxes of the oil and water, respectively, through the throat connecting pores i and j, g_{ij}^o and g_{ij}^w are the relative throat conductances for the oil and water phases, respectively, for the throat connecting pores i and j, p_i^o and p_i^j are the pressures in the oil and water, respectively, in pore i, μ^o and μ^w are the viscosities of the oil and water, respectively, S_i^o and S_i^w are the saturations of the oil and water, respectively, in pore i, and V_i is the volume of pore i.

We impose the constitutive laws that the pressure difference between the two phases in pore i is given by the capillary pressure, P_i^c, which is a prescribed function of the water saturation in the pore, and that the sum of the saturations equals unity to ensure that the entire volume within the pore is filled with fluid, which read

$$p_i^o = p_i^w + P_i^c(S_i^w), \qquad S_i^o + S_i^w = 1. \tag{5.4}$$

In order to implement this model, a constitutive law for the relative throat conductance for each phase, g_{ij}^o and g_{ij}^w, must be given. A common approach is to assume that $g_{ij}^o = \left(S_{ij}^o\right)^2 g_{ij}$, and $g_{ij}^w = \left(S_{ij}^w\right)^2 g_{ij}/\beta$, where S_{ij}^o and S_{ij}^w are the saturations of the oil and water phases, respectively, in the throat connecting pores i and j, which are usually taken to be the same as the saturations in the upstream pore, g_{ij} is the conductance of the throat in the case when only a single phase is present, and β is a function of the shape of throat.

The main advantage of this model is that there are no interfaces to track, since each phase is present throughout the network. However, this model is more computationally demanding than the Washburn equation model, and the shape parameter, β, is difficult to determine for real materials. Furthermore, this approach is of limited use to us since the annular model assumes a thick water region separating the oil from the throat surface, with thickness determined by the saturation, and the low salinity model we have developed in Chapter 2 has the oil separated from the rock surface by a thin film of water, with thickness determined by the salinity.

Thompson [103] presents a two-phase annular flow model for a network constructed from throats with square cross-section. He solves the pressure equations separately in each phase and, by assuming that each phase is present throughout

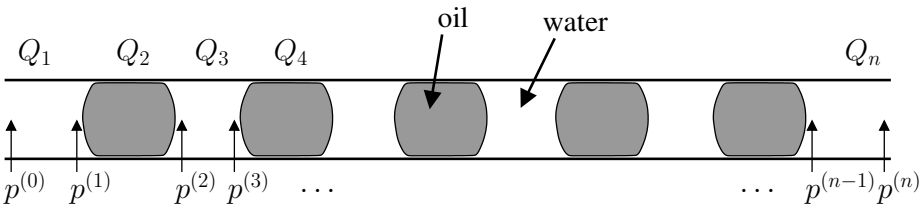


Figure 5.3: Schematic diagram showing the model of the pore throat, with multiple slugs along its length. The flux of each section is given by Q_i, and the pressure in the water phase at each interface is given by $p^{(i)}$.

the network, reduces the need for rule-based decision making as is often required in interface-tracking methods. Joekar-Niasar *et al.* [46] compute the local capillary-pressure-saturation relationship within a cubic pore body, which they use in their model to determine the macroscopic capillary-pressure-saturation relationship. Sheng & Thompson [93] present a unified dynamic network model which they use to study drainage and imbibition for both periodic and non-periodic networks. Their method permits the injection of both fluids simultaneously at the inlet. This enables them to study fractional flow through a non-periodic network, which they use to simulate steady-state relative permeability tests.

5.2 Model formulation

We propose a network model for two phase flow which combines aspects of both the Washburn equation and annular flow models. We suppose that both phases occupy the pores and throats simultaneously throughout the network, with the oil phase occupying the centre of the pores, and with both phases spanning the width of the throats, forming multiple slugs along its length, as shown in Figure 5.3. Between each oil slug and the wall, we assume, as in Chapter 2, that there is a thin film of water. We assume that the salinity of the water phase affects the thickness of this water later, and that this manifests itself as an increase in slip at the effective oil-throat interface. We suppose that the ions are advected with the water.

5.2.1 Throat saturation

In order to avoid tracking multiple interfaces, we perform a local averaging procedure to formulate our model in terms the saturation by considering a single throat of length L^t and radius R^t. We define $P^{c(i)}$ to be the capillary pressure at the i^{th} interface in the throat, $p^{(i)}$ to be the pressure in the water phase at the i^{th} interface in the throat,

$p^{(0)}$ to be the pressure at the inlet, and $p^{(n)}$ to be the pressure at the outlet, so that the flux of fluid in the k^{th} slug is given by

$$Q_k = \begin{cases} g^w \left(p^{(k-1)} - p^{(k)}\right) L^t/\Delta x^{(k)}, & \text{if the } k^{\text{th}} \text{ slug contains water,} \\ g^o \left([p^{(k-1)} + P^{c(k-1)}] - [p^{(k)} + P^{c(k)}]\right) L^t/\Delta x^{(k)}, & \text{if the } k^{\text{th}} \text{ slug contains oil,} \end{cases} \tag{5.5}$$

where $\Delta x^{(k)}$ is the length of the k^{th} slug (so that $\sum_k \Delta x^{(k)} = L^t$), and

$$g^w = \frac{\pi R^{t4}}{8\mu_w L^t}, \qquad g^o = \frac{\pi}{8\mu_o L^t}\left(R^{t4} + 2\lambda_s(c^k) R^{t3}\right), \tag{5.6}$$

are the relative conductivities of the throat in the sections containing water and oil, respectively. We have chosen the relative conductivites (5.6) to be of the form given by the hydraulic radius approximation (3.65) for a uniform cylindrical throat containing water and oil, as appropriate. We suppose that the effective slip length along the oil-throat interface, λ_s, varies with the salinity, i.e. the concentration of each ion species in the throat, c^k for $k = 1, 2$. Using the result from Chapter 2, (2.156), we choose $\lambda_s(c^k)$ to be given by the viscosity difference, $(\mu_o/\mu_w - 1)$, multiplied by the thickness of the thin water film separating the oil from the clay surface in the quasi-static limit, (2.161), so that

$$\lambda_s(c^1, c^2) = \left(\frac{\mu_o}{\mu_w} - 1\right)\left(\frac{\varepsilon_w k_B T}{2\left(c^1 + 4c^2\right) q^2}\right)^{1/2} \cosh^{-1}\left(\frac{s^* \sigma_{c0}\sigma_{o0} + \sqrt{\left(\sigma_{c0}^2 + \Gamma\right)\left(s^{*2}\sigma_{o0}^2 + \Gamma\right)}}{\Gamma}\right), \tag{5.7}$$

where ε_w, k_B, T, q, s^*, σ_{c0}, σ_{o0}, and Γ are defined in Chapter 2.

Using the result from Chapter 2 that the radii of curvature of the advancing and receding menisci at the front and rear of the oil slugs are identical to leading order, we find that $P^{c(k-1)} = P^{c(k)}$, for all k, and therefore (5.5) yields

$$Q_k = \begin{cases} g^w \left(p^{(k-1)} - p^{(k)}\right) L^t/\Delta x^{(k)}, & \text{if the } k^{\text{th}} \text{ slug contains water,} \\ g^o \left(p^{(k-1)} - p^{(k)}\right) L^t/\Delta x^{(k)}, & \text{if the } k^{\text{th}} \text{ slug contains oil,} \end{cases} \tag{5.8}$$

which we rearrange to read

$$p^{(k-1)} - p^{(k)} = \begin{cases} Q_k \Delta x^{(k)}/g^w L^t, & \text{if the } k^{\text{th}} \text{ slug contains water,} \\ Q_k \Delta x^{(k)}/g^o L^t, & \text{if the } k^{\text{th}} \text{ slug contains oil.} \end{cases} \tag{5.9}$$

We assume that the flux is conserved along the length of the throat so that $Q_k = Q$, for all k, where Q is the uniform flux along the channel. By summing (5.9) over k, we find that

$$p^{(0)} - p^{(n)} = Q\left(\frac{1}{g^w L^t}\sum_{\text{water}} \Delta x^{(k)} + \frac{1}{g^o L^t}\sum_{\text{oil}} \Delta x^{(k)}\right), \tag{5.10}$$

where the two summations are over the values of k for which the k^{th} slug contain water and oil, respectively. Since the width of the channel is uniform, and $\Delta x^{(k)}$ corresponds to the length of the k^{th} slug, we observe that these two summations are precisely the volume fraction of water and oil in the throat, respectively. We therefore define the proportion of the throat filled with water, i.e. the water saturation, to be

$$S^t = \frac{1}{L^t} \sum_{\text{water}} \Delta x^{(k)}. \tag{5.11}$$

Using the fact that $\sum_{\text{oil}} \Delta x^{(k)}/L^t = 1 - S^t$, we rearrange (5.10) to obtain an expression for the flux through the throat as a function of the water saturation and the pressure difference,

$$Q = (p^{(0)} - p^{(n)}) \frac{g^w g^o}{g^o S^t + g^w (1 - S^t)}. \tag{5.12}$$

By using the fact that the capillary pressure is the same at the advancing and receding fronts, we were able to cancel the capillary pressure terms in (5.5). If we were to consider a model in which these terms were different, we would find that each oil slug contributes an additional pressure difference due to the difference between the advancing and receding interfaces. In this case, we need to keep track of the number of oil slugs within the throat, and develop a method for determining when oil slugs are produced or destroyed. However, this is beyond the scope of this thesis.

Instead of keeping track of the number of oil slugs within the throat, we keep track of the saturation and assume that the flux of each phase is given by the saturation of the phase multiplied by the flux through the throat. Thus, in our network model, we write the flux of each phase through the throat connecting pores i and j as

$$Q_{ij}^w = S_{ij}^t Q_{ij}, \qquad Q_{ij}^o = \left(1 - S_{ij}^t\right) Q_{ij}, \tag{5.13}$$

where the w and o superscripts correspond to the water phase and oil phase, respectively, and Q_{ij} is the total flux through the throat which we compute in terms of the throat saturation, S_{ij}^t, using (5.12).

5.2.2 Phase-weighted pressure

Since we assume that there is a pressure difference between the two phases in the pores resulting from the capillary pressure, the pressures at the inlet and outlet of a given throat, $p^{(0)}$ and $p^{(n)}$ respectively (see Figure 5.3), depend on which phase is entering and leaving the throat at any given time. Since we track the saturation (rather than the position of each phase) within the throat, we take the pressures at

the inlet and outlet to be the weighted averages of the pressures in each phase. We choose the weighting to be given by the saturation in the neighbouring pore so that, for the throat connecting pores i and j, the inlet and outlet pressures are given by

$$p^{(0)} = S_i^w p_i^w + S_i^o p_i^o, \qquad p^{(n)} = S_j^w p_j^w + S_j^o p_j^o, \tag{5.14}$$

respectively, where S_k^w and S_k^o are the saturations of water and oil, respectively, and p_k^w and p_k^o are the pressures in the water and oil phases, respectively, in pore k. By substituting $p_k^o = p_k^w + P_k^c$ and $S^o + S^w = 1$ into (5.14), and defining $S_k := S_k^w$, we find that

$$p^{(0)} = p_i^w + (1 - S_i)P_i^c(S_i), \qquad p^{(n)} = p_j^w + (1 - S_j)P_j^c(S_j), \tag{5.15}$$

where the capillary-pressure-saturation relationship, $P_k^c(S_k)$, depends on the geometry of the pore.

5.2.3 Governing equations

We simplify the notation by defining

$$P_k = p_k^w + (1 - S_k)P_k^c(S_k), \tag{5.16}$$

to be the phase-weighted pressure at node k. Substituting (5.15) into (5.12), and writing the result in terms of the phase-weighted pressure using (5.16) yields the total flux through the throat connecting pores i and j,

$$Q_{ij} = (P_i - P_j)\,\frac{g_{ij}^w g_{ij}^o}{g_{ij}^o S_{ij}^t + g_{ij}^w(1 - S_{ij}^t)}. \tag{5.17}$$

We assume that the net flux through each pore is conserved, and that the rate of change of the volume of water in a pore is given by the net flux of water into the pore. At pore i, our model reads

$$\sum_j Q_{ij} = 0, \qquad V_i \frac{\mathrm{d}S_i}{\mathrm{d}t} = -\sum_j S_{ij}^t Q_{ij}, \tag{5.18}$$

where V_i is the volume of the i^{th} pore. We only need to solve for the saturation of the water phase, since the saturation of the oil phase in pore i is given by $1 - S_i$.

In order for the oil phase to enter the throat connecting pores i and j, the capillary pressure in the upstream pore must exceed an entry pressure, p_{ij}^e, which is determined by the geometry of the throat. Since changes in the salinity affect the slip length,

which is equivalent to increasing the throat radius by $2\lambda_s$, we assume that the entry pressure is given by

$$p_{ij}^e = \frac{2\gamma}{R_{ij}^t + 2\lambda_s(c_{ij}^k)}, \tag{5.19}$$

where R_{ij}^t is the radius of the throat connecting pores i and j, and c_{ij}^k is the concentration of each ion species in the throat, for $k = \pm, 2\pm$.

We assume that the saturation in the throat is given by the saturation in the upstream pore if the capillary pressure exceeds the entry pressure, otherwise the throat is entirely filled with water. The upstream pore is determined by the sign of $P_i - P_j$, so that

$$S_{ij}^t = \begin{cases} S_i, & \text{if } P_i > P_j \text{ and } P_i^c\left(S_i\right) > p_{ij}^e(c_{ij}^k), \\ S_j, & \text{if } P_i < P_j \text{ and } P_j^c\left(S_j\right) > p_{ij}^e(c_{ij}^k), \\ 1, & \text{otherwise.} \end{cases} \tag{5.20}$$

We assume that the rate of change of the total number of each ion species in a pore is equal to the net flux of ions into the pore, and that the concentration of ions in the throat is given by the concentration in the upstream pore. This reads

$$V_i \frac{\mathrm{d}\left(c_i^k S_i\right)}{\mathrm{d}t} = -\sum_j c_{ij}^k S_{ij}^t Q_{ij}, \qquad c_{ij}^k = \begin{cases} c_i^k, & \text{if } P_i > P_j, \\ c_j^k, & \text{if } P_i < P_j, \end{cases} \tag{5.21}$$

where c_i^k is the concentration of each ion species in pore i, for $k = \pm, 2\pm$.

5.2.4 Boundary conditions

The initial and boundary conditions depend on the particular problem being studied. In §5.4, we will study drainage and waterflooding for a simple two-dimensional grid network, and discuss the appropriate initial and boundary conditions in each case. However, in both cases, we will assume that the outlet nodes are subject to a prescribed reference pressure, $\tilde{P}$. We prescribe the pressure and saturation at the inlet nodes, S_i^{in} and $\tilde{P} + P_i^{\text{in}}$ respectively, which may be different at each node in order to ensure that the pressure in each phase is consistent across the inlet. We also assume that the concentration of ions at the inlet are prescribed functions of time, $c_i^k = c_{\text{in}}^k(t)$, to allow us to study, for example, a high-salinity waterflood followed by a low-salinity waterflood. The boundary conditions read

$$S_i = S_i^{\text{in}}, \quad P_i = \tilde{P} + P_i^{\text{in}}, \quad c_i^k = c_{\text{in}}^k(t), \quad \text{for nodes } i \text{ connected to the inlet,} \tag{5.22}$$

$$P_i = \tilde{P}, \qquad \text{for nodes } i \text{ connected to the outlet.} \tag{5.23}$$

We prescribe an initial saturation at each node, S_{Ii}, and an initial ion concentration throughout the network, c_I, so that

$$S_i = S_{Ii}, \qquad c_i^k = c_I^k, \qquad \text{at } t = 0. \tag{5.24}$$

For a given capillary pressure function, P_i^c, (5.17) – (5.24) defines a system of equations for c_i^k, S_i, and P_i, from which we can compute p_i^w and p_i^o. The form of the capillary-pressure-saturation depends on the geometry of the pore. However, in our model, we assume that the pores are square, and we define the capillary pressure function for pore i to be

$$P_i^c = \frac{2\gamma}{R_i^p}\sqrt{\frac{4-\pi}{S_i}}, \tag{5.25}$$

where $2R_i^p$ is the length of each side of the pore. For a derivation of (5.25), see Appendix B.

5.3 Model solution

We wish to solve the two-phase flow network model presented in §5.2 for a network consisting of N pores, including a inlet pores, and b outlet pores. We suppose that the pores (represented by nodes in our network) are square, with pore i having side length $2R_i^p$, and we suppose that the radius and length of the throat connecting pores i and j (represented by an edge in our network) are given by R_{ij}^t and L_{ij}^t, respectively. We define R^p, R^t, and L^t, to be the average values of R_i^p, R_{ij}^t, and L_{ij}^t, respectively.

The two-phase flow through the internal nodes, $a < i \leq N - b$, of the network is governed by equations (5.17) – (5.25), with the conductivities of the throats given by (5.6). Substituting (5.17) into (5.18) and (5.21), the system reads

$$\sum_i G_{ij}(P_i - P_j) = 0, \qquad \text{for } a < i \leq N - b, \tag{5.26}$$

$$V_i \frac{\mathrm{d}S_i}{\mathrm{d}t} = -\sum_j S_{ij}^t G_{ij}(P_i - P_j), \qquad \text{for } a < i \leq N - b, \tag{5.27}$$

$$V_i \frac{\mathrm{d}\left(c_i^k S_i\right)}{\mathrm{d}t} = -\sum_j c_{ij}^k S_{ij}^t G_{ij}(P_i - P_j), \qquad \text{for } a < i \leq N - b, \tag{5.28}$$

subject to

$$S_i = S_i^{\text{in}}, \qquad P_i = \tilde{P} + P_i^{\text{in}}, \qquad c_i^k = c_{\text{in}}^k(t), \qquad \text{for } 1 \leq i \leq a, \tag{5.29}$$

$$P_i = \tilde{P}, \qquad \text{for } N - b < i \leq N, \tag{5.30}$$

$$S_i = S_{Ii}, \qquad c_i^k = c_I^k, \qquad \text{at } t = 0, \tag{5.31}$$

where

$$G_{ij} = \frac{\pi {R_{ij}^t}^4}{8L_{ij}^t} \frac{1 + 2\frac{\lambda_s}{R_{ij}^t}}{\mu_w \left(1 + 2\frac{\lambda_s}{R_{ij}^t}\right) S_{ij}^t + \mu_o (1 - S_{ij}^t)}, \tag{5.32}$$

$$S_{ij}^t = \begin{cases} S_i, & \text{if } P_i > P_j \text{ and } P_i^c(S_i) > p_{ij}^e, \\ S_j, & \text{if } P_i < P_j \text{ and } P_j^c(S_j) > p_{ij}^e, \\ 1, & \text{otherwise,} \end{cases} \tag{5.33}$$

$$p_{ij}^e = \frac{2\gamma}{R_{ij}^t + 2\lambda_s}, \tag{5.34}$$

$$c_{ij}^k = \begin{cases} c_i^k, & \text{if } P_i > P_j, \\ c_j^k, & \text{if } P_i < P_j, \end{cases} \tag{5.35}$$

$$\lambda_s = \left(\frac{\mu_o}{\mu_w} - 1\right) \left(\frac{\varepsilon_w k_B T}{2\left(c^1 + 4c^2\right) q^2}\right)^{1/2} \cosh^{-1}\left(\frac{s^* \sigma_{c0} \sigma_{o0} + \sqrt{\left(\sigma_{c0}^2 + \Gamma\right)\left(s^{*2}\sigma_{o0}^2 + \Gamma\right)}}{\Gamma}\right), \tag{5.36}$$

$$P_i^c = \frac{2\gamma}{R_i^p} \sqrt{\frac{4 - \pi}{S_i}}. \tag{5.37}$$

5.3.1 Non-dimensionalisation

We define $\mathcal{P}$ to be a typical size for the inlet pressures, P_i^{in}, which we will define explicitly in §5.4.1 and §5.4.2 when we come to study drainage and waterflooding models, respectively. We non-dimensionalise the model using the scalings

$$\begin{gathered} P_i = \tilde{P} + \mathcal{P}\hat{P}_i, \qquad P_i^{\text{in}} = \tilde{P} + \mathcal{P}\hat{P}_i^{\text{in}}, \qquad P_i^c = \mathcal{P}\hat{P}_i^c \qquad p_{ij}^e = \mathcal{P}\hat{p}_{ij}^e, \\ R_i^p = R^p \hat{R}_i^p, \qquad R_{ij}^t = R^t \hat{R}_{ij}^t, \qquad \lambda_s = R^t \hat{\lambda}_s, \qquad L_{ij}^t = L^t \hat{L}_{ij}^t, \\ V_i = R^{p3} \hat{V}_i, \qquad G_{ij} = \frac{\pi R^{t4}}{8\mu_w L^t} \hat{G}_{ij}, \qquad t = \frac{8\mu_w L^t R^{p3}}{\pi R^{t4} \mathcal{P}} \hat{t}, \\ c_i^k = c_I^k \hat{c}_i^k, \qquad c_{ij}^k = c_I^k \hat{c}_{ij}^k, \qquad c_{\text{in}}^k = c_I^k \hat{c}_{\text{in}}^k. \end{gathered} \tag{5.38}$$

Writing (5.26) – (5.37) in terms of the dimensionless variables, and dropping the hat notation, yields

$$\sum_i G_{ij}(P_i - P_j) = 0, \qquad \text{for } a < i \leq N - b, \tag{5.39}$$

$$V_i \frac{\mathrm{d}S_i}{\mathrm{d}t} = -\sum_j S_{ij}^t G_{ij}(P_i - P_j), \qquad \text{for } a < i \leq N - b, \tag{5.40}$$

$$V_i \frac{\mathrm{d}\left(c_i^k S_i\right)}{\mathrm{d}t} = -\sum_j c_{ij}^k S_{ij}^t G_{ij}(P_i - P_j), \qquad \text{for } a < i \leq N - b, \tag{5.41}$$

subject to

$$S_i = S_i^{\text{in}}, \qquad P_i = P_i^{\text{in}}, \qquad c_i^k = c_{\text{in}}^k(t), \qquad \text{for } 1 \le i \le a, \tag{5.42}$$

$$P_i = 0, \qquad \text{for } N - b < i \le N, \tag{5.43}$$

$$S_i = S_{Ii}, \qquad c_i^k = 1, \qquad \text{at } t = 0, \tag{5.44}$$

where

$$G_{ij} = \frac{{R_{ij}^t}^4}{L_{ij}^t} \frac{1 + 2\frac{\lambda_s}{R_{ij}^t}}{\left(1 + 2\frac{\lambda_s}{R_{ij}^t}\right) S_{ij}^t + \mu^*(1 - S_{ij}^t)}, \tag{5.45}$$

$$S_{ij}^t = \begin{cases} S_i, & \text{if } P_i > P_j \text{ and } P_i^c\left(S_i\right) > p_{ij}^e, \\ S_j, & \text{if } P_i < P_j \text{ and } P_j^c\left(S_j\right) > p_{ij}^e, \\ 1, & \text{otherwise,} \end{cases} \tag{5.46}$$

$$p_{ij}^e = \frac{2\Gamma_{\mathcal{P}}}{R_{ij}^t + 2\lambda_s}, \tag{5.47}$$

$$c_{ij}^k = \begin{cases} c_i^k, & \text{if } P_i > P_j, \\ c_j^k, & \text{if } P_i < P_j, \end{cases} \tag{5.48}$$

$$\lambda_s = \frac{\epsilon_2\left(\mu^* - 1\right)}{\left(c^1 + 4c^* c^2\right)^{1/2}} \cosh^{-1}\left(\frac{s^*\sigma_{c0}\sigma_{o0} + \sqrt{\left(\sigma_{c0}^2 + \Gamma\right)\left(s^{*2}\sigma_{o0}^2 + \Gamma\right)}}{\Gamma}\right), \tag{5.49}$$

$$P_i^c = \frac{2\Gamma_{\mathcal{P}} R^*}{R_i^p}\sqrt{\frac{4 - \pi}{S_i}}. \tag{5.50}$$

We have defined $\mu^* = \mu_o/\mu_w$ to be the viscosity ratio of the oil to the water, $\epsilon_2 = \left(\varepsilon_w k_B T/2c_I^1 q^2\right)^{1/2}/R^t$ to be the dimensionless Debye length, $c^* = c_I^2/c_I^1$ to be the ratio of divalent ions to monovalent ions, $R^* = R^t/R^p$ to be the ratio of the average throat radius to the average pore radius, and $\Gamma_{\mathcal{P}} = \gamma/R^t\mathcal{P}$ to be the dimensionless surface tension. We choose $R^p = 2\,\mu$m, c_I^k to be the concentration of the i^{th} ion species in the low salinity regime, and otherwise use the parameter values given in Table 2.1, so that the dimensionless parameter sizes are $\mu^* = 11$, $\epsilon_2 = 1.5 \times 10^{-3}$, $c^* = 0.3$, $s^* = 75$, $\Gamma = 0.08$, and $R^* = 0.5$. We will select $\mathcal{P}$, and therefore determine $\Gamma_{\mathcal{P}}$, differently depending on whether we are studying a drainage or waterflood problem, and will discuss each case in §5.4.

5.3.2 Vector formulation

We write $\mathbf{P}$, $\mathbf{S}$, and $\mathbf{c}^k$ as the vector forms of P_i, S_i, and c_i^k, respectively, which we separate into the components

$$\mathbf{P} = \left(\mathbf{P}_L, \mathbf{P}_M, \mathbf{P}_R\right), \qquad \mathbf{S} = \left(\mathbf{S}_L, \mathbf{S}_M, \mathbf{S}_R\right), \qquad \mathbf{c}^k = \left(\mathbf{c}^k{}_L, \mathbf{c}^k{}_M, \mathbf{c}_R^k\right), \tag{5.51}$$

where,

$$\mathbf{P}_L = \mathbf{P}^{\text{in}}, \qquad \mathbf{P}_R = \mathbf{0}, \qquad \mathbf{S}_L = \mathbf{S}^{\text{in}}, \qquad \mathbf{c}_L^k = c_{in}^k \cdot \mathbf{1}. \tag{5.52}$$

We have written $\mathbf{P}^{\text{in}}$ and $\mathbf{S}^{\text{in}}$ as the vector forms of P_i^{in} and S_i^{in}, respectively, and $\mathbf{P}_M$, $\mathbf{S}_M$, and $\mathbf{c}_M^k$ are the internal quantities which we need to determine. We have used the subscripts L, M, and R to denote left, middle, and right, respectively, and the corresponding vectors have length a, $N-a-b$, and b, respectively.

Denoting $\mathbf{V} = (\mathbf{V}_L, \mathbf{V}_M, \mathbf{V}_R)$ as the vector form of V_i, we write (5.39) – (5.41) in the form

$$\boldsymbol{L}\mathbf{P} = \mathbf{0}, \qquad \mathbf{V}_M \circ \frac{\mathrm{d}\mathbf{S}_M}{\mathrm{d}t} = -\boldsymbol{L}_S\mathbf{P}, \tag{5.53}$$

$$\mathbf{V}_M \circ \frac{\mathrm{d}\left(\mathbf{c}_M^k \circ \mathbf{S}_M\right)}{\mathrm{d}t} = -\boldsymbol{L}_c^k\mathbf{P}, \tag{5.54}$$

where $\circ$ denotes element-wise multiplication, and

$$(\boldsymbol{L})_{i-a,j} = \delta_{i-a,j}\left(\sum_k G_{i-a,k}\right) - G_{i-a,j} \qquad \text{for } a < i \le N-b, \tag{5.55}$$

$$(\boldsymbol{L}_S)_{i-a,j} = \delta_{i-a,j}\left(\sum_k S_{i-a,k}^t G_{i-a,k}\right) - S_{i-a,j}^t G_{i-a,j} \qquad \text{for } a < i \le N-b, \tag{5.56}$$

$$(\boldsymbol{L}_c^k)_{i-a,j} = \delta_{i-a,j}\left(\sum_l c_{i-a,l}^k S_{i-a,l}^t G_{i-a,l}\right) - c_{i-a,j}^k S_{i-a,j}^t G_{i-a,j} \qquad \text{for } a < i \le N-b. \tag{5.57}$$

We separate the non-square $(N-a-b)\times N$ matrix, $\boldsymbol{L}$, into the following components,

$$\boldsymbol{L} = (\underbrace{\boldsymbol{L}_1}_{a} | \underbrace{\boldsymbol{L}_2}_{N-a-b} | \underbrace{\boldsymbol{L}_3}_{b})\}^{N-a-b}, \tag{5.58}$$

where the dimensions of $\boldsymbol{L}_1$, $\boldsymbol{L}_2$ and $\boldsymbol{L}_3$ have been shown. We substitute (5.58) into (5.53) and rearrange to obtain

$$\mathbf{P}_M = -\boldsymbol{L}_2^{-1}\left(\boldsymbol{L}_1\mathbf{P}_L\right), \qquad \mathbf{V}_M \circ \frac{\mathrm{d}\mathbf{S}_M}{\mathrm{d}t} = -\boldsymbol{L}_S\mathbf{P}, \tag{5.59}$$

which, along with (5.54), defines a system of equations for $\mathbf{P}_M$, $\mathbf{S}_M$, and $\mathbf{c}_M^k$. We solve (5.54) and (5.59) subject to

$$\mathbf{S}_M = \mathbf{S}_{IM}, \qquad \text{at } t = 0, \tag{5.60}$$

where $\mathbf{S}_{IM}$ is the vector form of the middle components of S_{Ii}.

Since $\boldsymbol{L}_1$, $\boldsymbol{L}_2$, $\boldsymbol{L}_S$, and $\boldsymbol{L}_c^k$ depend non-linearly on $\mathbf{P}$, $\mathbf{S}$, and $\mathbf{c}^k$ through equations (5.45) – (5.50), we solve (5.54), (5.59), and (5.60) using an implicit pressure explicit

saturation scheme with an adaptive time step. At each time step, we compute $\boldsymbol{L}_1$, $\boldsymbol{L}_2$, $\boldsymbol{L}_S$, and $\boldsymbol{L}_c^k$ using the solutions for $\mathbf{P}$, $\mathbf{S}$, and $\mathbf{c}^k$ from the previous time step, we then determine $\mathbf{P}_M$ from (5.59a), and use the updated solution for $\mathbf{P}_M$ in order to compute the saturations and concentrations using (5.54) and (5.59b). Denoting the n^{th} time step using a superscript, and letting Δt^n be the size of the n^{th} time step, this process reads

$$\mathbf{P}_M^{n+1} = -(\boldsymbol{L}_2^n)^{-1}\left(\boldsymbol{L}_1^n \mathbf{P}_L\right), \qquad \mathbf{S}_M^{n+1} = \mathbf{S}_M^n - \Delta t^n \left(\mathbf{L}_S^n \mathbf{P}^{n+1}\right) \oslash \mathbf{V}_M, \tag{5.61}$$

$$\mathbf{c}_M^{k\ n+1}\mathbf{S}_M^{n+1} = \mathbf{c}_M^{k\ n}\mathbf{S}_M^n - \Delta t^n \left(\boldsymbol{L}_c^{k n} \mathbf{P}^{n+1}\right) \oslash V_M, \tag{5.62}$$

with the initial conditions

$$\mathbf{S}_M^0 = \mathbf{S}_{IM}, \qquad \mathbf{c}_M^{k\ 0} = \mathbf{1}, \tag{5.63}$$

where $\oslash$ denotes element-wise division. We choose the time step, Δt^n, according to

$$\Delta t^n = \frac{1}{h}\min(\Delta t_0^n, \Delta t_1^n), \tag{5.64}$$

where

$$\Delta t_0^n = \min\left(\left[\mathbf{V}_M \circ \mathbf{S}_M^n \oslash \left(\boldsymbol{L}_S^n \mathbf{P}^{n+1}\right)\right]_i\right), \qquad \text{for } i \text{ s.t. } \left(\boldsymbol{L}_S^n \mathbf{P}^{n+1}\right)_i > 0, \tag{5.65}$$

and

$$\Delta t_1^n = \min\left(\left[\mathbf{V}_M \circ (\mathbf{S}_M^n - 1) \oslash \left(\boldsymbol{L}_S^n \mathbf{P}^{n+1}\right)\right]_i\right), \qquad \text{for } i \text{ s.t. } \left(\boldsymbol{L}_S^n \mathbf{P}^{n+1}\right)_i < 0, \tag{5.66}$$

are the minimum time steps required for a pore to reach saturation 0 or 1, respectively. Defining Δt^n in this way ensures that the saturation in each node stays strictly between 0 and 1, preventing numerical issues which may occur if an unphysical saturation develops. We choose $h = 10$ in our numerical simulations.

By using the solution from the previous time step to remove the non-linearities from the pressure equation, we find that we no longer have a well-defined initial condition. We need to know the pressure field in order to determine the direction of flow and, consequently, to determine S_{ij}^t and c_{ij}^k at $t = 0$ using (5.46) and (5.48). We can get around this issue by supposing that the throat saturations and ion concentrations are initially equal to the mean values of the neighbouring pores, $S_{ij}^t = \frac{1}{2}(S_i + S_j)$ and $c_{ij}^k = \frac{1}{2}\left(c_i^k + c_j^k\right)$ at $t = 0$, to remove the pressure dependence from the initial condition. Whilst this may not be physically accurate, we found during our numerical simulations that the appropriate directions of flow in the throats, and therefore the

correct throat saturations and ion concentrations, stabilise within a few time steps. Consequently, this initial condition has little impact on the solution.

In §5.4, we simulate a waterflood on an oil-filled network by numerically solving equations (5.61) – (5.66). We define an appropriate two-stage process, in which the initially water-saturated network is flushed with oil before a waterflood injection is performed, and we define the initial and boundary conditions for each stage of this process.

5.4 Waterflood simulation

In this section, we simulate a waterflood on an oil-filled network by numerically solving (5.61) – (5.66). Our numerical experiments show that the obvious initial state of having S_k be equal to some small prescribed value throughout the network is unsteady due the differences between the capillary pressures at a fixed saturation in the different-sized pores. This can take some time to settle during a waterflood simulation, which affects the results and can produce unwanted effects such as flow reversal. To prevent this issue, we separate the waterflooding process into two stages.

We initially suppose that the network is saturated with water. We connect oil to the inlet nodes of the network, and allow the oil to invade the pores by capillary forces until a small volume of water remains and a steady-state is obtained. This process replicates the initial formation of the oil reservoir, in which the oil phase slowly propagates through the water-filled reservoir rock until a steady state is reached. We refer to this as the 'drainage' stage.

We then use the steady-state solution found from the drainage stage as the initial condition for the 'waterflood' stage (sometimes referred to as imbibition), in which we inject water in one end of the network until a steady state is reached. We study two cases of waterflooding. First, we perform a secondary-stage waterflood, in which *either* high salinity or low salinity water is injected, and we compare the amount of oil recovered in each case. Second, we study the case in which the network is initially flooded with high-salinity water, *before* a low-salinity water is injected. This is known as a tertiary recovery process, in which the low salinity brine is used to obtain additional oil after the high-salinity waterflood has been performed.

5.4.1 Drainage stage

Since drainage occurs due to capillary forces alone, we assume that the pressure in the water phase, p_i^w, may be set to be zero without loss of generality at the

inlets and outlet nodes of the network. We suppose that the network is initially water-filled, and that the inlet nodes are connected to a bath of oil held at constant pressure, P_D, so that the capillary pressure in the inlet nodes is $P_i^c = P_D$, where the D subscript denotes the 'drainage' pressure. Therefore, the saturation in the inlet nodes is found by inverting the capillary pressure function, $S_i^{\text{in}} = (P_i^c)^{-1}(P_D)$, for $1 \leq i \leq a$. We impose a constant capillary pressure at the inlet nodes, rather than a constant saturation, in order to prevent flow reversal. For simplicity, we assume that the ion concentrations are constant (given by the high salinity regime) throughout the network during the drainage stage, and therefore set $\lambda_s = 0$ and neglect equation (5.62) from the model. Recalling that $P_i = p_i^w + (1 - S_i)P_i^c(S_i)$, we find that the dimensional inlet pressures are given by

$$P_i^{\text{in}} = \left[1 - (P_i^c)^{-1}(P_D)\right] P_D. \tag{5.67}$$

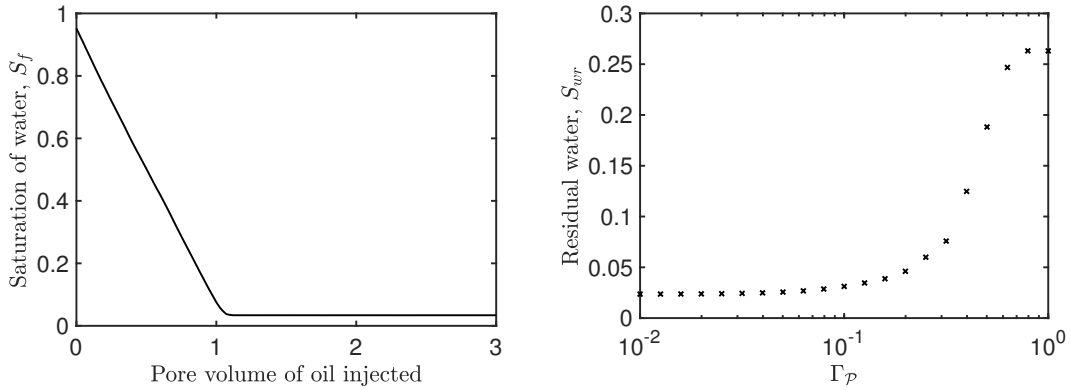
We set our pressure scale to be $\mathcal{P} = P_D$, so that the full set of dimensionless initial and boundary conditions read

$$\mathbf{S}_{IM} = \mathbf{1}, \qquad \text{at } t = 0, \tag{5.68}$$

$$P_i^{\text{in}} = 1 - (P_i^c)^{-1}(1), \qquad S_i^{\text{in}} = (P_i^c)^{-1}(1), \qquad \text{for } 1 \leq i \leq a. \tag{5.69}$$

We solve (5.61) – (5.66) numerically (neglecting the equations for the ion concentrations, (5.62) and (5.63b)), subject to the initial and boundary conditions (5.68) and (5.69) on a regular 30×30 grid network (so that $N = 900$ and $a = b = 30$), until a steady-state solution for the saturation is obtained. We randomly generate an appropriate network structure by selecting the pore and throat sizes, R_i^p and R_{ij}^t, respectively, from a uniform distribution on $[0.5, 1.5]$. By balancing (5.50) with (5.69) for a water saturation of 0.01, we choose our pressure scale to be $\mathcal{P} = P_D = 10^5 \text{ kg m s}^{-2}$, and find that $\Gamma_{\mathcal{P}} \approx 0.2$.

In Figure 5.4a, we plot the total volume fraction of water in the internal (non-boundary) nodes in the network, $S_f = \mathbf{S}_M \cdot \mathbf{V}_M / \sum_{i=a+1}^{N-b} V_i$, against the volume of oil injected, which we measure as a fraction of the 'pore volume' which we define to be the total volume of fluid space the network, $\sum_i V_i$. The network is initially saturated with water, $S_f = 1$, and the volume fraction decreases to an oil-dominated state, $S_f = 0.034$, after approximately one pore volume of oil has been injected. As $t \to \infty$, the solution approaches a steady-state limit, $\mathbf{S}_M \to \mathbf{S}_W^0$, where the W subscript denotes 'waterflood', since we use this as our initial condition for the saturation in the waterflood stage.



(a) (b)

Figure 5.4: (a) saturation of water against pore volume injected during the drainage stage, with $\Gamma_{\mathcal{P}} = 0.2$; (b) residual water saturation, S_{wr}, as a function of $\Gamma_{\mathcal{P}}$

In Figure 5.4b, we plot the residual water saturation, S_{wr}, against $\Gamma_{\mathcal{P}}$ after 4 pore volumes of oil have been injected. We observe that, as $\Gamma_{\mathcal{P}}$ decreases (i.e. the applied pressure increases), the residual water decreases due to the fact that the increased applied pressure enables additional oil to enter the corners of the pore.

5.4.2 Waterflood stage

Having determined an initial condition for the saturation, we need to define appropriate boundary conditions for the waterflood stage. We assume that the inlets and outlets of the network are connected to baths of water, so that the saturation is equal to unity at either end of the network, and we assume that the water phase is subject to a pressure difference, P_W, where the W subscript denotes the 'waterflood' pressure. We set our pressure scale to be $\mathcal{P} = P_W$, so that the dimensionless initial and boundary conditions for the pressure and saturation read

$$\mathbf{S}_{IM} = \mathbf{S}_W^0, \qquad \text{at } t = 0, \tag{5.70}$$

$$P_i^{\text{in}} = 1, \qquad S_i^{\text{in}} = 1, \qquad \text{for } 1 \leq i \leq a, \tag{5.71}$$

where we have used the fact that $P_i = p_i^w$ at the inlets and outlets, since $S_i = 1$. We take care to note that the dimensionless surface tension is different in the drainage and waterflood stages (given by $\Gamma_{\mathcal{P}} = \gamma/R^t P_D$ and $\Gamma_{\mathcal{P}} = \gamma/R^p P_W$, respectively), and must therefore be set appropriately at each stage of the process. During the waterflood stage, we set $\mathcal{P} = 1.35\ \text{kg}\,\text{m}\,\text{s}^{-2}$, since the network is 30 throats long in the direction of flow, and, as discussed in Chapter 2, a typical pressure drop across a

throat is $\Delta P = 0.045\ \mathrm{kg\,m\,s^{-2}}$. Hence, $\Gamma_{\mathcal{P}} \approx 1.48 \times 10^4$. We note that $\mathcal{P}$ is chosen to be significantly larger in the drainage stage, in comparison with the waterflood stage, due to the fact that the inlet nodes contain oil in the drainage case. We require the pressure to be much higher in the oil phase in order for oil to invade the pores, due to the capillary pressure between the two phases, which results in the greater prescribed value of $\mathcal{P}$.

We assume that, initially, the concentration of ions is given by the high-salinity regime, c^k_{high}, so that

$$c^k_I = c^k_{high}. \tag{5.72}$$

We suppose that the concentration of ions at the inlet is initially given by the high-salinity concentration, until a time, T, at which low salinity water is injected, which reads

$$c^k_{in}(t) = \begin{cases} c^k_{high}, & 0 \leq t \leq T, \\ c^k_{low}, & t > T. \end{cases} \tag{5.73}$$

Setting $T = 0$ corresponds to a secondary stage low-salinity waterflood, setting $T = \infty$ corresponds to a secondary stage high-salinity waterflood, and setting T to be finite but non-zero corresponds to a secondary high-salinity waterflood, followed by a tertiary low-salinity waterflood. We consider the three cases given by $T = 0$, $T = \infty$, and T finite but greater than the time taken for the high-salinity waterflood to reach a steady state.

In Figure 5.5a, we show the percentage of oil recovered (which, by conservation of mass, is the same as the percentage increase in the volume of water in the network which we calculate from the change in the saturation), against the pore volume injected for the secondary stage high-salinity and low-salinity waterfloods. We observe that, in both cases, the majority of the oil recovery is achieved after approximately 0.25 pore volumes of water have been injected. We calculate the percentage recovery increase in the low salinity case relative to the high salinity case as $(1 - S^{\mathrm{low}}_{or})/(1 - S^{\mathrm{high}}_{or}) - 1$, where S^{low}_{or} and S^{high}_{or} are the residual oil saturations in the low-salinity and high-salinity cases, respectively. The percentage increase is approximately 15%, showing that our network model is able to reproduce the low salinity effect. In Figure 5.5b, we show the initial period of injection. We observe that the rate of oil recovery is initially similar between the two cases, however, after approximately 0.1 pore volumes of water have been injected, the rate of recovery of the high salinity waterflood reduces, whereas the low salinity waterflood continues to produce oil at the same rate for a short period.

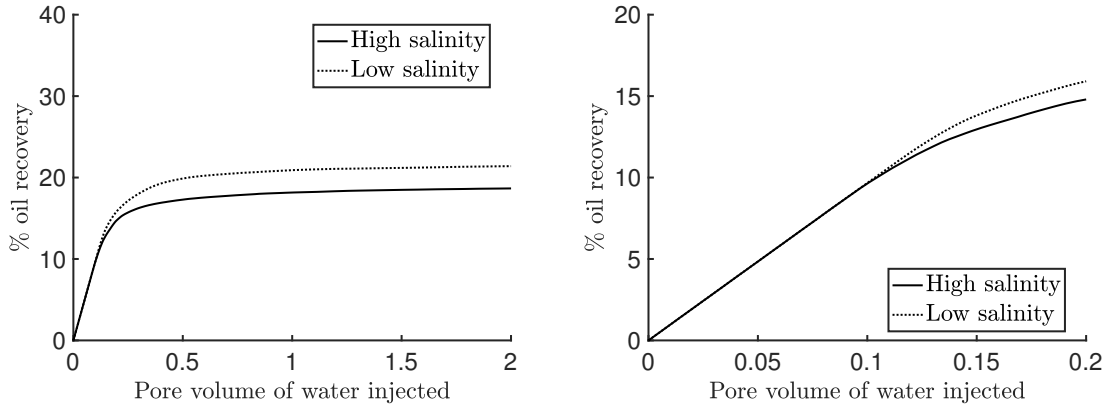


Figure 5.5: Graphs showing the percentage of oil recovered as a function of the pore volume of water injected, for secondary-stage high salinity and low salinity injections: (a) oil recovery over 2 pore volumes, during which a steady state is achieved; (b) oil recovery over the first 0.2 pore volumes, showing that initially the rates of recovery are the same for the high salinity and low salinity injections.

In Figure 5.6, we show the total oil recovered as a function of volume injected for the secondary stage high-salinity waterflood followed by a tertiary stage low-salinity waterflood. We initiate the low-salinity waterflood after 3 pore volumes of high-salinity water have been injected. We observe that the total amount of oil recovered increases after the low-salinity injection is initiated, showing that our model captures the low salinity effect during a tertiary recovery process. There is a short delay between the start of the low-salinity injection and the point at which the additional recovery is observed. The total oil recovered increases by 12% during the low-salinity injection phase.

In Figure 5.7a, we show the residual oil saturation, S_{or} against the ratio of the average pore throat radius to the the average pore radius, R^*, after 3 pore volumes of water have been injected for both the low-salinity and high salinity waterflood cases. We observe that the residual oil decreases as R^* increases, and is lower for the low-salinity waterflood for all values of R^*. In Figure 5.7b, we show the percentage recovery increase as a function of R^*. We observe that the percentage recovery increase is greater for larger values of R^*, suggesting that low-salinity water is more effective for a reservoir in which the pores and pore throats are of a similar size.

In Figure 5.8a, we show the residual oil saturation, S_{or}, against the oil-water viscosity ratio, μ^*, after 3 pore volumes of water have been injected for both the low-salinity and high salinity waterflood cases. We observe that the residual oil saturation

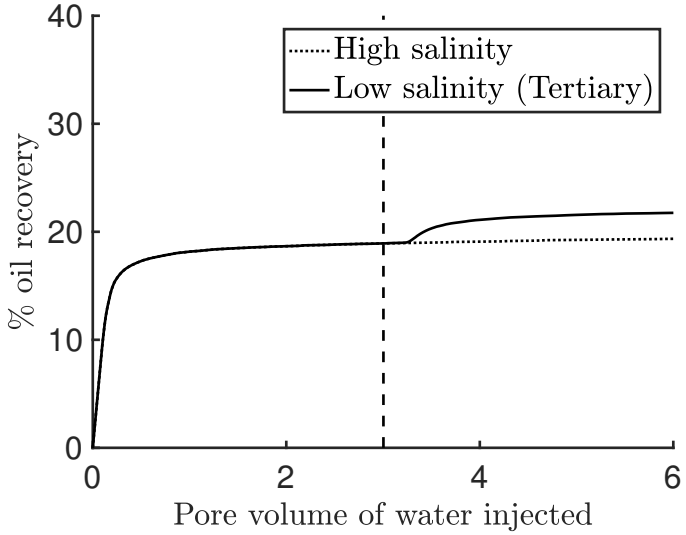
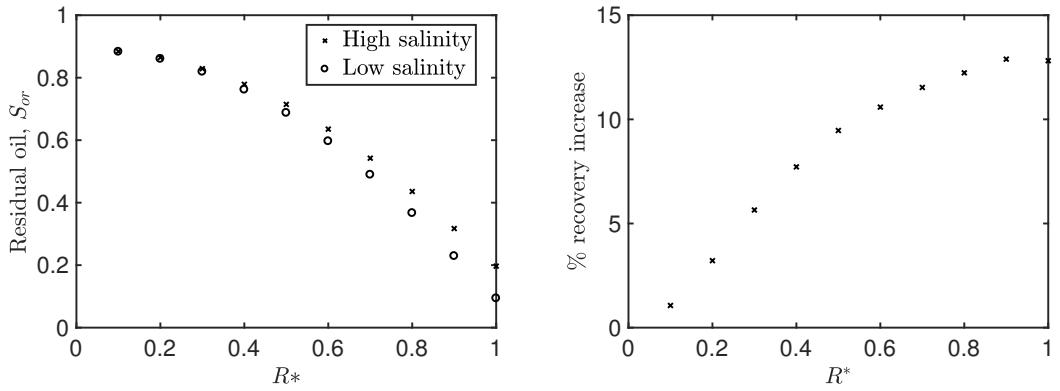
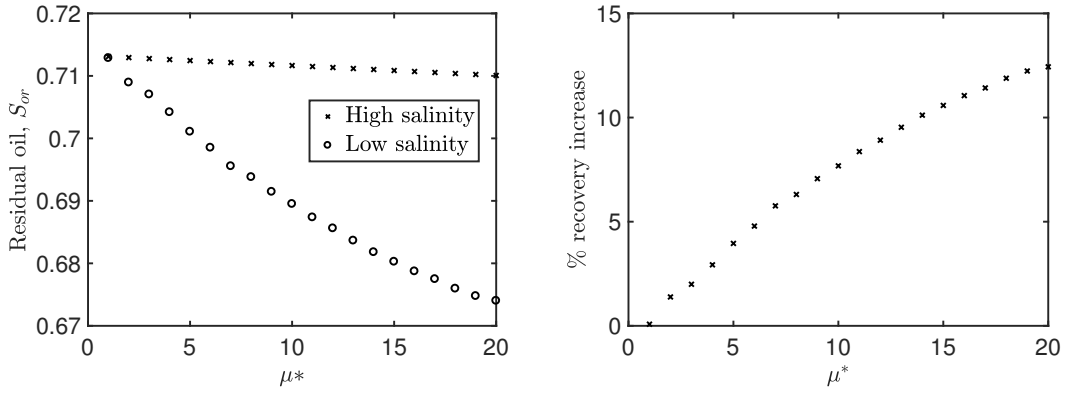


Figure 5.6: Graph showing the percentage of oil recovered as a function of the pore volume of water injected, for a secondary-stage high salinity injection followed by a tertiary-stage low salinity injection. The vertical dashed line indicates the point at which the low salinity injection is initiated, and the dotted line shows the oil recovery for the high-salinity waterflood in which no tertiary low-salinity waterflood is performed.



(a) (b)

Figure 5.7: Plots showing: (a) residual oil saturation, S_{or}, against R^* for the high-salinity and low-salinity secondary waterflood cases; (b) percentage oil recovery increase obtained during a low salinity waterflood relative to a high salinity waterflood as a function of R^*.



(a) (b)

Figure 5.8: Plots showing: (a) residual oil saturation, S_{or}, against μ^* for the high-salinity and low-salinity secondary waterflood cases; (b) percentage oil recovery increase obtained during a low salinity waterflood relative to a high salinity waterflood as a function of μ^*.

decreases as μ^* increases in both cases, but that the viscosity ratio only has a small effect in the high salinity case. In Figure 5.8b, we plot the percentage recovery increase as a function of μ^*. We observe that the percentage recovery increases as μ^* increases. This is due to the fact that the slip length increases proportionally with $\mu^* - 1$, as seen in (5.49).

5.5 Conclusions

In this chapter, we presented a model for two-phase flow through a network of pores and throats. In our model, we assume that both phases can be present in throats and pores at the same time, with the oil phase occupying the centres of the pores and forming slugs surrounded by a thin film of water along the throats. By using the result from Chapter 2 that the radii of curvature of the advancing and receding menisci of the oil slugs in a given throat are identical at leading order, we found that the conductivity of the throat, given by (5.12), is independent of the number of oil slugs formed, and depends only on the volume fraction of each phase within the throat. This enabled us to allow multiple oil slugs to form within a given throat in our model without having to track multiple interfaces, as is required in similar models such as those based on the Washburn equation discussed in §5.1.4.

In §5.2.3, we derived governing equations (5.18) for the total flux and water saturation using conservation of mass for both the total fluid and for the water phase. We formulated the model in terms of the phase-weighted pressure, given by (5.16),

in order to solve the system using a single set of pressure equations, rather than one for each phase as in the annular flow model discussed in §5.1.5, which reduces the computational effort required. We included the effect of salinity in our model by using the result from Chapter 2 that the relative conductivity of the oil phase, given by (5.6), and therefore the total conductivities of the throats, given by (5.12), depend on the slip length. This result suggests that a change in the slip length is equivalent to change in the throat radii, and therefore we assumed that the entry pressure of the throats, (5.19), varies with the slip length (i.e. the salinity). We derived the governing equations (5.21) for the concentrations of each ion species using conservation of mass. In §5.2.4, we prescribed appropriate boundary conditions for our model. In particular, we noted that it can be appropriate to prescribe non-uniform boundary conditions for the phase-weighted pressure and saturation across the inlet or outlet nodes, in order to ensure that the pressure within each phase is uniform at the inlet and outlet.

In §5.3.1, we non-dimensionalised our model and found that the system depends on seven dimensionless parameters; the oil-water viscosity ratio $\mu^* = \mu_o/\mu_w$, the ratio of the Debye length to the average pore radius, $\epsilon_2 = (\varepsilon_w k_B T/2c_I^1 q^2)^{1/2}/R^t$, the ratio of divalent ions to monovalent ions, $c^* = c_I^2/c_I^1$, the ratio of the average throat radius to the average pore radius, $R^* = R^t/R^p$, the ratio of the saturation concentration of the oil surface to the saturation concentration of the clay surface, $s^* = s_o^*/s_c^*$, the ratio of the surface tension induced pressure to the electrostatic pressure within the thin water film, $\Gamma = 2\gamma\varepsilon_w R^t/L^{t2}q^2 s_c^{*2}$, and the ratio of the surface tension induced pressure to the applied pressure, $\Gamma_{\mathcal{P}} = \gamma/R^t\mathcal{P}$. In §5.3.2, we formulated our model using vector notation, and derived an implicit pressure explicit saturation numerical scheme, (5.61) – (5.66), to solve for the pressure $\mathbf{P}$, saturation $\mathbf{S}$, and ion concentrations, $\mathbf{c}^k$.

In §5.4, we solved (5.61) – (5.66) numerically to simulate a waterflood process. We separated the simulation into two stages. First, we performed a 'drainage' stage in which oil invades a water-filled network by the action of capillary forces. This simulates the initial formation of the oil reservoir, and is required in order to determine an oil-filled steady state. Second, we performed a 'waterflood' stage, in which the oil-filled steady state determined during the drainage stage is injected with water to remove oil until a steady state is obtained. We compared the results of a high-salinity injection with a low-salinity injection, and found that, while the initial rate of recovery was the same in both cases, the high-salinity recovery rate decreased before the low-salinity injection rate, resulting in 15% more oil being produced during the low salinity injection. We also considered the case in which a high salinity injection

is followed by a low salinity injection, simulating a tertiary oil recovery process. We found that additional oil is produced during the low-salinity injection stage, resulting in 12% more oil being produced than for a high-salinity injection alone.

In summary, we used the mathematical model for an oil slug moving through a brine-filled capillary, derived in Chapter 2, to develop a model for two-phase flow through a network. We found that our model was able to reproduce the low salinity effect observed during experiments, as both a secondary-stage process and as a tertiary-stage process. In Chapter 6, we will use the method of multiple scales to homogenise the network model presented in this chapter, in order to derive macro-scale continuum equations for the salinity-dependent two-phase flow which will be appropriate on the core sample and oil reservoir scales.

Chapter 6

Network homogenisation

6.1 Introduction

In Chapter 5, we presented a network model for the two-phase flow of oil and water through a porous medium, in which ions are advected with the water phase. We assumed that both phases could occupy the throats and pores at any given time. We assumed that the oil is separated from the walls of the throats by a thin wetting film, and we included the effect of salinity by allowing the effective slip length on the oil-clay boundary to depend on the concentrations of each ion species. We also included the effect of entry pressure by assuming that oil can only enter the throat downstream of a pore if the capillary pressure between the two phases in the pore exceeds the entry pressure associated with the throat. We found that we are able to reproduce the low salinity effect, in which the total oil recovered during a waterflood increases as the salinity decreases.

However, one of the main issues with network models, such as the model presented in Chapter 5, is that they can be computationally expensive to run. In order to obtain useful data from a network simulation, the network needs to be large enough to be representative of the porous material being studied. Typically, this requires many thousands of pores to be included. Since the time-stepping process is limited by local, microscopic, variations in the saturation and salinity, it can take a long time to compute the variation in these quantities over a large network.

Instead of solving the network model directly, we can perform an averaging procedure on the network model in order to derive a system of simplified, computationally-efficient equations which hold over long lengthscales but accurately capture the microscale behaviour. This averaging procedure, known as 'homogenisation', requires a separation of lengthscales, in which the complexity of the heterogeneity within the porous medium occurs on a microscopic length scale which is much smaller than the

macroscopic length scale associated with the full domain. The method of multiple scales is traditionally used to derive simplified macroscale models from continuum equations that hold on the microscale, such as the derivation of Darcy's law from Stokes flow [113, 114]. In this chapter, we will present a *discrete* form of the method of multiple scales which we use to homogenise our network model, assuming that the network is periodic on the microscopic scale. Through this homogenisation technique, we will derive a system of continuum equations for the pressure, saturation, and ion concentrations, averaged over the microscopic length scale, in which the complexity of the network structure is contained within the parameters of the continuum equations.

In §6.2, we will apply the multiple-scales method to a simple model of single-phase flow through a one-dimensional network, which we assume to be periodic on the microscale. We will derive a system of continuum equations for the macroscale pressure and flux through the network, and compute the effective permeability of the network in terms of the microscale network structure. In §6.3, we will homogenise a simplified form of our two-phase network model, in which we neglect the effects of entry pressure by prescribing the saturation in a given throat to be equal to the saturation in the upstream pore, in two dimensions. We will derive macroscale continuum equations for the pressure, saturation, and ion concentrations in §6.3.2, §6.3.3, and §6.3.4, respectively, and, in §6.3.5, we will perform numerical waterflood simulations to compare the homogenised model with the full network model in the one-dimensional case. We will compare the homogenised model in the high-salinity and low-salinity regimes, and derive an expression for the speed of the saturation front. In §6.4.1 and §6.4.2, we will homogenise our full network model, including the effects of entry pressure, in one dimension. We will derive a system of continuum equations for the saturation and ion concentrations, as well as an expression relating the saturation in the pores (which may contain trapped oil) to the saturation of the fluid within the throats. In §6.4.3, we will perform numerical waterflood simulations to compare the homogenised model with the full network model. We will compare the total oil recovery in the high-salinity and low-salinity regimes, and study how the dimensionless parameters in the model affect the relative increase in the oil recovery when performing a low-salinity waterflood. In §6.4.4, we will compare our homogenised network model to the Buckley-Leverett model for two phase flow through porous media, and study the effect of salinity on the fractional flow function. Finally, in §6.5, we will discuss our findings.

6.1.1 Previous work

Homogenisation approaches are typically applied to discrete models in the context of random walks on lattices. Such models arise, for example, due to particle movement in crystalline solids, in which the discrete particle motion on the microscale is found to act diffusively on the macroscopic scale [34]. Kehr *et al.* [49] model the movement of interstitial atoms within crystals using a discrete lattice model. They assume periodicity on the microscale in order to derive an expression for the effective diffusivity on the macroscale for the case in which the net rate at which atoms move into a lattice site is equal to the net rate at which atoms leave the site. Braun & Sholl [14] later generalise this result to determine the effective diffusivity for a network with arbitrary transition rates. Koza [56] also determine the effective diffusivity for particle motion on an arbitrary lattice, comparing the results for a continuous-time formalism with a discrete-time formalism. They find that the macroscale drift coefficient is the same in each case, but that the effective diffusivity differs in the two cases. However, they are able to show, by making an appropriate transformation to the transition probabilities in the discrete-time case, that the diffusivities match in a suitable limit. Chapman & Shabala [21] use a discrete form of the method of multiple scales to derive the macroscale properties of a random walk on an arbitrary periodic lattice. The effective diffusivity recovered through their method agrees with the result found by Kehr *et al.* [49]. However, in contrast to the methods used by the previous authors, their approach retains the microscale information since the solution they obtain is given by the discrete probability density function on the periodic cell modulated by the macroscale diffusivity.

Discrete homogenisation methods have also been used to study network models in which diffusion occurs on the microscale. Kropat & Meyer-Nieberg [57] use a separation of scales method to determine the effective macroscale model for a singularly perturbed diffusion-advection-reaction system on a periodic network, and derive the effective macroscale equation coefficients in terms of the microscale network structure. They consider the limit in which the microscale diffusive term is small, and demonstrate good agreement between the the homogenised model and the full network model. The work by Kropat & Meyer-Nieberg is the discrete analogy of the work by Rubinstein & Mauri [86], in which they use the method of multiple scales to homogenise the continuum advection-diffusion equation on the microscale, assuming a periodic domain. For both the discrete microscale model [57], and the continuum microscale model [86], the homogenised macroscale equations are of the same form.

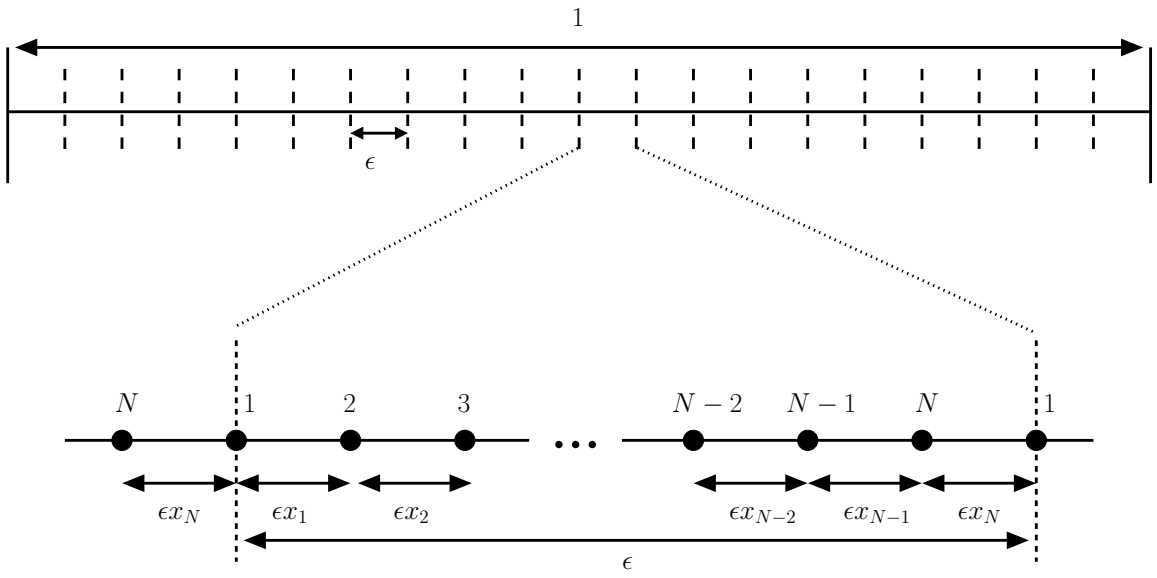


Figure 6.1: Schematic diagram of a one-dimensional network of unit length, constructed from a repeated cell of length ϵ.

6.2 Single-phase, one-dimensional flow

To demonstrate the discrete multiple scales method, we consider the simple example of single-phase flow through a porous medium. We model the porous structure as a network, in which the nodes represent pores and the edges represent throats. For simplicity, we restrict our attention to a one-dimensional network. We suppose that the network has unit length, and is constructed from a repeated cell of length ϵ. We suppose that each cell contains N nodes, and that the distance between nodes i and $i+1$ in the *cell* is ϵx_i, for $1 \leq i \leq N$, as shown in Figure 6.1. Since the total length of the cell is ϵ, we therefore impose that $\sum_{i=1}^{N} x_i = 1$. We define p_i to be the dimensionless pressure at the i^{th} pore in the *network*, $Q_{i,i+1}$ to be the dimensionless flux through the throat connecting pores i and $i+1$, and $g_{i,i+1}$ to be the dimensionless conductance of the throat connecting pores i and $i+1$, so that

$$Q_{i,i+1} = g_{i,i+1}\left(p_i - p_{i+1}\right). \tag{6.1}$$

We assume that the total flux through each pore is conserved, which reads

$$Q_{i-1,i} = Q_{i,i+1}, \qquad \text{for all } i. \tag{6.2}$$

6.2.1 Multiple scales

We suppose that the length of the repeated cell is small in comparison to the total length of the network, $\epsilon \ll 1$, and exploit these two lengthscales by performing a multiple-scales analysis. In the traditional multiple-scales method [10, 35, 88], the microscopic and macroscopic length scales are both assumed to be continuous. However, in our network model, the position of the i^{th} pore is given by $X_i = \sum_{k=1}^{i} x_k$, and therefore $\{X_i\}$ defines our microscale with respect to the *discrete* pore index i. We define the macroscopic length scale to be $x = \epsilon X_i$, which we treat as continuous in the limit $\epsilon \to 0$.

We suppose that the variables in the model depend on both lengthscales independently. The additional freedom this provides enables us to impose periodicity on the microscale, while still allowing the solution to vary on the macroscale. This enables us to determine the small-scale behaviour independently of the overall solution, and to rigorously derive a simplified system of equations for the macroscopic variation, in which the complexity of the small-scale is captured in the parameters of the equation.

We treat the two length scales as independent by writing $p_i = p_i(x)$, and we define the cyclic notation $\bar{i} = (i - 1 \mod N) + 1$. We impose periodicity on the small scale by setting $p_i(x) = p_{\bar{i}}(x)$ for all i. Substituting (6.1) into (6.2), writing the equation in terms of $p_{\bar{i}}(x)$, and using the fact that nodes $\overline{i-1}$ and $\overline{i+1}$ are at a distance $-\epsilon x_{i-1}$ and ϵx_i, respectively, relative to node $\bar{i}$ on the macroscopic scale, gives

$$\left(g_{\overline{i-1}\,\bar{i}} + g_{\bar{i}\,\overline{i+1}}\right) p_{\bar{i}}(x) - g_{\overline{i-1}\,\bar{i}} p_{\overline{i-1}}(x - \epsilon x_{i-1}) - g_{\bar{i}\,\overline{i+1}} p_{\overline{i+1}}(x + \epsilon x_i) = 0. \tag{6.3}$$

We Taylor expand (6.3) about x to find that

$$\begin{aligned}\left(g_{\overline{i-1}\,\bar{i}} + g_{\bar{i}\,\overline{i+1}}\right) p_{\bar{i}} - g_{\overline{i-1}\,\bar{i}} p_{\overline{i-1}} - g_{\bar{i}\,\overline{i+1}} p_{\overline{i+1}} + \epsilon \left(x_{i-1} g_{\overline{i-1}\,\bar{i}} \frac{\mathrm{d}p_{\overline{i-1}}}{\mathrm{d}x} - x_i g_{\bar{i}\,\overline{i+1}} \frac{\mathrm{d}p_{\overline{i+1}}}{\mathrm{d}x} \right) \\ - \frac{\epsilon^2}{2} \left(x_{i-1}^2 g_{\overline{i-1}\,\bar{i}} \frac{\mathrm{d}^2 p_{\overline{i-1}}}{\mathrm{d}x^2} + x_i^2 g_{\bar{i}\,\overline{i+1}} \frac{\mathrm{d}^2 p_{\overline{i+1}}}{\mathrm{d}x^2} \right) = O(\epsilon^3),\end{aligned} \tag{6.4}$$

which we write as

$$\boldsymbol{A}\mathbf{p} - \epsilon \boldsymbol{B} \frac{\mathrm{d}\mathbf{p}}{\mathrm{d}x} - \epsilon^2 \boldsymbol{C} \frac{\mathrm{d}^2 \mathbf{p}}{\mathrm{d}x^2} = O(\epsilon^3), \tag{6.5}$$

where $\mathbf{p}(x)$ is the vector form of $p_{\bar{i}}(x)$, and

$$\boldsymbol{A} = \begin{pmatrix} g_{n1}+g_{12} & -g_{12} & 0 & 0 & \cdots & -g_{n1} \\ -g_{12} & g_{12}+g_{23} & -g_{23} & 0 & \cdots & 0 \\ 0 & -g_{23} & g_{23}+g_{34} & -g_{34} & \cdots & 0 \\ 0 & 0 & -g_{34} & g_{34}+g_{45} & \cdots & 0 \\ \vdots & \vdots & \vdots & \vdots & \ddots & \vdots \\ -g_{n1} & 0 & 0 & 0 & \cdots & g_{n-1,n}+g_{n1} \end{pmatrix}, \tag{6.6}$$

$$\boldsymbol{B} = \begin{pmatrix} 0 & x_1 g_{12} & 0 & 0 & \cdots & -x_n g_{n1} \\ -x_1 g_{12} & 0 & x_2 g_{23} & 0 & \cdots & 0 \\ 0 & -x_2 g_{23} & 0 & x_3 g_{34} & \cdots & 0 \\ 0 & 0 & -x_3 g_{34} & 0 & \cdots & 0 \\ \vdots & \vdots & \vdots & \vdots & \ddots & \vdots \\ x_n g_{n1} & 0 & 0 & 0 & \cdots & 0 \end{pmatrix}, \tag{6.7}$$

$$\boldsymbol{C} = \frac{1}{2}\begin{pmatrix} 0 & x_1^2 g_{12} & 0 & 0 & \cdots & x_n^2 g_{n1} \\ x_1^2 g_{12} & 0 & x_2^2 g_{23} & 0 & \cdots & 0 \\ 0 & x_2^2 g_{23} & 0 & x_3^2 g_{34} & \cdots & 0 \\ 0 & 0 & x_3^2 g_{34} & 0 & \cdots & 0 \\ \vdots & \vdots & \vdots & \vdots & \ddots & \vdots \\ x_n^2 g_{n1} & 0 & 0 & 0 & \cdots & 0 \end{pmatrix}. \tag{6.8}$$

6.2.2 Asymptotic solution

We look for an asymptotic solution for $\mathbf{p}$ of the form $\mathbf{p} \sim \mathbf{p}_0 + \epsilon \mathbf{p}_1 + \epsilon^2 \mathbf{p}_2 + \ldots$, and substitute into (6.5) to find that, at leading order in ϵ,

$$\boldsymbol{A}\mathbf{p}_0 = 0, \tag{6.9}$$

which has solution

$$\mathbf{p}_0 = p(x)\mathbf{u}, \tag{6.10}$$

where $\mathbf{u} = (1, 1, \ldots, 1)^T$, and $p(x)$ is a function, to be determined, which depends only on the macroscale. The solution (6.10) corresponds to uniform pressure within each cell on the microscopic scale, which may vary on the macroscopic scale according to $p(x)$. We can think of $p(x)$ as the macroscopic 'homogenised' pressure. However, $p(x)$ is not determined from the leading-order problem and so we proceed to higher orders in ϵ in order to find an appropriate solvability condition which p must satisfy.

Equating the first-order terms in (6.5), and substituting for $\mathbf{p}_0$ using (6.10), yields

$$\boldsymbol{A}\mathbf{p}_1 - \frac{\mathrm{d}p}{\mathrm{d}x}\boldsymbol{B}\mathbf{u} = 0. \tag{6.11}$$

Since $\boldsymbol{A}\mathbf{u} = 0$, this has the solution

$$\mathbf{p}_1 = \frac{\mathrm{d}p}{\mathrm{d}x}\mathbf{w} + f(x)\mathbf{u}, \tag{6.12}$$

where $f(x)$ is a function which depends only on the large length scale, x, and $\mathbf{w}$ is any solution to

$$\boldsymbol{A}\mathbf{w} = \boldsymbol{B}\mathbf{u}. \tag{6.13}$$

Equation (6.13) is known as a 'cell problem', which depends only on the microscale properties of the network (i.e. g_{ij} and x_i). From (6.12), we observe that the magnitude of the first-order variations[1] in the pressure in a particular cell are given by the leading-order pressure gradient multiplied by $\mathbf{w}$, and therefore the solution to the cell problem, $\mathbf{w}$, captures the relative variations in the pressure throughout a particular cell. Hence, by solving (6.13), we determine the microscale behaviour independently of the macroscale solution. This is similar to the derivation of Darcy flow we presented in §4.2, in which the cell problem described the small-scale variation of the flow velocity within a particular cell.

We are still unable to determine $p(x)$ from the $O(\epsilon)$ problem, so we proceed to the next order. Equating $O(\epsilon^2)$ terms in (6.5), and substituting in the expressions for $\mathbf{p}_0$ and $\mathbf{p}_1$, yields

$$\boldsymbol{A}\mathbf{p}_2 - \frac{\mathrm{d}f}{\mathrm{d}x}\boldsymbol{B}\mathbf{u} - (\boldsymbol{B}\mathbf{w} + \boldsymbol{C}\mathbf{u})\frac{\mathrm{d}^2p}{\mathrm{d}x^2} = 0. \tag{6.14}$$

Since $\boldsymbol{A}$ is symmetric, $\mathbf{u}^T\boldsymbol{A} = 0$ and therefore the Fredholm Alternative Theorem [83] implies that the appropriate solvability condition for (6.14) is found by applying $\mathbf{u}^T$ to (6.14), which yields

$$\frac{\mathrm{d}f}{\mathrm{d}x}\mathbf{u}^T\boldsymbol{B}\mathbf{u} + \left(\mathbf{u}^T\boldsymbol{B}\mathbf{w} + \mathbf{u}^T\boldsymbol{C}\mathbf{u}\right)\frac{\mathrm{d}^2p}{\mathrm{d}x^2} = 0. \tag{6.15}$$

From (6.7), since $\boldsymbol{B}$ is antisymmetric, $\mathbf{u}^T\boldsymbol{B}\mathbf{u} = 0$, and therefore (6.15) reduces to

$$\frac{\mathrm{d}^2p}{\mathrm{d}x^2} = 0. \tag{6.16}$$

6.2.3 Flux

By (6.2), the flux through each throat is equal to the flux through the network, which we write as $Q_{\bar{i}\,\overline{i+1}} = Q$ for all i. Using the fact that $\sum_i x_i = 1$, we write the flux as

$$Q = Q\sum_{i=1}^{N} x_{\bar{i}} = \sum_{i=1}^{N} x_{\bar{i}} Q_{\bar{i}\,\overline{i+1}}. \tag{6.17}$$

[1]The first-order pressure also depends on the macroscale function f, however this does not affect the pore-to-pore variation within a particular cell.

Substituting (6.1) into (6.17), and rearranging the sum, yields

$$Q = \sum_{i=1}^{N} x_{\bar{i}} g_{\bar{i}\,\overline{i+1}}(p_{\bar{i}} - p_{\overline{i+1}}) = \sum_{i=1}^{N} \left(x_{\overline{i-1}} g_{\overline{i-1}\,\bar{i}} p_{\overline{i-1}} - x_{\bar{i}} g_{\bar{i}\,\overline{i+1}} p_{\overline{i+1}} \right) = -\mathbf{u}^T \boldsymbol{B} \mathbf{p}. \quad (6.18)$$

Substituting (6.10) and (6.12) into (6.18) gives

$$Q = -\mathbf{u}^T \boldsymbol{B} \mathbf{p} \sim -\mathbf{u}^T \boldsymbol{B} \mathbf{p}_0 - \epsilon \mathbf{u}^T \boldsymbol{B} \mathbf{p}_1 + O(\epsilon^2) \quad (6.19)$$

$$= -\mathbf{u}^T \boldsymbol{B} \mathbf{u} p_0 - \epsilon \mathbf{u}^T \boldsymbol{B} \mathbf{w} \frac{\mathrm{d}p}{\mathrm{d}x} - \epsilon \mathbf{u}^T \boldsymbol{B} \mathbf{u} f + O(\epsilon^2) \quad (6.20)$$

$$= -\epsilon \mathbf{u}^T \boldsymbol{B} \mathbf{w} \frac{\mathrm{d}p}{\mathrm{d}x}, \quad (6.21)$$

where we have used the fact that $\mathbf{u}^T \boldsymbol{B} \mathbf{u} = 0$.

Since the total network has unit length, and each cell has length ϵ, the number of cells in the network is $1/\epsilon$. The total flux through the network, q, is given by the flux through each cell multiplied by the number of cells, $q = Q/\epsilon$. Hence, in terms of p and q, (6.21) and (6.16) read

$$q = -K \frac{\mathrm{d}p}{\mathrm{d}x}, \qquad \frac{\mathrm{d}q}{\mathrm{d}x} = 0, \quad (6.22)$$

where

$$K = \mathbf{u}^T \boldsymbol{B} \mathbf{w}. \quad (6.23)$$

We observe that the homogenised system of equations for the macroscale pressure and flux, (6.22), are of the form of a one-dimensional Darcy flow model, where K is the permeability of the network. Traditionally, the permeability, and therefore the microscale information which determines the permeability, is defined as an input to the Darcy flow model. However, as a result of the homogenisation process, the microscale information is contained in the expression for K, which we can compute directly in terms of the geometric properties of the network, g_{ij} and x_i.

6.3 Homogenisation of a two-dimensional network, neglecting the effects of entry pressure

Having outlined the steps required to homogenise a simple network model in §6.2, we now turn our attention to a more complicated example. We consider two-phase flow through a two-dimensional network of unit length and width, in which ions are advected with the water phase. We suppose that the network is constructed from a repeated cell of length ϵL_x and width ϵL_y, and we suppose that each cell contains N

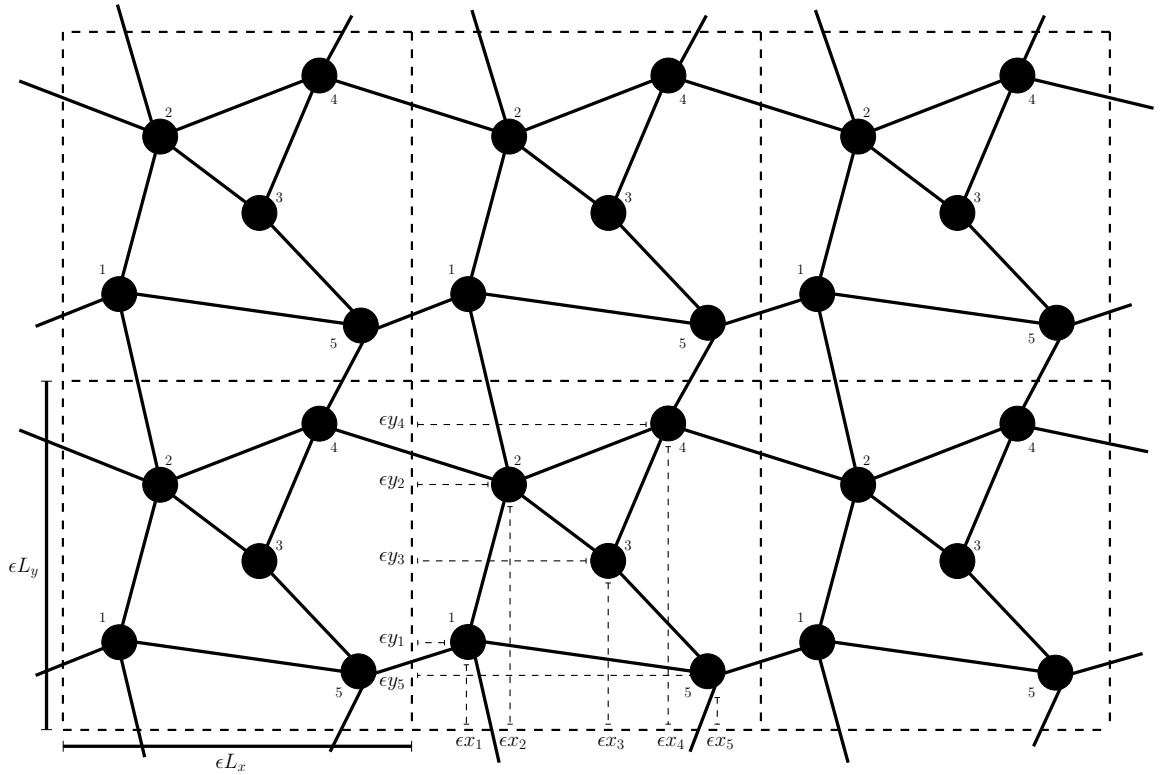


Figure 6.2: Schematic diagram of a two-dimensional network constructed from a repeated cell of size $(\epsilon L_x, \epsilon L_y)$. The coordinates of the i^{th} node in a particular cell, relative to the lower left corner of the cell, are $(\epsilon x_i, \epsilon y_i)$.

pores, represented by nodes, at positions $(\epsilon x_i, \epsilon y_i)$ relative to the lower left corner of the cell, for $1 \leq i \leq N$, as shown in Figure 6.2.

We suppose that the throat connecting pores i and j has radius R_{ij}^t and length L_{ij}^t, which we represent by an edge in our network model. If pores i and j are not connected by a throat, we suppose that $R_{ij}^t = L_{ij}^t = 0$. We suppose that the two-phase flow of oil and water occurs on the network according to the dimensionless model presented in Chapter 5, (5.39) – (5.50). We define P_i, S_i, and c_i^k to be the phase-weighted pressure, water saturation, and concentration of the k^{th} ion species, respectively, at the i^{th} node in the network. For simplicity, we neglect the effects of entry pressure in our model, so that the saturation and ion concentrations in the throat connecting pores i and j are given by

$$S_{ij}^t = \begin{cases} S_i, & \text{if } P_i \geq P_j, \\ S_j, & \text{if } P_i < P_j, \end{cases} \qquad c_{ij}^k = \begin{cases} c_i^k, & \text{if } P_i \geq P_j, \\ c_j^k, & \text{if } P_i < P_j. \end{cases} \tag{6.24}$$

If pores i and j are not connected by a throat, we suppose that $S_{ij}^t = c_{ij}^k = 0$. In §6.4, we will discuss the consequences of neglecting the effects of entry pressure from our model, and consider the case in which these effects are included.

In order to perform the Taylor expansions required in the multiple scales method, we approximate the discontinuous expressions, (6.24), with the continuous equations

$$S_{ij}^t = \frac{1}{2}\left[S_i + S_j + (S_j - S_i)\tanh\left(\frac{P_j - P_i}{\delta}\right)\right], \tag{6.25}$$

$$c_{ij}^k = \frac{1}{2}\left[c_i^k + c_j^k + (c_j^k - c_i^k)\tanh\left(\frac{P_j - P_i}{\delta}\right)\right], \tag{6.26}$$

where δ is a small parameter, which we take to be $\epsilon \ll \delta \ll 1$. In the limit $\delta \to 0$, equations (6.25) and (6.26) approach (6.24).

With these simplifications, the equations which hold at node i read

$$\sum_j G_{ij}(P_i - P_j) = 0, \tag{6.27}$$

$$V_i \frac{\mathrm{d}S_i}{\mathrm{d}t} = -\frac{1}{2}\sum_j G_{ij}\left(S_i + S_j + (S_j - S_i)\tanh\left(\frac{P_j - P_i}{\delta}\right)\right)(P_i - P_j), \tag{6.28}$$

$$\begin{aligned} V_i \frac{\mathrm{d}\left(c_i^k S_i\right)}{\mathrm{d}t} = &-\frac{1}{4}\sum_j G_{ij}\left(c_i^k + c_j^k + (c_j^k - c_i^k)\tanh\left(\frac{P_j - P_i}{\delta}\right)\right) \\ &\times \left(S_i + S_j + (S_j - S_i)\tanh\left(\frac{P_j - P_i}{\delta}\right)\right)(P_i - P_j), \end{aligned} \tag{6.29}$$

where

$$G_{ij} = \frac{{R_{ij}^t}^4}{L_{ij}^t} \frac{1 + 2\frac{\lambda_s(c_{ij}^k)}{R_{ij}^t}}{\left(1 + 2\frac{\lambda_s(c_{ij}^k)}{R_{ij}^t}\right) S_{ij}^t + \mu^* \left(1 - S_{ij}^t\right)}, \tag{6.30}$$

if pores i and j are connected ($G_{ij} = 0$ otherwise), $\lambda_s(c^k)$ is the dimensionless effective slip length at the oil-solid interface, which we assume depends on the salinity according to (5.7), which reads

$$\lambda_s(c^1, c^2) = \frac{\epsilon_2 \left(\mu^* - 1\right)}{(c^1 + 4c^* c^2)^{1/2}} \cosh^{-1}\left(\frac{s^* \sigma_{c0} \sigma_{o0} + \sqrt{\left(\sigma_{c0}^2 + \Gamma\right)\left(s^{*2} \sigma_{o0}^2 + \Gamma\right)}}{\Gamma}\right), \tag{6.31}$$

where σ_{c0} and σ_{o0} are the salinity-dependent surface charge densities of the oil and clay surfaces, given by (2.107), and the dimensionless parameters μ^*, Γ, ϵ_2, c^*, and s^* are defined in Chapter 2.

From (6.25), (6.26) and (6.30), we can write G_{ij} in terms of the pressures, saturations, and ion concentrations in the pores, i.e.

$$G_{ij} = G_{ij}(S_{ij}, c_{ij}^k) = G_{ij}(P_i, P_j, S_i, S_j, c_i^k, c_j^k). \tag{6.32}$$

6.3.1 Multiple scales

We introduce the macroscale coordinate system, (x, y), using the same approach as in §6.2, and perform a multiple scales analysis by supposing that the pressure, saturation, and ion concentrations depend on the microscale discrete pore index, i, and macroscopic length scale, (x, y), independently, so that $P_i(t) = P_i(x, y, t)$, $S_i(t) = S_i(x, y, t)$, and $c_i^k(t) = c_i^k(x, y, t)$. We define the notation $\bar{i} = (i - 1 \mod N) + 1$, and impose periodicity on the small scale by setting $P_i = P_{\bar{i}}$, $S_i = S_{\bar{i}}$, and $c_i^k = c_{\bar{i}}^k$.

We let $G_{\bar{i},\bar{j}}^{00}$ denote the conductance of the throat connecting pores $\bar{i}$ and $\bar{j}$ within the same cell, and let $G_{\bar{i},\bar{j}}^{rs}$ denote the conductance of the throat connecting the $\bar{i}^{\text{th}}$ pore in a cell to the $\bar{j}^{\text{th}}$ pore in the neighbouring cell at relative position $(r\epsilon L_x, s\epsilon L_y)$. Since the conductivity of a throat is independent of the direction of flow, it follows that $G_{\bar{i},\bar{j}}^{rs} = G_{\bar{j},\bar{i}}^{-r-s}$. We assume that pores may only be connected to pores within the same cell, or within a neighbouring cell, so that $r, s, \in \{-1, 0, 1\}$.

Evaluating (6.27) – (6.29) at the position of the $\bar{i}^{\text{th}}$ node, (x, y), and dropping the bar notation for convenience, yields

$$\sum_{r=-1}^{1} \sum_{s=-1}^{1} \sum_{j=1}^{N} G_{ij}^{rs} \left(x, y, x + \epsilon \Delta x_{ij}^r, y + \epsilon \Delta y_{ij}^s, t\right) \times \left[P_i(x, y, t) - P_j(x + \epsilon \Delta x_{ij}^r, y + \epsilon \Delta y_{ij}^s, t)\right] = 0, \tag{6.33}$$

$$V_i\frac{\partial S_i(x,y,t)}{\partial t} = -\frac{1}{2}\sum_{r=-1}^{1}\sum_{s=-1}^{1}\sum_{j=1}^{N} G_{ij}^{rs}\left(x,y,x+\epsilon\Delta x_{ij}^r, y+\epsilon\Delta y_{ij}^s,t\right)$$
$$\times\left[S_i(x,y,t)+S_j(x+\epsilon\Delta x_{ij}^r,y+\epsilon\Delta y_{ij}^s,t)\right.$$
$$\left.+\left(S_j(x+\epsilon\Delta x_{ij}^r,y+\epsilon\Delta y_{ij}^s,t)-S_i(x,y,t)\right)\tanh\left(\frac{P_j(x+\epsilon\Delta x_{ij}^r,y+\epsilon\Delta y_{ij}^s,t)-P_i(x,y,t)}{\delta}\right)\right]$$
$$\times\left[P_i(x,y,t)-P_j(x+\epsilon\Delta x_{ij}^r,y+\epsilon\Delta y_{ij}^s,t)\right], \quad (6.34)$$

$$V_i\frac{\partial\left(c_i^k(x,y,t)S_i(x,y,t)\right)}{\partial t} = -\frac{1}{4}\sum_{r=-1}^{1}\sum_{s=-1}^{1}\sum_{j=1}^{N} G_{ij}^{rs}\left(x,y,x+\epsilon\Delta x_{ij}^r, y+\epsilon\Delta y_{ij}^s,t\right)$$
$$\times\left[c_i^k(x,y,t)+c_j^k(x+\epsilon\Delta x_{ij}^r,y+\epsilon\Delta y_{ij}^s,t)\right.$$
$$\left.+\left(c_j^k(x+\epsilon\Delta x_{ij}^r,y+\epsilon\Delta y_{ij}^s,t)-c_i^k(x,y,t)\right)\tanh\left(\frac{P_j(x+\epsilon\Delta x_{ij}^r,y+\epsilon\Delta y_{ij}^s,t)-P_i(x,y,t)}{\delta}\right)\right]$$
$$\times\left[S_i(x,y,t)+S_j(x+\epsilon\Delta x_{ij}^r,y+\epsilon\Delta y_{ij}^s,t)\right.$$
$$\left.+\left(S_j(x+\epsilon\Delta x_{ij}^r,y+\epsilon\Delta y_{ij}^s,t)-S_i(x,y,t)\right)\tanh\left(\frac{P_j(x+\epsilon\Delta x_{ij}^r,y+\epsilon\Delta y_{ij}^s,t)-P_i(x,y,t)}{\delta}\right)\right]$$
$$\times\left[P_i(x,y,t)-P_j(x+\epsilon\Delta x_{ij}^r,y+\epsilon\Delta y_{ij}^s,t)\right], \quad (6.35)$$

where

$$\Delta x_{ij}^r = -rL_x + x_j - x_i, \qquad \Delta y_{ij}^s = -sL_y + y_j - y_i, \quad (6.36)$$

and we have written

$$G_{ij}^{rs}(x,y,\tilde{x},\tilde{y},t) = G_{ij}^{rs}(P_i(x,y,t),P_j(\tilde{x},\tilde{y},t),S_i(x,y,t),S_j(\tilde{x},\tilde{y},t),c_i^k(x,y,t),c_j^k(\tilde{x},\tilde{y},t)), \quad (6.37)$$

where (x,y) and $(\tilde{x},\tilde{y})$ correspond to the coordinates of the i^{th} and j^{th} node, respectively.

Taylor expanding (6.33) – (6.35) about (x,y) yields

$$\sum_{r=-1}^{1}\sum_{s=-1}^{1}\sum_{j=1}^{N}\left\{G_{ij}^{rs}+\epsilon\left[\Delta x_{ij}^r\frac{\partial G_{ij}^{rs}}{\partial\tilde{x}}+\Delta y_{ij}^s\frac{\partial G_{ij}^{rs}}{\partial\tilde{y}}\right]\right.$$
$$\left.+\frac{\epsilon^2}{2}\left[(\Delta x_{ij}^r)^2\frac{\partial^2 G_{ij}^{rs}}{\partial\tilde{x}^2}+(\Delta y_{ij}^s)^2\frac{\partial^2 G_{ij}^{rs}}{\partial\tilde{y}^2}+2\Delta x_{ij}^r\Delta y_{ij}^s\frac{\partial^2 G_{ij}^{rs}}{\partial\tilde{x}\partial\tilde{y}}\right]\right\}$$
$$\times\left\{P_i-P_j-\epsilon\left[\Delta x_{ij}^r\frac{\partial P_j}{\partial x}+\Delta y_{ij}^s\frac{\partial P_j}{\partial y}\right]\right.$$
$$\left.-\frac{\epsilon^2}{2}\left[(\Delta x_{ij}^r)^2\frac{\partial^2 P_j}{\partial x^2}+(\Delta y_{ij}^s)^2\frac{\partial^2 P_j}{\partial y^2}+2\Delta x_{ij}^r\Delta y_{ij}^s\frac{\partial^2 P_j}{\partial x\partial y}\right]\right\}=O(\epsilon^3), \quad (6.38)$$

$$V_i\frac{\partial S_i}{\partial t} = -\frac{1}{2}\sum_{r=-1}^{1}\sum_{s=-1}^{1}\sum_{j=1}^{N}\left\{G_{ij}^{rs} + \epsilon\left[\Delta x_{ij}^r\frac{\partial G_{ij}^{rs}}{\partial\tilde{x}} + \Delta y_{ij}^s\frac{\partial G_{ij}^{rs}}{\partial\tilde{y}}\right] + O(\epsilon^2)\right\}$$
$$\times\left\{S_i + S_j + (S_j - S_i)\tanh\left(\frac{P_j - P_i}{\delta}\right)\right.$$
$$+\epsilon\left[\Delta x_{ij}^r\frac{\partial S_j}{\partial x} + \Delta y_{ij}^s\frac{\partial S_j}{\partial y}\right]\left[1 + \tanh\left(\frac{P_j - P_i}{\delta}\right)\right]$$
$$\left. + \frac{\epsilon}{\delta}(S_j - S_i)\,\mathrm{sech}^2\left(\frac{P_j - P_i}{\delta}\right)\left[\Delta x_{ij}^r\frac{\partial P_j}{\partial x} + \Delta y_{ij}^s\frac{\partial P_j}{\partial y}\right] + O(\epsilon^2)\right\}$$
$$\times\left\{P_i - P_j - \epsilon\left[\Delta x_{ij}^r\frac{\partial P_j}{\partial x} + \Delta y_{ij}^s\frac{\partial P_j}{\partial y}\right]\right.$$
$$\left. -\frac{\epsilon^2}{2}\left[(\Delta x_{ij}^r)^2\frac{\partial^2 P_j}{\partial x^2} + (\Delta y_{ij}^s)^2\frac{\partial^2 P_j}{\partial y^2} + 2\Delta x_{ij}^r\Delta y_{ij}^s\frac{\partial^2 P_j}{\partial x\partial y}\right]\right\} + O(\epsilon^3), \quad (6.39)$$

$$V_i\frac{\partial\left(c_i^k S_i\right)}{\partial t} = -\frac{1}{4}\sum_{r=-1}^{1}\sum_{s=-1}^{1}\sum_{j=1}^{N}\left\{G_{ij}^{rs} + \epsilon\left[\Delta x_{ij}^r\frac{\partial G_{ij}^{rs}}{\partial\tilde{x}} + \Delta y_{ij}^s\frac{\partial G_{ij}^{rs}}{\partial\tilde{y}}\right] + O(\epsilon^2)\right\}$$
$$\times\left\{c_i^k + c_j^k + (c_j^k - c_i^k)\tanh\left(\frac{P_j - P_i}{\delta}\right)\right.$$
$$+\epsilon\left[\Delta x_{ij}^r\frac{\partial c_j^k}{\partial x} + \Delta y_{ij}^s\frac{\partial c_j^k}{\partial y}\right]\left[1 + \tanh\left(\frac{P_j - P_i}{\delta}\right)\right]$$
$$\left. + \frac{\epsilon}{\delta}\left(c_j^k - c_i^k\right)\mathrm{sech}^2\left(\frac{P_j - P_i}{\delta}\right)\left[\Delta x_{ij}^r\frac{\partial P_j}{\partial x} + \Delta y_{ij}^s\frac{\partial P_j}{\partial y}\right] + O(\epsilon^2)\right\}$$
$$\times\left\{S_i + S_j + (S_j - S_i)\tanh\left(\frac{P_j - P_i}{\delta}\right)\right.$$
$$+\epsilon\left[\Delta x_{ij}^r\frac{\partial S_j}{\partial x} + \Delta y_{ij}^s\frac{\partial S_j}{\partial y}\right]\left[1 + \tanh\left(\frac{P_j - P_i}{\delta}\right)\right]$$
$$\left. + \frac{\epsilon}{\delta}(S_j - S_i)\,\mathrm{sech}^2\left(\frac{P_j - P_i}{\delta}\right)\left[\Delta x_{ij}^r\frac{\partial P_j}{\partial x} + \Delta y_{ij}^s\frac{\partial P_j}{\partial y}\right] + O(\epsilon^2)\right\}$$
$$\times\left\{P_i - P_j - \epsilon\left[\Delta x_{ij}^r\frac{\partial P_j}{\partial x} + \Delta y_{ij}^s\frac{\partial P_j}{\partial y}\right]\right.$$
$$\left. -\frac{\epsilon^2}{2}\left[(\Delta x_{ij}^r)^2\frac{\partial^2 P_j}{\partial x^2} + (\Delta y_{ij}^s)^2\frac{\partial^2 P_j}{\partial y^2} + 2\Delta x_{ij}^r\Delta y_{ij}^s\frac{\partial^2 P_j}{\partial x\partial y}\right]\right\} + O(\epsilon^3), \quad (6.40)$$

where $\partial/\partial\tilde{x}$ and $\partial/\partial\tilde{y}$ denote the derivatives with respect to the spatial coordinate of the j^{th} node. For the first-order derivatives this reads

$$\frac{\partial G_{ij}^{rs}(P_i, P_j, S_i, S_j, c_i^k, c_j^k)}{\partial\tilde{x}} = \frac{\partial G_{ij}^{rs}}{\partial P_j}\frac{\partial P_j}{\partial\tilde{x}} + \frac{\partial G_{ij}^{rs}}{\partial S_j}\frac{\partial S_j}{\partial\tilde{x}} + \sum_k\frac{\partial G_{ij}^{rs}}{\partial c_j^k}\frac{\partial c_j^k}{\partial\tilde{x}}, \quad (6.41)$$

$$\frac{\partial G_{ij}^{rs}(P_i, P_j, S_i, S_j, c_i^k, c_j^k)}{\partial\tilde{y}} = \frac{\partial G_{ij}^{rs}}{\partial P_j}\frac{\partial P_j}{\partial\tilde{y}} + \frac{\partial G_{ij}^{rs}}{\partial S_j}\frac{\partial S_j}{\partial\tilde{y}} + \sum_k\frac{\partial G_{ij}^{rs}}{\partial c_j^k}\frac{\partial c_j^k}{\partial\tilde{y}}. \quad (6.42)$$

We will solve (6.38) – (6.40) by considering each equation separately. From (6.38), we will determine the form of the pressure, which we will then use as an input in (6.39)

to determine the form of the saturation. We will then use both the saturation and pressure as inputs in (6.40) to determine the concentrations of each ion species.

6.3.2 Pressure

To determine the macroscale pressure in the network, we write (6.38) in vector form, which reads

$$\boldsymbol{A}\mathbf{P} - \epsilon\left(\boldsymbol{B}_x\frac{\partial \mathbf{P}}{\partial x} + \boldsymbol{B}_y\frac{\partial \mathbf{P}}{\partial y} + \boldsymbol{B}'_x\mathbf{P} + \boldsymbol{B}'_y\mathbf{P}\right) - \epsilon^2\left(\boldsymbol{C}_{xx}\frac{\partial^2 \mathbf{P}}{\partial x^2} + 2\boldsymbol{C}_{xy}\frac{\partial^2 \mathbf{P}}{\partial x \partial y} + \boldsymbol{C}_{yy}\frac{\partial^2 \mathbf{P}}{\partial y^2}\right.$$
$$\left. + \boldsymbol{C}'_{xx}\frac{\partial \mathbf{P}}{\partial x} + \boldsymbol{C}'_{yx}\frac{\partial \mathbf{P}}{\partial x} + \boldsymbol{C}'_{xy}\frac{\partial \mathbf{P}}{\partial y} + \boldsymbol{C}'_{yy}\frac{\partial \mathbf{P}}{\partial y} + \boldsymbol{C}''\mathbf{P}\right) = 0, \quad (6.43)$$

where $\mathbf{P}$ is the vector form of P_i, and

$$\boldsymbol{A}_{ij} = \delta_{ij}\left(\sum_{r=-1}^{1}\sum_{s=-1}^{1}\sum_{k=1}^{N} G_{ik}^{rs}\right) - \sum_{r=-1}^{1}\sum_{s=-1}^{1} G_{ij}^{rs}, \tag{6.44}$$

$$\boldsymbol{B}_{x\,ij} = \sum_{r=-1}^{1}\sum_{s=-1}^{1} \Delta x_{ij}^{r} G_{ij}^{rs}, \tag{6.45}$$

$$\boldsymbol{B}_{y\,ij} = \sum_{r=-1}^{1}\sum_{s=-1}^{1} \Delta y_{ij}^{s} G_{ij}^{rs}, \tag{6.46}$$

$$\boldsymbol{B}'_{x\,ij} = \sum_{r=-1}^{1}\sum_{s=-1}^{1} \Delta x_{ij}^{r} \frac{\partial G_{ij}^{rs}}{\partial \tilde{x}} - \delta_{ij}\left(\sum_{r=-1}^{1}\sum_{s=-1}^{1}\sum_{k=1}^{N} \Delta x_{ik}^{r} \frac{\partial G_{ik}^{rs}}{\partial \tilde{x}}\right), \tag{6.47}$$

$$\boldsymbol{B}'_{y\,ij} = \sum_{r=-1}^{1}\sum_{s=-1}^{1} \Delta y_{ij}^{s} \frac{\partial G_{ij}^{rs}}{\partial \tilde{y}} - \delta_{ij}\left(\sum_{r=-1}^{1}\sum_{s=-1}^{1}\sum_{k=1}^{N} \Delta y_{ik}^{s} \frac{\partial G_{ik}^{rs}}{\partial \tilde{y}}\right), \tag{6.48}$$

$$\boldsymbol{C}_{xx\,ij} = \frac{1}{2}\sum_{r=-1}^{1}\sum_{s=-1}^{1} \left(\Delta x_{ij}^{r}\right)^2 G_{ij}^{rs}, \tag{6.49}$$

$$\boldsymbol{C}_{xy\,ij} = \frac{1}{2}\sum_{r=-1}^{1}\sum_{s=-1}^{1} \Delta x_{ij}^{r} \Delta y_{ij}^{s} G_{ij}^{rs}, \tag{6.50}$$

$$\boldsymbol{C}_{yy\,ij} = \frac{1}{2}\sum_{r=-1}^{1}\sum_{s=-1}^{1} \left(\Delta y_{ij}^{s}\right)^2 G_{ij}^{rs}, \tag{6.51}$$

$$\boldsymbol{C}'_{xx\,ij} = \sum_{r=-1}^{1}\sum_{s=-1}^{1} \left(\Delta x_{ij}^{r}\right)^2 \frac{\partial G_{ij}^{rs}}{\partial \tilde{x}}, \tag{6.52}$$

$$\boldsymbol{C}'_{yx\,ij} = \sum_{r=-1}^{1}\sum_{s=-1}^{1} \Delta x_{ij}^{r} \Delta y_{ij}^{s} \frac{\partial G_{ij}^{rs}}{\partial \tilde{y}}, \tag{6.53}$$

$$\boldsymbol{C}'_{xy\,ij} = \sum_{r=-1}^{1}\sum_{s=-1}^{1} \Delta x_{ij}^{r} \Delta y_{ij}^{s} \frac{\partial G_{ij}^{rs}}{\partial \tilde{x}}, \tag{6.54}$$

$$\boldsymbol{C}'_{yy\,ij} = \sum_{r=-1}^{1}\sum_{s=-1}^{1} \left(\Delta y_{ij}^{s}\right)^2 \frac{\partial G_{ij}^{rs}}{\partial \tilde{y}}, \tag{6.55}$$

$$\begin{aligned}\boldsymbol{C}''_{ij} = \sum_{r=-1}^{1}\sum_{s=-1}^{1} &(\Delta x_{ij}^{r})^2 \frac{\partial^2 G_{ij}^{rs}}{\partial \tilde{x}^2} + (\Delta y_{ij}^{s})^2 \frac{\partial^2 G_{ij}^{rs}}{\partial \tilde{y}^2} + 2\Delta x_{ij}^{r} \Delta y_{ij}^{s} \frac{\partial^2 G_{ij}^{rs}}{\partial \tilde{x} \partial \tilde{y}} \\ &- \delta_{ij}\left(\sum_{r=-1}^{1}\sum_{s=-1}^{1}\sum_{k=1}^{N} (\Delta x_{ik}^{r})^2 \frac{\partial^2 G_{ik}^{rs}}{\partial \tilde{x}^2} + (\Delta y_{ik}^{s})^2 \frac{\partial^2 G_{ik}^{rs}}{\partial \tilde{y}^2} + 2\Delta x_{ik}^{r} \Delta y_{ik}^{s} \frac{\partial^2 G_{ik}^{rs}}{\partial \tilde{x} \partial \tilde{y}}\right).\end{aligned} \tag{6.56}$$

In Appendix C, we prove the following properties of the matrices with entries given by (6.44) – (6.56) which will be of use,

$$\boldsymbol{A}\mathbf{u} = \boldsymbol{B}'_x\mathbf{u} = \boldsymbol{B}'_y\mathbf{u} = \boldsymbol{C}''\mathbf{u} = 0, \qquad \mathbf{u}^T\boldsymbol{A} = 0, \qquad \mathbf{u}^T\boldsymbol{B}_x\mathbf{u} = \mathbf{u}^T\boldsymbol{B}_y\mathbf{u} = 0. \tag{6.57}$$

We expand $\mathbf{P}$, $\boldsymbol{A}$, $\boldsymbol{B}_x$, $\boldsymbol{B}_y$, $\boldsymbol{B}'_x$, $\boldsymbol{B}'_y$, $\boldsymbol{C}_{xx}$, $\boldsymbol{C}_{xy}$, $\boldsymbol{C}_{yy}$, $\boldsymbol{C}'_{xx}$, $\boldsymbol{C}'_{yx}$, $\boldsymbol{C}'_{xy}$, $\boldsymbol{C}'_{yy}$, and $\boldsymbol{C}''$ in powers of ϵ (noting that we have to expand the matrices since they depend on P_i,

S_i, and c_i^k through G_{ij}^{rs}), and equate the leading-order terms in (6.43), to find that

$$\boldsymbol{A}_0\mathbf{P}_0 = 0, \tag{6.58}$$

which has the solution

$$\mathbf{P}_0 = P(x,y,t)\mathbf{u}. \tag{6.59}$$

This corresponds to a uniform pressure on the microscale, as in the single-phase, one-dimensional case, which may vary on the macroscopic scale. We are unable to determine P from the leading-order problem, so, using a similar method to the one-dimensional model presented in §6.2, we must proceed to higher orders to determine an appropriate solvability condition for P.

Substituting (6.59) into (6.43), equating the first-order terms, and using the fact that $\boldsymbol{A}_1\mathbf{u} = \boldsymbol{B}'_{x0}\mathbf{u} = \boldsymbol{B}'_{y0}\mathbf{u} = 0$ by (6.57), yields

$$\boldsymbol{A}_0\mathbf{P}_1 - \boldsymbol{B}_{x0}\mathbf{u}\frac{\partial P}{\partial x} - \boldsymbol{B}_{y0}\mathbf{u}\frac{\partial P}{\partial y} = 0. \tag{6.60}$$

Since $\boldsymbol{A}_0\mathbf{u} = 0$, equation (6.60) has the solution

$$\mathbf{P}_1 = \mathbf{w}_x\frac{\partial P}{\partial x} + \mathbf{w}_y\frac{\partial P}{\partial y} + f(x,y,t)\mathbf{u}, \tag{6.61}$$

which is the two-dimensional analogue of (6.12), where $\mathbf{w}_x$ and $\mathbf{w}_y$ satisfy

$$\boldsymbol{A}_0\mathbf{w}_x = \boldsymbol{B}_{x0}\mathbf{u}, \qquad \boldsymbol{A}_0\mathbf{w}_y = \boldsymbol{B}_{y0}\mathbf{u}, \tag{6.62}$$

and $f(x,y,t)$ is an arbitrary function of the macroscale variables.

Substituting (6.59) and (6.61) into (6.43), equating the second-order terms, and using the fact that $\boldsymbol{A}_1\mathbf{u} = \boldsymbol{A}_2\mathbf{u} = \boldsymbol{B}'_{x0}\mathbf{u} = \boldsymbol{B}'_{y0}\mathbf{u} = \boldsymbol{B}'_{x1}\mathbf{u} = \boldsymbol{B}'_{y1}\mathbf{u} = \boldsymbol{C}''_0\mathbf{u} = 0$ by (6.57), yields

$$\begin{aligned}
\boldsymbol{A}_0\mathbf{P}_2 + \boldsymbol{A}_1\mathbf{w}_x\frac{\partial P}{\partial x} + \boldsymbol{A}_1\mathbf{w}_y\frac{\partial P}{\partial y} - \boldsymbol{B}_{x0}\frac{\partial}{\partial x}\left(\mathbf{w}_x\frac{\partial P}{\partial x} + \mathbf{w}_y\frac{\partial P}{\partial y}\right) - \boldsymbol{B}_{y0}\frac{\partial}{\partial y}\left(\mathbf{w}_x\frac{\partial P}{\partial x} + \mathbf{w}_y\frac{\partial P}{\partial y}\right) \\
- \boldsymbol{B}_{x0}\mathbf{u}\frac{\partial f}{\partial x} - \boldsymbol{B}_{y0}\mathbf{u}\frac{\partial f}{\partial y} - \boldsymbol{B}'_{x0}\left(\mathbf{w}_x\frac{\partial P}{\partial x} + \mathbf{w}_y\frac{\partial P}{\partial y}\right) - \boldsymbol{B}'_{y0}\left(\mathbf{w}_x\frac{\partial P}{\partial x} + \mathbf{w}_y\frac{\partial P}{\partial y}\right) \\
- \boldsymbol{B}_{x1}\mathbf{u}\frac{\partial P}{\partial x} - \boldsymbol{B}_{y1}\mathbf{u}\frac{\partial P}{\partial y} - \boldsymbol{C}_{xx0}\mathbf{u}\frac{\partial^2 P}{\partial x^2} - 2\boldsymbol{C}_{xy0}\mathbf{u}\frac{\partial^2 P}{\partial x\partial y} - \boldsymbol{C}_{yy0}\mathbf{u}\frac{\partial^2 P}{\partial y^2} \\
- \boldsymbol{C}'_{xx0}\mathbf{u}\frac{\partial P}{\partial x} - \boldsymbol{C}'_{yx0}\mathbf{u}\frac{\partial P}{\partial x} - \boldsymbol{C}'_{xy0}\mathbf{u}\frac{\partial P}{\partial y} - \boldsymbol{C}'_{yy0}\mathbf{u}\frac{\partial P}{\partial y} = 0.
\end{aligned} \tag{6.63}$$

Since $\boldsymbol{A}_0$ is symmetric, $\mathbf{u}^T\boldsymbol{A}_0 = 0$, and therefore the Fredholm Alternative Theorem implies that the appropriate solvability condition for (6.63) is found by premultiplying

(6.63) by $\mathbf{u}^T$, which yields

$$\begin{aligned}
\mathbf{u}^T\boldsymbol{B}_{x0}\frac{\partial}{\partial x}\left(\mathbf{w}_x\frac{\partial P}{\partial x}+\mathbf{w}_y\frac{\partial P}{\partial y}\right)+\mathbf{u}^T\boldsymbol{B}_{y0}\frac{\partial}{\partial y}\left(\mathbf{w}_x\frac{\partial P}{\partial x}+\mathbf{w}_y\frac{\partial P}{\partial y}\right)\\
+\mathbf{u}^T\boldsymbol{B}'_{x0}\left(\mathbf{w}_x\frac{\partial P}{\partial x}+\mathbf{w}_y\frac{\partial P}{\partial y}\right)+\mathbf{u}^T\boldsymbol{B}'_{y0}\left(\mathbf{w}_x\frac{\partial P}{\partial x}+\mathbf{w}_y\frac{\partial P}{\partial y}\right)\\
+\mathbf{u}^T\boldsymbol{C}_{xx0}\mathbf{u}\frac{\partial^2 P}{\partial x^2}+2\mathbf{u}^T\boldsymbol{C}_{xy0}\mathbf{u}\frac{\partial^2 P}{\partial x\partial y}+\mathbf{u}^T\boldsymbol{C}_{yy0}\mathbf{u}\frac{\partial^2 P}{\partial y^2}\\
+\mathbf{u}^T\boldsymbol{C}'_{xx0}\mathbf{u}\frac{\partial P}{\partial x}+\mathbf{u}^T\boldsymbol{C}'_{yx_0}\mathbf{u}\frac{\partial P}{\partial x}+\mathbf{u}^T\boldsymbol{C}'_{xy_0}\mathbf{u}\frac{\partial P}{\partial y}+\mathbf{u}^T\boldsymbol{C}'_{yy_0}\mathbf{u}\frac{\partial P}{\partial y}=0, \quad (6.64)
\end{aligned}$$

where we have used the fact that $\mathbf{u}^T\boldsymbol{B}_{x0}\mathbf{u}=\mathbf{u}^T\boldsymbol{B}_{y0}\mathbf{u}=\mathbf{u}^T\boldsymbol{B}_{x1}\mathbf{u}=\mathbf{u}^T\boldsymbol{B}_{y1}\mathbf{u}=0$, and $\mathbf{u}^T\boldsymbol{A}_0=\mathbf{u}^T\boldsymbol{A}_1=0$ by (6.57).

Equation (6.64) describes the behaviour of the macroscale pressure, P, in terms of the network structure. However, in contrast to the single-phase flow model presented in §6.2, $\boldsymbol{B}_{x0}$, $\boldsymbol{B}_{y0}$, $\boldsymbol{B}'_{x0}$, $\boldsymbol{B}'_{y0}$, $\boldsymbol{C}_{xx0}$, $\boldsymbol{C}_{xy0}$, $\boldsymbol{C}_{yy0}$, $\boldsymbol{C}_{xx0}'$, $\boldsymbol{C}_{yx0}'$, $\boldsymbol{C}_{xy0}'$, and $\boldsymbol{C}_{yy0}'$ also depend on the saturation and ion concentrations, S_i and c_i^k, respectively, through G_{ij}^{rs}. Hence, in order to determine P, we must first determine S_i and c_i^k.

6.3.3 Saturation

Asymptotically expanding P_i in powers of ϵ, and substituting (6.59) and (6.61) into (6.39), yields

$$\begin{aligned}
V_i\frac{\partial S_i}{\partial t}=-\frac{1}{2}\sum_{r=-1}^{1}\sum_{s=-1}^{1}\sum_{j=1}^{N}\epsilon G_{ij}^{rs}\left(S_i+S_j\right)\left((w_{xi}-w_{xj}-\Delta x_{ij}^r)\frac{\partial P}{\partial x}+(w_{y_i}-w_{y_j}-\Delta y_{ij}^s)\frac{\partial P}{\partial y}\right)\\
+\epsilon^2\left[\left(\Delta x_{ij}^r\frac{\partial G_{ij}^{rs}}{\partial\tilde{x}}+\Delta y_{ij}^r s\frac{\partial G_{ij}^{rs}}{\partial\tilde{y}}\right)\left(S_i+S_j\right)\left((w_{xi}-w_{xj}-\Delta x_{ij}^r)\frac{\partial P}{\partial x}+(w_{y_i}-w_{y_j}-\Delta y_{ij}^s)\frac{\partial P}{\partial y}\right)\right.\\
+G_{ij}^{rs}\left(\Delta x_{ij}^r\frac{\partial S_j}{\partial x}+\Delta y_{ij}^r s\frac{\partial S_j}{\partial y}\right)\left((w_{xi}-w_{xj}-\Delta x_{ij}^r)\frac{\partial P}{\partial x}+(w_{y_i}-w_{y_j}-\Delta y_{ij}^s)\frac{\partial P}{\partial y}\right)\\
-\frac{1}{\delta}G_{ij}^{rs}(S_j-S_i)\left((w_{xi}-w_{xj}-\Delta x_{ij}^r)\frac{\partial P}{\partial x}+(w_{y_i}-w_{y_j}-\Delta y_{ij}^s)\frac{\partial P}{\partial y}\right)^2\\
+G_{ij}^{rs}\left(S_i+S_j\right)\left(P_{2i}-P_{2j}-\Delta x_{ij}^r\frac{\partial f}{\partial x}-\Delta y_{ij}^s\frac{\partial f}{\partial y}\right.\\
-\Delta x_{ij}^r\frac{\partial}{\partial x}\left(w_{xj}\frac{\partial P}{\partial x}+w_{y_j}\frac{\partial P}{\partial y}\right)-\Delta y_{ij}^s\frac{\partial}{\partial y}\left(w_{xj}\frac{\partial P}{\partial x}+w_{y_j}\frac{\partial P}{\partial y}\right)\\
\left.\left.-\frac{\left(\Delta x_{ij}^r\right)^2}{2}\frac{\partial^2 P}{\partial x^2}-\Delta x_{ij}^r\Delta y_{ij}^s\frac{\partial^2 P}{\partial x\partial y}-\frac{\left(\Delta y_{ij}^s\right)^2}{2}\frac{\partial^2 P}{\partial y^2}\right)\right], \quad (6.65)
\end{aligned}$$

where w_{xi} is the i^{th} component of $\mathbf{w}_x$, and w_{y_i} is the i^{th} component of $\mathbf{w}_y$.

Asymptotically expanding S_i and G_{ij}^{rs} in powers of ϵ, and equating the leading-order terms in (6.65), yields

$$\frac{\partial S_{i0}}{\partial t}=0. \quad (6.66)$$

Hence, the saturation is constant over the timescale t. This is a result of the fact that, to leading order in ϵ, the pressure is locally uniform, so the leading-order flux, and therefore the change in the saturation, is zero on the macroscale. To study the variation in the saturation, we must rescale onto a longer timescale, $t = \epsilon^{-1}\tilde{t}$, so that the $O(\epsilon)$ terms in (6.65) read

$$\mathbf{V} \circ \frac{\partial \mathbf{S_0}}{\partial \tilde{t}} = -\boldsymbol{D}_{x0}\mathbf{S}_0 \frac{\partial P}{\partial x} - \boldsymbol{D}_{y0}\mathbf{S}_0 \frac{\partial P}{\partial y}, \tag{6.67}$$

where $\mathbf{V}$ is the vector form of V_i, $\mathbf{S} \sim \mathbf{S}_0 + \epsilon\mathbf{S}_1 + \cdots$ is the vector form of S_i, and $\boldsymbol{D}_{x0}$ and $\boldsymbol{D}_{y0}$ are the leading-order terms of the matrices $\boldsymbol{D}_x$ and $\boldsymbol{D}_y$, given by

$$\begin{aligned} \boldsymbol{D}_{xij} = \frac{1}{2}\Bigg[\delta_{ij}\left(\sum_{r=-1}^{1}\sum_{s=-1}^{1}\sum_{k=1}^{N}(w_{xi} - w_{xk} - \Delta x_{ik}^{r})G_{ik}^{rs}\right) \\ - \sum_{r=-1}^{1}\sum_{s=-1}^{1}(w_{xi} - w_{xj} - \Delta x_{ij}^{r})G_{ij}^{rs}\Bigg], \end{aligned} \tag{6.68}$$

$$\begin{aligned} \boldsymbol{D}_{y_{ij}} = \frac{1}{2}\Bigg[\delta_{ij}\left(\sum_{r=-1}^{1}\sum_{s=-1}^{1}\sum_{k=1}^{N}(w_{y_i} - w_{y_k} - \Delta y_{ik}^{s})G_{ik}^{rs}\right) \\ - \sum_{r=-1}^{1}\sum_{s=-1}^{1}(w_{y_i} - w_{y_j} - \Delta y_{ij}^{s})G_{ij}^{rs}\Bigg]. \end{aligned} \tag{6.69}$$

Equation (6.67) describes the transient behaviour of the saturation for a given macroscopic pressure gradient, over which the saturation reaches a local equilibrium. Since we are primarily interested in how the saturation varies on a macroscopic scale, we rescale the timescale again, $t = \epsilon^{-2}T$, and (6.67) reduces to

$$\boldsymbol{D}_{x0}\mathbf{S}_0 \frac{\partial P}{\partial x} + \boldsymbol{D}_{y0}\mathbf{S}_0 \frac{\partial P}{\partial y} = 0. \tag{6.70}$$

Assuming that $\mathbf{S}_0$ is independent of P, $\boldsymbol{D}_{x0}\mathbf{S}_0 = \boldsymbol{D}_{y0}\mathbf{S}_0 = 0$, and therefore the solution to (6.70) is

$$\mathbf{S}_0 = S(x, y, T)\mathbf{u}, \tag{6.71}$$

where $S(x, y, T)$ is a function of the macroscale variables. Hence, the saturation is locally uniform to leading order. To derive the governing equation for S, we must proceed to the next order and determine an appropriate solvability condition. Substituting (6.71) into (6.65), equating the $O(\epsilon^2)$ terms, and using the fact that

$\boldsymbol{D}_{x1}\mathbf{u} = \boldsymbol{D}_{y_1}\mathbf{u} = \boldsymbol{A}_1\mathbf{u} = \boldsymbol{A}_2\mathbf{u} = \boldsymbol{B}_{x0}'\mathbf{u} = \boldsymbol{B}_{y0}'\mathbf{u} = \boldsymbol{B}_{x1}'\mathbf{u} = \boldsymbol{B}_{y1}'\mathbf{u} = \boldsymbol{C}_0''\mathbf{u} = 0$, yields

$$\begin{aligned}
\mathbf{V}\frac{\partial S}{\partial T} = &-\boldsymbol{D}_{x0}\mathbf{S}_1\frac{\partial P}{\partial x} - \boldsymbol{D}_{y_0}\mathbf{S}_1\frac{\partial P}{\partial y} \\
&+ \boldsymbol{K}_{xx0}\mathbf{u}\frac{\partial S}{\partial x}\frac{\partial P}{\partial x} + \boldsymbol{K}_{xy_0}\mathbf{u}\frac{\partial S}{\partial x}\frac{\partial P}{\partial y} + \boldsymbol{K}_{yx_0}\mathbf{u}\frac{\partial S}{\partial y}\frac{\partial P}{\partial x} + \boldsymbol{K}_{yy_0}\mathbf{u}\frac{\partial S}{\partial y}\frac{\partial P}{\partial y} \\
&- S\left[\boldsymbol{A}_0\mathbf{P}_2 + \boldsymbol{A}_1\mathbf{w}_x\frac{\partial P}{\partial x} + \boldsymbol{A}_1\mathbf{w}_y\frac{\partial P}{\partial y} - \boldsymbol{B}_{x0}\frac{\partial}{\partial x}\left(\mathbf{w}_x\frac{\partial P}{\partial x} + \mathbf{w}_y\frac{\partial P}{\partial y}\right)\right. \\
&\quad - \boldsymbol{B}_{y_0}\frac{\partial}{\partial y}\left(\mathbf{w}_x\frac{\partial P}{\partial x} + \mathbf{w}_y\frac{\partial P}{\partial y}\right) - \boldsymbol{B}_{x0}\mathbf{u}\frac{\partial f}{\partial x} - \boldsymbol{B}_{y_0}\mathbf{u}\frac{\partial f}{\partial y} \\
&- \boldsymbol{B}_{x0}'\left(\mathbf{w}_x\frac{\partial P}{\partial x} + \mathbf{w}_y\frac{\partial P}{\partial y}\right) - \boldsymbol{B}_{y_0}'\left(\mathbf{w}_x\frac{\partial P}{\partial x} + \mathbf{w}_y\frac{\partial P}{\partial y}\right) - \boldsymbol{B}_{x1}\mathbf{u}\frac{\partial P}{\partial x} - \boldsymbol{B}_{y_1}\mathbf{u}\frac{\partial P}{\partial y} \\
&\quad - \boldsymbol{C}_{xx0}\mathbf{u}\frac{\partial^2 P}{\partial x^2} - 2\boldsymbol{C}_{xy_0}\mathbf{u}\frac{\partial^2 P}{\partial x\partial y} - \boldsymbol{C}_{yy_0}\mathbf{u}\frac{\partial^2 P}{\partial y^2} \\
&\quad \left.-\boldsymbol{C}_{xx0}'\mathbf{u}\frac{\partial P}{\partial x} - \boldsymbol{C}_{yx_0}'\mathbf{u}\frac{\partial P}{\partial x} - \boldsymbol{C}_{xy_0}'\mathbf{u}\frac{\partial P}{\partial y} - \boldsymbol{C}_{yy_0}'\mathbf{u}\frac{\partial P}{\partial y}\right], \quad (6.72)
\end{aligned}$$

where $\boldsymbol{K}_{xx0}$, $\boldsymbol{K}_{xy_0}$, $\boldsymbol{K}_{yx_0}$, and $\boldsymbol{K}_{yy_0}$, are the leading-order terms of the matrices $\boldsymbol{K}_{xx}$, $\boldsymbol{K}_{xy}$, $\boldsymbol{K}_{yx}$, and $\boldsymbol{K}_{yy}$, respectively, which are given by

$$\boldsymbol{K}_{xxij} = \frac{1}{2}\sum_{r=-1}^{1}\sum_{s=-1}^{1}\Delta x_{ij}^r(w_{xj} - w_{xi} + \Delta x_{ij}^r)G_{ij}^{rs}, \quad (6.73)$$

$$\boldsymbol{K}_{xy_{ij}} = \frac{1}{2}\sum_{r=-1}^{1}\sum_{s=-1}^{1}\Delta x_{ij}^r(w_{y_j} - w_{y_i}) + \Delta y_{ij}^s G_{ij}^{rs}, \quad (6.74)$$

$$\boldsymbol{K}_{yx_{ij}} = \frac{1}{2}\sum_{r=-1}^{1}\sum_{s=-1}^{1}\Delta y_{ij}^s(w_{xj} - w_{xi} + \Delta x_{ij}^r)G_{ij}^{rs}, \quad (6.75)$$

$$\boldsymbol{K}_{yy_{ij}} = \frac{1}{2}\sum_{r=-1}^{1}\sum_{s=-1}^{1}\Delta y_{ij}^s(w_{y_j} - w_{y_i} + \Delta y_{ij}^s)G_{ij}^{rs}. \quad (6.76)$$

We observe that the term in the square brackets in (6.72) vanishes, since this is equal to the second-order equation for the pressure, (6.63). By premultiplying (6.72) by $\mathbf{u}^T$, and using the fact that $\mathbf{u}^T\boldsymbol{D}_{x0} = \mathbf{u}^T\boldsymbol{D}_{y_0} = 0$, we find that

$$\begin{aligned}
\mathbf{u}^T\mathbf{V}\frac{\partial S}{\partial T} = &\mathbf{u}^T\boldsymbol{K}_{xx0}\mathbf{u}\frac{\partial S}{\partial x}\frac{\partial P}{\partial x} + \mathbf{u}^T\boldsymbol{K}_{xy_0}\mathbf{u}\frac{\partial S}{\partial x}\frac{\partial P}{\partial y} \\
&+ \mathbf{u}^T\boldsymbol{K}_{yx_0}\mathbf{u}\frac{\partial S}{\partial y}\frac{\partial P}{\partial x} + \mathbf{u}^T\boldsymbol{K}_{yy_0}\mathbf{u}\frac{\partial S}{\partial y}\frac{\partial P}{\partial y}, \quad (6.77)
\end{aligned}$$

which we write in the form

$$\frac{\partial S}{\partial T} - \frac{1}{\mathbf{u}^T\mathbf{V}}(\boldsymbol{K}\nabla P)\cdot\nabla S = 0, \quad (6.78)$$

where $\mathbf{K}$ is the tensor given by

$$\boldsymbol{K} = \begin{pmatrix} \mathbf{u}^T \boldsymbol{K}_{xx_0} \mathbf{u} & \mathbf{u}^T \boldsymbol{K}_{xy_0} \mathbf{u} \\ \mathbf{u}^T \boldsymbol{K}_{yx_0} \mathbf{u} & \mathbf{u}^T \boldsymbol{K}_{yy_0} \mathbf{u} \end{pmatrix}. \tag{6.79}$$

We can relate $\boldsymbol{K}$ to $\boldsymbol{B}_x$, $\boldsymbol{B}_y$, $\boldsymbol{C}_{xx}$, $\boldsymbol{C}_{xy}$, and $\boldsymbol{C}_{yy}$, by summing over the rows and columns of (6.73), substituting (6.45) and (6.49), and using the fact that $\boldsymbol{B}_x$ is anti-symmetric, which yields

$$\mathbf{u}^T \boldsymbol{K}_{xx} \mathbf{u} = \frac{1}{2} \sum_{i=1}^{N} \sum_{j=1}^{N} \sum_{r=-1}^{1} \sum_{s=-1}^{1} \Delta x_{ij}^r (w_{xj} - w_{xi} + \Delta x_{ij}^r) G_{ij}^{rs} \tag{6.80}$$

$$= \frac{1}{2} \left(\mathbf{u}^T \boldsymbol{B}_x \mathbf{w}_x - \mathbf{w}_x^T \boldsymbol{B}_x \mathbf{u} \right) + \mathbf{u}^T \boldsymbol{C}_{xx} \mathbf{u} \tag{6.81}$$

$$= \mathbf{u}^T \boldsymbol{B}_x \mathbf{w}_x + \mathbf{u}^T \boldsymbol{C}_{xx} \mathbf{u}. \tag{6.82}$$

Similarly,

$$\mathbf{u}^T \boldsymbol{K}_{yx} \mathbf{u} = \mathbf{u}^T \boldsymbol{B}_y \mathbf{w}_x + \mathbf{u}^T \boldsymbol{C}_{xy} \mathbf{u}, \tag{6.83}$$

$$\mathbf{u}^T \boldsymbol{K}_{xy} \mathbf{u} = \mathbf{u}^T \boldsymbol{B}_x \mathbf{w}_y + \mathbf{u}^T \boldsymbol{C}_{xy} \mathbf{u}, \tag{6.84}$$

$$\mathbf{u}^T \boldsymbol{K}_{yy} \mathbf{u} = \mathbf{u}^T \boldsymbol{B}_y \mathbf{w}_y + \mathbf{u}^T \boldsymbol{C}_{yy} \mathbf{u}. \tag{6.85}$$

6.3.4 Ion concentrations

Asymptotically expanding P_i and S_i in powers of ϵ, rescaling onto the macroscopic timescale, $t = \epsilon^{-2}T$, and substituting (6.59), (6.61), and (6.71) into (6.39), yields

$$\begin{aligned}
\epsilon^2 V_i \frac{\partial \left(c_i^k S\right)}{\partial T} = -\frac{1}{2}\sum_{r=-1}^{1}\sum_{s=-1}^{1}\sum_{j=1}^{N}\epsilon G_{ij}^{rs}\left(c_i^k + c_j^k\right) S\left((w_{xi} - w_{xj} - \Delta x_{ij}^r)\frac{\partial P}{\partial x}\right. \\
\left. +(w_{y_i} - w_{y_j} - \Delta y_{ij}^s)\frac{\partial P}{\partial y}\right) \\
+\epsilon^2\left[G_{ij}^{rs}\left(\Delta x_{ij}^r \frac{\partial c_j^k}{\partial x} + \Delta y_{ij}^s \frac{\partial c_j^k}{\partial y}\right) S\left((w_{xi} - w_{xj} - \Delta x_{ij}^r)\frac{\partial P}{\partial x} + (w_{y_i} - w_{y_j} - \Delta y_{ij}^s)\frac{\partial P}{\partial y}\right)\right. \\
-\frac{1}{\delta}G_{ij}^{rs}(c_j^k - c_i^k)S\left((w_{xi} - w_{xj} - \Delta x_{ij}^r)\frac{\partial P}{\partial x} + (w_{y_i} - w_{y_j} - \Delta y_{ij}^s)\frac{\partial P}{\partial y}\right)^2 \\
G_{ij}^{rs}\left(c_i^k + c_j^k\right)\frac{\left(S_{i1} + S_{j1}\right)}{2}\left((w_{xi} - w_{xj} - \Delta x_{ij}^r)\frac{\partial P}{\partial x} + (w_{y_i} - w_{y_j} - \Delta y_{ij}^s)\frac{\partial P}{\partial y}\right) \\
+G_{ij}^{rs}\frac{\left(c_i^k + c_j^k\right)}{2}\left(\Delta x_{ij}^r \frac{\partial S}{\partial x} + \Delta y_{ij}^r s\frac{\partial S}{\partial y}\right)\left((w_{xi} - w_{xj} - \Delta x_{ij}^r)\frac{\partial P}{\partial x} + (w_{y_i} - w_{y_j} - \Delta y_{ij}^s)\frac{\partial P}{\partial y}\right) \\
\left(\Delta x_{ij}^r \frac{\partial G_{ij}^{rs}}{\partial \tilde{x}} + \Delta y_{ij}^r s\frac{\partial G_{ij}^{rs}}{\partial \tilde{y}}\right)\left(c_i^k + c_j^k\right) S\left((w_{xi} - w_{xj} - \Delta x_{ij}^r)\frac{\partial P}{\partial x} + (w_{y_i} - w_{y_j} - \Delta y_{ij}^s)\frac{\partial P}{\partial y}\right) \\
+G_{ij}^{rs}\left(c_i^k + c_j^k\right) S\left(P_{2i} - P_{2j} - \Delta x_{ij}^r \frac{\partial f}{\partial x} - \Delta y_{ij}^s \frac{\partial f}{\partial y}\right. \\
-\Delta x_{ij}^r \frac{\partial}{\partial x}\left(w_{xj}\frac{\partial P}{\partial x} + w_{y_j}\frac{\partial P}{\partial y}\right) - \Delta y_{ij}^s \frac{\partial}{\partial y}\left(w_{xj}\frac{\partial P}{\partial x} + w_{y_j}\frac{\partial P}{\partial y}\right) \\
\left.\left. -\frac{\left(\Delta x_{ij}^r\right)^2}{2}\frac{\partial^2 P}{\partial x^2} - \Delta x_{ij}^r \Delta y_{ij}^s \frac{\partial^2 P}{\partial x \partial y} - \frac{\left(\Delta y_{ij}^s\right)^2}{2}\frac{\partial^2 P}{\partial y^2}\right)\right]. \quad (6.86)
\end{aligned}$$

By expanding c_i^k and G_{ij}^{rs}, and equating the $O(\epsilon)$ terms in (6.86), we find that

$$\boldsymbol{D}_{x0}\mathbf{c}_0^k S\frac{\partial P}{\partial x} + \boldsymbol{D}_{y_0}\mathbf{c}_0^k S\frac{\partial P}{\partial y} = 0, \quad (6.87)$$

where $\mathbf{c}^k \sim \mathbf{c}_0^k + \epsilon\mathbf{c}_1^k + \cdots$ is the vector form of c_i^k, for each ion species, k. Assuming that $\mathbf{c}_0^k$ is independent of P, $\boldsymbol{D}_{x0}\mathbf{c}_0^k = \boldsymbol{D}_{y_0}\mathbf{c}_0^k = 0$, and therefore (6.87) has the solution

$$\mathbf{c}_0^k = c^k(x, y, T)\mathbf{u}, \quad (6.88)$$

where the macroscale functions $c^k(x, y, T)$ are currently arbitrary and will have to be determined later. Hence, like the saturation and pressure, the ion concentrations are locally uniform on the small scale for each ion species. Substituting (6.88) into (6.86), equating the $O(\epsilon^2)$ terms and using the fact that $\boldsymbol{D}_{x1}\mathbf{u} = \boldsymbol{D}_{y_1}\mathbf{u} = \boldsymbol{A}_1\mathbf{u} = \boldsymbol{A}_2\mathbf{u} =$

$\boldsymbol{B}_{x0}'\mathbf{u} = \boldsymbol{B}_{y0}'\mathbf{u} = \boldsymbol{B}_{x1}'\mathbf{u} = \boldsymbol{B}_{y1}'\mathbf{u} = \boldsymbol{C}_0''\mathbf{u} = 0$, yields

$$\begin{aligned}
\mathbf{V}\frac{\partial\left(c^k S\right)}{\partial T} &= -\boldsymbol{D}_{x0}\mathbf{c}_1^k\frac{\partial P}{\partial x} - \boldsymbol{D}_{y0}\mathbf{c}_1^k\frac{\partial P}{\partial y} \\
&+ S\left(\boldsymbol{K}_{xx0}\mathbf{u}\frac{\partial c^k}{\partial x}\frac{\partial P}{\partial x} + \boldsymbol{K}_{xy0}\mathbf{u}\frac{\partial c^k}{\partial x}\frac{\partial P}{\partial y} + \boldsymbol{K}_{yx0}\mathbf{u}\frac{\partial c^k}{\partial y}\frac{\partial P}{\partial x} + \boldsymbol{K}_{yy0}\mathbf{u}\frac{\partial c^k}{\partial y}\frac{\partial P}{\partial y}\right) \\
&+ c^k\left\{-\boldsymbol{D}_{x0}\mathbf{S}_1\frac{\partial P}{\partial x} - \boldsymbol{D}_{y0}\mathbf{S}_1\frac{\partial P}{\partial y}\right. \\
&+ \boldsymbol{K}_{xx0}\mathbf{u}\frac{\partial S}{\partial x}\frac{\partial P}{\partial x} + \boldsymbol{K}_{xy0}\mathbf{u}\frac{\partial S}{\partial x}\frac{\partial P}{\partial y} + \boldsymbol{K}_{yx0}\mathbf{u}\frac{\partial S}{\partial y}\frac{\partial P}{\partial x} + \boldsymbol{K}_{yy0}\mathbf{u}\frac{\partial S}{\partial y}\frac{\partial P}{\partial y} \\
&- S\left[\boldsymbol{A}_0\mathbf{P}_2 + \boldsymbol{A}_1\mathbf{w}_x\frac{\partial P}{\partial x} + \boldsymbol{A}_1\mathbf{w}_y\frac{\partial P}{\partial y} - \boldsymbol{B}_{x0}\frac{\partial}{\partial x}\left(\mathbf{w}_x\frac{\partial P}{\partial x} + \mathbf{w}_y\frac{\partial P}{\partial y}\right)\right. \\
&- \boldsymbol{B}_{y0}\frac{\partial}{\partial y}\left(\mathbf{w}_x\frac{\partial P}{\partial x} + \mathbf{w}_y\frac{\partial P}{\partial y}\right) - \boldsymbol{B}_{x0}\mathbf{u}\frac{\partial f}{\partial x} - \boldsymbol{B}_{y0}\mathbf{u}\frac{\partial f}{\partial y} \\
&- \boldsymbol{B}_{x0}'\left(\mathbf{w}_x\frac{\partial P}{\partial x} + \mathbf{w}_y\frac{\partial P}{\partial y}\right) - \boldsymbol{B}_{y0}'\left(\mathbf{w}_x\frac{\partial P}{\partial x} + \mathbf{w}_y\frac{\partial P}{\partial y}\right) - \boldsymbol{B}_{x1}\mathbf{u}\frac{\partial P}{\partial x} - \boldsymbol{B}_{y1}\mathbf{u}\frac{\partial P}{\partial y} \\
&- \boldsymbol{C}_{xx0}\mathbf{u}\frac{\partial^2 P}{\partial x^2} - 2\boldsymbol{C}_{xy0}\mathbf{u}\frac{\partial^2 P}{\partial x\partial y} - \boldsymbol{C}_{yy0}\mathbf{u}\frac{\partial^2 P}{\partial y^2} \\
&\left.\left.-\boldsymbol{C}_{xx0}'\mathbf{u}\frac{\partial P}{\partial x} - \boldsymbol{C}_{yx0}'\mathbf{u}\frac{\partial P}{\partial x} - \boldsymbol{C}_{xy0}'\mathbf{u}\frac{\partial P}{\partial y} - \boldsymbol{C}_{yy0}'\mathbf{u}\frac{\partial P}{\partial y}\right]\right\}. \qquad (6.89)
\end{aligned}$$

We observe that the term inside the curly brackets is the same as the expression on the right hand side of (6.72). Hence, multiplying (6.72) by c^k, and substituting the result into (6.89), yields

$$\begin{aligned}
S\mathbf{V}\frac{\partial c^k}{\partial T} &= -\boldsymbol{D}_{x0}\mathbf{c}_1^k\frac{\partial P}{\partial x} - \boldsymbol{D}_{y0}\mathbf{c}_1^k\frac{\partial P}{\partial y} \\
&+ S\left(\boldsymbol{K}_{xx0}\mathbf{u}\frac{\partial c^k}{\partial x}\frac{\partial P}{\partial x} + \boldsymbol{K}_{xy0}\mathbf{u}\frac{\partial c^k}{\partial x}\frac{\partial P}{\partial y} + \boldsymbol{K}_{yx0}\mathbf{u}\frac{\partial c^k}{\partial y}\frac{\partial P}{\partial x} + \boldsymbol{K}_{yy0}\mathbf{u}\frac{\partial c^k}{\partial y}\frac{\partial P}{\partial y}\right). \qquad (6.90)
\end{aligned}$$

Since $\mathbf{u}^T\boldsymbol{D}_{x0} = \mathbf{u}^T\boldsymbol{D}_{y0} = 0$, premultiplying (6.90) by $\mathbf{u}^T$ yields

$$\begin{aligned}
\mathbf{u}^T\mathbf{V}\frac{\partial c^k}{\partial T} &= \mathbf{u}^T\boldsymbol{K}_{xx0}\mathbf{u}\frac{\partial c^k}{\partial x}\frac{\partial P}{\partial x} + \mathbf{u}^T\boldsymbol{K}_{xy0}\mathbf{u}\frac{\partial c^k}{\partial x}\frac{\partial P}{\partial y} \\
&+ \mathbf{u}^T\boldsymbol{K}_{yx0}\mathbf{u}\frac{\partial c^k}{\partial y}\frac{\partial P}{\partial x} + \mathbf{u}^T\boldsymbol{K}_{yy0}\mathbf{u}\frac{\partial c^k}{\partial y}\frac{\partial P}{\partial y}, \qquad (6.91)
\end{aligned}$$

which we write in the form

$$\frac{\partial c^k}{\partial T} - \frac{1}{\mathbf{u}^T\mathbf{V}}\left(\boldsymbol{K}\nabla P\right)\cdot\nabla c^k = 0. \qquad (6.92)$$

We are now in a position to solve (6.64), (6.78), and (6.92) for P, S, and c^k. However, we can simplify (6.64) further by relating the derivatives of G_{ij}^{rs} with respect

to the spatial coordinates of the j^{th} node, $\partial G_{ij}^{rs}/\partial\tilde{x}$ and $\partial G_{ij}^{rs}/\partial\tilde{y}$, to the derivatives of G_{ij}^{rs} with respect to x and y. This enables us to relate $\boldsymbol{B}'_x$, $\boldsymbol{B}'_y$, $\boldsymbol{C}'_{xx}$, $\boldsymbol{C}'_{yx}$, $\boldsymbol{C}'_{xy}$, and $\boldsymbol{C}'_{yy}$ to the derivatives of $\boldsymbol{B}_x$, $\boldsymbol{B}_y$, $\boldsymbol{C}_{xx}$, $\boldsymbol{C}_{xy}$, and $\boldsymbol{C}_{yy}$.

Since P_{i0} is locally uniform, from (6.25) and (6.26) we find that $G_{ij\,0}^{rs}$ is independent of P_i and P_j, and that $S_{ij0}^t = \frac{1}{2}(S_{i0} + S_{j0})$, and $c_{ij0}^k = \frac{1}{2}(c_{i\,0}^k + c_{j\,0}^k)$. Writing $G_{ij}^{rs} = G_{ij}^{rs}(S_{ij}, c_{ij}^k)$, and differentiating with respect to the $\tilde{x}$ coordinate of the j^{th} node, yields

$$\frac{\partial G_{ij\,0}^{rs}}{\partial\tilde{x}} = \frac{\partial G_{ij\,0}^{rs}}{\partial S_{ij_0}}\frac{\partial S_{ij0}}{\partial S_{j0}}\frac{\partial S_{j0}}{\partial\tilde{x}} + \sum_k \frac{\partial G_{ij\,0}^{rs}}{\partial c_{ij_0}^k}\frac{\partial c_{ij0}^k}{\partial c_{j\,0}^k}\frac{\partial c_{j\,0}^k}{\partial\tilde{x}} \tag{6.93}$$

$$= \frac{1}{2}\frac{\partial G_{ij\,0}^{rs}}{\partial S_{ij_0}}\frac{\partial S_{j0}}{\partial\tilde{x}} + \frac{1}{2}\sum_k \frac{\partial G_{ij\,0}^{rs}}{\partial c_{ij_0}^k}\frac{\partial c_{j\,0}^k}{\partial\tilde{x}}. \tag{6.94}$$

On the other hand, differentiating with respect to x, applying the chain rule, and using the fact that the saturation and ion concentrations are locally uniform, yields

$$\frac{\partial G_{ij\,0}^{rs}}{\partial x} = \frac{\partial G_{ij\,0}^{rs}}{\partial S_{ij_0}}\left(\frac{\partial S_{ij0}}{\partial S_{i0}}\frac{\partial S_{i0}}{\partial x} + \frac{\partial S_{ij0}}{\partial S_{j0}}\frac{\partial S_{j0}}{\partial x}\right) + \sum_k \frac{\partial G_{ij\,0}^{rs}}{\partial c_{ij_0}^k}\left(\frac{\partial c_{ij0}^k}{\partial c_{i\,0}^k}\frac{\partial c_{i\,0}^k}{\partial x} + \frac{\partial c_{ij0}^k}{\partial c_{j\,0}^k}\frac{\partial c_{j\,0}^k}{\partial x}\right) \tag{6.95}$$

$$= \frac{1}{2}\frac{\partial G_{ij\,0}^{rs}}{\partial S_{ij_0}}\left(\frac{\partial S_{i0}}{\partial x} + \frac{\partial S_{j0}}{\partial x}\right) + \frac{1}{2}\sum_k \frac{\partial G_{ij\,0}^{rs}}{\partial c_{ij_0}^k}\left(\frac{\partial c_{i\,0}^k}{\partial x} + \frac{\partial c_{j\,0}^k}{\partial x}\right). \tag{6.96}$$

Since $\mathbf{S}_0$ and $\mathbf{c}_0^k$ are locally uniform, $\partial S_{j0}/\partial\tilde{x} = \partial S_{i0}/\partial x$ and $\partial c_{j\,0}^k/\partial\tilde{x} = \partial c_{i\,0}^k/\partial x$, and therefore

$$\frac{\partial G_{ij\,0}^{rs}}{\partial\tilde{x}} = \frac{1}{2}\frac{\partial G_{ij\,0}^{rs}}{\partial x}. \tag{6.97}$$

By a similar argument, we find that

$$\frac{\partial G_{ij\,0}^{rs}}{\partial\tilde{y}} = \frac{1}{2}\frac{\partial G_{ij\,0}^{rs}}{\partial y}. \tag{6.98}$$

By substituting $G_{ij}^{rs} = G_{ji}^{-r-s}$ into (6.47), relabelling the indices, and substituting

(6.97) into the result, we find that

$$\mathbf{u}^T \boldsymbol{B}'_x = \sum_r \sum_s \sum_k (-rL_x + x_j - x_k) \frac{\partial G^{rs}_{kj}}{\partial \tilde{x}} - \sum_r \sum_s \sum_k (-rL_x + x_k - x_j) \frac{\partial G^{rs}_{jk}}{\partial \tilde{x}} \tag{6.99}$$

$$= \sum_r \sum_s \sum_k (-rL_x + x_j - x_k) \frac{\partial G^{rs}_{kj}}{\partial \tilde{x}} - \sum_r \sum_s \sum_k (-rL_x + x_k - x_j) \frac{\partial G^{-r-s}_{kj}}{\partial \tilde{x}} \tag{6.100}$$

$$= \sum_r \sum_s \sum_k (-rL_x + x_j - x_k) \frac{\partial G^{rs}_{kj}}{\partial \tilde{x}} - \sum_r \sum_s \sum_k (rL_x + x_k - x_j) \frac{\partial G^{rs}_{kj}}{\partial \tilde{x}} \tag{6.101}$$

$$= 2 \sum_r \sum_s \sum_k (-rL_x + x_j - x_k) \frac{\partial G^{rs}_{kj}}{\partial \tilde{x}} \tag{6.102}$$

$$= \sum_r \sum_s \sum_k (-rL_x + x_j - x_k) \frac{\partial G^{rs}_{kj}}{\partial x} \tag{6.103}$$

$$= \frac{\partial \mathbf{u}^T \boldsymbol{B}_x}{\partial x}. \tag{6.104}$$

A similar analysis yields

$$\mathbf{u}^T \boldsymbol{B}'_y = \frac{\partial \mathbf{u}^T \boldsymbol{B}_y}{\partial y}, \qquad \mathbf{u}^T \boldsymbol{C}'_{xx} = \frac{\partial \mathbf{u}^T \boldsymbol{C}_{xx}}{\partial x}, \qquad \mathbf{u}^T \boldsymbol{C}'_{yy} = \frac{\partial \mathbf{u}^T \boldsymbol{C}_{yy}}{\partial y}, \tag{6.105}$$

$$\mathbf{u}^T \boldsymbol{C}'_{xy} = \frac{\partial \mathbf{u}^T \boldsymbol{C}_{xy}}{\partial x}, \qquad \mathbf{u}^T \boldsymbol{C}'_{yx} = \frac{\partial \mathbf{u}^T \boldsymbol{C}_{xy}}{\partial y}. \tag{6.106}$$

Finally, substituting (6.104) – (6.106) into (6.64) yields

$$\nabla \cdot (\boldsymbol{K} \nabla P) = 0. \tag{6.107}$$

We can therefore think of $\boldsymbol{K}$ as the permeability tensor of the network, which depends on the saturation and ion concentrations (i.e. the salinity). For completeness, we reproduce equations (6.78) and (6.92),

$$\frac{\partial S}{\partial T} - \frac{1}{\mathbf{u}^T \mathbf{V}} (\boldsymbol{K} \nabla P) \cdot \nabla S = 0, \qquad \frac{\partial c^k}{\partial T} - \frac{1}{\mathbf{u}^T \mathbf{V}} (\boldsymbol{K} \nabla P) \cdot \nabla c^k = 0, \tag{6.108}$$

so that (6.107) and (6.108) defines a system of equations for the macroscopic pressure, water saturation and ion concentration variables P, S and c^k.

6.3.5 Results for a one-dimensional network

We compare the homogenised model, (6.107) – (6.108), with the full network model, (6.27) – (6.31), for the case in which periodicity occurs only in the horizontal direction. We consider a one-dimensional periodic network constructed from n repetitions of a 10-node cell. We prescribe $L_x = 1$, and suppose that the total network has unit

length, so that the size of each cell is $\epsilon = 1/n$. We select the pore radii R_i^p, and throat radii, R_{ij}^t, from a uniform distribution on $[0.5, 1.5]$, and prescribe the pore volumes to be $V_i = R_i^{p3}$. For simplicity, we set the throat lengths to be equal to unity, $L_{ij}^t = 1$. Our homogenised model reduces to the following system of PDEs,

$$\frac{\partial}{\partial x}\left(K\frac{\partial P}{\partial x}\right) = 0, \qquad \frac{\partial S}{\partial T} - \frac{K}{\mathbf{u}^T\mathbf{V}}\frac{\partial P}{\partial x}\frac{\partial S}{\partial x} = 0, \qquad \frac{\partial c^k}{\partial T} - \frac{K}{\mathbf{u}^T\mathbf{V}}\frac{\partial P}{\partial x}\frac{\partial c^k}{\partial x} = 0, \quad (6.109)$$

where

$$K = \mathbf{u}^T\boldsymbol{B}_x\mathbf{w}_x + \mathbf{u}^T\boldsymbol{C}_{xx}\mathbf{u}. \quad (6.110)$$

We suppose that initially the network is almost saturated with oil (we pick $S = 0.01$) and that the concentration of each ion species is given by the concentration in the high salinity regime, c^k_{high}, where $c^1_{\text{high}} = 100$ and $c^2_{\text{high}} = 18$. We choose these values in order for the dimensionless parameters in our network model to be consistent with the model presented in Chapter 2. We simulate a waterflood by imposing a pressure drop of unity across the length of the network, and prescribing $S = 1$ at the inlet.

In Figures 6.3a and 6.3b, we plot the saturation profile along the length of the network after 0.25 and 0.75 pore volumes (the total volume of fluid space in the network, $\sum_i V_i$) of water have been injected, respectively. We compare the results for the homogenised model, (6.109) and (6.110), with the full network model, (6.27) – (6.31), for the three cases in which the number of repeated cells in the full network are given by $n = 10, 50, 100$, respectively. In all cases, the saturation upstream of the propagating front is given by $S = 1$. This corresponds to all of the oil being removed during the waterflood process. This suggests that, by neglecting entry pressure from the model, there is no mechanism for oil to become trapped in the pores. We observe that, as the number of repeated cells in the full network model, n, increases (i.e. as $\epsilon = 1/n$ decreases), the profile of the saturation front approaches the homogenised solution. This agrees with the theory, since the homogenised solution is valid in the limit $\epsilon = 1/n \to 0$.

In Figure 6.4, we plot the percentage oil recovered against the number of pore volumes injected, for the homogenised model and the full network model in the three cases $n = 10, 50, 100$. There is excellent agreement between the homogenised model and the full network model in the cases $n = 50$ and $n = 100$. The oil produced is proportional to the volume of water injected for the majority of the recovery process. However, the rate of recovery decreases as the pore volume injected approaches one, which corresponds to water breakthrough at the outlet.

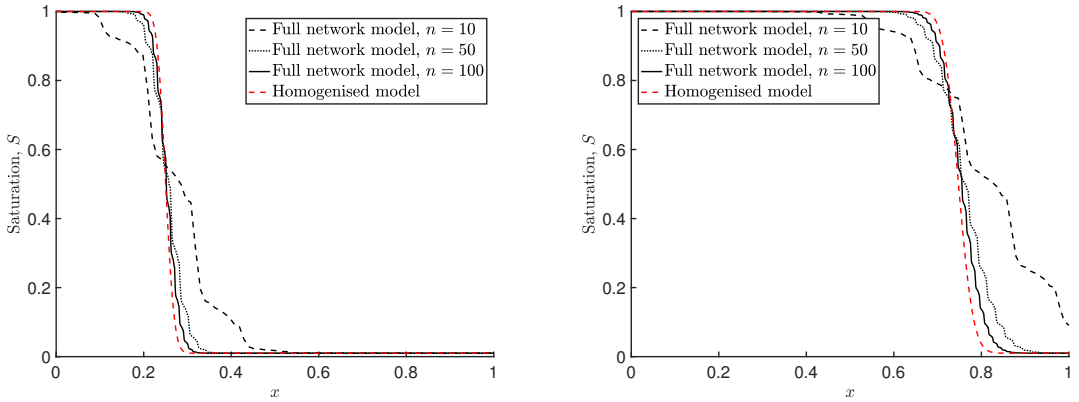


Figure 6.3: Saturation profile of the network after (a) 0.25, and (b) 0.75 pore volumes of water have been injected, for both the homogenised model and the full network model with $n = 10, 50, 100$ repeated 10-node cells.

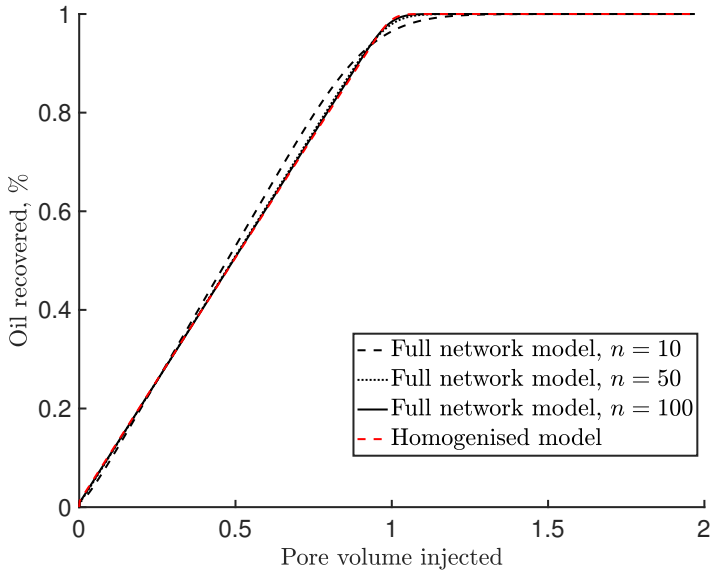
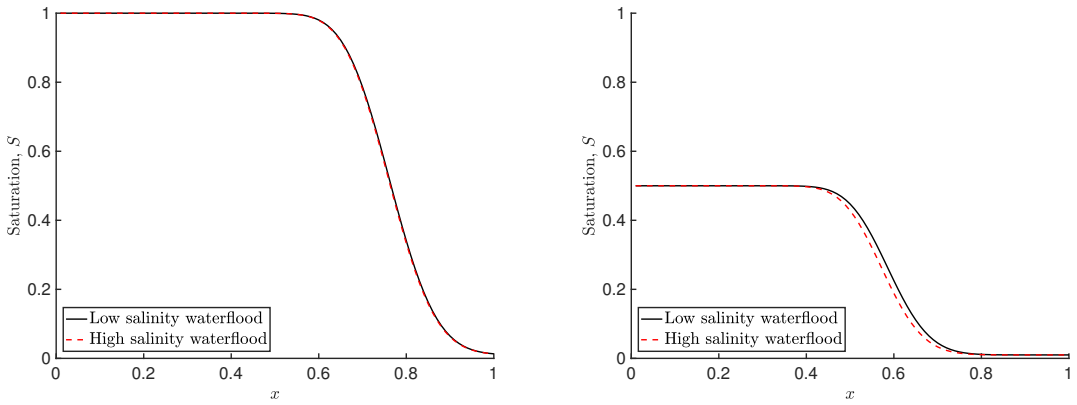
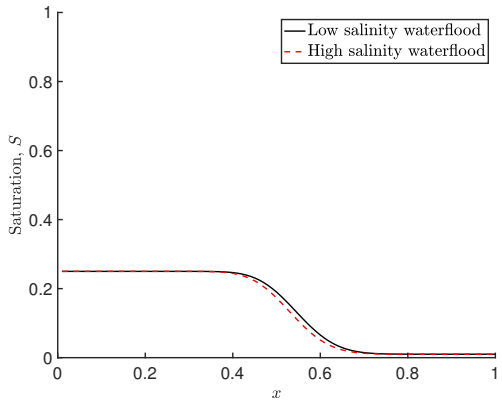


Figure 6.4: Percentage oil recovered as a function of the pore volume of water injected, for both the homogenised model and the full network model with $n = 10, 50, 100$ repeated cells.



(a) $S_{\text{in}} = 1$ (b) $S_{\text{in}} = 0.5$



(c) $S_{\text{in}} = 0.25$

Figure 6.5: Saturation profile of the network at $T = T^*$ for a high salinity and low salinity waterflood, in the three cases (a) $S_{\text{in}} = 1$, (b) $S_{\text{in}} = 0.5$, and (c) $S_{\text{in}} = 0.25$

In Figure 6.5, we plot the saturation profile of the network at $T = T^*$, which we define to be the time taken for 0.75 pore volumes of water to be injected during a high salinity waterflood, assuming a unit pressure drop across the network. We compare the saturation profiles for the high salinity and low salinity regimes for the three cases in which the inlet saturation is given by $S_{\text{in}} = 1, 0.5, 0.25$. We observe that the residual oil is identical between the high salinity and low salinity regimes (given by the inlet saturation), and that the shape of the saturation profile is the same in the two cases. We observe that, for $S_{\text{in}} = 1$, there is a negligible difference between the positions the saturation front in the two regimes at $T = T^*$, and therefore the speed at which the front advances is the same in the two cases. As S_{in} decreases, the speed of the saturation front decreases, however the *relative* speed of the low-salinity front increases.

To understand this result further, we solve (6.109a), subject to $P(x = 0) = 1$ and

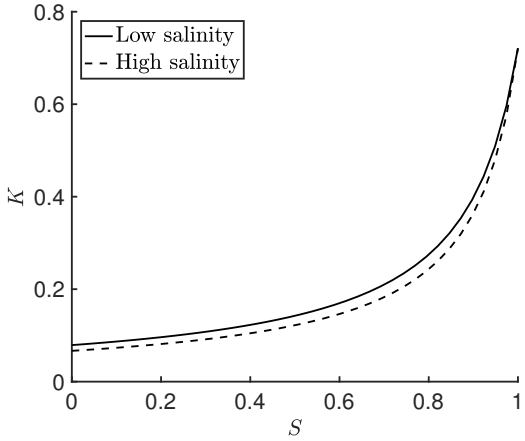


Figure 6.6: Plot of K against the saturation, S, in the high-salinity and low-salinity regimes.

$P(x = 1) = 0$, to find that

$$P = \frac{1}{\int_0^1 \frac{1}{K} \mathrm{d}x} \int_x^1 \frac{1}{K} \mathrm{d}x. \tag{6.111}$$

By substituting (6.111) into (6.109b), we find that the characteristic speed of the saturation front is given by

$$-\frac{K}{\mathbf{u}^T \mathbf{V}} \frac{\partial P}{\partial x} = \frac{1}{\mathbf{u}^T \mathbf{V}} \frac{1}{\int_0^1 \frac{1}{K} \mathrm{d}x}. \tag{6.112}$$

We see that the speed is proportional to the harmonic mean of K. In Figure 6.6, we plot K against S for both the high salinity and low salinity regimes. We observe that K increases as the saturation increases, and that K is greater in the low salinity regime than in the high salinity regime. Furthermore, we observe that the difference in K between the two regimes decreases as S approaches unity due to the fact that the salinity affects the model through the effective slip length along the oil-solid interface, and in the absence of oil this has no effect. Hence, for the case $S_{\text{in}} = 1$ shown in Figure 6.5a, the values of K which contribute to the integral in (6.112) are identical for the points downstream of the front (since the water is initially high salinity in both cases), and identical upstream of the saturation front (since $S = 1$). Therefore, the difference between the speed of the saturation front in the high salinity and low salinity regimes is negligible. As S_{in} decreases, the difference in K between the two regimes at the points upstream of the saturation front increases, resulting in a noticeable difference in the speed at which the front advances.

In this section, we homogenised a network model of two-phase flow in order to derive macroscopic continuum equations for the pressure, saturation, and ion con-

centrations, and found good agreement between the homogenised model and the full network model. However, by neglecting the effects of entry pressure in our model, we are unable produce the effects of oil trapping, and are therefore unable to study the effect of salinity on the total amount of oil recovered. In §6.4, we extend our model to include the effects of entry pressure for a one-dimensional network.

6.4 Homogenisation of a one-dimensional network, including the effects of entry pressure

One of the key results found during the homogenisation process of the network model presented in §6.3 is that the saturation within the pores and throats is uniform on the small scale, (6.71). This is a direct consequence of the fact that, since the effect of entry pressure is neglected in the model, the saturation in the throats is equal to the saturation in each of the neighbouring pores. In order to extend the model to include the effects of entry pressure, we need to know the direction of flow within each throat of the network since the throat saturation depends on both the saturation in the upstream pore and the capillary pressure (which may be different in each of the neighbouring pores even if the saturations are the same). This causes numerous issues, since the flow direction in the throats within a cell will depend on the saturation profile in the cell, the pressure profile in the cell, the macroscopic pressure gradient, the network structure, and, furthermore, there may be hysteresis effects. To avoid these issues, and gain some insight into how one might homogenise a network model with the effect of entry pressure included, we consider a one-dimensional network model for the remainder of this thesis. This ensures that we know the direction of flow *a priori.*, since the fluid can only travel in one direction. Additional work is required in order to generalise the homogenisation process into multiple dimensions, however this is beyond the scope of this thesis.

6.4.1 Model formulation

We consider two-phase flow through a one-dimensional network of unit length, in which ions are advected with the water phase. We suppose that the network is constructed from a repeated cell of length ϵ, and that each cell contains N nodes. We suppose that the length of the edge between the i^{th} and $(i+1)^{\text{th}}$ nodes in the repeated cell is ϵx_i, for $1 \leq i \leq N$. Since the length of the cell is ϵ, we therefore impose that $\sum_i x_i = 1$. We define V_i, P_i, S_i, and c_i^k to be the pore volume, phase-weighted pressure, saturation, and concentration of the k^{th} ion species, respectively,

at the i^{th} node in the network, and we suppose that two-phase flow occurs on the network according to the dimensionless model presented in Chapter 5, (5.39) – (5.50), which reads

$$G_{i-1,i}(P_{i-1}-P_i) = G_{i,i+1}(P_i - P_{i+1}), \qquad \text{for } a < i \leq N-b, \quad (6.113)$$

$$\begin{aligned} V_i \frac{\mathrm{d}S_i}{\mathrm{d}t} &= S^t_{i-1,i} G_{i-1,i}(P_{i-1}-P_i) \\ &\quad - S^t_{i,i+1} G_{i,i+1}(P_i - P_{i+1}), \end{aligned} \qquad \text{for } a < i \leq N-b, \quad (6.114)$$

$$\begin{aligned} V_i \frac{\mathrm{d}\left(c^k_i S_i\right)}{\mathrm{d}t} &= c^k_{i-1,i} S^t_{i-1,i} G_{i-1,i}(P_{i-1}-P_i) \\ &\quad - c^k_{i,i+1} S^t_{i,i+1} G_{i,i+1}(P_i - P_{i+1}), \end{aligned} \qquad \text{for } a < i \leq N-b, \quad (6.115)$$

where

$$G_{i,i+1} = \frac{{R^t_{i,i+1}}^4}{L^t_{i,i+1}} \frac{1 + 2\frac{\lambda_s}{R^t_{i,i+1}}}{\left(1 + 2\frac{\lambda_s}{R^t_{i,i+1}}\right) S^t_{i,i+1} + \mu^*(1 - S^t_{i,i+1})}, \quad (6.116)$$

$$\lambda_s = \frac{\epsilon_2 \left(\mu^* - 1\right)}{\left(c^1 + 4c^* c^2\right)^{1/2}} \cosh^{-1}\left(\frac{s^* \sigma_{c0}\sigma_{o0} + \sqrt{\left(\sigma_{c0}^2 + \Gamma\right)\left(s^{*2}\sigma_{o0}^2 + \Gamma\right)}}{\Gamma}\right), \quad (6.117)$$

$$S^t_{i,i+1} = \begin{cases} S_i, & \text{if } P_i > P_{i+1} \text{ and } P^c_i\left(S_i\right) > p^e_{i,i+1}, \\ S_{i+1}, & \text{if } P_i < P_{i+1} \text{ and } P^c_{i+1}\left(S_{i+1}\right) > p^e_{i,i+1}, \\ 1, & \text{otherwise}, \end{cases} \quad (6.118)$$

$$p^e_{i,i+1} = \frac{2\Gamma_{\mathcal{P}}}{R^t_{i,i+1} + 2\lambda_s}, \quad (6.119)$$

$$c^k_{i,i+1} = \begin{cases} c^k_i, & \text{if } P_i > P_{i+1}, \\ c^k_{i+1}, & \text{if } P_i < P_{i+1}, \end{cases} \quad (6.120)$$

$$P^c_i = 2\Gamma_{\mathcal{P}} R^* \sqrt{\frac{4-\pi}{S_i}}, \quad (6.121)$$

where $R^* = R^t/R^p$ is the ratio of the average throat radius length to the average pore radius, which we choose to be 0.5.

Since we are considering a one-dimensional network, we can simplify the problem by assuming that the direction of flow is from left to right, so that $P_i > P_{i+1}$ for all i. Using the fact that the capillary pressure in the pores is a monotonic function of the saturation, (6.121), we reformulate the entry pressure condition, (6.118), as an 'entry saturation' condition by defining the entry saturation, $S^e_i(c^k_i)$, to be the value which satisfies $P^c_i(S^e_i) = p^e_{i,i+1}$. Equating (6.119) and (6.121) yields

$$S^e_i = (4-\pi)R^{*2}\left(\frac{R^t_{i,i+1}(R^t_{i,i+1} + 2\lambda_s(c^k_{i,i+1}))}{R^p_i}\right)^2. \quad (6.122)$$

This represents the maximum water saturation in pore i at which oil may enter the exit throat. If the water saturation increases above this value, the capillary pressure becomes too low for oil to enter, and the throat becomes filled with water. By (6.113), the flux in each throat, $Q_{i,i+1} = G_{i,i+1}(P_i - P_{i+1})$, is equal to some constant Q for all i. Substituting $Q_{i,i+1} = G_{i,i+1}(P_i - P_{i+1}) = Q$ into (6.113) – (6.121), and using the fact that, by (6.120), the concentration of ions in a throat is equal to the concentration in the upstream pore, $c^k_{i,i+1} = c^k_i$, we find that

$$V_i \frac{\mathrm{d}S_i}{\mathrm{d}t} = Q\left(S^t_{i-1,i} - S^t_{i,i+1}\right), \qquad V_i \frac{\mathrm{d}\left(c^k_i S_i\right)}{\mathrm{d}t} = Q\left(c^k_{i-1} S^t_{i-1,i} - c^k_i S^t_{i,i+1}\right), \quad (6.123)$$

where

$$S^t_{i,i+1} = \begin{cases} S_i, & \text{if } S_i < S^e_i(c^k_i), \\ 1, & \text{otherwise.} \end{cases} \quad (6.124)$$

We follow the approach presented in §6.2 and §6.3 and perform a multiple-scales analysis by introducing the large-scale continuous spatial coordinate, x, which we treat as independent of the small-scale discrete index, i. We suppose that the pore saturation, throat saturation, and the salinity are functions of both lengthscales, so that $S_i(t) = S_i(x,t)$, $S^t_{i,i+1}(t) = S^t_{i,i+1}(x,t)$, and $c^k_i(t) = c^k_i(x,t)$, and use the extra freedom provided by the separation of scales to impose periodicity on the microscale.

We introduce the cyclic notation $\bar{i} = (i-1 \mod N)+1$, so that, by writing $S_i = S_{\bar{i}}$, $S^t_{i,i+1} = S^t_{\bar{i},\overline{i+1}}$, and $c^k_i = c^k_{\bar{i}}$, we automatically impose the periodicity condition on the small scale. Writing (6.123) and (6.124) in terms of the two spatial coordinates reads

$$V_{\bar{i}} \frac{\partial S_{\bar{i}}(x,t)}{\partial t} = Q\left(S^t_{\overline{i-1},\bar{i}}(x - \epsilon x_{i-1}, t) - S^t_{\bar{i},\overline{i+1}}(x,t)\right), \quad (6.125)$$

$$V_{\bar{i}} \frac{\partial\left(c^k_{\bar{i}}(x,t) S_{\bar{i}}(x,t)\right)}{\partial t} = Q\left(c^k_{\overline{i-1}}(x - \epsilon x_{i-1}, t) S^t_{\overline{i-1},\bar{i}}(x - \epsilon x_{i-1}, t) - c^k_{\bar{i}}(x,t) S^t_{\bar{i},\overline{i+1}}(x,t)\right), \quad (6.126)$$

where

$$S^t_{\bar{i},\overline{i+1}}(x,t) = \begin{cases} S_{\bar{i}}(x,t), & \text{if } S_{\bar{i}}(x,t) < S^e_{\bar{i}}(c^k_{\bar{i}}(x,t)), \\ 1, & \text{otherwise.} \end{cases} \quad (6.127)$$

We evaluate $S^t_{\overline{i-1},\bar{i}}$ and $S^t_{\bar{i},\overline{i+1}}$ at $x - \epsilon x_{i-1}$ and x, respectively, since, by (6.127), we know that the saturation in a given throat depends only on the saturation in the upstream pore.

6.4.2 Homogenisation

Taylor expanding (6.125) – (6.127) about x yields

$$V_{\bar{i}}\frac{\partial S_{\bar{i}}}{\partial t} = Q\left(S^t_{\overline{i-1},\bar{i}} - S^t_{\bar{i},\overline{i+1}} - \epsilon x_{i-1}\frac{\partial S^t_{\overline{i-1},\bar{i}}}{\partial x} + O(\epsilon^2)\right), \tag{6.128}$$

$$V_{\bar{i}}\frac{\partial\left(c^k_{\bar{i}}S_{\bar{i}}\right)}{\partial t} = Q\left(c^k_{\overline{i-1}}S^t_{\overline{i-1},\bar{i}} - c^k_{\bar{i}}S^t_{\bar{i},\overline{i+1}} - \epsilon x_{i-1}\frac{\partial\left(c^k_{\overline{i-1}}S^t_{\overline{i-1},\bar{i}}\right)}{\partial x} + O(\epsilon^2)\right), \tag{6.129}$$

$$S^t_{\bar{i},\overline{i+1}}(x,t) = \begin{cases} S_{\bar{i}}(x,t), & \text{if } S_{\bar{i}}(x,t) < S^e_{\bar{i}}(c^k_{\bar{i}}(x,t)), \\ 1, & \text{otherwise,} \end{cases} \tag{6.130}$$

which we write in vector format as

$$\mathbf{V}\circ\frac{\partial\mathbf{S}}{\partial t} = Q\left(\boldsymbol{M}\mathbf{S}^t - \epsilon\boldsymbol{A}\frac{\partial\mathbf{S}^t}{\partial x} + O(\epsilon^2)\right), \tag{6.131}$$

$$\mathbf{V}\circ\frac{\partial\left(\mathbf{c}^k\circ\mathbf{S}\right)}{\partial t} = Q\left(\boldsymbol{M}\left(\mathbf{c}^k\circ\mathbf{S}^t\right) - \epsilon\boldsymbol{A}\frac{\partial\left(\mathbf{c}^k\circ\mathbf{S}^t\right)}{\partial x} + O(\epsilon^2)\right), \tag{6.132}$$

$$(\mathbf{S}^t)_i = \begin{cases} (\mathbf{S})_i, & \text{if } (\mathbf{S})_i < (\mathbf{S}^e(\mathbf{c}^\mathbf{k}))_i, \\ 1, & \text{otherwise,} \end{cases} \tag{6.133}$$

where $\mathbf{V}$, $\mathbf{S}$, $\mathbf{S}^t$, $\mathbf{S}^e$ and $\mathbf{c}^k$ correspond to the vector forms of $V_{\bar{i}}$, $S_{\bar{i}}$, $S^t_{\bar{i},\overline{i+1}}$, $S^e_{\bar{i}}$, and $c^k_{\bar{i}}$, respectively, and

$$\boldsymbol{M} = \begin{pmatrix} -1 & 0 & 0 & \dots & 0 & 1 \\ 1 & -1 & 0 & \dots & 0 & 0 \\ 0 & 1 & -1 & \dots & 0 & 0 \\ \vdots & \vdots & \vdots & \ddots & \vdots & \vdots \\ 0 & 0 & 0 & \dots & 1 & -1 \end{pmatrix}, \qquad \boldsymbol{A} = \begin{pmatrix} 0 & 0 & 0 & \dots & 0 & x_n \\ x_1 & 0 & 0 & \dots & 0 & 0 \\ 0 & x_2 & 0 & \dots & 0 & 0 \\ \vdots & \vdots & \vdots & \ddots & \vdots & \vdots \\ 0 & 0 & 0 & \dots & x_{n-1} & 0 \end{pmatrix}. \tag{6.134}$$

We expand $\mathbf{S}$, $\mathbf{S}^t$, $\mathbf{S}^e$, and $\mathbf{c}^k$ in powers of ϵ, and substitute into (6.131) – (6.133) to find that, at leading order,

$$\mathbf{V}\circ\frac{\partial\mathbf{S}_0}{\partial t} = Q\boldsymbol{M}\mathbf{S}^t_0, \tag{6.135}$$

$$\mathbf{V}\circ\frac{\partial\left(\mathbf{c}^k_0\circ\mathbf{S}_0\right)}{\partial t} = Q\boldsymbol{M}\left(\mathbf{c}^k_0\circ\mathbf{S}^t_0\right), \tag{6.136}$$

$$(\mathbf{S}^t_0)_i = \begin{cases} (\mathbf{S}_0)_i, & \text{if } (\mathbf{S}_0)_i < (\mathbf{S}^e_0(\mathbf{c}^k_0))_i, \\ 1, & \text{otherwise,} \end{cases} \tag{6.137}$$

Given an appropriate set of initial conditions within a particular cell, equations (6.135) – (6.137) describe the transient behaviour of the saturation and ion concentration distributions within the cell, assuming periodic boundary conditions. Following

the methodology outlined in §6.3.3, we wish to determine the leading-order saturation and ion concentrations within each pore in the cell on the macroscopic timescale, $T = \epsilon t$, given values for the cell-averaged saturation, S, and ion concentrations, c^k. For the model presented in §6.3, we were able to do this be rescaling time and computing the unique leading-order solutions over the macroscopic timescale directly, which we found to be uniformly distributed throughout the cell. However, due to the non-linear, discontinuous nature of (6.137), we expect that the saturation may be non-uniform in our current model, and, furthermore, may depend on the initial conditions for a given total saturation. Hence, we determine the appropriate leading-order solutions (valid on the macroscopic timescale) by finding the steady-state solutions, $\mathbf{S}_0 \to \bar{\mathbf{S}}_0$, $\mathbf{S}_0^t \to \bar{\mathbf{S}}_0^t$, and $\mathbf{c}_0^k \to \bar{\mathbf{c}}_0^k$, to (6.135) – (6.137) in the limit $t \to \infty$.

To overcome the issue of non-uniqueness in the microscale solution, we focus our attention on computing $\bar{\mathbf{S}}_0(S)$ for a waterflood process using an inductive method. We initially set the total water saturation in the cell to be zero, $S = 0$, so that the water saturation in each pore and throat is equal to zero, $\mathbf{S}_0 = \mathbf{S}_0^t = \mathbf{0}$, and therefore the steady-state solution to (6.135) and (6.137) is $\bar{\mathbf{S}}_0 = \mathbf{0}$. Then, given $\bar{\mathbf{S}}_0(S)$, we compute the value of $\bar{\mathbf{S}}_0(S + \Delta S)$, for some small ΔS, by solving (6.135) and (6.137) numerically subject to

$$\mathbf{S}_0(S + \Delta S) = \bar{\mathbf{S}}_0(S) + \boldsymbol{\delta}\Delta S, \qquad \text{at } t = 0, \tag{6.138}$$

until a steady state is obtained, where $\boldsymbol{\delta}$ is the prescribed relative increase in the saturation in each pore in the cell. We choose $\boldsymbol{\delta}$ such that the increase in the total saturation in the cell is ΔS, and the relative saturation increase in each pore is weighted by the oil saturation in the pore (i.e. the remaining space for the water to fill), so that

$$\mathbf{V} \cdot \boldsymbol{\delta} = \sum_i V_i, \qquad \boldsymbol{\delta} \propto \mathbf{1} - \bar{\mathbf{S}}_0(S). \tag{6.139}$$

From (6.139), we find that the appropriate form of $\boldsymbol{\delta}$ is given by

$$\boldsymbol{\delta} = \left(1 - \bar{\mathbf{S}}_0(S)\right) \frac{\sum_i V_i}{\mathbf{V}^T \left(1 - \bar{\mathbf{S}}_0(S)\right)}. \tag{6.140}$$

In Figure 6.7, we plot the saturation in each pore for a periodic 10-node network, given by the solution to (6.135) and (6.137) at $t = 5$ (i.e. the long term behaviour in the limit $t \to \infty$), against the mean saturation within the cell,

$$S = \frac{\mathbf{V} \cdot \bar{\mathbf{S}}_0}{\sum_i V_i}. \tag{6.141}$$

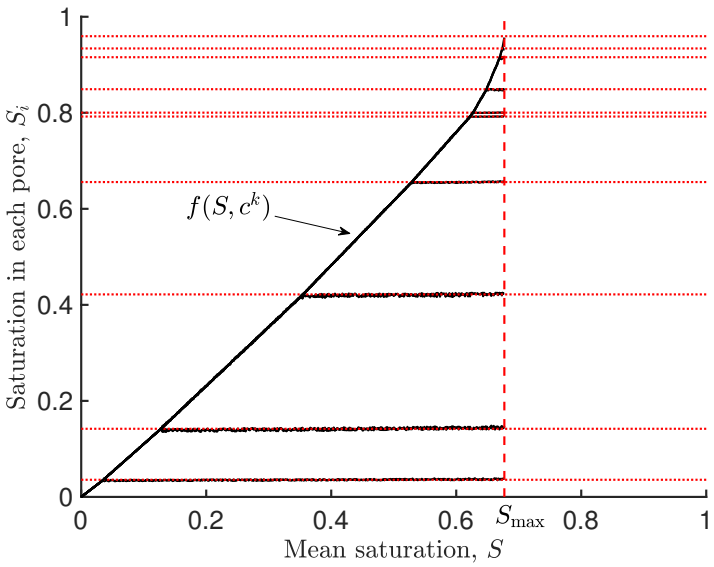


Figure 6.7: Plots of the long-term behaviour of the saturation within each pore of a 10-node network against the average saturation within the total network. The horizontal red dashed lines correspond to the entry saturation of each throat in the network.

We select the pore volume at each node from a uniform distribution on [0.5, 1.5], and, for simplicity, we assume that the ion concentrations are uniform within the cell. We therefore neglect (6.136), and choose the entry saturation for each throat from a uniform distribution between 0 and 1. We prescribe the flux to be given by $Q = 1$. We show the saturation in each pore separately using a solid black line, and show the entry saturations for each pore using dotted red lines.

We restrict our model to the region $S < S_{\max}$ ($S_{\max}$ is shown by the vertical dashed red line in Figure 6.7), since the solution for $S > S_{\max}$ is unphysical due to the fact that, by imposing periodicity across the cell, we force the pores to fill with water (i.e. we force oil to be expelled) despite the pore saturations being greater than the entry saturations of the downstream throats. This is a result of the fact that (6.138) corresponds to artificially 'injecting' water into each of the pores. In a real system, water enters the pores through the throats and the pore saturation is limited by the entry saturation of the downstream throat. Since the total saturation in the cell is given by (6.141), the critical saturation is given by

$$S_{\max} = \frac{\mathbf{V} \cdot \mathbf{S}_0^e}{\sum_i V_i}. \tag{6.142}$$

We observe that, for $S \leq S_{\max}$, the saturation within the pores increases uniformly until a particular pore reaches the entry saturation of the downstream throat (i.e.

the capillary pressure in the pore falls below the entry pressure of the exit throat). At this point, the saturation within the pore oscillates about the entry saturation, S^e_{0i}, and the saturation in the remaining pores continues to increase uniformly. The small oscillations correspond to slugs of oil being released from the pore into the downstream throat as a result of the following cyclic process: As the pore fills with water, the capillary pressure in the pore decreases until it reaches the entry pressure of the exit throat. At this point, oil cannot exit the pore and, since the saturation in the upstream throat is in general less than unity, the net flux of oil into the pore increases[2]. This results in an increase in the capillary pressure, which enables a slug of oil to be released into the downstream throat. As the oil in the pore is released, the capillary pressure decreases once again until it reaches the entry pressure of the exit throat.

Extra physics is required to model the cyclic slug formation process, in order to determine the size and frequency of the slugs being produced. However, we can avoid this additional complication and regularise the model by modifying (6.124) according to

$$S^t_{i,i+1} = \begin{cases} S_i, & \text{if } S_i < S^e_i, \\ S^t_{i-1,i}, & \text{if } S_i = S^e_i, \\ 1, & \text{otherwise.} \end{cases} \tag{6.143}$$

This corresponds to setting the flow at the outlet to be the same as the flow at the inlet when the pore is at the entry saturation, so that the pore is effectively bypassed.

With this modification to the model, the saturation in the pores approaches a steady state as $t \to \infty$, and the saturation in the throats is uniform and equal to the saturation in the (non-bypassed) pores, so that, for $S < S_{\max}$, the steady-state solution satisfies

$$\bar{\mathbf{S}}_0 = \min\left(f, \mathbf{S}^e_0\right), \qquad \bar{\mathbf{S}}^t_0 = f\mathbf{u}, \tag{6.144}$$

where $\mathbf{u} = (1, 1, \ldots, 1)^T$, and $f(x,t)$ is a function to be determined which varies on the macroscopic scale. We can think of $f(x,t)$ as the saturation within the throats, which is locally uniform and related to the saturation in the pores by (6.144).

To determine the macroscopic ion concentrations, we substitute (6.135) into (6.136) to find that

$$\mathbf{V} \circ \mathbf{S}_0 \circ \frac{\partial \mathbf{c}^k_0}{\partial t} = Q\left(\boldsymbol{M}\left(\mathbf{c}^k_0 \circ \mathbf{S}^t_0\right) - \mathbf{c}^k_0 \circ \left(\boldsymbol{M}\mathbf{S}^t_0\right)\right). \tag{6.145}$$

[2]If the water saturation in the upstream throat is equal to one, we consider the first pore for which the upstream throat saturation is not unity, apply the theory to show that small amounts of oil are released, and note that the released oil then propagates through the downstream pores, resulting in the observed oscillations in all of the downstream nodes.

We assume that $\mathbf{c}_0^k$ approaches a steady-state solution, $\bar{\mathbf{c}}_0^k$, (so that $\partial \mathbf{c}_0^k/\partial t \to 0$ as $t \to \infty$), and use the fact that $\boldsymbol{M}\mathbf{S}_0^t \to 0$ and $\mathbf{S}_0^t \to f\mathbf{u}$ as $t \to \infty$, by (6.135) and (6.144) respectively, to find that $\boldsymbol{M}\mathbf{c}_0^k \to \boldsymbol{M}\bar{\mathbf{c}}_0^k = 0$ as $t \to \infty$. This has the solution

$$\bar{\mathbf{c}}_0^k = c^k(x,t)\mathbf{u}, \tag{6.146}$$

where $c^k(x,t)$ are the macroscopic ion concentrations for each ion species, to be determined. We note that, in contrast to the saturation in the pores, the microscale ion concentrations are uniform throughout each cell and equal to the macroscopic variable.

Equations (6.144) define the pore and throat saturations within a cell in terms of the macroscale function, $f(x,t)$. We relate f to the macroscopic saturation and ion concentrations, $S(x,t)$ and $c^k(x,t)$, by substituting (6.144) into (6.141), which yields

$$S = \frac{\mathbf{V} \cdot \min(f, \mathbf{S}_0^e(c^k))}{\sum_i V_i}. \tag{6.147}$$

Since $S(f, c^k)$ is a strictly increasing monotonic function of f, for $0 \leq S < S_{\max}$, we invert (6.147) in this range in order to write $f(x,t) = f(S(x,t), c^k(x,t))$. The function $f(S, c^k)$ is given by the bounding curve in the region $S < S_{\max}$, shown in Figure 6.7.

In order to determine f, S, and c^k, we must proceed to the first-order problem to find the appropriate solvability conditions. Since the timescale chosen for (6.131) and (6.132) is the transient timescale over which the saturation and salinity in the pores reach local equilibrium, and we are primarily interested in the larger scale dynamics, we introduce the long timescale, $T = \epsilon t$, and find that the first order terms in (6.131) and (6.132) read

$$\mathbf{V} \circ \frac{\partial \mathbf{S}_0}{\partial T} = Q\left(\boldsymbol{M}\mathbf{S}_1^t - \boldsymbol{A}\frac{\partial \mathbf{S}_0^t}{\partial x}\right), \tag{6.148}$$

$$\mathbf{V} \circ \frac{\partial\left(\mathbf{S}_0 \circ \mathbf{c}_0^k\right)}{\partial T} = Q\left(\boldsymbol{M}\left(\mathbf{c}_1^k \circ \mathbf{S}_0^t\right) + \boldsymbol{M}\left(\mathbf{c}_0^k \circ \mathbf{S}_1^t\right) - \boldsymbol{A}\frac{\partial\left(\mathbf{c}_0^k \circ \mathbf{S}_0^t\right)}{\partial x}\right). \tag{6.149}$$

On the T timescale, the leading-order saturation and ion concentrations are given by (6.144) and (6.146), which we substitute into (6.148) and (6.149) to get

$$\frac{\partial\left(\mathbf{V} \circ \bar{\mathbf{S}}_0\right)}{\partial T} = Q\left(\boldsymbol{M}\mathbf{S}_1^t - \frac{\partial f}{\partial x}\boldsymbol{A}\mathbf{u}\right), \tag{6.150}$$

$$c^k\frac{\partial\left(\mathbf{V} \circ \bar{\mathbf{S}}_0\right)}{\partial T} + \mathbf{V} \circ \bar{\mathbf{S}}_0\frac{\partial c^k}{\partial T} = Q\left(f\boldsymbol{M}\mathbf{c}_1^k + c^k\boldsymbol{M}\mathbf{S}_1^t - f\frac{\partial c^k}{\partial x}\boldsymbol{A}\mathbf{u} - c^k\frac{\partial f}{\partial x}\boldsymbol{A}\mathbf{u}\right). \tag{6.151}$$

We multiply (6.150) by c^k, and substitute into (6.151), to find that

$$\mathbf{V} \circ \bar{\mathbf{S}}_0 \frac{\partial c^k}{\partial T} = fQ \left(\boldsymbol{M}\mathbf{c}_1^k - \frac{\partial c^k}{\partial x} \boldsymbol{A}\mathbf{u} \right). \tag{6.152}$$

The appropriate solvability conditions for (6.150) and (6.152) are found by premultiplying (6.150) and (6.152) by $\boldsymbol{u}^T$ and using the fact that, by (6.134), $\boldsymbol{u}^T\boldsymbol{M} = \mathbf{0}$ and $\boldsymbol{u}^T\mathbf{A}\boldsymbol{u} = \sum_i x_i = 1$, which yields

$$\frac{\partial \left(\mathbf{V} \cdot \bar{\mathbf{S}}_0 \right)}{\partial T} = -Q \frac{\partial f}{\partial x}, \qquad \mathbf{V} \cdot \bar{\mathbf{S}}_0 \frac{\partial c^k}{\partial T} = -Qf \frac{\partial c^k}{\partial x}. \tag{6.153}$$

We substitute (6.141) into (6.153) to find that

$$\frac{\partial S}{\partial T} + \frac{Q}{\sum_i V_i} \frac{\partial f}{\partial x} = 0, \qquad \frac{\partial c^k}{\partial T} + \frac{Q}{\sum_i V_i} \left(\frac{f}{S} \right) \frac{\partial c^k}{\partial x} = 0. \tag{6.154}$$

Subject to appropriate initial and boundary conditions, (6.147) and (6.154) defines a system of three equations for S, c^k, and $f(S, c^k)$.

6.4.3 Results

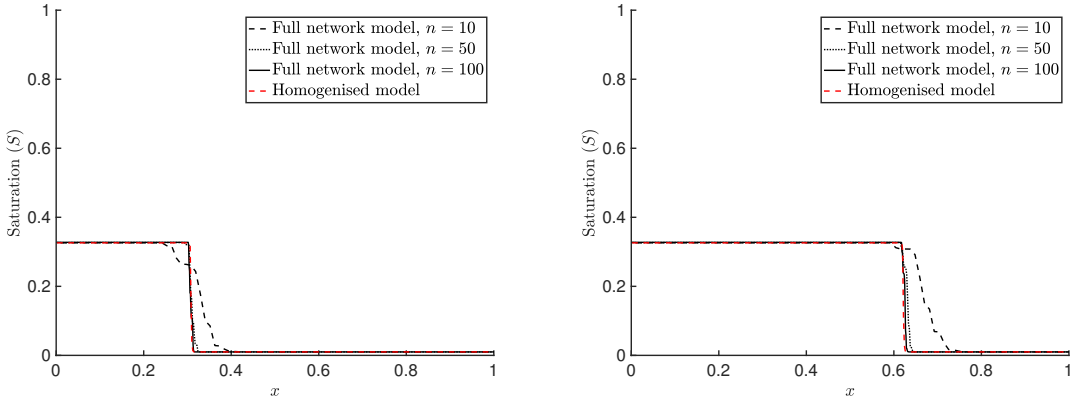
We compare the homogenised model, (6.147) and (6.154), with the full network model, (6.113) – (6.121), for a one-dimensional network constructed from n repetitions of a 10-node cell. We suppose that the total network has unit length, so that the size of each cell is $\epsilon = 1/n$. We select the pore radii, R_i^p, and throat radii, R_{ij}^t, from a uniform distribution on $[0.5, 1.5]$, and prescribe the pore volumes to be $V_i = R_i^{p3}$.

To simulate a waterflood we suppose that, initially, the network is almost saturated with oil, (we prescribe $S = 0.01$), and that the concentration of each ion species is given by the concentration in the high salinity regime, $c^k = c^k_{\text{high}}$. We specify the concentration of each ion species, $c^k = c^k_{\text{in}}$, at the inlet (which we can vary to simulate a low-salinity or high-salinity waterflood). We inject water at $x = 0$, so that the throat saturation at the inlet is given by inverting $f(S, c^k_{\text{in}}) = 1$, from which we obtain $S = S_{\max}(c^k_{\text{in}})$ at $x = 0$. Thus, the initial and boundary conditions read

$$S = 0.01, \qquad c^k = c^k_{\text{high}}, \qquad \text{at } t = 0, \tag{6.155}$$

$$S = S_{\max}(c^k_{\text{in}}), \qquad c^k = c^k_{\text{in}}, \qquad \text{at } x = 0. \tag{6.156}$$

We solve (6.147) and (6.154) – (6.156) numerically for S and c^k using a fourth-order Runge-Kutta scheme. In Figure 6.8a and 6.8b, we plot the saturation profile along the length of the network after 0.1 and 0.2 pore volumes of high-salinity water have



(a) Pore volume injected = 0.1

(b) Pore volume injected = 0.2

Figure 6.8: Saturation profile of the network after (a) 0.1, and (b) 0.2, pore volumes of high-salinity water have been injected, comparing the homogenised model with the full network model for the cases $n = 10, 50, 100$.

been injected. We compare the homogenised model and the full network model for the three cases in which the number of repeated cells is $n = 10, 50, 100$. We observe that, as the number of repeated cells in the network increases, the solution for the full network model approaches the homogenised solution. The steady-state residual water saturation is uniform along the length of the network, and equal to the inlet saturation, $S_{\max}$.

In Figure 6.9, we plot the percentage oil recovered as a function of the pore volume injected for a high-salinity waterflood ($c_{\text{in}}^k = c_{\text{high}}^k$), comparing the results for the homogenised model and the full network model for the three cases in which the number of repeated cells is $n = 10, 50, 100$. There is excellent agreement between the homogenised solution and the full network solution for the cases $n = 50, 100$. The maximum amount of oil is recovered after approximately 0.3 pore volumes of water have been injected. In Figure 6.10, we plot the percentage oil recovered as a function of the pore volume injected for the homogenised model, comparing the cases of a high-salinity waterflood ($c_{\text{in}}^k = c_{\text{high}}^k$), and a low-salinity waterflood ($c_{\text{in}}^k = c_{\text{low}}^k$). We observe that the rate of recovery is initially the same for each case. However, after approximately 0.32 pore volumes of water have been injected, the high-salinity waterflood ceases to produce more oil, whereas the low-salinity waterflood continues to produce oil until 0.4 pore volumes of water have been injected. The low-salinity waterflood produces approximately 25% more oil than the high-salinity waterflood.

We can compute the residual oil saturation in the network as a function of the

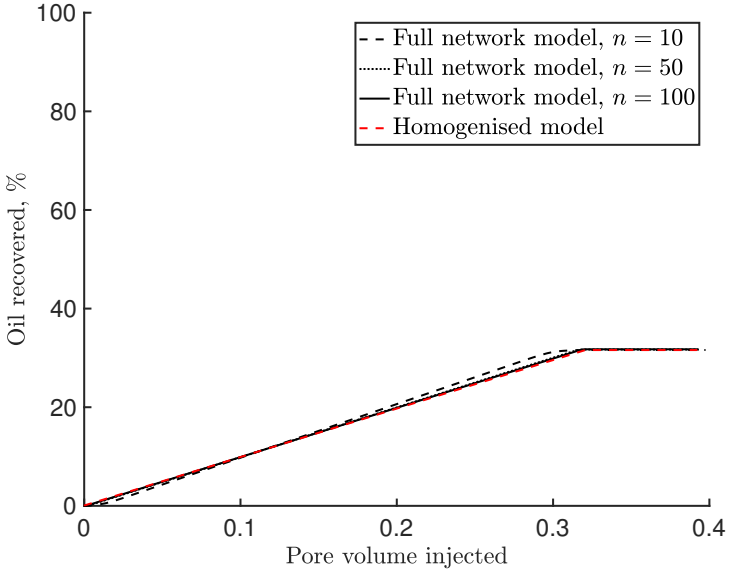


Figure 6.9: Percentage oil recovered as a function of the pore volume of water injected, for both the homogenised model and the full network model with $n = 10, 50, 100$ repeated cells.

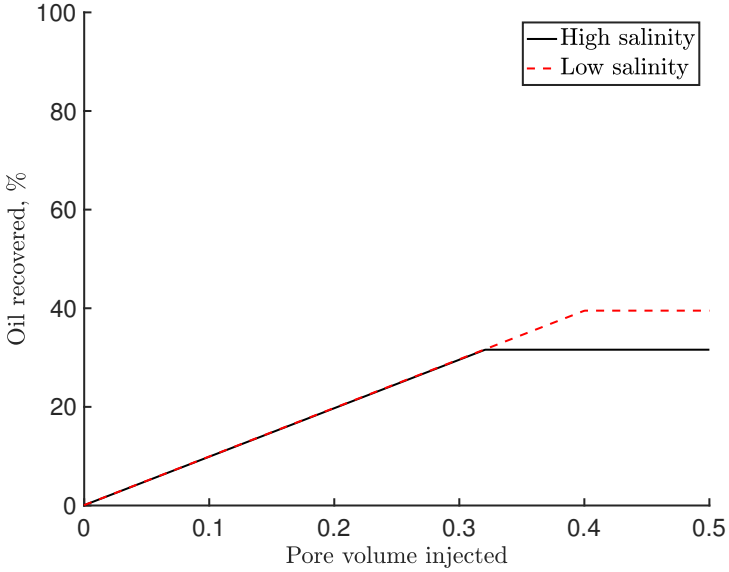


Figure 6.10: Percentage oil recovered as a function of the pore volume of water injected for the homogenised model, comparing a high-salinity waterflood (black line) with a low salinity waterflood (red dashed line).

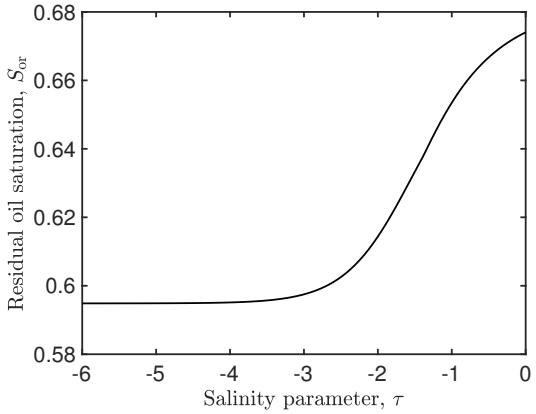


Figure 6.11: Residual oil saturation as a function of the salinity.

salinity directly from

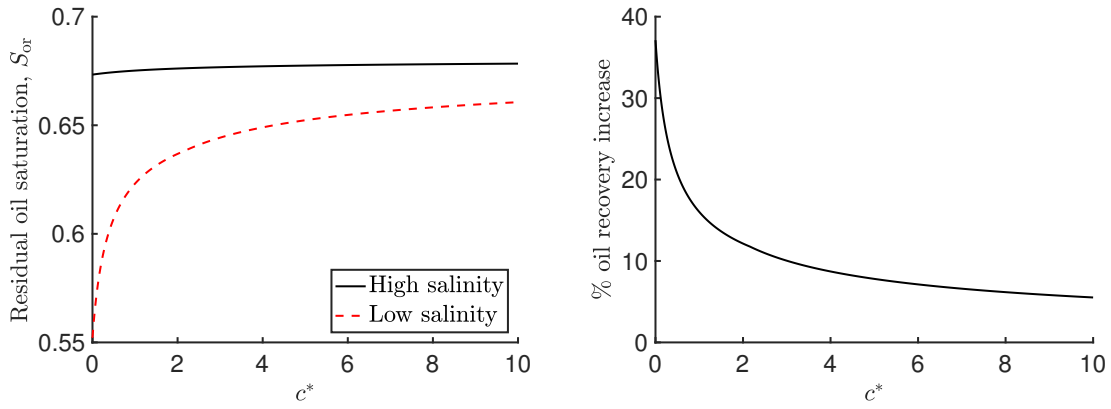
$$S_{\text{or}}(c^k) = 1 - S_{\max}(c^k) = 1 - \frac{\mathbf{V} \cdot \mathbf{S}_0^e(c^k)}{\sum_i V_i}. \tag{6.157}$$

We introduce the salinity parameter, τ, in order to vary the concentrations of the multiple ion species simultaneously using a single parameter as we did in Chapter 2. In Figure 6.11, we plot the residual oil saturation, (6.157), against τ, for $-6 < \tau \leq 0$, where the concentration of each ion species is given by

$$c^k(\tau) = c^k_{\text{low}} + 10^\tau \left(c^k_{\text{high}} - c^k_{\text{low}} \right). \tag{6.158}$$

The values $\tau = -6$ and $\tau = 0$ correspond to the low and high salinity regimes, respectively. We observe that the residual oil decreases as the salinity decreases, which is consistent with the low salinity effect observed experimentally [60, 67, 124].

In Figure 6.12a we plot the residual oil saturation, S_{or}, against the ratio of divalent ions to monovalent ions, $c^* = c^2_{\text{low}}/c^1_{\text{low}}$, for a high-salinity and low salinity waterflood. We observe that, in both cases, the residual oil increases as c^* increases, i.e. as the relative number of divalent ions increases. This is consistent with the multi-component ionic exchange mechanism described in Chapter 2, in which the divalent ions bind the oil to clay surface in the reservoir rock. An increase in the relative number of divalent ions leads to an increase the attraction between the oil and clay surfaces, and therefore a decrease in the amount of oil recovered. In Figure 6.12b, we plot the percentage oil recovery increase observed during a low salinity waterflood (calculated using $(1 - S^{\text{low}}_{\text{or}})/(1 - S^{\text{high}}_{\text{or}}) - 1$ where $S^{\text{low}}_{\text{or}}$ and $S^{\text{high}}_{\text{or}}$ correspond to the residual oil saturation in the low salinity and high salinity regimes, respectively)



(a) (b)

Figure 6.12: (a) Residual oil saturation as a function of c^* for a high-salinity and low-salinity waterflood. (b) Percentage oil recovery increase observed during a low salinity waterflood as a function of c^*.

against c^*. The recovery improvement observed during a low salinity waterflood decreases as the relative number of divalent ions increases.

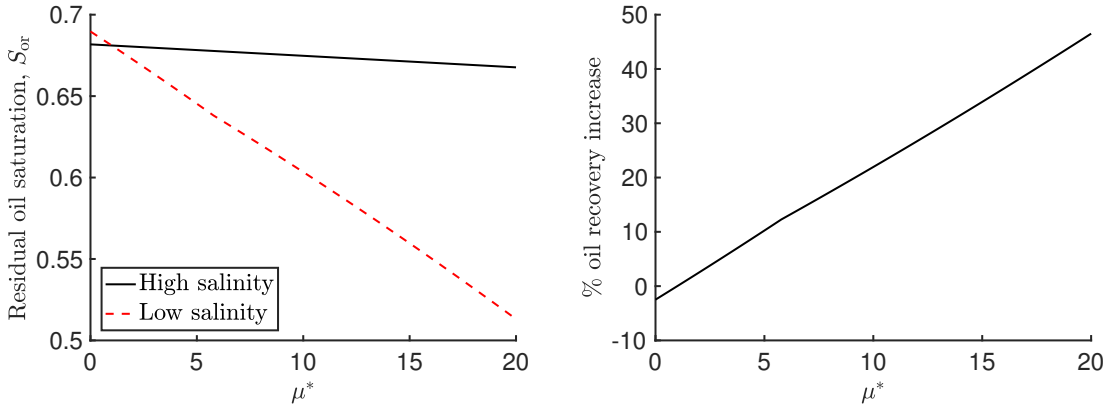
In Figure 6.13a we plot the residual oil saturation, S_{or}, against the viscosity ratio, $\mu^* = \mu_o/\mu_w$, for a high-salinity and low salinity waterflood. We observe that the residual oil decreases linearly as μ^* increases, and that the μ^*-dependence is greater for a low salinity-waterflood. For $\mu^* < 1$, the residual oil saturation is greater for the low salinity waterflood than the high salinity waterflood, since, in this case, the thin water layer separating the oil from the clay acts as a viscous layer which *restricts* the motion of the oil. In Figure 6.13b, we plot the percentage oil recovery increase observed during a low salinity waterflood against μ^*. The recovery improvement observed during a low salinity waterflood increases as the viscosity ratio increases, since the effective slip due to the low-viscosity water layer is enhanced.

6.4.4 Comparison with Buckley-Leverett theory

We observe that (6.154) is of a similar form to the traditional one-dimensional Buckley-Leverett equation [20] for two-phase flow through a porous material, which reads

$$\frac{\partial S}{\partial T} + \frac{\partial}{\partial x}\left(\frac{q}{\phi A}F(S)\right) = 0, \tag{6.159}$$

where q is the macroscale flux, ϕ is the porosity of the material, A is the cross sectional area, and $F(S)$ is the fractional flow function, which measures the relative mobility of the two phases. For a porous material, ϕA measures the total fluid volume per unit



(a) (b)

Figure 6.13: (a) Residual oil saturation as a function of μ^* for a high-salinity and low-salinity waterflood. (b) Percentage oil recovery increase observed during a low salinity waterflood as a function of μ^*.

length. The equivalent for our one-dimensional homogenised network model is the total pore volume in each cell divided by the length of the cell, ϵ, so that $\phi A = \sum_i V_i/\epsilon$. The macroscale volumetric flux is related to the microscale volumetric flux through $q = Q/\epsilon$. Therefore, by equating terms in (6.154) and (6.159) for constant q, ϕ, and A, we find that the two models are the same if we pick the Buckley-Leverett fractional flow function to be equal to the throat saturation, $F = f(S, c^k)$.

In Figure 6.14, we plot $f(S, c^k)$ for a one-dimensional network constructed from a repeated 1000-pore cell, comparing the result in the high-salinity and low-salinity regimes. We select the pore radii, R_i^p, and throat radii, $R_{i,i+1}^t$, uniformly on $[0.5, 1.5]$. We observe that f increases as S increases until the critical point $S = S_{\max}$. This point is related to the residual oil saturation by $S_{or} = 1 - S_{\max}$. We observe that a decrease in the salinity results in a decrease in the residual oil saturation, which is consistent with the experimentally-observed low salinity effect [60, 67, 124]. Furthermore, we observe that f decreases as the salinity decreases, which is consistent with the experimental data gathered by Ligthelm *et al.* [67]. However, the shape of the curve is inconsistent with traditional 'S-shaped' fractional flow curves. This is likely due to the fact that we are considering a one-dimensional network.

6.5 Conclusions

In this chapter, we used the method of multiple scales to derive the continuum equations which govern the effective macroscopic properties of network models of single-

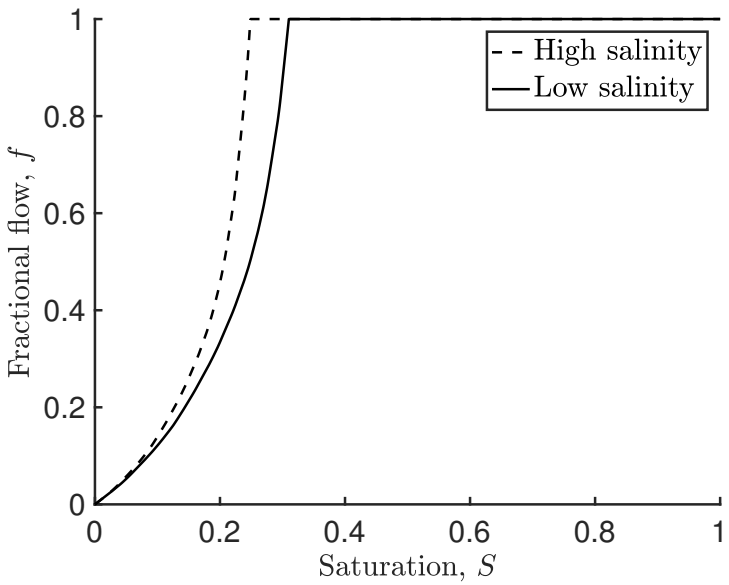


Figure 6.14: Fractional flow as a function of salinity for a network constructed from a repeated 1000-node cell.

phase and two-phase flow. Traditionally, when the method of multiple scales is applied to a continuum model, the multiple length scales in the model are assumed to be continuous. However, in order to apply this method to a network model, we described the microscopic length scale using a discrete pore index, which we assumed could be treated as independent from the continuous macroscopic length scale.

In §6.2 we demonstrated how to apply the discrete method of multiple scales to the simple example of single-phase flow through a one-dimensional network. We found that the leading-order solution for the pressure is locally uniform within the periodic cell, but varies on the macroscopic scale, (6.10). By relating the macroscale flux to the pressure gradient, we showed that the macroscale modulation in the pressure and flux satisfies the one-dimensional Darcy law (6.22), and derived an expression for the effective permeability of the network in terms of the network structure (6.23).

In §6.3, we used a similar approach to homogenise the network model for two-phase flow we presented in Chapter 5, for a two-dimensional periodic network. We neglected the effects of entry pressure, and instead assumed that the saturation and ion concentrations in the throats were equal to the saturation and ion concentrations in the upstream pores. Despite the additional algebraic complexity introduced due to the multiple spatial dimensions, we found that the pressure, (6.59), saturation, (6.71), and ion concentrations, (6.88), are all locally uniform at leading order, but may vary on the macroscopic scale. We derived an expression for the saturation-

and-salinity-dependent effective permeability of the network in terms of the network structure, (6.79), and found that the macroscopic modulation in the pressure satisfies a two-dimensional Darcy law (6.107), which is coupled to advection equations for the macroscale modulation in the saturation and ion concentrations (6.108). We performed numerical simulations on a one-dimensional network, and found that the continuum model, (6.107) – (6.108), agrees with the full network model, (6.27) – (6.31), in the asymptotic limit $\epsilon = 1/n \to 0$, where n is the number of repeated cells per unit length. We derived an expression for the speed of the saturation front in terms of the effective permeability of the network, and showed that the speed increases as the salinity decreases.

In §6.4, we applied the method of multiple scales to the full network model we presented in Chapter 5, including the effects of entry pressure. We focused our attention on the one-dimensional case since the direction of flow becomes important when entry pressure is included in the model, and, in one dimension, the flow direction is prescribed by the applied pressure difference whereas in multiple dimensions this must be found as part of the solution. We found that the leading-order equations for the saturation, (6.135) and (6.137), describe the transient behaviour within the cell. By considering the limiting behaviour of the transient system as $t \to \infty$, we derived an expression (6.144) for the saturation in the pores in terms of the macroscale modulation of the saturation in the throats, $f(S, c^k)$, which is applicable on the slower timescale over which the macroscale system varies. In contrast to the models studied in §6.2 and §6.3, the leading-order saturation in the pores is locally non-uniform due to the effect of entry pressure restricting the motion of the oil phase. However, the saturation in the throats, (6.144), and the ion concentrations, (6.146), *are* locally uniform at leading order. We derived a system of continuum advection equations, (6.154), for the macroscopic variation of the ion concentrations and the average saturation within each cell (weighted by the pore volumes since the saturation is locally non-uniform). We numerically simulated high-salinity and low-salinity waterfloods, and found that the continuum model, (6.154), agrees with the full network model, (6.123) and (6.124), in the limit $\epsilon = 1/n \to 0$. We found that the continuum model is able to reproduce the low salinity effect [60, 67, 84, 124], in which the percentage oil recovered is greater during a low-salinity waterflood than during a high-salinity waterflood, and derived an analytical expression for the residual oil saturation as a function of the salinity (6.157). By comparing the homogenised network model, (6.154), with the Buckley-Leverett model for two-phase flow through porous media,

(6.159), we showed that the macroscale variation of the saturation in the pore throats, $f(S, c^k)$, is equivalent to the fractional flow function in the Buckley-Leverett model.

In summary, we used the method of multiple scales to derive the effective continuum equations for the salinity-dependent two-phase flow network model we developed in Chapter 5. We showed numerically that the continuum model agrees with the network model in the appropriate asymptotic limit, and we are able to relate the model to standard Buckley-Leverett theory for two-phase flow. Our model is able to reproduce the low salinity effect, in which the amount of oil produced during a waterflood increases in the low salinity regime, and we have derived an analytical expression for the amount of oil recovered as a function of the salinity.

Chapter 7

Conclusions

In this thesis, we study the effect of salinity on the two-phase flow of oil and water through a clay-coated porous rock. Our investigation spans multiple scales, with the aim of understanding how the microscale interactions between the oil, clay, and salt ions affect the macroscale oil recovery process. In this chapter, we summarise our results and suggest some possible extensions.

7.1 Summary of results

In Chapter 2, we present a model for the motion of an oil slug through a water-filled clay pore throat, in which the water phase contains diluted salt ions. We assume that the multicomponent ionic exchange (MIE) reactions described by Lager *et al.* [60] occur between the ions and the oil and clay surfaces. By modelling the MIE mechanism using an ion dissociation model, we derive expressions for the effective surface charge densities on the oil and clay surfaces as functions of the salinity of the surrounding fluid. We find that the surfaces become more negatively charged as the salinity decreases, which is consistent with experimental and theoretical studies of the MIE mechanism. We assume that there is a thin water layer between the oil and the clay surfaces, and, by balancing the viscous, capillary, and electrostatic forces in the thin film limit, we determine the thickness of this layer as a function of the salinity. We find that, as the salinity decreases, the thickness of the water layer increases. On the scale of the oil slug within the pore throat, this water layer is very thin and supplies an effective slip boundary condition for the oil at the clay interface, in which the salinity-dependent slip length is given by the thickness of the water film. We use the slip boundary condition in later chapters to study the effect of salinity on the movement of oil, since all of the information relating to the MIE mechanism is contained within the expression for the slip length. By studying the macroscopic flow

problem, we show that a decrease in the salinity results in an increase in the velocity of the oil slug for a given pressure difference across the ends of the throat.

In Chapter 3, we study the effect of salinity on oil-flow through a throat with varying elliptical cross section, using the result from Chapter 2 that the salinity of the surrounding brine affects the flow of oil through the effective slip condition at the throat surface. We assume that the aspect ratio of the channel is small, so that the lubrication approximation is applicable. We also assume that the slip length is small in comparison to the width of the throat, and, by performing an asymptotic expansion in the slip length, we derive an expression for the flux. We find that the flux is given by the harmonic mean of the equivalent flux at each cross section along the length of the throat. We derive a simplified expression for the flux by considering the limit in which the eccentricity is small, and find that there is agreement to within 16.8% between the full solution and the solution in the small-eccentricity limit. Using our expression for the flux in the small eccentricity limit, we present two methods for estimating the flux through an arbitrarily-shaped throat. We formulate these methods as extensions to the Aissen approximation [2] and hydraulic radius approximation [115], respectively, which are commonly used for estimating the flux through a non-circular cylindrical channel. We compare our approach with existing flux-estimation methods by numerically computing the flux through a pore throat extracted from a Micro-CT image of a Berea sandstone. We find that our approach more accurately estimates both the leading-order flux and the first-order relative flux increase due to slip. Furthermore, our approach appears to be less susceptible to the systematic errors observed with the existing methods.

In Chapter 4, we study slip-flow through a periodic porous structure constructed from a repeated unit cell in order to investigate how the salinity of the surrounding brine affects the flow of oil through a porous reservoir rock. We restrict our attention to two dimensions for simplicity. Starting from the Stokes equations for incompressible viscous flow subject to a slip boundary condition, we use the method of multiple scales to derive a cell problem for the permeability of the porous structure. By solving the cell problem numerically for a cell containing a circular inclusion, we find that the permeability increases as the slip length increases (i.e. as the salinity decreases). This is consistent with experimental investigations into the effect of the salinity on the relative permeability of the oil phase for the two-phase flow of oil and water through a reservoir rock. To determine a reasonable estimate for the permeability of a periodic porous structure, without having to numerically solve the cell problem, we

study the case in which the unit cell contains a single inclusion. We define the boundaries of the cell to pass through the centre of the inclusion, so that the fluid domain comprises a single channel spanning the width of the cell, and derive an expression for the flux through a thin, irregularly-shaped channel, which we use to estimate the flux through the cell. We define our permeability estimate by relating the flux to the permeability of the periodic porous structure constructed from the repeated cell. We compare our permeability estimate with the permeability computed by numerically solving the cell problem for four simple geometries. We find good agreement between our estimate and the numerical solution, and find that our approach provides a significant improvement over the alternative methods of estimating the flux using the area of the inclusion or the minimum width of the fluid domain across the length of the cell. We extend our method to unit cells containing multiple inclusions by modelling the multiply-connected domain as a network of pores and throats. We use the expression for the flux through a thin, irregularly-shaped channel with straight central axis to estimate the conductivity of each throat in the network. We define and solve a suitable network flow model in order to estimate the flux through the cell, and consequently estimate the permeability of the periodic porous structure. We compare our permeability estimate with the numerical solution to the cell problem for two examples, and find good agreement between the solutions.

In Chapter 5, we present a model for the two phase flow of oil and water through a network of pores and throats. We assume that both phases are present throughout the network, with the oil phase occupying the centres of the pores, and forming slugs along the length of the throats. By using the result from Chapter 2 that the radii of curvature of the advancing and receding menisci of the oil slugs in a given throat are identical, we show that the conductivity of the throat is independent of the number of oil slugs formed, and depends only on the saturation of each phase within the throat. This result enables us to only track the saturation within the pores and throats, rather than the position of each phase, in order to avoid interface-tracking issues which arise in similar two-phase flow models. We include the effects of salinity in our model by assuming that there is a thin water layer separating the oil slugs from the pore throats, with thickness determined by the salinity. Since an increase in the slip length is mathematically equivalent to an increase in the throat radius, we assume that the entry pressure of a given throat varies with the slip length. We numerically solve our network model to simulate a waterflood process, separating the simulation into two stages. First, we suppose that oil invades the water-filled network by the action of capillary forces in order to simulate the initial formation of

an oil reservoir; we refer to this stage as the 'drainage' stage. Second, we perform a 'waterflood' stage by injecting water into the steady-state solution obtained during the drainage stage in order to remove oil. We compare the total oil recovered during a high-salinity waterflood and a low-salinity waterflood, and find that, while the initial rate of recovery is the same in both cases, the low salinity waterflood produces 15% more oil. We find that the increase in the amount of oil produced is also observed when performing the low-salinity injection as a tertiary process. Hence, our network model is able to reproduce the low salinity effect observed experimentally, as both a secondary and tertiary process.

In Chapter 6, we use the method of multiple scales to homogenise network models of fluid flow. We first present the method for a model of single-phase flow in one dimension. In contrast to the standard multiple scales method applied to a continuum model, our microscale is described by a discrete pore index and we assume that our macroscale spatial variable is continuous. We find that the pressure is locally uniform, but varies on the macroscopic scale. We show that the macroscale equations for the homogenised pressure are of the form of a one-dimensional Darcy law, and we derive an expression for the permeability of the network in terms of the network structure. We then apply the multiple scales method to the two-phase flow model developed in Chapter 5, in which ions are advected with the water phase. We consider the case in which the effects of entry pressure are neglected for a two-dimensional network. This case is significantly more complex than the single-phase flow model due to the fact that the conductivities of the throats in the model depend on the pressure, saturation, and salinity. Similarly to the single-phase flow model, we find that the pressure, saturation, and ion concentrations are locally uniform but vary on the macroscopic scale. We show that the macroscale equations are of the form of Darcy's law for the pressure, coupled to advection equations for the saturation and ion concentrations. We numerically compare our homogenised model with the full network model for a one-dimensional network constructed from n repetitions of a 10-node cell, and we find excellent agreement in the limit in which n is large. Since we neglect the effects of entry pressure in our model, we find that there is no mechanism for oil to become trapped and therefore the total oil recovered during a waterflood is the same in the low-salinity and high-salinity regimes. Finally, we apply the multiple scales method to the full network model presented in Chapter 5, including the effects of entry pressure. Since the direction of flow through each throat in the cell is important when entry pressure is included, we restrict our attention to the one-dimensional network models due to the fact that the flow direction is known *a priori.* in this case. We use the

result from Chapter 5 that the capillary pressures within the pores are monotonic functions of the saturation, and therefore we formulate the entry pressures of the throats as equivalent 'entry saturations' associated with the upstream pores. We find that, similarly to the case in which entry pressures are neglected, the pressure, throat saturation, and ion concentrations are locally uniform. However, since oil cannot enter a downstream throat once the water saturation in the upstream pore exceeds the entry saturation, we find that the water saturation within each pore of the network is limited by the entry saturation. Therefore, the saturation in the pores is not locally uniform, and is instead equal to the minimum of the entry saturation and the locally-uniform throat saturation. This leads to a one-to-one relationship between the saturation in the throats and the cell-averaged saturation in the pores. We show that the homogenised macroscale equations are of the form of a one-dimensional Buckley-Leverett model for the cell-averaged pore saturation, in which the fractional flow function is given by the saturation in the throats, coupled to advection equations for the ion concentrations. We compare our homogenised model with the full network model for a network constructed from n repetitions of a 10-node cell. We again find excellent agreement between the two solutions in the limit in which n is large. We compare a high-salinity waterflood with a low-salinity waterflood, and find that the our model is able to reproduce the low salinity effect in which the total amount of oil recovered increases in the low-salinity regime. We derive an analytic expression for the residual oil saturation as a function of the salinity, and show that the residual oil saturation decreases as the salinity decreases.

7.2 Future work

One of the main limitations of the oil-slug model presented in Chapter 2 is that we restricted our attention to two-dimensional flow. While we expect the slip length to remain the same when we extend to three-dimensional slug-flow models (since it is determined by a balance between the electrostatic pressure and capillary pressure), the interface profile, and therefore the correction to the velocity of the oil slug due to the difference between the radii of the front and rear menisci, may be different in the two cases. This becomes especially important when considering slug flow through non-uniform throats, such as the elliptical channels with varying cross section studied in Chapter 3. Further work would be required to combine the results from these two chapters in order to study slug flow through a non-uniform channel in both two and three dimensions.

A further extension to the work presented in Chapter 2, which would be important in order to apply the results to a realistic scenario, would be to include the effects of surface heterogeneity in the model. Surface heterogeneity may arise as the result of surface roughness [82], or due to pinning regions [13, 89], in which the oil phase is only in effective contact with the pore surface in certain regions.

The model for flow through a channel with varying elliptic cross section presented in Chapter 3 could be extended to allow the central axis of the channel to be curved. By assuming that the curvature of the central axis is small in comparison to the width of the channel, we would expect the final expression for the flux to remain unchanged. However, this assumption may not be reasonable when using the elliptical model to approximate a pore throat, and higher order effects due to the curvature of the channel would need to be considered. Similarly, higher-order effects due to the torsion of the channel could be important in some cases, in which case it would be necessary to extend the model to include these effects.

In Chapter 4, we restricted our attention to periodic porous structures constructed from two-dimensional cells. To apply the method for estimating the permeability to a real sample of porous rock, a three-dimensional model would be required. The process for extracting the appropriate network structure would be more complicated in this case. However, existing methods for doing this are discussed in Chapter 3. In the three-dimensional case, the conductivities of the pore throats could be modelled using the elliptical channel model presented in Chapter 3. Furthermore, the network model itself would be unchanged in this case, since the model depends only on the conductivity-weighted adjacency matrix, not the spatial position of each of the nodes.

The network model for two phase flow presented in Chapter 5 could be extended to allow the advancing and receding capillary pressures to be different. This would enable us to include the effect of changes in the contact angle associated with changes in the composition of the underlying rock. However, in this case, we would need to keep track of the number of oil slugs produced or destroyed at each throat/pore interface, since the effective conductivity of each throat would depend on both the volume fraction of the two phases and the number of slugs within the throat at any given time. In order to avoid the issues which arise in interface-tracking models, which we discuss in Chapter 5, it may be possible to derive a model in which only the number of oil slugs being created or destroyed is tracked, not the position of each interface. Such a model would be useful for the network homogenisation process used in Chapter 6, since the slug creation process becomes important when the saturation of a pore reaches the entry saturation of the downstream throat.

In Chapter 6, we limited our study of the full network model, with the effects of entry pressure included, to the one dimensional case, since this enabled us to impose the flow direction *a priori*. In order to extend this work to multiple spatial dimensions, a framework for determining the local flow direction would be required. By comparison with the two-dimensional case in which the effects of entry pressure are neglected, we would still expect the leading-order pressure to be locally uniform. Hence, the flow direction would be determined by first-order variation in the pressure, which is given by the solution to the cell problem in each spatial direction multiplied by the macroscopic pressure gradient. However, the cell problem which defines the first-order pressure depends on the saturation in the throats, which in turn depends on the flow direction and therefore also depends on the first-order pressure. Therefore, for the multiple spatial dimension case, the cell problem is coupled to the macroscopic pressure gradient, which complicates the mathematics considerably.

7.3 Closing remarks

The research described in this thesis was motivated by the experimental observation that the injection of lower salinity water during the oil recovery process can lead to an increase in the amount of oil recovered. Experimental evidence suggests that the presence of salt ions in an oil reservoir causes oil to adhere to the clay particles in the rocks. The injection of low salinity water disrupts this bond, releasing the oil, and enabling the additional oil recovery. In this thesis, we have modelled the microscale ion-exchange reactions, and, by using a number of upscaling methods, we have successfully developed a macroscale model for the oil recovery process in which the effect of salinity is included. Although our model is simplistic in many respects, due to the number of assumptions we have made, we are able to use it to predict the low salinity effect observed experimentally.

Whilst the microscale reactions, and the macroscopic low-salinity recovery process, are well understood in an industrial setting, there is a limited understanding of how to quantitatively describe the low salinity effect in terms of the ion-exchange mechanisms. The work in this thesis provides a framework for bridging the gap between the microscale reactions and the macroscale injection process, and gives key insights into the effect of the salinity at each length scale in the problem. It is our hope that the methodology outlined in this thesis may provide a foundation from which a comprehensive, quantitative theory for the effect of salinity on the oil recovery process may be developed.

Appendix A

Transition region boundary conditions

At first glance it may appear that there are not enough boundary conditions to solve the fourth-order differential equation, (2.126). In order to examine this, we consider the behaviour of H as $Y \to \pm\infty$.

As $Y \to -\infty$, we set $H = H^* + \bar{H}$, and linearise in $\bar{H}(Y)$, to give

$$\bar{H}_{YYY} - a\bar{H}_Y - b\bar{H} = 0, \tag{A.1}$$

where

$$a = \frac{2}{\Gamma \sinh^3 H^*}\left[(s^{*2}\sigma_{o0}^2 + \sigma_{c0}^2)\cosh H^* + (\cosh^2 H^* + 1)s^*\sigma_{o0}\sigma_{c0}\right], \tag{A.2}$$

$$b = \frac{6P^*V}{\epsilon_2^{3/2}\Gamma H^{*3}}. \tag{A.3}$$

The solution is

$$\bar{H} = A_1 \mathrm{e}^{k_1 Y} + A_2 \mathrm{e}^{k_2 Y} + A_3 \mathrm{e}^{k_3 Y}, \tag{A.4}$$

where k_i are the roots of $k^3 - ak - b = 0$. By rescaling $k = b^{1/3}\hat{k}$, we can show that finding these roots is equivalent to finding the roots of

$$\hat{k}^3 - \frac{a}{b^{2/3}}\hat{k} - 1 = 0. \tag{A.5}$$

This equation has precisely two roots with negative real part, and one root with positive real part, for any real value of $ab^{-2/3}$. A plot of the real part of these roots is given in Figure A.1.

We require $\bar{H}$ to decay as $Y \to -\infty$. At the front meniscus, $V > 0$, so $b > 0$; hence, the coefficients of the two exponentials corresponding to the roots with negative real part must be zero. Thus, the boundary condition $H \to H^*$ (for unknown H^*) as $Y \to -\infty$ eliminates two degrees of freedom of the solution.

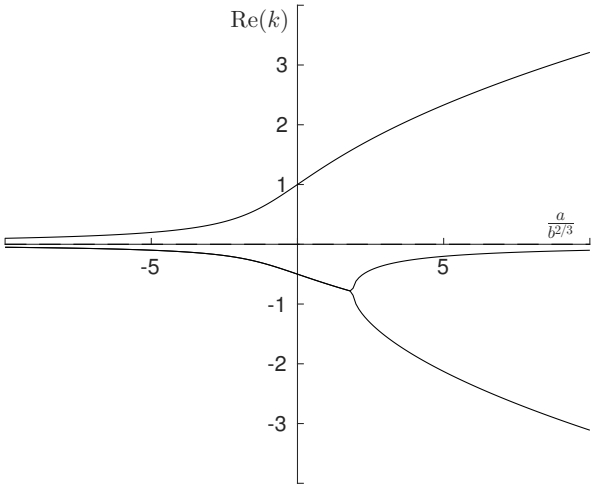


Figure A.1: Plot of the real parts of the roots of (A.5) as $\frac{a}{b^{2/3}}$ varies.

By translational invariance, we can set the final coefficient in (A.4) to be unity without loss of generality. Hence, as $Y \to -\infty$ in the front meniscus region, the film thickness is given by

$$H \sim H^* + \mathrm{e}^{k_1 Y}. \tag{A.6}$$

The remaining degree of freedom, H^*, is constrained by the condition $H_{YY} \to 1$ as $Y \to \infty$. Hence, the two boundary conditions (2.127) and (2.128) are sufficient to solve (2.126) (for $V > 0$, i.e. at the front of the oil slug), and to determine H^*. Numerically, we find H^* by using a shooting method. We treat (2.129) as an initial value problem, using (A.6) as the initial value, and vary H^* until $\lim_{Y\to\infty} H_{YY} = 1$.

At the rear meniscus, we solve the same differential equation with $V < 0$. In this case, $b < 0$, so $k = b^{1/3}\hat{k}$ has only one root with negative real part, and thus only one coefficient is determined (to be zero) in (A.4). After setting one of the remaining coefficients to be unity by translational invariance, there is still one degree of freedom. Explicitly,

$$H \sim H^* + \mathrm{e}^{k_1 Y} + A\mathrm{e}^{k_2 Y}, \tag{A.7}$$

as $Y \to -\infty$, for some A to be determined. Since H^* is determined by the solution to the equation at the front meniscus, this leaves one unknown to be found, which is determined by imposing the condition $H_{YY} \to 1$ as $Y \to \infty$. Hence, (2.127) and (2.128) are sufficient to solve (2.126) for $V < 0$, provided H^* is known. This is what we expect; the shape of the front end of the oil slug determines the film thickness, which in turn determines the shape of the rear end of the oil slug, i.e. the

information travels in the direction of the flow in a frame of reference in which the oil slug is stationary.

To determine A numerically, we solve (2.129) using a shooting method, similarly to the $V > 0$ case. We use (A.7) as the initial value, and vary A until $\lim_{Y\to\infty} H_{YY} = 1$.

It can be shown that the roots of (A.5) with negative real part are complex-valued for $ab^{-2/3} < 3/2^{2/3}$. Thus, the rear of the oil slug is non-monotonic for

$$P^*V > \frac{\epsilon_2^{3/2}\sqrt{2\Gamma}H^{*3}}{9\sqrt{3}\sinh^{3/2} H^*}\sqrt{(s^{*2}\sigma_{o0}^2 + \sigma_{c0}^2)\cosh H^* + (\cosh^2 H^* + 1)s^*\sigma_{o0}\sigma_{c0}}. \quad \text{(A.8)}$$

Using equation (2.158) to estimate the velocity at leading order, we find that this inequality holds for approximately $P^* > 7.2 \times 10^{-4}$ in the high salinity regime, and $P^* > 1.6 \times 10^{-3}$ in the low salinity regime, where σ_{c0} and σ_{o0} are given by (2.107) and the values for the dimensionless parameters are given in Table 2.2.

The limit of (A.1) in which the electrostatics become unimportant is given by $a \to 0$. In this limit, (A.8) is satisfied and thus the profile of the rear meniscus is non-monotonic. This is in agreement with the Bretherton model of a bubble moving through a capillary tube [15], in which electrostatic effects are neglected.

Appendix B

Capillary-pressure-saturation relationship

The capillary pressure between the two phases in a pore depends on both the saturation and the geometry of the pore. As a simple example, we consider a square pore in two dimensions as shown in Figure B.1. We suppose that the pore has sides of length $2R^p$, and that the radius of the throat through which the invading phase enters is R^t. We non-dimensionalise by scaling the lengths with $2R^p$, so that the pore has dimensionless side-length of unity.

Following the approach of Joekar-Niasar *et al.* [46], we separate the pore-filling process into five stages, shown in Figure B.1. These are

- Stage I: The invading phase first enters the pore, and the curvature of the interface is determined by the radius of the entry throat.
- Stage II: The invading phase is pinned at the corners of the entry throat, occupying a truncated circular region which expands within the pore until the interface reaches the edges of the pore.
- Stage III: The interface of the invading fluid advances through the pore until it reaches the side opposite the entry throat.
- Stage IV: The interface remains pinned at the entry throat corners, and the curvature of the interface increases until it lies tangentially to the pore walls.
- Stage V: The interface expands into the corners of the pore, with the curvature of the interface increasing in order to remain tangential to the pore walls.

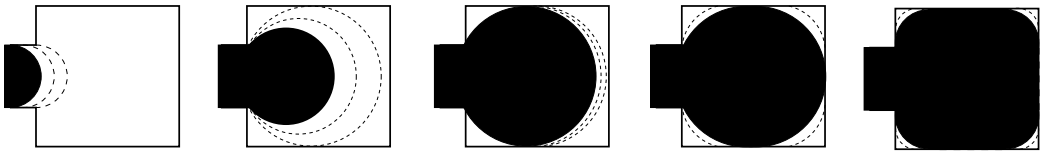


Figure B.1: Schematic diagram showing the five stages of the pore-filling process.

During stage I, when the invading phase first enters the pore, the curvature of the interface is determined by the radius of the pore throat through which the fluid enters, and the capillary pressure is given by

$$P^c = 4\Gamma_{\mathcal{P}}, \tag{B.1}$$

where $\Gamma_{\mathcal{P}} = \gamma/R^t\mathcal{P}$ is the ratio of the surface tension-induced pressure to the applied pressure, $\mathcal{P}$. The capillary pressure remains at this value until the invading fluid reaches the corners of the entrance to the pore, forming a semi-circular cap. By subtracting the area of the semi-circular oil region from the area of the pore, we find that the water saturation at the end of stage I is given by $S = 1 - \frac{\pi}{8}R^{*2}$, where $R^* = R^t/R^p$ is the ratio of the throat radius to the pore radius. Hence, for $1 - \frac{\pi}{8}R^{*2} < S \leq 1$, the capillary pressure is given by (B.1).

During stage II, the invading phase forms a truncated circle, with the edge of the circle being pinned to the two corners at the entrance of the pore. By computing the area outside the truncated circle, for a given radius r, we find that the saturation during this stage is given by

$$S = 1 - r^2\left(\pi - \arcsin\left(\frac{R^*}{2r}\right) + \frac{R^*}{2r}\sqrt{1 - \left(\frac{R^*}{2r}\right)^2}\right). \tag{B.2}$$

The capillary-pressure-saturation relationship may then be found implicitly from $P^c = 2R^*\Gamma_{\mathcal{P}}/r$. As the saturation decreases, r increases until $r = 1/2$, at which point the invading phase touches the upper and lower pore walls and the saturation is given by

$$S = 1 - \frac{1}{4}\left(\pi - \arcsin R^* + R^*\sqrt{1 - R^{*2}}\right). \tag{B.3}$$

During stage III, the advancing front moves forward with constant curvature, and the capillary pressure remains constant, given by $P^c = 4R^*\Gamma_{\mathcal{P}}$, until the interface reaches the far pore wall. We compute the saturation at which the interface touches the far pore wall by computing the area of the water region, which reads

$$S = 1 - \frac{1}{4}\left(2 + \pi - \arcsin R^* + (R^* - 2)\sqrt{1 - R^{*2}}\right). \tag{B.4}$$

During stage IV, the invading phase is pinned to the corners at the entrance of the pore, and the saturation is given by

$$S = r^2 \left(2 - \pi + \arcsin\left(\frac{2r + R^* - 1}{2r} \right) + \frac{2r - R^* + 1}{2r} \sqrt{1 - \left(\frac{2r + R^* - 1}{2r} \right)^2} \right), \quad \text{(B.5)}$$

where r is the radius of curvature of the invading fluid in the corners of the pore. The capillary pressure is determined implicitly using $P^c = 2R^*\Gamma_{\mathcal{P}}/r$, and increases until the fluid interface lies tangentially to the pore wall, at which point $r = (1 - R^*)/2$.

In the final stage, the invading phase is squeezed into the corners of the pore, and the saturation is found by computing the area outside the quarter-circular regions with radius r in each of the four corners of the pore, which reads

$$S = (4 - \pi)\, r^2. \quad \text{(B.6)}$$

Hence, by substituting $P^c = 2R^*\Gamma_{\mathcal{P}}/r$ and rearranging, we find that the capillary pressure is given by

$$P^c = 2R^*\Gamma_{\mathcal{P}} \sqrt{\frac{4 - \pi}{S}}. \quad \text{(B.7)}$$

In Figure B.2 we plot the capillary pressure, given by (B.1) – (B.7), against the saturation, for $R^* = 0.5$ and $\Gamma_{\mathcal{P}} = 0.2$, indicating each stage of the invasion process using dashed red lines. During stages I and III, the capillary pressure is constant as the saturation varies, during stage II, the capillary pressure decreases as the saturation decreases, and, during stages IV and V, the capillary pressure increases as the saturation decreases, asymptotically approaching a singularity at $S = 0$. Since the capillary pressure must be greater than the throat entry pressure in order for the invading phase to enter the throat in the first place, we find that, when the invading fluid first enters the pore, the pore rapidly fills to the point during the fourth or fifth stage of the pore-filling process at which the capillary pressure is equal to the entry pressure of the throat. Hence, the pore fills instantaneously, so we can simplify the capillary-pressure-saturation function by neglecting the first three stages of the pore filling process during invasion. In Figure B.3, we show a schematic diagram of how the saturation 'jumps' as the invading fluid enters the pore, and we highlight in red the section of the capillary-pressure-saturation function which may be inverted to determine the saturation during invasion.

To simplify the computations, we approximate the fourth and fifth stages of the pore filling process using a power-law model. We suppose that the capillary pressure is of the form $2R^*\Gamma_{\mathcal{P}}/aS^b$ in regions IV and V, rearrange to write $\log a + b \log S =$

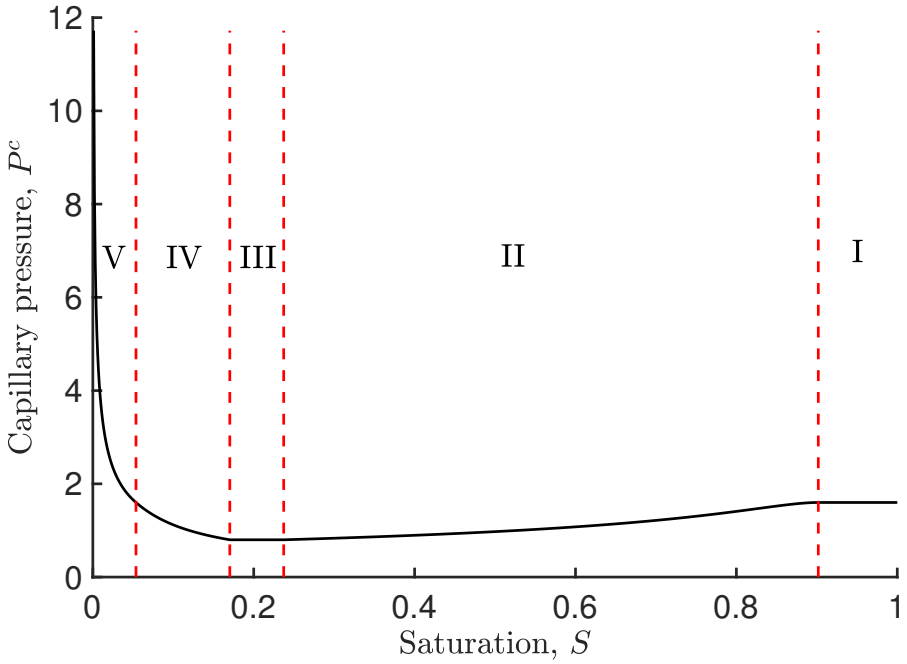


Figure B.2: Graph showing the dimensionless capillary pressure, given by (B.1) – (B.7), as a function of the saturation with $R^* = 0.5$ and $\Gamma_{\mathcal{P}} = 0.2$. The boundaries of the five stages of the invasion process are shown with dashed red lines.

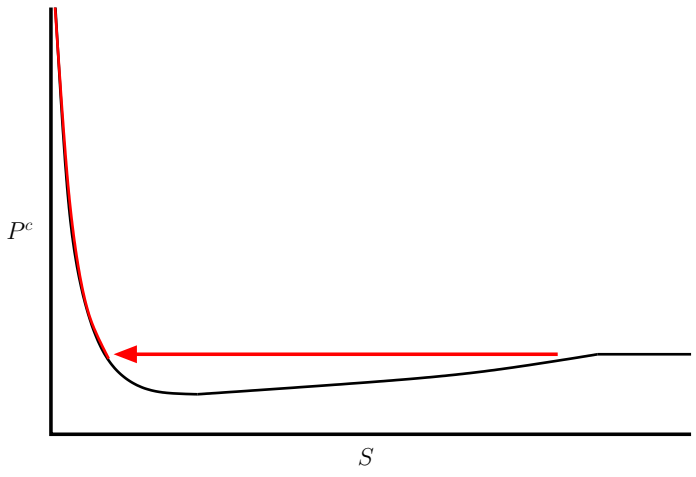


Figure B.3: Schematic diagram of the saturation rapidly decreasing during the pore-filling process, in order for the capillary pressure in the pore to match the capillary pressure of the entry throat. The region highlighted in red indicates the permissible range of capillary pressures and saturations after the initial invasion phase has taken place.

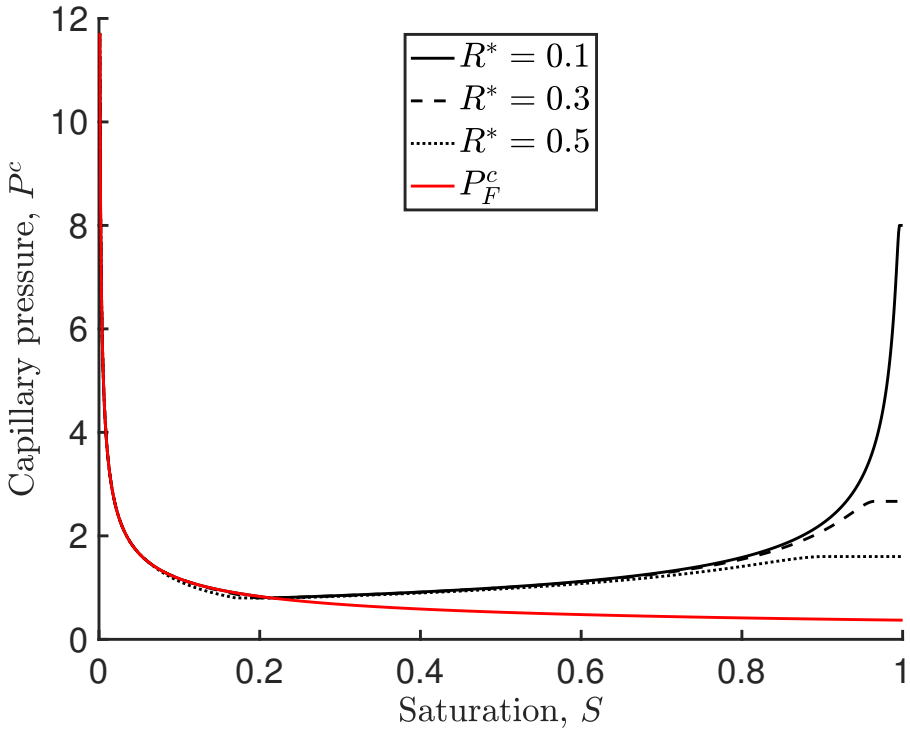


Figure B.4: Plots of the capillary pressure as a function of the saturation, given by (B.1) – (B.7), with $R^* = 0.1, 0.3, 0.5$ and $\Gamma_{\mathcal{P}} = 0.2$, compared with the fitted solution, P_F^c, given by (B.8).

$\log(2R^*\Gamma_{\mathcal{P}}/P^c)$, and fit $\log a$ and b to the solution for $R^* = 0.3$ in regions IV and V using a least-squares algorithm, to find that $a \approx 1.1 \approx 1/\sqrt{4-\pi}$, and $b \approx 0.5$. We therefore define

$$P_F^c := 2R^*\Gamma_{\mathcal{P}}\sqrt{\frac{4-\pi}{S}}, \tag{B.8}$$

to be our 'fitted' capillary pressure curve, valid in regions IV and V, noting that this is simply the extension of (B.7) into region IV. In Figure B.4, we plot (B.8) against the full capillary pressure model, (B.1) – (B.7), for $R^* = 0.1, 0.3, 0.5$. We see that R^* has little impact on the solution in stages IV and V, and that the power-law model is in good agreement with the solutions for all values of R^* in these latter stages of the invasion process. This is important, since $R^*\Gamma_{\mathcal{P}} = \gamma/R^p\mathcal{P}$ is independent of the throat radius and therefore our fitted capillary pressure curve, given by (B.8), depends only on the size of the pore. Hence, we can use a single capillary-pressure-saturation relationship for each pore in our network during the drainage stage, regardless of the throat through which the invading phase enters.

During a waterflood process, the pore is initially oil-filled. Hence, the saturation is

low and the capillary pressure is determined by the region highlighted in red in Figure B.3. As water is injected, oil is expelled from the pore through an exit throat, and the water saturation increases. The capillary pressure decreases until it reaches the entry pressure of the exit throat. At this point, oil cannot exit the pore, and therefore the saturation cannot increase further. Hence, the pore remains filled according to stages IV and V of the filling process, and therefore we can use (B.8) to approximate the capillary-pressure-saturation relationship during waterflooding, as well as during drainage.

Appendix C

Matrix properties

In this appendix, we prove some basic properties of the matrices defined by (6.44) – (6.56). Summing over the columns of $\boldsymbol{A}$ yields

$$\sum_j \boldsymbol{A}_{ij} = \sum_{r=-1}^{1}\sum_{s=-1}^{1}\sum_{k=1}^{N} G_{ik}^{rs} - \sum_{j=1}^{N}\sum_{r=-1}^{1}\sum_{s=-1}^{1} G_{ij}^{rs} = 0, \tag{C.1}$$

which we write in vector form as $\boldsymbol{A}\mathbf{u} = 0$, where $\mathbf{u} = (1, 1, \cdots, 1)^T$. A similar analysis yields $\boldsymbol{B}'\mathbf{u} = \boldsymbol{C}''\mathbf{u} = \boldsymbol{D}_x\mathbf{u} = \boldsymbol{D}_y\mathbf{u}$. Since $\boldsymbol{A}$, $\boldsymbol{D}_x$, and $\boldsymbol{D}_y$ are symmetric, it follows that $\mathbf{u}^T\boldsymbol{A} = \mathbf{u}^T\boldsymbol{D}_x = \mathbf{u}^T\boldsymbol{D}_y = 0$.

Summing over the rows and columns of $\boldsymbol{B}_x$, and substituting (6.36), yields

$$\sum_i\sum_j \boldsymbol{B}_{xij} = \sum_i\sum_j\sum_{r=-1}^{1}\sum_{s=-1}^{1}(-rL_x + x_j - x_i)G_{ij}^{rs} \tag{C.2}$$

$$= \sum_i\sum_j\sum_{r=-1}^{1}\sum_{s=-1}^{1} -rL_x G_{ij}^{rs} + \sum_{r=-1}^{1}\sum_{s=-1}^{1}\sum_i\sum_j (x_j - x_i)G_{ij}^{rs} \tag{C.3}$$

$$= 0, \tag{C.4}$$

since

$$\sum_i\sum_j\sum_{r=-1}^{1}\sum_{s=-1}^{1} -rL_x G_{ij}^{rs} = \sum_i\sum_j\sum_{r=-1}^{1}\sum_{s=-1}^{1} -rL_x G_{ji}^{-r-s} \qquad (G_{ij}^{rs} = G_{ji}^{-r-s}) \tag{C.5}$$

$$= \sum_i\sum_j\sum_{p=-1}^{1}\sum_{q=-1}^{1} pL_x G_{ji}^{pq} \qquad (p = -r, q = -s) \tag{C.6}$$

$$= \sum_i\sum_j\sum_{r=-1}^{1}\sum_{s=-1}^{1} rL_x G_{ij}^{rs} \qquad \text{(Relabelling indices)} \tag{C.7}$$

$$= 0, \tag{C.8}$$

and

$$\sum_i \sum_j \sum_{r=-1}^{1} \sum_{s=-1}^{1} (x_i - x_j) G_{ij}^{rs} = \sum_i \sum_j \sum_{r=-1}^{1} \sum_{s=-1}^{1} (x_i - x_j) G_{ji}^{-r-s} \quad (G_{ij}^{rs} = G_{ji}^{-r-s}) \tag{C.9}$$

$$= \sum_i \sum_j \sum_{p=-1}^{1} \sum_{q=-1}^{1} (x_i - x_j) G_{ji}^{pq} \qquad (p = -r, q = -s) \tag{C.10}$$

$$= \sum_i \sum_j \sum_{r=-1}^{1} \sum_{s=-1}^{1} (x_j - x_i) G_{ij}^{rs} \qquad \text{(Relabelling indices)} \tag{C.11}$$

$$= 0. \tag{C.12}$$

We write (C.4) in vector form as $\mathbf{u}^T \boldsymbol{B}_x \mathbf{u} = 0$. A similar analysis yields $\mathbf{u}^T \boldsymbol{B}_y \mathbf{u} = 0$.

Bibliography

[1] A. Adamson and A. Gast, *Physical chemistry of surfaces*, Interscience publishers, New York, 1967.

[2] M. I. Aissen, *On the estimation and computation of torsional rigidity*, Ph.D. thesis, Department of Mathematics, Stanford University, 1951.

[3] M. S. Al-Gharbi and M. J. Blunt, *Dynamic network modeling of two-phase drainage in porous media*, Physical Review E **71** (2005), no. 1, 016308.

[4] A. S. Al-Kharusi and M. J. Blunt, *Multiphase flow predictions from carbonate pore space images using extracted network models*, Water Resources Research **44** (2008), no. 6, W06S01.

[5] C. Andresen, *Physical chemistry of mechanisms for low salinity waterflood*, Master's thesis, Department of Chemistry, The University of Bergen, 2013.

[6] F. Arand and J. Hesser, *Accurate and efficient maximal ball algorithm for pore network extraction*, Computers & Geosciences **101** (2017), 28–37.

[7] T. Austad, A. RezaeiDoust, and T. Puntervold, *Chemical mechanism of low salinity water flooding in sandstone reservoirs*, SPE improved oil recovery symposium, Society of Petroleum Engineers, 2010, p. 129767.

[8] M. Bahrami, A. Tamayol, and P. Taheri, *Slip-flow pressure drop in microchannels of general cross section*, Journal of Fluids Engineering **131** (2009), no. 3, 031201.

[9] D. Ben-Yaakov and D. Andelman, *Revisiting the Poisson-Boltzmann theory: Charge surfaces, multivalent ions and inter-plate forces*, Physica A: Statistical Mechanics and its Applications **389** (2010), no. 15, 2956–2961.

[10] A. Bensoussan, J.-L. Lions, and George Papanicolaou, *Asymptotic analysis for periodic structures*, vol. 374, American Mathematical Soc., 2011.

[11] D. P. Bentz and N. S. Martys, *Hydraulic radius and transport in reconstructed model three-dimensional porous media*, Transport in Porous Media **17** (1994), no. 3, 221–238.

[12] S. Berg, A. Cense, E. Jansen, and K. Bakker, *Direct experimental evidence of wettability modification by low salinity*, Petrophysics **51** (2010), no. 5, 314–322.

[13] P. V. Brady, N. R. Morrow, A. Fogden, V. Deniz, and N. Loahardjo, *Electrostatics and the low salinity effect in sandstone reservoirs*, Energy & Fuels **29** (2015), no. 2, 666–677.

[14] O. M. Braun and C. A. Sholl, *Diffusion in generalized lattice-gas models*, Physical Review B **58** (1998), no. 22, 14870–14879.

[15] F. P. Bretherton, *The motion of long bubbles in tubes*, Journal of Fluid Mechanics **10** (1961), no. 2, 166–188.

[16] H. C. Brinkman, *A calculation of the viscous force exerted by a flowing fluid on a dense swarm of particles*, Flow, Turbulence and Combustion **1** (1949), no. 1, 27–34.

[17] R. H. Brooks and A. T. Corey, *Properties of porous media affecting fluid flow*, Journal of the Irrigation and Drainage Division **92** (1966), no. 2, 61–90.

[18] J. S. Buckley, *Mechanisms and consequences of wettability alteration by crude oils*, Ph.D. thesis, Department of Petroleum Engineering, Heriot-Watt University, 1996.

[19] J. S. Buckley, K. Takamura, N. R. Morrow, et al., *Influence of electrical surface charges on the wetting properties of crude oils*, SPE Reservoir Engineering **4** (1989), no. 3, 332–340.

[20] S. E. Buckley and M. C. Leverett, *Mechanism of fluid displacement in sands*, Transactions of the AIME **146** (1942), no. 1, 107–116.

[21] S. J. Chapman and A. Shabala, *Effective transport properties of lattices*, SIAM Journal on Applied Mathematics **77** (2017), no. 5, 1631–1652.

[22] R. R. Cohen and C. J. Radke, *Streaming potentials of nonuniformly charged surfaces*, Journal of Colloid and Interface Science **141** (1991), no. 2, 338–347.

[23] A. T. Corey et al., *The interrelation between gas and oil relative permeabilities*, Producers monthly **19** (1954), no. 1, 38–41.

[24] H. K. Dahle and M. A. Celia, *A dynamic network model for two-phase immiscible flow*, Computational Geosciences **3** (1999), no. 1, 1–22.

[25] P. G. de Gennes, *On fluid/wall slippage*, Langmuir **18** (2002), no. 9, 3413–3414.

[26] B. V. Derjaguin and L. Landau, *Theory of the stability of strongly charged lyophobic sols and of the adhesion of strongly charged particles in solutions of electrolytes*, Acta physicochim. URSS **14** (1941), no. 6, 633–662.

[27] Z. Duan and Y. S. Muzychka, *Slip flow in elliptic microchannels*, International Journal of Thermal Sciences **46** (2007), no. 11, 1104–1111.

[28] A. G. Egorov, K. G. Kornev, and A. V. Neimark, *Meniscus motion in a prewetted capillary*, Physics of Fluids (1994-present) **15** (2003), no. 10, 3134–3143.

[29] D. Erickson and D. Li, *Streaming potential and streaming current methods for characterizing heterogeneous solid surfaces*, Journal of Colloid and Interface Science **237** (2001), no. 2, 283–289.

[30] E. Eslinger and D. Pevear, *Clay minerals for petroleum geologists and engineers*, Society of Economic Paleontologists and Mineralogists, 1988.

[31] P. Fletcher and G. Sposito, *Chemical modeling of clay/electrolyte interactions of montmorillonite*, Clay Minerals **24** (1989), no. 2, 375–391.

[32] P. Fournier, E. H. Oelkers, R. Gout, and G. Pokrovski, *Experimental determination of aqueous sodium-acetate dissociation constants at temperatures from 20 to 240 C*, Chemical Geology **151** (1998), no. 1, 69–84.

[33] S. Ghosal, *Lubrication theory for electro-osmotic flow in a microfluidic channel of slowly varying cross-section and wall charge*, Journal of Fluid Mechanics **459** (2002), 103–128.

[34] S. Godoy and L. S. Garcia-Colin, *From the quantum random walk to classical mesoscopic diffusion in crystalline solids*, Physical Review E **53** (1996), no. 6, 5779–5785.

[35] B. Hassani and E. Hinton, *A review of homogenization and topology optimization I–homogenization theory for media with periodic structure*, Computers & Structures **69** (1998), no. 6, 707–717.

[36] R. J. Held and M. A. Celia, *Modeling support of functional relationships between capillary pressure, saturation, interfacial area and common lines*, Advances in Water Resources **24** (2001), no. 3-4, 325–343.

[37] J. O. Helland and S. M. Skjaeveland, *Relationship between capillary pressure, saturation, and interfacial area from a model of mixed-wet triangular tubes*, Water resources research **43** (2007), no. 12, W12S10.

[38] R. Hilfer, *Macroscopic equations of motion for two-phase flow in porous media*, Physical Review E **58** (1998), no. 2, 2090.

[39] G. Hirasaki, *Wettability: Fundamentals and surface forces*, SPE Formation Evaluation **6** (1991), no. 2, 217–226.

[40] S. Hodges and O. Jensen, *Spreading and peeling dynamics in a model of cell adhesion*, Journal of Fluid Mechanics **460** (2002), 381–409.

[41] R. G. Hughes and M. J. Blunt, *Pore scale modeling of rate effects in imbibition*, Transport in Porous Media **40** (2000), no. 3, 295–322.

[42] N. A. Idowu and M. J. Blunt, *Pore-scale modelling of rate effects in waterflooding*, Transport in porous media **83** (2010), no. 1, 151–169.

[43] P. Jadhunandan, *Effects of brine composition, crude oil, and aging conditions on wettability and oil recovery*, Ph.D. thesis, Department of Petroleum Engineering, New Mexico Institute of Mining & Technology, 1990.

[44] P. Jadhunandan and N. R. Morrow, *Spontaneous imbibition of water by crude oil/brine/rock systems*, In Situ;(United States) **15** (1991), no. 4, 319–345.

[45] P. Jadhunandan and N. R. Morrow, *Effect of wettability on waterflood recovery for crude-oil/brine/rock systems*, SPE Reservoir Engineering **10** (1995), no. 1, 40–46.

[46] V. Joekar-Niasar, S. M. Hassanizadeh, and H. K. Dahle, *Non-equilibrium effects in capillarity and interfacial area in two-phase flow: dynamic pore-network modelling*, Journal of Fluid Mechanics **655** (2010), 38–71.

[47] V. Joekar-Niasar, S. M. Hassanizadeh, and A. Leijnse, *Insights into the relationships among capillary pressure, saturation, interfacial area and relative permeability using pore-network modeling*, Transport in Porous Media **74** (2008), no. 2, 201–219.

[48] N. R. Joseph, *The dissociation constants of organic calcium complexes*, Journal of Biological Chemistry **164** (1946), no. 2, 529–541.

[49] K. W. Kehr, D Richter, and R. H. Swendsen, *The influence of impurities on interstitial diffusion*, Journal of Physics F: Metal Physics **8** (1978), no. 3, 433–446.

[50] S. Kirkpatrick, *Percolation and conduction*, Reviews of modern physics **45** (1973), no. 4, 574–588.

[51] L. J. Klinkenberg, *The permeability of porous media to liquids and gases*, Drilling and production practice, American Petroleum Institute, 1941, pp. 200–213.

[52] H. A. Knudsen, E. Aker, and A. Hansen, *Bulk flow regimes and fractional flow in 2D porous media by numerical simulations*, Transport in Porous Media **47** (2002), no. 1, 99–121.

[53] J. Koplik and T. J. Lasseter, *One-and two-phase flow in network models of porous media*, Chemical Engineering Communications **26** (1984), no. 4-6, 285–295.

[54] J. Koplik, C. Lin, and M. Vermette, *Conductivity and permeability from microgeometry*, Journal of Applied Physics **56** (1984), no. 11, 3127–3131.

[55] A. Kovscek, H. Wong, and C. Radke, *A pore-level scenario for the development of mixed wettability in oil reservoirs*, AIChE Journal **39** (1993), no. 6, 1072–1085.

[56] Z. Koza, *General technique of calculating the drift velocity and diffusion coefficient in arbitrary periodic systems*, Journal of Physics A: Mathematical and General **32** (1999), no. 44, 7637–7651.

[57] E. Kropat and S. Meyer-Nieberg, *Homogenization of singularly perturbed diffusion-advection-reaction equations on periodic networks*, IFAC Proceedings Volumes **45** (2012), no. 25, 83–88.

[58] I. V. Kuchin, O. K. Matar, R. V. Craster, and V. M. Starov, *Influence of the disjoining pressure on the equilibrium interfacial profile in transition zone between a thin film and a capillary meniscus*, Colloids and Interface Science Communications **1** (2014), 18–22.

[59] I. V. Kuchin, O. K. Matar, R. V. Craster, and V. M. Starov, *Modeling the effect of surface forces on the equilibrium liquid profile of a capillary meniscus*, Soft Matter **10** (2014), no. 32, 6024–6037.

[60] A. Lager, K. Webb, C. Black, M. Singleton, and K. Sorbie, *Low salinity oil recovery–an experimental investigation*, Petrophysics **49** (2008), no. 1, 28–35.

[61] D. Lasseux, M. Quintard, and S. Whitaker, *Determination of permeability tensors for two-phase flow in homogeneous porous media: theory*, Transport in Porous Media **24** (1996), no. 2, 107–137.

[62] S. Lee, K. Webb, I. Collins, A. Lager, S. Clarke, M. O'Sullivan, A. Routh, and X. Wang, *Low salinity oil recovery: Increasing understanding of the underlying mechanisms*, SPE improved oil recovery symposium, Society of Petroleum Engineers, 2010, p. 129722.

[63] Y. Levin, *Electrostatic correlations: From plasma to biology*, Reports on progress in physics **65** (2002), no. 11, 1577.

[64] W. C. M. Lewis, *The electric charge at an oil-water interface*, Transactions of the Faraday Society **33** (1937), 708–713.

[65] K. Li and R. N. Horne, *Comparison of methods to calculate relative permeability from capillary pressure in consolidated water-wet porous media*, Water resources research **42** (2006), no. 6, W06405.

[66] S. Li and R. Xu, *Electrical double layers interaction between oppositely charged particles as related to surface charge density and ionic strength*, Colloids and Surfaces A: Physicochemical and Engineering Aspects **326** (2008), no. 3, 157–161.

[67] D. J. Ligthelm, J. Gronsveld, J. Hofman, N. Brussee, F. Marcelis, and H. van der Linde, *Novel waterflooding strategy by manipulation of injection brine composition.*, EUROPEC/EAGE Conference and Exhibition, Society of Petroleum Engineers, 2009, p. 119835.

[68] W. B. Lindquist, S. M. Lee, D. A. Coker, K. W. Jones, and P. Spanne, *Medial axis analysis of void structure in three-dimensional tomographic images of porous media*, Journal of Geophysical Research: Solid Earth **101** (1996), no. B4, 8297–8310.

[69] C. G. Malmberg and A. A. Maryott, *Dielectric constant of water from 0 to 100 C*, J Res Nat Bureau Stand **56** (1956), 1–8.

[70] C. M. Marle, *On macroscopic equations governing multiphase flow with diffusion and chemical reactions in porous media*, International Journal of Engineering Science **20** (1982), no. 5, 643–662.

[71] D. McCormack, S. Carnie, and D. Chan, *Calculations of electric double-layer force and interaction free energy between dissimilar surfaces*, Journal of Colloid and Interface Science **169** (1995), no. 1, 177–196.

[72] P. L. McGuire, J. R. Chatham, F. K. Paskvan, D. M. Sommer, and F. H. Carini, *Low salinity oil recovery: An exciting new EOR opportunity for Alaska's North Slope*, SPE Western Regional Meeting, Society of Petroleum Engineers, 2005, p. 93903.

[73] D. Moore and R. Reynolds, *X-ray diffraction and the identification and analysis of clay minerals*, vol. 378, Oxford university press, Oxford, 1989.

[74] N. A. Mortensen, F. Okkels, and H. Bruus, *Reexamination of Hagen-Poiseuille flow: Shape dependence of the hydraulic resistance in microchannels*, Physical Review E **71** (2005), no. 5, 057301.

[75] T. G. Myers, *Thin films with high surface tension*, Siam Review **40** (1998), no. 3, 441–462.

[76] P. Nelson, *Pore-throat sizes in sandstones, tight sandstones, and shales*, AAPG bulletin **93** (2009), no. 3, 329–340.

[77] V. H. Nguyen, A. P. Sheppard, M. A. Knackstedt, and W. V. Pinczewski, *The effect of displacement rate on imbibition relative permeability and residual saturation*, Journal of Petroleum Science and Engineering **52** (2006), no. 1-4, 54–70.

[78] C. O'Carroll and K. S. Sorbie, *Generalization of the Poiseuille law for one-and two-phase flow in a random capillary network*, Physical Review E **47** (1993), no. 5, 3467.

[79] H. Ohshima, *Diffuse double layer interaction between two parallel plates with constant surface charge density in an electrolyte solution I*, Colloid and Polymer Science **252** (1974), no. 3, 158–164.

[80] H. Ohshima, *Diffuse double layer interaction between two parallel plates with constant surface charge density in an electrolyte solution II*, Colloid and Polymer Science **252** (1974), no. 3, 257–267.

[81] V. Parsegian and D. Gingell, *On the electrostatic interaction across a salt solution between two bodies bearing unequal charges*, Biophysical Journal **12** (1972), no. 9, 1192–1204.

[82] B. Raeesi, N. R. Morrow, and G. Mason, *Effect of surface roughness on wettability and displacement curvature in tubes of uniform cross-section*, Colloids and Surfaces A: Physicochemical and Engineering Aspects **436** (2013), 392–401.

[83] A. G. Ramm, *A simple proof of the fredholm alternative and a characterization of the fredholm operators*, The American Mathematical Monthly **108** (2001), no. 9, 855–860.

[84] A. RezaeiDoust, T. Puntervold, and T. Austad, *Chemical verification of the EOR mechanism by using low saline/smart water in sandstone*, Energy & Fuels **25** (2011), no. 5, 2151–2162.

[85] A. RezaeiDoust, T. Puntervold, S. Strand, and T. Austad, *Smart water as wettability modifier in carbonate and sandstone: A discussion of similarities/differences in the chemical mechanisms*, Energy & fuels **23** (2009), no. 9, 4479–4485.

[86] J. Rubinstein and R. Mauri, *Dispersion and convection in periodic porous media*, SIAM Journal on Applied Mathematics **46** (1986), no. 6, 1018–1023.

[87] E. Samson, J. Marchand, and K. A. Snyder, *Calculation of ionic diffusion coefficients on the basis of migration test results*, Materials and Structures **36** (2003), no. 3, 156–165.

[88] E. Sanchez-Palencia, *Homogenization in mechanics. A survey of solved and open problems*, Rend. Sem. Mat. Univ. Politec. Torino **44** (1986), no. 1, 1–45.

[89] J. Schmatz, J. L. Urai, S. Berg, and H. Ott, *Nanoscale imaging of pore-scale fluid-fluid-solid contacts in sandstone*, Geophysical research letters **42** (2015), no. 7, 2189–2195.

[90] O. Schnitzer, I. Frankel, and E. Yariv, *Streaming-potential phenomena in the thin-Debye-layer limit. Part 2. Moderate Péclet numbers*, Journal of Fluid Mechanics **704** (2012), 109–136.

[91] V. K. S. Shante and S. Kirkpatrick, *An introduction to percolation theory*, Advances in Physics **20** (1971), no. 85, 325–357.

[92] D. Shaw, *Introduction to colloid and surface chemistry*, Elsevier, 1992.

[93] Q. Sheng and K. Thompson, *A unified pore-network algorithm for dynamic two-phase flow*, Advances in Water Resources **95** (2016), 92–108.

[94] D. Silin and T. Patzek, *Pore space morphology analysis using maximal inscribed spheres*, Physica A: Statistical mechanics and its applications **371** (2006), no. 2, 336–360.

[95] S. Sisavath, X. Jing, and R. W. Zimmerman, *Creeping flow through a pipe of varying radius*, Physics of Fluids **13** (2001), no. 10, 2762–2772.

[96] S. Sisavath, X. Jing, and R. W. Zimmerman, *Laminar flow through irregularly-shaped pores in sedimentary rocks*, Transport in Porous Media **45** (2001), no. 1, 41–62.

[97] E. Skjetne and J. Auriault, *Homogenization of wall-slip gas flow through porous media*, Transport in porous Media **36** (1999), no. 3, 293–306.

[98] K. Sorbie and I. Collins, *A proposed pore-scale mechanism for how low salinity waterflooding works*, SPE Improved Oil Recovery Symposium, Society of Petroleum Engineers, 2010, p. 129833.

[99] V. M. Starov, V. V. Kalinin, and V. I. Ivanov, *Influence of surface forces on hydrodynamics of wetting*, Colloids and Surfaces A: Physicochemical and Engineering Aspects **91** (1994), 149–154.

[100] S. P. Sutera and R. Skalak, *The history of Poiseuille's law*, Annual Review of Fluid Mechanics **25** (1993), no. 1, 1–20.

[101] G. Q. Tang and N. R. Morrow, *Influence of brine composition and fines migration on crude oil/brine/rock interactions and oil recovery*, Journal of Petroleum Science and Engineering **24** (1999), no. 2, 99–111.

[102] L. H. Tanner, *The spreading of silicone oil drops on horizontal surfaces*, Journal of Physics D: Applied Physics **12** (1979), no. 9, 1473–1484.

[103] K. E. Thompson, *Pore-scale modeling of fluid transport in disordered fibrous materials*, AIChE journal **48** (2002), no. 7, 1369–1389.

[104] J. F. Thovert, J. Salles, and P. M. Adler, *Computerized characterization of the geometry of real porous media: their discretization, analysis and interpretation*, Journal of Microscopy **170** (1993), no. 1, 65–79.

[105] F. J. Valdes-Parada, J. A. Ochoa-Tapia, and J. Alvarez-Ramirez, *On the effective viscosity for the Darcy-Brinkman equation*, Physica A: Statistical Mechanics and its Applications **385** (2007), no. 1, 69–79.

[106] P. H. Valvatne and M. J. Blunt, *Predictive pore-scale modeling of two-phase flow in mixed wet media*, Water Resources Research **40** (2004), no. 7, W07406.

[107] V. Vancauwenberghe, P. Di Marco, and D. Brutin, *Wetting and evaporation of a sessile drop under an external electrical field: A review*, Colloids and Surfaces A: Physicochemical and Engineering Aspects **432** (2013), 50–56.

[108] E. J. W. Verwey and J. Th. G. Overbeek, *Theory of the stability of lyophobic colloids.*, Elsevier, 1948.

[109] O. I. Vinogradova, *Drainage of a thin liquid film confined between hydrophobic surfaces*, Langmuir **11** (1995), no. 6, 2213–2220.

[110] P. R. Waghmare and S. K. Mitra, *Investigation of combined electro-osmotic and pressure-driven flow in rough microchannels*, Journal of Fluids Engineering **130** (2008), no. 6, 061204.

[111] C. Y. Wang, *Stokes slip flow through square and triangular arrays of circular cylinders*, Fluid dynamics research **32** (2003), no. 5, 233–246.

[112] E. W. Washburn, *The dynamics of capillary flow*, Physical review **17** (1921), no. 3, 273–283.

[113] S. Whitaker, *Flow in porous media I: A theoretical derivation of Darcy's law*, Transport in porous media **1** (1986), no. 1, 3–25.

[114] S. Whitaker, *Flow in porous media II: The governing equations for immiscible, two-phase flow*, Transport in porous media **1** (1986), no. 2, 105–125.

[115] F. M. White, *Viscous fluid flow*, McGraw-Hill, 1991.

[116] H. Whitney, *Congruent graphs and the connectivity of graphs*, Hassler Whitney Collected Papers, Springer, 1992, pp. 61–79.

[117] Z. M. Wilmott, C. J. W. Breward, and S. J. Chapman, *The effect of ions on the motion of an oil slug through a charged capillary*, Journal of Fluid Mechanics **841** (2018), 310–350.

[118] Z. M. Wilmott, C. J. W. Breward, and S. J. Chapman, *Slip flow through channels with varying elliptic cross section*, IMA Journal of Applied Mathematics **83** (2018), no. 5, 874–893.

[119] H. Wong, S. Morris, and C. Radke, *Three-dimensional menisci in polygonal capillaries*, Journal of Colloid and Interface Science **148** (1992), no. 2, 317–336.

[120] H. Wong, C. J. Radke, and S. Morris, *The motion of long bubbles in polygonal capillaries. Part 1. Thin films*, Journal of Fluid Mechanics **292** (1995), 71–94.

[121] H. Wong, C. J. Radke, and S. Morris, *The motion of long bubbles in polygonal capillaries. Part 2. Drag, fluid pressure and fluid flow*, Journal of Fluid Mechanics **292** (1995), 95–110.

[122] L. Xiao, Q. Cai, X. Ye, J. Wang, and R. Luo, *Electrostatic forces in the Poisson-Boltzmann systems*, The Journal of Chemical Physics **139** (2013), no. 9, 094106.

[123] R. J. Yang, L. M. Fu, and C. C. Hwang, *Electroosmotic entry flow in a microchannel*, Journal of Colloid and Interface Science **244** (2001), no. 1, 173–179.

[124] H. Yildiz, *Effect of brine composition on oil recovery by waterflooding*, Ph.D. thesis, Department of Petroleum Engineering, New Mexico Institute of Mining & Technology, 1995.

[125] H. Yildiz and N. R. Morrow, *Effect of brine composition on recovery of Moutray crude oil by waterflooding*, Journal of Petroleum Science and Engineering **14** (1996), no. 3, 159–168.

[126] A. G. Yiotis, A. K. Stubos, A. G. Boudouvis, and Y. C. Yortsos, *A 2D pore-network model of the drying of single-component liquids in porous media*, Advances in Water Resources **24** (2001), no. 3-4, 439–460.